

The Magnetic Isotope Effect and Anomalous Case of Mercury Stable Isotope Fractionation

by

Laura Motta

A dissertation submitted in partial fulfillment
of the requirements for the degree of
Doctor of Philosophy
(Earth and Environmental Sciences and Chemistry)
in the University of Michigan
2019

Doctoral Committee:

Professor Joel D. Blum, Co-Chair
Associate Professor Paul M Zimmerman, Co-Chair
Associate Professor Rose Corey
Professor Brian N. Popp, University of Hawaii
Assistant Professor Kerri Pratt

Laura Motta Medina
laumot@umich.edu

ORCID iD: 0000-0002-4098-904X

© Laura Motta Medina 2019

Dedication

To my parents for their unconditional love and support

Acknowledgements

I would like to express my sincere gratitude to my co-chair Dr. Joel Blum. Without his continuous support, guidance, and patience, I would not have been able to complete the work in this thesis. His hard work and incredible insight for science encourage me to become a better scientist. I am forever thankful that he took countless hours to edit my never-ending rough drafts and pushed me to be a better writer. I would also like to extend my gratitude to my co-chair Dr. Paul Zimmerman, who accepted me in his lab and believed in my ideas, even when they were sometimes wrong. I am thankful that he took the time to learn about mercury stable isotopes to help me and guide me in the investigation of the magnetic isotope effect from a physical chemistry perspective.

I would also like to thank my dissertation committee members, they played an important role in the completion of my degree. I would especially like to thank Brian Popp, who taught me so much about oceanography and helped to improve this dissertation and expand my scientific knowledge. And I thank Kerri Pratt, for understanding how much it meant to me to get a joint degree with chemistry.

To my fellow graduate students, I learned so many valuable lessons from them in the last past five years. Spencer Washburn, helped me navigate life in Ann Arbor and even to fix my car tires on a winter night. Brian Konecke and Tristan Childress, who were my family away from home. Alan Chien, for his willingness to listen to my ideas, helping me uncover the magnetic isotope effect, and for being a good friend. Alan Rask and Cody Aldaz, for teaching me so much about computational photochemistry. I would also like to thank all the post-docs, research

scientists, and lab manager, especially Laura Sherman, Jason Demers, Jamie Gleason, and Marcus Johnson. Thank you to my other friends in Earth and Environmental Sciences, especially Sae Yun Kwon, Patrick Donovan, Jennifer Bowen, Kirk Townsend, Maria Rodriguez, Juliana Mesa, and Aaron Kurz.

In addition to my lab mates, I would like to specifically thank my undergraduate advisors John R. Reinfelder and K. Kritee at Rutgers University. Nine years ago, in John's lab I carried out the first mercury stable isotope experiment with marine phytoplankton. They have been great friends and mentors to this day. I still often remember the analogy of holding hands Kritee used to explained to me intersystem crossing. There are also many people outside the lab that have had a great impact in my graduate student life, specially Abneris Rodriguez, Wesley Marrero, Nadiya Kostyuk, and Renato Navarro.

Finally, I would like to give my sincere gratitude to my family. Thank you, for always making me laugh, calling me late at night to remind me not to work too late, sending me my favorite Colombian cereal, but more importantly for your unconditional love and support. I would not have been able to complete this degree without you. And finally I thank my partner, Jesús, for the constant support, love, and patience and my dear Mr. Schrodinger, my loyal feline companion and friend.

Table of Contents

Dedication	ii
Acknowledgements	iii
List of Tables	viii
List of Figures	ix
Abstract	x
Chapter 1 Introduction	1
1.1 Mercury: A historical perspective	1
1.2 Mercury Stable Isotopes	4
1.3 Theoretical Considerations for Photochemical Isotope Effects	6
1.4 Dissertation Narrative	7
References	11
Chapter 2 Mercury Cycling in the North Pacific Subtropical Gyre as Revealed by Mercury Stable Isotope ratios	14
2.1 Introduction	15
2.2 Material and Methods	18
2.2.1 Precipitation collection and analysis	18
2.2.2 Dissolved Hg and particulate collection and analysis	20
2.2.3 Zooplankton collection and analysis	21
2.2.4 Fish collection and analysis	23
2.2.5 Hg isotope analysis	23
2.3 Results	25
2.3.1 Precipitation	25
2.3.2 THg isotopic composition of marine particles	26
2.3.3 Zooplankton	27
2.3.4 Pelagic Fish	29
2.4 Discussion	30
2.4.1 Dissolved THg and MeHg vertical profiles	31
2.4.2 Hg isotope ratios as indicators of Hg transformation in the NPSG	31
2.4.2.1 Hg isotope ratios in surface waters (25 m)	31
2.4.2.2 Hg stable isotope ratios in the lower epipelagic and upper mesopelagic (150-700)	34
2.4.3 Methylation of Hg in the water column	35
2.4.4 Demethylation of MMHg in the water column	39
2.4.4.1 Photochemical demethylation within the mixed layer	39
2.4.4.2 Demethylation below the mixed layer	42
2.5 Conclusions	43
References	49
2.6 Supporting information	58
Chapter 3 Mercury Stable Isotopes in Flying Fish as Flying Fish as a Monitor of Photochemical Degradation of Methylmercury in the Atlantic and Pacific Oceans	74
3.1 Introduction	75

3.2 Materials and Methods	77
3.2.1 Flying fish sampling and preparation	78
3.2.2 THg analysis	78
3.2.3 Hg stable isotope analysis	78
3.2.4 Environmental Modeled Satellite Data	79
3.2.5 The Magnetic Isotope Effect: Theoretical Considerations	80
3.3 Results and Discussion	82
3.3.1 The magnetic isotope effect and photochemical degradation of MeHg	82
3.3.2 $\Delta^{199}\text{Hg}/\delta^{202}\text{Hg}$ spatial trends	84
3.3.3 Relative photochemical degradation and controlling environmental factors	86
3.3.3.1 Relative degree of photochemical degradation of MeHg	86
3.3.3.2 Factors controlling the photochemical degradation of MeHg	87
References	93
3.4 Supporting information	98
Chapter 4 Mercury Isotope Fractionation During the Photochemical Reduction of Hg(II)	
Coordinated with Organic Ligands	100
4.1 Introduction	101
4.2 Materials and Methods	106
4.2.1 Experimental materials	106
4.2.2 Photochemical reduction of Hg(II)	106
4.2.3 Hg concentrations and isotope analysis	108
4.3 Results	110
4.3.1 Reaction kinetics	110
4.3.2 Mercury stable isotope fractionation of Hg(II) in the presence of cysteine	111
4.3.3 Mercury stable isotope fractionation of Hg(II) in the presence of serine	112
4.3.4 Mercury stable isotope fractionation of Hg(II) in the presence of ethylenediamine	113
4.4 Discussion	113
4.4.1 Photochemical reduction of Hg(II) in the presence of LMWOL	114
4.4.1.1 Cysteine experiments	114
4.4.1.2 Serine experiments	116
4.4.1.3 Ethylenediamine experiments	118
4.4.2 Photophysical control of MIE during the photochemical reduction	119
4.4.3 Environmental implications	120
References	128
4.5 Supporting information	137
Chapter 5 Methylmercury Photodecomposition and Incorporation in Marine Plankton	144
5.1 Introduction	145
5.2 Photochemically reactive complexes of MeHg in seawater	146
5.3 Photochemical MeHg decomposition experiments	148
5.4 MeHg uptake and bioaccumulation at the base of the oceanic marine food webs	150
5.5 Conclusions	153
5.6 Methods	155
5.6.1 Rooftop experiments	155
5.6.2 Shipboard experiments	155
5.6.3 Zooplankton analyses	155
5.6.4 Electronic structure simulations	156

References	162
5.7 Supporting information	166
Chapter 6 Mercury Magnetic Isotope Effect: A Plausible Photochemical Mechanism	185
6.1 Introduction	185
6.2 Results and Discussion	187
6.3 Environmental Impact	193
6.4 Supporting Information	201
6.4.1 Computational Details	201
6.4.2 Non-equilibrium water solvation	202
6.4.3 Marcus rate for intersystem crossing	202
6.4.4 Photodissociation of the Hg-Cl bond in CH ₃ HgCl	203
Chapter 7 Conclusion	213
References	220

List of Tables

Table S2.1a Marine fish isotope ratios and THg	68
Table S2.1b Mercury isotopic data for reference materials used for process quality control and evaluation	69
Table S2.1c Small and large particles THg isotope ratios	70
Table S2.1d Zooplankton THg isotope ratios	71
Table S2.1e Daytime zooplankton THg concentrations and Hg isotope ratios May 2015	72
Table S2.1f Precipitation THg concentrations and Hg isotope ratios	73
Table S3.1 Flying fish collection data, THg concentrations, and THg isotope ratios	98
Table S3.2 Calculated photochemical parameters, modeled environmental variables, and reference materials	99
Table S4.1 Experimental details of Hg(II) photoreduction in the presence of serine, cysteine, and ethylenediamine	137
Table S4.2 Dissolved Hg(II) species in solution	138
Table S4.3a Hg stable isotope values for cysteine experiments	139
Table S4.3b Hg stable isotope values for the serine experiments.	140
Table S4.3c Hg stable isotope values for ethylenediamine experiments.	141
Table S4.4 MDF and MIF fractionation factor for all experiments	142
Table S4.5 Summary of fractionation factors for visible serine experiments	143
Table 5.1 Vertical excitation energies for MeHg complexes	157
Table S5.1 Experimental details and environmental conditions	173
Table S5.2a Shipboard experiments: Hg stable isotope data and concentrations	174
Table S5.2b laboratory experiments: Hg stable isotope data and concentrations	175
Table S5.2c Zooplankton Hg stable isotope data and bulk concentrations	176
Table S5.3 Surface zooplankton THg and MeHg concretions and calculated MeHg isotopic composition	177
Tables S5.4 Hg complexes optimized geometries (MP2)	178
Table S5.5 Vertical excitation energies and non-equilibrium solvation corrections for water.	181
Table S6.1 Vertical excitation energies CH ₃ HgCl	204
Table S6.2 Vertical excitation energies HgCl ₂	205
Table S6.3 Vertical excitation energies CH ₃ HgX (X= Cl, Br, I, and SCH ₃) at 4.0Å separated distances	206
Table S6.4 Vertical excitation energies HgX ₂ (X= Cl, Br, I, and SCH ₃) at 4.0Å bond distance	207
Table S6.5 Vertical excitation energies CH ₃ HgBr	208
Table S6.6 Vertical excitation energies CH ₃ HgI	209
Table S6.7 Vertical excitation energies HgBr ₂	210
Table S6.8 Vertical excitation energies HgI ₂	211

List of Figures

Figure 1 Mercury stable isotope fractionation	5
Figure 2.1 Biogeochemical cycle of Hg at Station ALOHA	45
Figure 2.2 (A) $\delta^{202}\text{Hg}$ and (B) $\Delta^{199}\text{Hg}$ values of samples as a function of depth in meters.	46
Figure 2.3 Vertical profiles of total Hg recovered from zooplankton biomass	47
Figure 2.4. A) $\Delta^{201}\text{Hg}$ versus $\Delta^{199}\text{Hg}$ and B) $\delta^{202}\text{Hg}$ versus $\Delta^{199}\text{Hg}$	48
Figure S2.1 Vertical Profiles of (A) dissolved total Hg and (B) dissolved MeHg	63
Figure S2.2. Vertical profile of total Hg concentration in particles per liter of water filtered	64
Figure S2.3. (A) $\Delta^{200}\text{Hg}$ and (B) $\Delta^{204}\text{Hg}$ values of samples as a function of depth	65
Figure S2.4 (A) $\delta^{202}\text{Hg}$ and (B) $\Delta^{199}\text{Hg}$ values of total Hg in zooplankton	66
Figure 3.1 Sample locations	90
Figure 3.2 (a) Plot of $\Delta^{199}\text{Hg}$ versus $\Delta^{201}\text{Hg}$ and (b) Plot of MIF ($\Delta^{199}\text{Hg}$) versus MDF ($\delta^{202}\text{Hg}$)	91
Figure 3.3 $\Delta^{199}\text{Hg}$ plotted against environmental variables	92
Figure 4.1. Radical Pair mechanism for the XHgX complex, where $\text{X}=\text{S}$, N , or O ligand	123
Figure 4.2. Rayleigh distillation plots of the mass-dependent (A–C) and mass-independent fractionation (D–F)	124
Figure 4.3. Three-isotope plots illustrating correlations between MIF ($\Delta^{199}\text{Hg}$) and MDF ($\delta^{202}\text{Hg}$) for the serine exp.	125
Figure 4.4. Summary diagram of MIF in the residual Hg(II) during the photolysis $\text{Hg}-\text{X}_n$	126
Figure 4.5. Three isotope plot illustrating correlation between $\Delta^{199}\text{Hg}$ and $\Delta^{201}\text{Hg}$ (both MIF)	127
Figure 5.1. Plot of $\Delta^{199}\text{Hg}_t - \Delta^{199}\text{Hg}_{t=0}$ versus $\delta^{202}\text{Hg}_t - \delta^{202}\text{Hg}_{t=0}$.	158
Figure 5.2. Plot of $\Delta^{199}\text{Hg}$ versus $\delta^{202}\text{Hg}$	159
Figure 5.3. A) Plot of $\Delta^{199}\text{Hg}_t - \Delta^{199}\text{Hg}_{t=0}$ versus $\Delta^{201}\text{Hg}_t - \Delta^{201}\text{Hg}_{t=0}$.	160
Figure 5.4. Diagram of MeHg photodecomposition, uptake, and incorporation of MeHg in the marine food web.	161
Figure S5.1. Plot of $\Delta^{199}\text{Hg}_t - \Delta^{199}\text{Hg}_{t=0}$ versus $\ln(\text{fraction remaining})$ of all the MMHg photochemistry experiments.	172
Figure 6.1. The radical pair mechanism for the magnetic isotope effect	194
Figure 6.2. Potential energy curves of low-lying excited states of CH_3HgCl	195
Figure 6.3. Absolute values of complex SO-Hamiltonian matrix elements for CH_3HgCl	196
Figure 6.4. Potential energy curves of low-lying excited states of HgCl_2	197
Figure 6.5. Absolute values of complex SO-Hamiltonian matrix HgCl_2	198
Figure 6.6. Low lying electronically excited states during Hg-Cl dissociation for CH_3HgCl .	199
Figure 6.7. Vertical excitation energies at the ground state equilibrium geometry and at bond dissociated distances for A) $\text{SCH}_3\text{HgCH}_3$ and B) $\text{Hg}(\text{SCH}_3)_2$.	200
Figure S6.1. Potential energy curves of low-lying excited states of CH_3HgCl . PEC as a function of the Hg–Cl bond	203

Abstract

Mercury (Hg) is a global pollutant that poses a public health threat because exposure through consumption of fish or rice can lead to adverse neurological and immunological effects. Despite decades of research there are significant gaps in the understanding of Hg biogeochemistry and the measurement of Hg stable isotopes has proven to be an effective tool for answering some of the outstanding questions. Mass-dependent fractionation (MDF, reported as $\delta^{202}\text{Hg}$) and mass-independent fractionation (MIF, reported as $\Delta^{199}\text{Hg}$) of Hg isotopes occur during many biogeochemical processes and can be diagnostic of specific chemical reactions.

This dissertation enhances our understanding of key pathways that control Hg toxicity in marine waters and pinpoints the key dissolved Hg species that may limit Hg methylation and bioaccumulation. The overarching goal of this research was to investigate the biogeochemical cycle of Hg in marine waters with a focus on enhancing the understanding of the photochemical decomposition of Hg in surface marine waters, which reduces the pool of Hg available for incorporation into the marine foodweb. With this goal in mind, Hg stable isotopes were used to investigate Hg cycling in North Pacific Ocean. This resulted in the first Hg stable isotope analysis of marine particles, zooplankton and open ocean precipitation (Chapter 2, 3, 5). In order to fully interpret the Hg stable isotopic composition of natural samples associated with Hg photochemistry, a number of Hg photochemistry studies were conducted on the rooftop of a laboratory building and onboard the research vessel R/V Kilo Moana in the North Pacific Subtropical Gyre (Chapter 4,5). Finally, to connect the Hg stable isotopes studies with the photochemical decomposition

mechanism, a series of high-level electronic structure calculations of environmentally relevant complexes were conducted (Chapter 6).

The body of research presented in this dissertation highlights the advantages of utilizing Hg stable isotopes to study Hg cycling in the environment, bypassing the limitations of traditional field and laboratory experiments. The environmental isotope measurements indicated that precipitation is the main source of Hg to surface marine waters, that both methylation and demethylation of Hg takes place in the water column, that surface marine zooplankton record a diurnal $\Delta^{199}\text{Hg}$ variation indicative of methylmercury (MeHg) photochemistry, and that there is seasonal variability in the Hg isotope composition of particulate Hg. The MeHg photochemistry isotope experiments demonstrated that the photodecomposition of MeHg in marine waters may be controlled intracellularly by phytoplankton or by reactive inorganic MeHg complexes (e.g. MeHgOH) but not by dissolved organic matter as previously hypothesized. The isotope experiments indicate that direct photolysis of Hg may be the dominant photochemical mechanism for decomposition and reduction in aquatic ecosystems, which is contrary to previous investigations. Finally, the high-level computational simulations demonstrate that spin-orbit coupling may not quench mass-independent fractionation ($\Delta^{199}\text{Hg}$) and that the magnetic isotope effect is a plausible mechanism for the $\Delta^{199}\text{Hg}$ recorded in natural samples around the world. Specifically, the simulations indicate that spin-orbit coupling may limit mass-independent isotope fractionation for divalent inorganic Hg(II) complexes (e.g. Hg(thiol)₂), but that spin-orbit coupling does not have any effect on mass-independent isotope fractionation of MeHg complexes.

Chapter 1 Introduction

1.1 Mercury: A historical perspective

Mercury (Hg) has captivated the curiosity of countless individuals since the Middle Ages. This shiny “water-silver” liquid was a central part of alchemy, a philosophical tradition that greatly influenced modern chemistry. It is well known that alchemists believed that Hg was key to creating the philosopher stone to achieve transmutation of metals to gold or silver, but what is less known is the role Hg played in the Scientific Revolution.^{1,2} The Scientific Revolution was a series of events that marked the beginning of modern science in the 18th century. To understand the role Hg had we need to go back a few centuries, to the publication of the third book of Aristotle’s treatise *Meteorology*³; this book contains the justification for the belief that metals are composed of two principle components, later identified as Hg and sulfur. These ideas were solidified in the 13th century by the Latin corpus attributed to Geber^{4,5} and it was from these principles that alchemists set out to understand the fundamental truths by means of experiment with natural materials.^{4,5} In the *Summa Perfectionis*, Geber investigated in great detail the relationship between Hg and sulfur and it was from his observations of Hg-sulfur mixtures’ resistance to heat that he concluded that Hg and sulfur made a “very strong composition”⁴. Geber described this interaction as very small particles coming together to form strong discrete corpuscles. This idea of corpuscles made up of Hg and sulfur could be interpreted as an early description of a chemical bond.^{1,5}

The notion that Hg and sulfur were central to the composition of metals was so pervasive that in the 16th century Paracelsus von Hohenheim proposed the concept that three principle components (*tria prima*), mercury, sulfur, and salt (likely cinnabar) contained the poisons

contributing to all diseases.⁶ Paracelsus von Hohenheim is considered the father of toxicology⁷ and was an avid alchemist⁸ often credited for the use of Hg to treat syphilis.^{7,9} This was one of the early applications of Hg in medicine, in subsequent years Hg would be seen as a miracle drug and was used to combat other ailments including bronchitis and cancer. Hg salts were routinely used as topical antiseptics to treat minor wounds until 1998 when they were discontinued in the United States, but it may still be available in some other countries¹⁰.

We know now that the theory of sulfur and Hg was incorrect and that Hg does not have any beneficial medical purposes. On the contrary, Hg is a known neurotoxin in all of its chemical forms. Yet, it is remarkable that ancient philosophers realized that Hg and sulfur had such high affinities resulting in an extremely stable chemical bond. But despite centuries of investigation on Hg and sulfur, their relationship in natural environments remains poorly understood. Many aspects of my dissertation highlight the need for a greater understanding of the Hg coordination to sulfur-bearing organic ligands to be able to comprehend the biogeochemical cycle of this neurotoxin in a changing environment.

In our current day, anthropogenic emissions from mining and coal combustion have significantly increased the amount of Hg in the atmosphere. Hg has a long residence time in the atmosphere and is mobilized into every corner of the Earth after it has been emitted, making it a global pollutant. This poses a great public health concern because once Hg is deposited from the atmosphere it may get methylated to the potent neurotoxin monomethyl-Hg (MeHg), which biomagnifies in aquatic food webs, reaching elevated concentrations in fish^{11,12}. Hg poisoning has been linked to IQ deficits in prenatally exposed children^{13,14} and may include cardiovascular effects in adults.¹⁵ And even more recently, it has been demonstrated that exposure to inorganic Hg (IHg) may lead to immunotoxicity^{16,17} and increased antibiotic resistance.¹⁸ But Hg poisoning

is more than a health hazard, it is also an economic burden due to the lost wages and medical costs from IQ deficits and nonfatal heart attacks.^{19,20}

Despite many decades of research on Hg many details remain unclear about how and in which environments MeHg is produced and degraded. The limited understanding of the Hg cycle has been in part due to technical challenges associated with tracking and measuring different chemical forms of Hg in the environment. To facilitate the investigation of complex biogeochemical cycles, researchers seek ways to fingerprint the key pathways that control its mobility. Light-element stable isotope ratios have been an efficient tool to fingerprint complex biogeochemical cycles in the environment, for example, sulfur stable isotopes were key to determining timing of the great oxygenation event, and nitrogen isotopes in the understanding of food webs. However, it had been long hypothesized that elements heavier than $Z=40$ ²¹ would never exhibit isotope effects because the relative mass differences of the isotopes would be too small to detect isotope effects. But centuries later Hg keeps on surprising us; in 2001 technological innovations in mass spectrometry allowed the accurate measurements of Hg stable isotope ratios demonstrating significant mass dependent isotope effects (MDF).²² In 2007 Hg surprised us yet again, when Bergquist and Blum²³ identified a phenomenon whereby magnetic isotopes of Hg react during photochemical reactions at different rates from the even-mass isotopes, resulting in mass independent isotopes effects (MIF). Since then, Hg stable isotopes have been instrumental in the investigation of critical aspects of the global biogeochemical cycle of Hg. For example, Hg stable isotopes have elucidated Hg methylation in the marine water column²⁴ and mechanisms of polar atmospheric Hg deposition^{25,26}.

Although Hg stable isotopes have been proven to be powerful tools for investigating the biogeochemical cycle of Hg, it is still challenging to interpret Hg stable isotope signatures in

biological samples due to the limited understanding of the underlying isotope fractionation mechanisms. Over a decade after the first measurements, it is still not fully understood why a heavy element like Hg would exhibit MDF and MIF. The MDF of heavy elements is thought to be controlled by the nuclear volume effect,^{21,27} however, the theory has never been extended to kinetic reactions²⁸. The elevated MIF of Hg has been attributed to photochemical transformations of Hg mediated by the magnetic isotope effect (MIE)²³. While the MIE is widely considered the cause of photochemical isotope fractionation signatures, it has been long theorized that heavy elements would not express MIE due to the relativistic effects inherent to heavy elements.²⁹ Thus, little is known about the photochemical transformation of Hg that occur in the environment and expresses the MIE.

Inspired by the rich history of this neurotoxic global pollutant and the scientific mysteries surrounding Hg stable isotope fractionation, the overarching goal of my dissertation was to understand the underlying chemistry of the major forms of this unusual element in the environment. To accomplish this, I took a multidisciplinary approach combining state-of-the-art quantum mechanical calculations to investigate the role of relativistic effects in the photochemistry of Hg, Hg stable isotope photochemistry experiments in natural sunlight, and marine field collections and isotopic analyses to reconstruct the marine Hg biogeochemical cycle.

1.2 Mercury Stable Isotopes

Hg stable isotope ratios exhibit traditional mass dependent fractionation (MDF; represented by $\delta^{202}\text{Hg}$ values in ‰; Equation 1; Figure 1) during all abiotic and biotic physicochemical reactions that have been investigated, where the lighter isotope reacts faster than the heavy one in kinetic reactions, and heavier isotopes are accumulated in the stiffer bond in equilibrium reactions.³⁰ In addition to MDF, Hg isotope ratios exhibit large magnitude ($\geq 0.4\text{‰}$) MIF of odd-mass isotopes

(MIF; represented by $\Delta^{199}\text{Hg}$ and $\Delta^{201}\text{Hg}$ values in ‰, Equation 2; Figure 1) that has been attributed to photochemical transformations of Hg. In addition, MIF of even isotopes (even-MIF; represented by $\Delta^{200}\text{Hg}$ and $\Delta^{204}\text{Hg}$ values) is sometimes observed, particularly in rain and snow samples, and it is potentially linked to atmospheric photo-oxidation reactions^{31,32}.

$$\delta^{202}\text{Hg} (\text{‰}) = \left(\frac{(^{202}\text{Hg}/^{198}\text{Hg})_{\text{unknown}}}{(^{202}\text{Hg}/^{198}\text{Hg})_{\text{SRM3133}}} - 1 \right) \times 1000 \quad (\text{Equation 1})$$

$$\Delta^{\text{xxx}}\text{Hg} = \delta^{\text{xxx}}\text{Hg} - (\delta^{202}\text{Hg} \times \beta) \quad (\text{Equation 2})$$

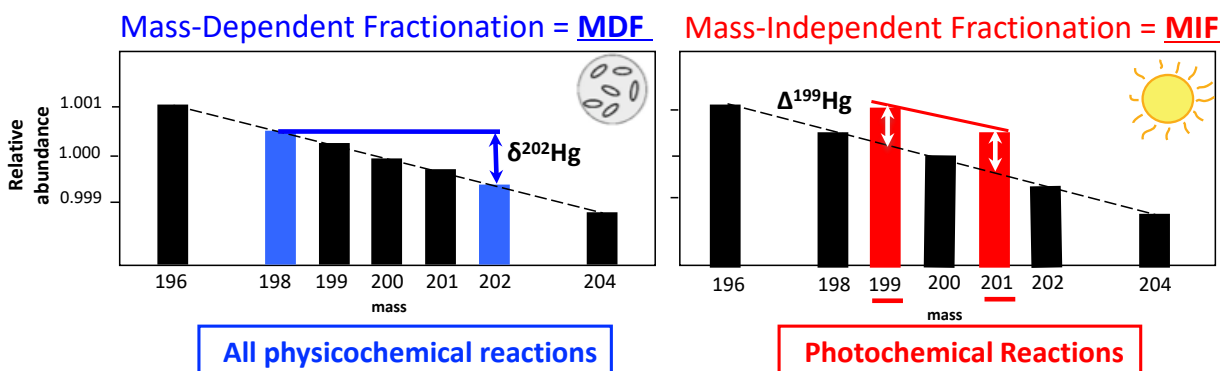


Figure 1: Hg stable isotopes of Hg and relative abundance. On the left mass dependent isotope fractionation and on the right mass independent fractionation of the odd isotope of Hg (^{199}Hg and ^{201}Hg).

The production of Hg MIF isotope signatures in conjunction with MDF signatures has made Hg stable isotope ratios a powerful environmental fingerprinting tool because marine organisms preserve the $\Delta^{199}\text{Hg}$ values associated with photochemical reduction of Hg prior to its incorporation into the marine food-web. $\Delta^{199}\text{Hg}$ signatures are preserved because there is no $\Delta^{199}\text{Hg}$ associated with trophic transfer or microbial reactions^{33,34}. In addition, ratios of $\Delta^{199}\text{Hg}$ to $\Delta^{201}\text{Hg}$ and $\delta^{202}\text{Hg}$ values have been shown to be sensitive to the chemical bonding environment³⁵, wavelength of light³⁶, and types and amounts of DOM^{37,38}. The sensitivity of $\Delta^{199}\text{Hg}$ to reaction conditions has allowed the investigation of photochemical reactions of Hg within phytoplankton³⁹ and the elucidation of a diurnal MeHg photochemistry cycle in marine surface water

zooplankton.⁴⁰ However, it is challenging to interpret $\Delta^{199}\text{Hg}$ values in biological samples due to the limited understanding of the controlling isotope fractionation mechanism(s).

1.3 Theoretical Considerations for photochemical isotope effects

The theoretical framework developed for kinetic MDF is inadequate for investigating photochemical reactions because MDF assumes that the chemical reaction follows a unique potential energy trajectory during bond dissociation³⁰, however, this does not apply to photochemical reactions⁴¹. In a photochemical transformation a photon of light promotes an electron from the ground state to an excited one, and this newly excited state is described by a different potential energy trajectory. This explains why all MIF signatures of stable isotopes recorded today are associated with photochemical reactions, for example $\Delta^{33}\text{S}$ from SO_2 photolysis in the atmosphere^{42,43} or $\Delta^{17}\text{O}$ from destruction of ozone by photolysis⁴⁴. The MIF signatures of MeHg ($\Delta^{199}\text{Hg}$ and $\Delta^{201}\text{Hg}$) in marine biological samples have been proposed to be inherited from partial direct photolysis of Hg complexes in surface waters by MIE²³. Direct photolysis occurs via the absorption of a photon by MeHg-ligand complexes and leads to homolytic cleavage of Hg-ligand bonds. While the MIE is widely considered the cause of photochemical isotope fractionation signatures, similar to the mechanism proposed for the fractionation of the lighter elements (e.g., C, N, S)⁴⁵ during photolysis, it is unlikely for heavy elements to exhibit MIE due the relativistic effects inherent to heavy elements and the chemical complexity.⁴⁶

As such, to accurately interpret $\Delta^{199}\text{Hg}$ and $\Delta^{201}\text{Hg}$ signatures in nature we must investigate the susceptibility of environmentally relevant MeHg complexes to undergo direct photolysis and evaluate the role of relativistic effects in the mechanism for the MIE. The appropriate theoretical description of the MIE for heavy elements, such as Hg, requires the inclusion of relativistic effects, but no theoretical model has accounted for these effects. Relativistic effects can be divided

between scalar relativistic effects, associated with the relativistic mass increase of the electron, and spin-orbit interaction. The latter effect may change reaction paths potentially altering or inhibiting the MIE.

1.4 Dissertation Narrative

In our quest to understand the environmental chemistry of Hg in aquatic ecosystems and expand our understanding of stable isotope fractionation signatures of heavy elements, we set out to reconstruct the marine biogeochemical cycle of Hg. Our emphasis on determining the photochemical reaction involving Hg that is behind the MIF preserved in pelagic fish. This dissertation enhances our understanding of key pathways that control Hg toxicity in marine waters and pin point the key dissolved Hg species that may limit Hg methylation and bioaccumulation. The worked presented here also raises questions about the biogeochemical cycle of Hg and our understanding of the environmental chemistry of Hg (Chapter 7).

In Chapter 2 (published in *Global Biogeochemical Cycles*) we used Hg isotope ratios and total Hg concentrations to explore Hg biogeochemistry in oligotrophic marine environments in the open ocean north of Hawaii. We present the first measurements of the vertical water column distribution of Hg concentrations and the Hg isotopic composition in precipitation, marine particles, and zooplankton at Station ALOHA (22°45' N 158° W). Our results reveal production and demethylation of methylmercury in both the euphotic (0-175 m) and mesopelagic zones (200-1000 m). We document a strong relationship between Hg isotopic composition and depth in particles, zooplankton and fish in the water column, and diurnal variations of $\Delta^{199}\text{Hg}$ values in zooplankton sampled near the surface (25 m). Based on these observations and stable Hg isotope relationships in the marine foodweb, we suggest that the Hg found in large pelagic fish at Station ALOHA was originally deposited mainly by rainfall, transformed into methyl-Hg and

bioaccumulated *in situ* in the water column. Our results highlight how Hg isotopic compositions reflect abiotic and biotic production and degradation of methyl-Hg throughout the water column, and the importance of particles and zooplankton in the vertical transport of Hg.

After reporting the strong relationship between $\Delta^{199}\text{Hg}$ values in zooplankton and pelagic fish in the North Pacific Ocean, we sought to use $\Delta^{199}\text{Hg}$ values in flying fish tissue containing Hg mostly in the form of MeHg to assess the relative degree of photochemical decomposition across the world's oceans (Chapter 3 in review at *Marine Chemistry*). The photochemical decomposition of this neurotoxin limits its bioaccumulation, but the spatial pattern of demethylation in the oceans is not well understood. The reaction mechanism is also uncertain and there is currently no way of monitoring the degree of photochemical degradation in pelagic waters across the oceans. Here, we show that the Hg isotopic composition of flying fish allows us to investigate and monitor the controlling factors for the photodecomposition of residual methylmercury available for bioaccumulation in the food web of marine pelagic fish, which is the dominant source of methylmercury that humans are exposed to. In 19 specimens of flying fish, the magnitude of MIF varies by a factor of ~ 2 . We estimate that 56 to 80% of MeHg was photo-degraded prior to entering the food web, depending on the location. The proportion of MeHg degradation does not correlate with latitude, solar radiation or estimates of the concentration of DOC or chlorophyll at the collection sites, but it does correlate with proxies for water clarity. The ratio of MIF for the two odd mass isotopes, $\Delta^{199}\text{Hg} / \Delta^{201}\text{Hg}$, is constant in all flying fish sampled (1.20 ± 0.03) suggesting that there is a common mechanism for photodegradation of MeHg in surface waters across oceans and hemispheres. The ratio of $\Delta^{199}\text{Hg}$ to $\delta^{202}\text{Hg}$ is generally consistent with photochemical degradation but is more variable (2.71 ± 0.14), suggesting that there is minimal internal

demethylation of MeHg and that variable amounts of MDF occur at different locations in the ocean, likely driven by variable rates of methylation and demethylation of Hg in the water column.

In Chapter 4 (in review at *Physical Chemistry A*), we report on laboratory photochemistry experiments. In Chapter 2 and 3 we demonstrated that $\Delta^{199}\text{Hg}$ values were excellent proxies from investigating Hg in marine ecosystems and monitoring the degree of photochemical degradation in open ocean waters. However, the mechanisms behind MIF and the role of photochemical degradation of HgX_2 (Hg(II) ; X=S, N, O organic ligands) remained unclear and limited our interpretation of MIF. The photochemical reduction of Hg(II) is an important pathway in the environmental Hg cycle because it competes with Hg methylation and potentially limits the formation of neurotoxic MeHg. This study investigated Hg isotope fractionation during the photochemical reduction of Hg(II) complexed to organic ligands representative of the available binding sites in natural dissolved organic matter. Our Hg stable isotope results suggest that MDF and MIF are induced at different steps in the overall photochemical reduction reaction, and that MIF does not depend on the rate determining step, but instead on photophysical aspects of the reaction, such as intersystem crossing and hyperfine coupling. The behavior of Hg isotopes reported here will allow for a better understanding of the underlying reaction mechanisms controlling the Hg isotope signatures recorded in natural samples.

In Chapter 5 (Submitted to *Nature Geoscience*) we build upon our marine measurements at Station ALOHA and our laboratory photochemistry experiments, and provide a multidisciplinary approach to determine MeHg photodecomposition and incorporation in marine plankton. We use *ab initio* methods to investigate the photoreactivity of MeHg complexes in seawater, together with mercury stable isotope ratios from laboratory and shipboard photodegradation experiments and in zooplankton from the central tropical and subtropical North

Pacific Ocean. Until recently, it has been assumed that dissolved MMHg is either photodegraded in the water column or taken up by phytoplankton, but that little to no degradation of MMHg occurs after incorporation in phytoplankton. This assumption is an oversimplification of the biogeochemical cycle of Hg in the ocean. We trace the pathways by which MeHg is incorporated into planktonic organisms at the base of pelagic marine food webs. Significant differences in the Hg stable isotope composition ($\delta^{202}\text{Hg}$, $\Delta^{199}\text{Hg}$, and $\Delta^{201}\text{Hg}$) between small versus intermediate and large size classes are documented for zooplankton from the upper layer of the photic zone (25 m) of the North Pacific Ocean. Our results suggest that much of the MeHg accumulated by phytoplankton and small zooplankton in the upper layers of the ocean's photic zone is not transferred to large consumers, while MeHg accumulated by phytoplankton and zooplankton living at the base of the euphotic zone is retained in the planktonic food web and effectively transferred to higher trophic level consumers. These results illuminate a critical link in the accumulation of MeHg in oceanic food webs and inform efforts to trace the accumulation of pollutant Hg in marine seafood.

In Chapters 2 through 5 we demonstrated that Hg stable isotope measurements can elucidate reaction mechanisms, ligands associated with Hg, and many complex environmental processes involving Hg. However, one big question remained: what is the underlying chemical mechanism of the MIF that produces $\Delta^{199}\text{Hg}$ anomalies? It is still impossible to fully grasp which aspects of the photochemical reaction that formation of $\Delta^{199}\text{Hg}$ values represents due to the lack of information about Hg complexes available for direct photolysis or reaction mechanisms in natural waters. In Chapter 6 (in preparation for submission to *JACS communications*) we use high level electronic structure methods to evaluate the potential photochemical mechanisms for MIF effects in HgX_2 and CH_3HgX (X= Cl, Br, I, and SCH_3). Here we demonstrate that the spin-orbit

coupling for the electronic transitions available for geminate recombination to the ground state are smaller than anticipated for HgX₂ and CH₃HgX (X=Cl and SCH₃) and therefore photochemical decomposition may result in magnetic isotope effects. This was unexpected because it has been long hypothesized that heavy elements could not undergo magnetic isotope fractionation²⁹ due to radical spin relaxation inhibiting geminate recombination mediated by spin-orbit coupling. The simulations presented here show that photochemical reduction of HgX₂ complexes can result in positive or negative MIEs, while CH₃HgX complexes exclusively result in positive MIE, explaining the MIE recorded in natural samples.

References

1. Newman, W. R. What have we learned from the recent historiography of alchemy? *Isis* **102**, 313–321 (2011).
2. Newman, W. R. Introduction: The Problematic Position of Alchemy in the Scientific Revolution. in *Atoms and Alchemy: Chymistry and the Experimental Origins of the Scientific Revolution* 1–20 (University of Chicago, 2006).
3. Aristotle & Lee, H. D. P. *Meteorology. Ed. and trans.* (Harvard University Press, 1952).
4. Newman, W. R. *The 'Summa perfectionis' of Pseudo-Geber: A Critical Edition, Translation and Study.* William R. Newman. (E.J Brill, 1991). doi:10.2307/2865163
5. Newman, W. R. One: The Mise en Scène before Sennert. in *Atoms and Alchemy: Chymistry and the Experimental Origins of the Scientific Revolution* (University of Chicago Press, 2006).
6. Pagel, W. The prime matter of paracelsus. *Ambix* **9**, 117–135 (1961).
7. Deichmann, W. B., Henschler, D., Holmstedt, B. & Keil, G. What is there that is not poison? A study of the Third Defense by Paracelsus. *Arch. Toxicol.* **58**, 207–213 (1986).
8. Multhauf, R. P. John of Rupescissa and the origin of medical chemistry. *Isis.* **45**, 359–367 (1954).
9. Temkin, O. Therapeutic Trends and the Treatment of Syphilis before 1900. *Bull. Hist. Med.* **29**, 309–316 (1955).
10. Deleu, D., Hanssens, Y., Al-Salmy, H. S. & Hastie, I. Peripheral polyneuropathy due to chronic use of topical ammoniated mercury. *J. Toxicol. - Clin. Toxicol.* **36**, 233–237 (1998).
11. Mahaffey, K. R. *et al.* Balancing the benefits of n-3 polyunsaturated fatty acids and the risks of methylmercury exposure from fish consumption. *Nutr. Rev.* **69**, 493–508 (2011).
12. Sunderland, E. M., Li, M. & Bullard, K. Decadal Changes in the Edible Supply of Seafood and Methylmercury Exposure in the United States. *Environ. Health Perspect.* **126**, 029003 (2018).
13. Grandjean, P., Satoh, H., Murata, K. & Eto, K. Adverse effects of methylmercury: Environmental health research implications. *Environ. Health Perspect.* **118**, 1137–1145

- (2010).
14. Karagas, M. R. *et al.* Evidence on the human health effects of low-level methylmercury exposure. *Environ. Health Perspect.* **120**, 799–806 (2012).
 15. Roman, H. A. *et al.* Evaluation of the cardiovascular effects of methylmercury exposures: Current evidence supports development of a dose-response function for regulatory benefits analysis. *Environ. Health Perspect.* **119**, 607–614 (2011).
 16. Nyland, J. F. *et al.* Biomarkers of methylmercury exposure immunotoxicity among fish consumers in amazonian Brazil. *Environ. Health Perspect.* **119**, 1733–1738 (2011).
 17. Silbergeld, E. K., Silva, I. A. & Nyland, J. F. Mercury and autoimmunity: Implications for occupational and environmental health. *Toxicol. Appl. Pharmacol.* **207**, 282–292 (2005).
 18. Eagles-Smith, C. A. *et al.* Modulators of mercury risk to wildlife and humans in the context of rapid global change. *Ambio* **47**, 170–197 (2018).
 19. Giang, A. & Selin, N. E. Benefits of mercury controls for the United States. *Proc. Natl. Acad. Sci.* **113**, 201514395 (2015).
 20. Trasande, L., Landrigan, P. J. & Schechter, C. Public health and economic consequences of methyl mercury toxicity to the developing brain. *Environ. Health Perspect.* **113**, 590–596 (2005).
 21. Bigeleisen, J., Brook, S. & York, N. Nuclear Size and Shape Effects in Chemical Reactions . Isotope Chemistry of the Heavy Elements. *J. Am. Chem. Soc.* **118**, 3676–3680 (1996).
 22. Lauretta, D. S., Klaue, B., Blum, J. D. & Buseck, P. R. Mercury abundances and isotopic compositions in the murchison (CM) and Allende (CV) carbonaceous chondrites. *Geochim. Cosmochim. Acta* **65**, 2807–2818 (2001).
 23. Bergquist, B. A. & Blum, J. D. Mass-dependent and -independent fractionation of hg isotopes by photoreduction in aquatic systems. *Science* **318**, 417–420 (2007).
 24. Blum, J. D., Popp, B. N., Drazen, J. C., Anela Choy, C. & Johnson, M. W. Methylmercury production below the mixed layer in the North Pacific Ocean. *Nat. Geosci.* **6**, 879–884 (2013).
 25. Sherman, L. S. *et al.* Mass-independent fractionation of mercury isotopes in Arctic snow driven by sunlight. *Nat. Geosci.* **3**, 173–177 (2010).
 26. Obrist, D. *et al.* Tundra uptake of atmospheric elemental mercury drives Arctic mercury pollution. *Nature* **547**, 201–204 (2017).
 27. Schauble, E. A. Role of nuclear volume in driving equilibrium stable isotope fractionation of mercury, thallium, and other very heavy elements. *Geochim. Cosmochim. Acta* **71**, 2170–2189 (2007).
 28. Dauphas, N. & Schauble, E. A. Mass Fractionation Laws , Mass-Independent Effects , and Isotopic Anomalies. *Annu. Rev. Earth Planet. Sci.* **44**, 709–83 (2016).
 29. Steiner, U. E. & Ulrich, T. *Magnetic Field Effects in Chemical Kinetics and Related Phenomena.* *Chem. Rev.* **89**, (1989).
 30. Bigeleisen, J. & Wolfsberg, M. Theoretical and Experimental Aspects of Isotope Effects in Chemical Kinetics. *Adv. Chem. Phys.* **I**, 15–76 (1958).
 31. Gratz, L. E., Keeler, G. J., Blum, J. D. & Sherman, L. S. Isotopic composition and fractionation of mercury in Great Lakes precipitation and ambient air. *Environ. Sci. Technol.* **44**, 7764–7770 (2010).
 32. Chen, J., Hintelmann, H., Feng, X. & Dimock, B. Unusual fractionation of both odd and even mercury isotopes in precipitation from Peterborough, ON, Canada. *Geochim.*

- Cosmochim. Acta* **90**, 33–46 (2012).
33. Kwon, S. Y. *et al.* Absence of fractionation of mercury isotopes during trophic transfer of methylmercury to freshwater fish in captivity Absence of fractionation of mercury isotopes during trophic transfer of methylmercury to freshwater fish in captivity School of Natural R. *Environ. Sci. Technol.* **46**, 7527–7534 (2012).
 34. Kritee, K., Barkay, T. & Blum, J. D. Mass dependent stable isotope fractionation of mercury during mer mediated microbial degradation of monomethylmercury. *Geochim. Cosmochim. Acta* **73**, 1285–1296 (2009).
 35. Zheng, W. & Hintelmann, H. Isotope Fractionation of Mercury during Its Photochemical Reduction by Low-Molecular-Weight Organic Compounds. *J. Phys. Chem. A* **114**, 4246–4253 (2010).
 36. Rose, C. H., Ghosh, S., Blum, J. D. & Bergquist, B. A. Effects of ultraviolet radiation on mercury isotope fractionation during photo-reduction for inorganic and organic mercury species. *Chem. Geol.* **405**, 102–111 (2015).
 37. Chandan, P., Ghosh, S. & Bergquist, B. A. Mercury isotope fractionation during aqueous photoreduction of monomethylmercury in the presence of dissolved organic matter. *Environ. Sci. Technol.* **49**, 259–267 (2015).
 38. Zheng, W. & Hintelmann, H. Mercury isotope fractionation during photoreduction in natural water is controlled by its Hg/DOC ratio. *Geochim. Cosmochim. Acta* **73**, 6704–6715 (2009).
 39. Kritee, K., Motta, L. C., Blum, J. D., Tsui, M. T. & Reinfelder, J. R. Photo-microbial visible light-induced magnetic mass independent fractionation of mercury in a marine microalga. *Earth Sp. Chem.* (2017). doi:10.1021/acsearthspacechem.7b00056
 40. Motta, L. C. *et al.* Mercury cycling in the North Pacific Subtropical Gyre as revealed by mercury stable isotope ratios. *Global Biogeochem. Cycles* 2018GB006057 (2019). doi:10.1029/2018GB006057
 41. Turro, N. J., Ramamurthy, V. & Scaiano, J. C. *Modern Molecular Photochemistry of Organic Molecules.* (University Science Book, 2010).
 42. Hattori, S. *et al.* SO₂ photoexcitation mechanism links mass-independent sulfur isotopic fractionation in cryospheric sulfate to climate impacting volcanism. *Proc. Natl. Acad. Sci.* **110**, 17656–17661 (2013).
 43. Lyons, J. R. Mass-independent fractionation of sulfur isotopes by isotope-selective photodissociation of SO₂. *Geophys. Res. Lett.* **34**, 1–5 (2007).
 44. Thiemes and Jackson. The effect of variable wavelength ultraviolet light on the production of oxygen isotopic anomalies. *J. Chem. Inf. Model.* **53**, 1689–1699 (2013).
 45. Turro, N. J. Influence of nuclear spin on chemical reactions: Magnetic isotope and magnetic field effects (A Review). *Proc. Natl. Acad. Sci.* **80**, 609–621 (1983).
 46. Salikhov, K. *Magnetic Isotope Effect in Radical Reactions - Introduction.* (1996).

Chapter 2 Mercury Cycling in the North Pacific Subtropical Gyre as Revealed by Mercury Stable Isotope Ratios

Co-authored with Joel D. Blum, Marcus W. Johnson, Blaire P. Umhau, Brian N. Popp, Spencer J. Washburn, Jeffrey C. Drazen, Claudia R. Benitez-Nelson, Cecelia C.S. Hannides, Hilary G. Close, and Carl H. Lamborg. Mercury cycling in the North Pacific Subtropical Gyre as revealed by mercury stable isotope ratios. *Global Biogeochemical Cycles*, (Ii), 2018GB006057.

Abstract: The oceans are an important global reservoir for mercury (Hg) and marine fish consumption is the dominant human exposure pathway for its toxic methylated form. A more thorough understanding of the global biogeochemical cycle of Hg requires additional information on the mechanisms that control Hg cycling in pelagic marine waters. In this study, Hg isotope ratios and total Hg concentrations are used to explore Hg biogeochemistry in oligotrophic marine environments north of Hawaii. We present the first measurements of the vertical water column distribution of Hg concentrations and the Hg isotopic composition in precipitation, marine particles, and zooplankton near Station ALOHA (22°45' N 158° W). Our results reveal production and demethylation of methylmercury in both the euphotic (0-175 m) and mesopelagic zones (200-1000 m). We document a strong relationship between Hg isotopic composition and depth in particles, zooplankton and fish in the water column, and diurnal variations in $\Delta^{199}\text{Hg}$ values in zooplankton sampled near the surface (25 m). Based on these observations and stable Hg isotope relationships in the marine foodweb, we suggest that the Hg found in large pelagic fish at Station ALOHA was originally deposited largely by precipitation, transformed into methyl-Hg and bioaccumulated *in situ* in the water column. Our results highlight how Hg isotopic compositions

reflect abiotic and biotic production and degradation of methyl-Hg throughout the water column, and the importance of particles and zooplankton in the vertical transport of Hg.

2.1 Introduction

Mono-methylmercury (MMHg) is one of the most toxic forms of the global pollutant mercury (Hg) and is strongly retained at each trophic level in marine food webs, reaching high concentrations in piscivorous fish, the main source of exposure of MMHg to humans (Morel et al., 1998). Despite decades of research on Hg many details remain unclear about how, at what depths in the ocean, and in which marine environments, Hg transforms to the neurotoxic MMHg form and bioaccumulates in marine organisms. The current understanding of the biogeochemical cycle of Hg suggests that Hg exists in several forms including Hg(II), gaseous elemental mercury (Hg(0)) and methylated Hg (MeHg), both as MMHg and dimethyl-Hg. The major forms of Hg in aquatic ecosystems are Hg(II) complexed to organic ligands, chloride or sulfide, and organic mercury in the form of MMHg (Morel et al., 1998; Fitzgerald et al., 2007). Within the marine water column, Hg transformations include not only methylation of Hg(II) by abiotic and biotic processes (Munson et al., 2018; Sunderland et al., 2009), but also degradation of MMHg to Hg(II) and Hg(0) by photochemical and dark biotic processes (Fitzgerald et al., 2007; Sunderland et al., 2009). The limited understanding of the marine cycle of Hg is in part because of technical challenges associated with tracking and measuring different chemical forms of Hg in marine environments, especially in organisms like plankton at the base of the food web.

Plankton communities are known to be an important link between marine particles and higher trophic level pelagic marine organisms (See Figure 1 and references therein). However, there have been few studies of Hg speciation (e.g., MMHg, Hg(II)) in zooplankton, phytoplankton, or marine particles (Hammerschmidt et al., 2013; Gosnell and Mason, 2015), or the chemical and

biological pathways that control Hg speciation near the base of the foodweb (Morel et al., 1998; Munson et al., 2015). Although dissolved total Hg (THg = Hg(II) + MeHg) concentrations have been reported in marine pelagic waters (Sunderland et al., 2009; Hammerschmidt and Bowman, 2012; Munson et al., 2015), details concerning the sources, transformations, and bioavailability of this Hg pool for uptake and bioaccumulation remain elusive. In the Pacific Ocean, elevated dissolved Hg concentrations are generally known to occur in oxygen deficient waters (Sunderland et al., 2009; Hammerschmidt and Bowman, 2012). Elevated oceanic Hg concentrations have been attributed to evasion from sediments (Monperrus et al., 2003; Hammerschmidt et al., 2006), emission from seafloor hydrothermal vents (Lamborg et al., 2006), and horizontal advection from coastal areas (Hammerschmidt and Bowman, 2012). Elevated MMHg in the water column has been attributed to biotic methylation of Hg(II) on marine particles (Sunderland et al., 2009; Cossa et al., 2011; Blum et al., 2013) and abiotic methylation in the water column (Munson et al., 2018). Thus, the biogeochemical pathway(s) for MMHg production in the open ocean are complex and remain uncertain.

Our study investigates the biogeochemical and photochemical pathways that control the distribution and speciation of Hg in the marine pelagic food web utilizing THg concentrations and Hg stable isotope ratios that vary following mass-dependent fractionation (MDF) and mass-independent fractionation (MIF). Hg isotope ratios have proven to be effective at tracking the sources and sinks of Hg in a number of estuarine and marine ecosystems (e.g., Li et al., 2016; Kwon et al., 2015; Strok et al., 2015; Senn et al., 2010) and for exploring physicochemical reactions within the water column including reduction, photodegradation, oxidation, and methylation (e.g., Bergquist and Blum, 2007; Kritee et al., 2009; Chandan et al., 2015). Hg stable isotope ratios exhibit mass dependent fractionation (represented by $\delta^{202}\text{Hg}$ values) during all

abiotic and biotic physicochemical reactions that have been investigated. In addition to MDF, Hg isotope ratios exhibit large magnitude ($\geq 0.4\%$) MIF of odd-mass isotopes (odd-MIF; represented by $\Delta^{199}\text{Hg}$ and $\Delta^{201}\text{Hg}$ values) that has been attributed to photochemical transformations of Hg (Bergquist and Blum, 2007). Finally, MIF of even isotopes (even-MIF; represented by $\Delta^{200}\text{Hg}$ and $\Delta^{204}\text{Hg}$ values) is sometimes observed, particularly in rain and snow samples (e.g., Gratz et al., 2010; Chen et al., 2012), and it is strongly linked to atmospheric sources of Hg.

The objective of this study is to better understand the pathways of methylation and demethylation for the pool of Hg available for incorporation and bioaccumulation into marine foodwebs. To achieve this, we have analyzed Hg concentrations and stable isotope compositions of major components of the marine Hg cycle including precipitation, marine particles, zooplankton, and fish. We examine dissolved THg and MeHg concentrations, the relationship between the Hg isotopic composition of precipitation and surface marine particles, and Hg methylation in the water column, from the THg isotopic composition of marine particles and pelagic fish with depth. To assess Hg incorporation and bioaccumulation at the base of the foodweb, we examine THg concentrations and isotopic composition of marine zooplankton in three different size classes with depth. Finally, to investigate photochemical degradation of MMHg in surface waters we measure THg isotopic composition in zooplankton and pelagic fish.

The location of this study is Station ALOHA ($22^{\circ}45' \text{ N } 158^{\circ} \text{ W}$), the site of the Hawaiian Ocean Time Series located in oligotrophic waters about 100 km north of the Hawaiian island of Oahu in the North Pacific Subtropical Gyre (NPSG). This station is characterized by little seasonal variability in salinity, temperature or dissolved oxygen, resulting in a relatively stable thermocline and halocline (range 40 – 100 m) throughout the year. However, a rapid particle export pulse is typically observed from mid-July to mid-August and thus delivers bulk carbon (PC) and nitrogen

at an increased rate to below the mixed layer (150 m) and into the deep ocean (4000 m; Karl et al. 2012, Böttjer et al. 2017). Station ALOHA is near locations where previous work collected and analyzed pelagic fish for Hg concentrations and isotopic compositions (Choy et al., 2009; Blum et al., 2013).

2.2 Materials and methods

Sample types analyzed in this study include rainfall collected on-board the *R/V Kilo Moana* and on the Island of Hawaii, seawater from the surface to 1000 m depth, small (1-53 μm) and large (>53 μm) marine particles sampled at depths ranging from 25 to 700 m, and marine zooplankton in five size classes (ranging from 0.2 mm to >5 mm) collected from the surface to 1500 m depth. Marine samples were collected during three research cruises on board the *R/V Kilo Moana* at Station ALOHA (22.45°N, 158°W) in the NPSG in winter (KM 14-07, 19–28 February) of 2014, summer (KM 14-18, 29 August– 11 September) of 2014, and spring (KM 15-06, 2–11 May) of 2015. Measurements of water column dissolved oxygen and fluorescence were monitored during all sampling seasons using a Seabird SBE 9/11plus CTD deployed with two Sea-Bird SBE 3P temperature sensors, two Sea-Bird SBE 4C conductivity sensors, two Sea-Bird SBE 43 dissolved oxygen sensors and a Wetlabs ECO FLNTU Chlorophyll Fluorometer & Turbidity sensor. All reagents used in the laboratory and at sea were trace metal grade unless otherwise noted

2.2.1. Precipitation collection and analysis

Open ocean precipitation was collected during the summer season on an event basis using a manual collection method (Landis and Keeler, 1997). All of the Teflon and Pyrex glass components of the system were acid cleaned. The 1L sample bottles were deployed with 20 mL of 1% (wt/v) HCl to prevent reduction of Hg(II). Collection funnels were uncovered only when it was raining and the ship was steaming into a head wind to reduce possible contamination from

ship emissions. Due to infrequent precipitation, three separate rain events were combined into one sample to obtain sufficient Hg for isotope analysis. Additional samples were collected on land on the windward coast of the Island of Hawaii where trade winds bring moisture directly from the open ocean. These samples were collected at Hakalau Wildlife Refuge in December of 2005 (18 km from the coastline) on private property near the Waipio Valley lookout at the top of a cliff (300 m above the shoreline), and at the Nature Conservancy Ka'u Preserve (6 km inland from the ocean at shoreline level). Procedural field blanks were collected periodically during the sampling campaign using 1L of de-ionized water.

All precipitation samples were further oxidized with 1% BrCl (wt/v), which was allowed to react with the water sample in dark, refrigerated storage for a minimum of one month. The oxidized precipitation samples were subsequently reduced, purged and trapped into 1% KMnO₄ in 10% H₂SO₄ (wt/wt) solution for isotope analysis, following the procedure described by Washburn et al. (2017). Approximately 1L of previously acidified and oxidized sample was weighed into an acid-clean 2L borosilicate glass bottle and treated with 10 mL of 4.32 M NH₂OH-HCl to destroy free halogens, capped tightly, and allowed to react for a minimum of 30 minutes. Through one port of a three-port Teflon transfer cap, 100 mL of 10% SnCl₂ (wt/wt) in 20% HCl (wt/wt) was delivered to the reaction bottle via a peristaltic pump, at a rate of ~3.3 mL/min. Another port delivered Hg-free air (Au-filtered) into the reactor via an internal sparger, while the final port was connected to a sparger inserted into a borosilicate glass trap containing between 5.5 and 6.5 g of 1% KMnO₄ trapping solution. Samples were purged for 3 hours while reactor contents were mixed vigorously using an acid cleaned (10% wt/v HCl) Teflon stir bar. THg content of each sample bottle was determined by analyzing a small aliquot using cold vapor- atomic fluorescence spectrophotometry (CV-AFS; RA-3320FG+, Nippon Instruments). To determine Hg recovery the

THg concentration of small aliquots of each 1%KMnO₄ trapping solution was determined prior to transfer into a secondary trapping solution. The average purge and trap recoveries in precipitation samples was $93.7 \pm 6.1\%$ (1SD, n = 8) and procedural blanks yielded between 22.7 and 39.4 pg of Hg (n = 4), representing less than 1.4% of Hg in sample trap solutions. Periodically, procedural blanks and procedural standards (NIST-UM-Almadén) were prepared and analyzed in tandem with precipitation samples.

2.2.2 Dissolved Hg and particulate Hg collection and analysis

Seawater was collected for dissolved THg and MeHg analyses during the summer cruise using acid-cleaned (10% wt/v HCl) Go-Flo bottles deployed on an Amsteel line (Noble et al., 2012). THg dissolved concentrations were analyzed by dual Au-amalgamation cold vapor atomic fluorescence spectrometry (Tekran 2600) and dissolved MeHg concentrations were analyzed using ascorbic acid-assisted direct methylation (method adapted from Munson et al., 2015; Lamborg et al., 2012). Small (1-53 μm) and large (>53 μm) marine particles were sampled on all three cruises using *in situ* pumps (WTS-LV, standard, 8 L min⁻¹; McLane Research Laboratories, East Falmouth); water was passed sequentially through 53 μm pore-size nylon mesh and 1 μm pore-size quartz microfiber (QMA) filters with 142 mm diameter using a mini-MULVFS filter holder (Bishop et al., 2012). On the spring cruise, one pump was equipped with a pump head and motor with a maximum flow rate of 30 L min⁻¹, and high volume samples of particles >53 μm were collected. The large particles collected on the nylon mesh were sonicated and concentrated into a pre-combusted 47 mm QMA filter. The QMA filters of the small and large particles were digested using microwave assisted acid digestion and aliquots of the digestions were measured for THg by cold vapor atomic fluorescence spectrophotometry (CV-AFS; RA-3320FG+, Nippon Instruments). Details of the dissolved and particulate Hg analyses can be found in the supporting

information section 1.

In order to obtain enough Hg from small particles for isotope analysis, multiple 142 mm QMA filters were pooled from single depth horizons (± 15 m). For samples from 25 m, two filters containing particles from ~ 4000 L of filtered water were sufficient. In contrast, at all other depths (150, 400, and 690 m) larger numbers of filters representing particles from >6500 L of filtered water, were necessary (SI; Table S4a,b). Even more extensive pooling of material was required to obtain enough Hg from the >53 μm particles for a single isotope analysis. In the spring, a combined volume of $\sim 35,000$ L of water were filtered through 53 μm nylon mesh filters ($n = 10$ samples) at 30 L min^{-1} flow rates from 157 m. The combined nylon filters were rinsed onto three 47 mm diameter QMA filters (details in supporting material and references within). Following lyophilization, QMA filters from the same depth were processed together, and Hg was released from the particle matrix by two-stage combustion and trapping into an oxidizing solution (1% KMnO_4 in 10% H_2SO_4 (wt/wt)) (Biswas et al., 2008). A small aliquot of the trap solution was measured for THg concentration by CV-AFS (RA-3320FG+, Nippon Instruments). Combustion performance was monitored with procedural blanks, microfiber quartz filter blanks and combustion blanks (Table S4a,b).

For stable isotope ratio measurements of Hg the initial KMnO_4 trap solutions were chemically reduced with $\text{NH}_2\text{OH-HCl}$ and SnCl_2 and $\text{Hg}(0)$ was purged into smaller secondary traps containing 6 g of 1% KMnO_4 (wt/v) prepared in 10% H_2SO_4 (v/v) for additional purification and preconcentration.

2.2.3 Zooplankton collection and analysis

Zooplankton were collected in summer and spring at Station ALOHA using a 1 m^2 MOCNESS (Multiple Opening/Closing Net and Environmental Sensing System; Wiebe et al.,

1985) equipped with nine sampling nets. Most of the zooplankton were collected in summer during the day ($n = 2$ tows) and night ($n = 3$ tows). Each tow collected material from nine depth intervals spanning the ocean surface to 1500 m (0-50 m, 50-100 m, 100-150 m, 150-200 m, 200-300 m, 300-500 m, 500-700 m, 700-1000 m, 1000-1500 m). In spring, four separate net tows were conducted to collect additional samples from a single depth interval (500-700 m). This was done to provide enough sample material to assess variability in Hg content and isotopic composition in a pool of material well constrained in terms of depth, areal extent, and time. Following collection, the cod ends of each net were retrieved and immediately immersed in chilled surface seawater. Zooplankton samples collected in the cod ends were wet sieved into 5 separate size fractions using stacked 0.2, 0.5, 1.0, 2.0 and 5.0 mm mesh sieves, and the separated size fractions were filtered onto acid-cleaned, pre-weighed 47 mm diameter 0.2 mm synthetic nylon mesh filters. To make sure that the dominant species were zooplankton our smallest sieve was 0.2 mm, which in the oligotrophic gyre excludes nearly all phytoplankton species (Pasulka et al., 2013). Briefly, the dominant zooplankton in the 0.2 to 1 mm size fractions were copepods and ostracods, and the 5 mm size fraction included euphaeids, amphipods and chaetognaths. All samples were lyophilized and then homogenized using an acid cleaned agate mortar and pestle (Hannides et al., 2016).

For THg determination about 10 mg of zooplankton from each tow and size fraction was digested in reverse aqua regia (0.1 mL HCl:0.3 ml HNO₃; Optima, Fisher Scientific) overnight. Digest solutions were brought to a final volume of 4 mL with sequential additions of BrCl, H₂O₂ (Suprapur; MilliporeSigma, VWR Scientific) and deionized water. Multiple preparations of acid matrix blanks, combustion blanks, and certified reference material (TORT-2, National Research Council Canada) were analyzed for quality control.

For zooplankton, limited availability of bulk material necessitated pooling of samples for measurement of THg stable isotopic compositions, especially from depths below the euphotic zone (> 175 m; Table S2). Within each of six target depth intervals (Table S2) four zooplankton size fractions were combined to produce samples representing small (0.2-1 mm) and intermediate (1-5 mm) size zooplankton. The fifth and largest size class (> 5 mm), which included occasional small fish as well as large zooplankton, was analyzed separately. All samples measured for Hg isotope ratios included material from more than one tow. For the 3 depth intervals at 500 m and above (e.g., 0-50 m, 100-150 m, 300-500 m) day and night samples of the small, intermediate, and large size classes were measured separately for Hg isotope ratios. For the 3 depth intervals below 500 m (500-700 m, 700-1000 m, 1000-1500 m) separate day and night results could be obtained only for the intermediate and large size classes. Results for the small size class from the 3 depth intervals below 500 m include material combined from both day and night tows. Zooplankton samples were placed in ceramic boats in a two-stage combustion furnace, combusted similarly to the large and small particle QMA filters, and trapped in a 1% KMnO₄ solution for isotope analysis.

2.2.4 Fish collection and analysis

Twelve individual fish samples were analyzed for THg, from which ten THg isotopic measurements were obtained. Three different individuals of the *Lampris sp.* were combined to obtain enough Hg for isotope analysis; details can be found in the supplementary tables (Table S1a). Lyophilized fish samples were combusted similarly to the particles and zooplankton and trapped in a 1% KMnO₄ solution for isotope analysis.

2.2.5 Hg isotope analysis

Each combusted sample trapped in 1% KMnO₄ solution was purged into a secondary 1% KMnO₄ trapping solution to remove matrix interferences from combustion residues and to

concentrate THg for isotopic analysis (Blum and Johnson, 2017). All samples were pre-concentrated in a 1% KMnO₄ solution and analyzed for Hg stable isotope compositions using a multiple collector inductively coupled plasma mass spectrometer (MC-ICP-MS; Nu Instruments) with a continuous flow cold vapor generation inlet system with SnCl₂ reduction (Lauretta et al., 2001; Blum and Bergquist, 2007). Prior to isotope analysis, the Hg concentrations of the 1% KMnO₄ sample trap solutions were matched to the bracketing standards (SRM NIST 3133) for each of the mass spectrometry sessions. The THg concentrations of the 1% KMnO₄ sample trap solutions for all samples are provided in Tables S1a-e.

Mass dependent fractionation (MDF) of Hg isotopes is reported as $\delta^{202}\text{Hg}$ values in permil (‰) relative to NIST SRM 3133 (Equation 1). Mass independent fractionation (MIF) of Hg isotopes is calculated as the difference between the measured $\delta^{202}\text{Hg}$ value and that which would be predicted based on mass dependence for a given isotope. It is reported as $\Delta^{\text{xxx}}\text{Hg}$ in ‰ (Equation 2), where xxx is the mass of each Hg isotope, i.e., 199, 200, 201, 204, and β is the mass proportionality constant (0.2520, 0.5024, 0.7520, 1.493, respectively) (Blum and Bergquist, 2007).

$$\delta^{\text{xxx}}\text{Hg} (\text{‰}) = \left(\frac{(^{202}\text{Hg}/^{198}\text{Hg})_{\text{unknown}}}{(^{202}\text{Hg}/^{198}\text{Hg})_{\text{SRM3133}}} - 1 \right) \times 1000 \quad (\text{Equation 1})$$

$$\Delta^{\text{xxx}}\text{Hg} = \delta^{\text{xxx}}\text{Hg} - (\delta^{202}\text{Hg} \times \beta) \quad (\text{Equation 2})$$

Procedural process blanks and standard reference materials (TORT-2 and DORM-3 for combusted samples, and UM-Almadén for purge and trap samples) were processed alongside samples in an identical manner (Table S1a-f). Process yields from secondary purge and trapping of the 1% KMnO₄ trap solutions averaged 97% ± 8% (1SD, minimum = 85.5%). The long-term analytical uncertainty of Hg isotopic composition of the samples, most of which could be measured only once, was estimated as ± 2SD based on repeated measurements across runs of the appropriate standard reference materials (UM-Almadén, DORM-3, ERM-CE464, NIST-CRM1947, and

TORT-2) (Table S1b). When comparing specific samples with each other or a population of samples, ± 1 SD is reported (Blum and Bergquist, 2007). For data analysis the majority of statistical tests were completed using the Wilcoxon test (unless otherwise noted) because the sample size was usually too small for a t-test. Linear regressions were completed using the York regression, which considers errors in both the X and Y axes (York 1969).

2.3 Results

For all seasons the oxygen minimum was located at ~ 700 m and dissolved oxygen ranged from 25 to 34 $\mu\text{mol/kg}$. Fluorescence was lowest in February and highest in September and the deep chlorophyll maximum was at ~ 125 m for all seasons ($0.4\text{-}0.9 \text{ mg m}^{-3}$). The mixed layer depth was ~ 100 m for the winter and ~ 45 m for the spring and summer.

Vertical profiles of dissolved THg and MeHg measured at Station ALOHA during the summer are similar to results previously published by Munson et al. (2015) at $17^\circ\text{N } 154^\circ\text{W}$ and Sunderland et al. (2009) at $23^\circ\text{N } 152^\circ\text{W}$ and ranged from 0.07 to 0.43 ng/L for THg and 5.0×10^{-3} to 2.5×10^{-2} ng/L for MeHg (Figure S1). Small particles ($1\text{-}53 \mu\text{m}$) collected at Station ALOHA had the highest THg at the surface and declined with depth reaching an average of $4.57 \times 10^{-3} \pm 7.5 \times 10^{-4}$ ng/L (1SD, $n=5$; S2). Large particles were orders of magnitude lower in THg than the smaller fraction at the same depths (150 m) and ranged from 1.70×10^{-4} ng/L in September to 6.66×10^{-4} ng/L in May (Figure S2). Additional details regarding the vertical profiles are found in the supplementary material and all mercury isotope data and THg concentrations are presented in Supplementary Tables S1-4.

2.3.1 Precipitation

The average THg of samples collected on the Island of Hawaii was 11.8 ± 7.5 ng/L ($n = 8$, 1SD). For these land-based samples, the average isotopic values are $\delta^{202}\text{Hg} = 0.07 \pm 0.08\text{‰}$,

$\Delta^{199}\text{Hg}=0.33\pm 0.24\text{‰}$, and $\Delta^{200}\text{Hg}=0.14\pm 0.05\text{‰}$ ($n=7$; 1SD). The THg concentration of open ocean precipitation (9.6 ± 2.6 ng/L; 1SD, $n=2$) was within uncertainty of the land-based samples. The Hg stable isotope composition of the single open ocean precipitation sample was $\delta^{202}\text{Hg}=0.15\text{‰}$, $\Delta^{199}\text{Hg}=-0.02\text{‰}$, and $\Delta^{200}\text{Hg}=0.08\text{‰}$. This is within uncertainty of the average $\delta^{202}\text{Hg}$ and $\Delta^{200}\text{Hg}$ values determined for precipitation from the Island of Hawaii. The $\Delta^{199}\text{Hg}$ value was slightly more negative, however limited sampling does not allow for a general conclusion that open ocean precipitation has more negative $\Delta^{199}\text{Hg}$ than precipitation collected on land. The lack of distinction in isotopic composition between open ocean and land-based precipitation is supported by the observation that $\Delta^{201}\text{Hg}$ values from the samples collected on the island of Hawaii ($\Delta^{201}\text{Hg}=0.32\pm 0.23\text{‰}$, 1SD, $n=7$) overlap with the single open ocean sample within analytical uncertainty ($\Delta^{201}\text{Hg}=0.10\text{‰}$).

2.3.2 THg Isotopic Composition of Marine Particles

At the shallowest depth of 25 m, $\delta^{202}\text{Hg}$ values for small particles were on average $-0.10\pm 0.01\text{‰}$ (1SD, $n=3$) (Figure 2a; Table S1c), and there were no seasonal differences. At 150 m, values were statistically lower than at all other depths (-0.27 to -0.14‰ , $n=4$, 1SD= 0.06‰ , average= -0.20‰), and there was no statistically significant seasonal variation at this depth (Wilcoxon test, $W=33$, $p<0.01$). At 400 m, values ranged from $\delta^{202}\text{Hg}=-0.22\text{‰}$ in February to $\delta^{202}\text{Hg}=0.08\text{‰}$ in May. There was no sample collected in September. The February value from 400 m is statistically identical to the average at 150 m (Wilcoxon test, $W=18$, $p<0.03$), while the September value from 400 m has a similar value to the single sample analyzed from May at 690 m ($\delta^{202}\text{Hg}=0.17\text{‰}$).

The $\Delta^{199}\text{Hg}$ values in the small particles were relatively constant in the upper 150 m across seasons (Figure 2b, 0.06 to 0.18‰ , average= $0.12\pm 0.05\text{‰}$, 1SD, $n=7$) and the standard deviation

of the average value was equal to the measurement uncertainty (Almaden, 2SD $\Delta^{199}\text{Hg} \pm 0.10$). The deeper samples from all seasons, collected from 400 and 690 m, had significantly higher $\Delta^{199}\text{Hg}$ values than those from the upper 150 m (25-150 m average = 0.12‰; 400-690 m average = 0.27‰, Wilcoxon test, $W=23$, $p < 0.03$). The $\delta^{202}\text{Hg}$ and $\Delta^{199}\text{Hg}$ values for the large particles ($>53 \mu\text{m}$) collected in May at 150 m are nearly the same as for the small particles collected in the same season at the same depth ($\delta^{202}\text{Hg} = -0.17\text{‰}$ and $\Delta^{199}\text{Hg} = 0.11\text{‰}$). The $\Delta^{200}\text{Hg}$ values for all the particles were nearly the same throughout the water column (Figure S3, $\Delta^{200}\text{Hg} = 0.05 \pm 0.05\text{‰}$, 1SD, $n=12$)

2.3.3 Zooplankton

In the upper 125 m, THg concentrations in zooplankton are highest for the smallest size class by an average of 7.5 ng/g relative to the larger size classes (0.5-1, 1-2, and >5 mm, Wilcoxon test, $W=127$, $p < 0.01$), and THg increases with depth to 500-700 m for all size classes (Figure 3; Table S3). Below 700 m, THg within the smallest size class decreases with depth, while in the larger size classes (2 to >5 mm) THg increases with depth. There were significant THg diurnal variations within the mesopelagic (200 to 1500 m); zooplankton collected at night had significantly higher THg concentrations than samples collected during the day (Figure 3; Day-Night paired, Wilcoxon test, $W=137$, $p < 0.01$). To examine the effects of zooplankton diel migration on mobilization of Hg within the water column we normalized zooplankton Hg content to the volume of seawater filtered by each net (in units of ng Hg/ L_{seawater} ; Figure 3b). The Hg/L depth profiles of the zooplankton follow the same trend as for summer 2014 migrant zooplankton biomass (Hannides et al., 2016).

The Hg isotope composition of zooplankton clearly differs between size classes and between depth of collection over the six target mean depth intervals (0-50, 100-150, 300-500, 500-

700, 700-1000, 1000-1500 m; see Figure 2, Figure S4a,b, Table S1d). The $\delta^{202}\text{Hg}$ values decline with depth for all the size classes and there was no statistical difference in the rate of decline of $\delta^{202}\text{Hg}$ values with depth between the size classes (Figure S4a, average slope $\delta^{202}\text{Hg}/\text{Km} = -0.42 \pm 0.06$, $n=4$, 1SD, $p<0.02$), with the exception of the > 5 mm size fraction, where there was no relationship with depth for the samples collected during the day (Wilcoxon test, $W=15$, $p=0.05$). At each depth the range of $\delta^{202}\text{Hg}$ values across the different size classes is $\sim 0.35\%$. In surface waters both small and large size classes, respectively, have the highest (0.26%) and lowest (-0.02%) $\delta^{202}\text{Hg}$ values. At greater depths (100 to 1500 m) $\delta^{202}\text{Hg}$ values are lowest for the small size class ($\delta^{202}\text{Hg}$ average $= -0.31 \pm 0.15\%$), higher for the intermediate size class ($\delta^{202}\text{Hg}$ average $= -0.22 \pm 0.16\%$), and highest for the >5 mm size class ($\delta^{202}\text{Hg}$ average $= -0.11 \pm 0.13\%$).

In contrast to $\delta^{202}\text{Hg}$ values, surface water $\Delta^{199}\text{Hg}$ values varied more broadly, differing by 2% across size classes. The smallest size fraction had the highest $\Delta^{199}\text{Hg}$ values, and the samples collected during the day had higher $\Delta^{199}\text{Hg}$ values than those collected at night (Figure 2b, Figure S4b; Table S1d). Samples from greater depths (125-1250 m) had statistically lower $\Delta^{199}\text{Hg}$ values than those from the surface (Wilcoxon test, $W=15$, $p<0.02$) and had smaller ranges in $\Delta^{199}\text{Hg}$. Unlike $\delta^{202}\text{Hg}$ values, there were no significant changes in $\Delta^{199}\text{Hg}$ values below 125 m (100 -1500 m, average slope, $\Delta^{199}\text{Hg}/\text{Km} = -0.04$, $n=27$) and there was no diurnal signature (Wilcoxon test, $W=40.5$, $p>0.1$).

Zooplankton samples did not have a significant trend in $\Delta^{200}\text{Hg}$ with depth, and averaged $0.07 \pm 0.08\%$ (1SD, $n=33$). There was a small diurnal contrast in $\Delta^{200}\text{Hg}$ values obtained from the shallowest samples and from samples collected at 400 m (Figure S3). However, there was no diurnal contrast in $\Delta^{204}\text{Hg}$ values (which is also produced by even-MIF), suggesting that the negative values for $\Delta^{200}\text{Hg}$ at 400 m are likely due to an analytical artifact. $\Delta^{204}\text{Hg}$ values are

typically inversely correlated with $\Delta^{200}\text{Hg}$ values (Demers et al 2010; Blum and Johnson, 2016) and, therefore, negative $\Delta^{200}\text{Hg}$ and $\Delta^{204}\text{Hg}$ values are very rare (Blum et al., 2014). In addition, the magnitude of even-MIF is small relative to the measurement uncertainty for standard reference material TORT-2 ($\Delta^{200}\text{Hg}\pm 0.13\%$ and $\Delta^{204}\text{Hg}\pm 0.09\%$; 2SD, n=31).

Replicate collections of material from a single depth range were obtained to determine the variability in zooplankton Hg isotopic composition (Table S1e, 500-700 m). For the intermediate fraction, the variability associated with average $\delta^{202}\text{Hg}$, $\Delta^{199}\text{Hg}$, and $\Delta^{200}\text{Hg}$ values was 0.05‰, 0.07‰, and 0.06‰ (1SD), respectively. For the large fraction the 1SD of average $\delta^{202}\text{Hg}$, $\Delta^{199}\text{Hg}$ and $\Delta^{200}\text{Hg}$ values was 0.14‰, 0.2‰, and 0.04‰, respectively. Limited availability of <1mm zooplankton material prevented determination of external reproducibility for the small size class fraction. Instead, two single analyses were performed on < 1mm zooplankton material pooled from all four nets, but separated into <0.5 mm and 0.5-1mm sub-fractions. Small differences between these two sub-fractions for $\delta^{202}\text{Hg}$ (0.04‰), $\Delta^{199}\text{Hg}$ (0.11‰), and $\Delta^{200}\text{Hg}$ (0.02‰) suggests that within-class variability in the small size class (0.2-1 mm) is comparable to, or smaller than, that of the intermediate size class (1-5 mm).

2.3.4 Pelagic Fish

Dry-mass THg concentrations in fish range from less than 100 to more than 2000 ng/g. In the large pelagic species (*Lampris sp.* and *Thunnus obesus*) THg concentrations were a factor of 10 to 100 higher than THg concentrations in zooplankton from comparable depths. Small micronekton that feed in upper mesopelagic waters (~400 m, *Idiacanthus fasciola*) had average THg content less than a factor of two higher than zooplankton from comparable depths. However, deeper feeding micronekton (700 - >1000 m, *Anoplogaster cornuta*, *Cyclothone pallida*, *Melanocetus johnsonii*) had THg content almost an order of magnitude higher than zooplankton

from similar depths. Estimates of external variability associated with fish isotope results is hampered by the small number of individuals sampled per species. However, the results obtained from multiple individuals and the averages of 1SD uncertainties associated with species replicate $\delta^{202}\text{Hg}$, $\Delta^{199}\text{Hg}$, and $\Delta^{200}\text{Hg}$ values are 0.12‰, 0.13‰, and 0.03‰ respectively (Table S1e). $\delta^{202}\text{Hg}$ and $\Delta^{199}\text{Hg}$ values in Figure 2a,b illustrate that for the pelagic fish, $\delta^{202}\text{Hg}$ and $\Delta^{199}\text{Hg}$ values decline with depth. In contrast, there were no statistically significant differences with depth in $\Delta^{200}\text{Hg}$ values, which averaged $0.09 \pm 0.04\text{‰}$. A single sample of *Idiacanthus fasciola* at 400 m had an anomalous $\Delta^{200}\text{Hg}$ value of -0.16‰ , which may be an analytical artifact. The pelagic fish samples with a depth of occurrence between 225-400 meters had a similar Hg isotopic composition to fish samples from the NPSG at similar depths. Fish from greater depths (700-1000 m) also follow the same trend reported by Blum et al. (2013).

2.4. Discussion

Here we integrate measurements of the stable isotopic composition of Hg in components of the marine biogeochemical cycle in order to address some of the outstanding questions in marine Hg biogeochemistry. Our main focus is on understanding Hg dynamics in the pelagic food web, abiotic and biotic production and degradation of MMHg throughout the water column, and the importance of particles and zooplankton to the marine biogeochemical cycle of Hg. We report that in the NPSG, at the base of the marine food-web, the fraction of THg associated with marine particles or zooplankton per liter of water is very small relative to dissolved THg. For example, between 150-175 m dissolved THg (0.15 Hg ng/L) accounts for 96% of THg and is 5 orders of magnitude greater than zooplankton (0.2-5 mm; $1.24 \times 10^{-5} \pm 0.50 \times 10^{-5}$ ng/L, 1SD, n=16), 3 orders of magnitude greater than small particles (1-53 μm ; $6.46 \times 10^{-3} \pm 1.84 \times 10^{-3}$ Hg ng/L, n=3), and about 4 orders of magnitude greater than large particles (>53 μm ; 4.18×10^{-4} Hg ng/L, n=2). To guide our

discussion, we provide a graphic that displays our conceptual model of the marine Hg cycle (Figure 1).

2.4.1 Dissolved THg and MeHg vertical profiles

The vertical profiles of dissolved THg and MeHg (MMHg+dimethyl-Hg) that we measured at Station ALOHA are similar to those of other North Pacific Ocean profiles (Sunderland et al., 2009; Hammerschmidt and Bowman, 2012, Munson et al., 2015; Laurier et al., 2004). In our study, surface water MeHg was within the range of values reported by Sunderland et al. (2009) at 23°N 155°W but was somewhat greater than the values reported by Munson et al. (2015) at 17°N 155°W. This variability in surface ocean MeHg concentrations is likely the result of spatial variation in MeHg production and degradation rates as well as differences in partitioning of dissolved MeHg between water and particle surfaces due to seasonal changes in productivity (Laurier et al., 2004; Sunderland et al., 2009). Vertical profiles of dissolved Hg in the NPSG have been well characterized in previous work (Laurier et al., 2004; Sunderland et al., 2009; Hammerschmidt and Bowman, 2012; Munson et al., 2015) and will not be discussed further here. Details of the dissolved Hg speciation at Station ALOHA are found in the supporting information and references therein (SI section 2)

2.4.2 Hg isotope ratios as indicators of Hg transformation in the NPSG

2.4.2.1 Hg isotope ratios in surface waters (upper 25 m)

As a starting point for the interpretation of the Hg isotope ratios in our study we assume that a significant portion of the Hg available for bioaccumulation in the water column was originally derived from precipitation, as this is considered to be the major source of Hg to the surface ocean (Figure 1; Sunderland et al., 2009; Mason and Sheu, 2002; Fitzgerald et al., 2007). It is challenging to fully link the Hg isotopic composition of precipitation to that of Hg entry to the

food-web, because 50-70% of Hg in precipitation is potentially emitted back to the atmosphere (Strode et al., 2007; Andersson et al., 2011). The remaining dissolved Hg may undergo further transformation, including methylation, particle sorption, or additional photochemical reduction. There is also limited understanding of photochemical degradation of Hg(II), the potential uptake of gaseous Hg(0) in surface marine waters, and the impact of associated isotopic fractionation on the Hg isotopic composition of the dissolved Hg pool. This is because in ocean water the fraction of Hg complexed to organic ligands may not be the dominant form of THg (Lamborg et al., 2003) and it has been demonstrated that Hg stable isotope signatures associated with Hg(II) photoreduction depends on the complexing ligand (Zheng and Hintelmann, 2010). It is also difficult to evaluate the role of evasion and uptake of Hg(0) because a portion of Hg(0) may be re-oxidized in the marine boundary layer (Laurier et al., 2004; Hedgecock and Pirrone, 2001; Sprovieri et al., 2010) or re-deposited to the ocean in precipitation. Finally, direct measurements of Hg isotopic composition in the dissolved pool of THg are difficult due to the low THg concentrations in pelagic waters and the challenge associated with concentrating sufficient quantities of dissolved Hg for analysis. The Hg isotopic composition of seawater has been measured in only one study, in a costal location (Štok et al., 2015). The $\Delta^{199}\text{Hg}$ values for dissolved THg from Arctic coastal waters ($\Delta^{199}\text{Hg}$ average= $0.22\pm 0.06\text{‰}$, 1SD) are within the range of values measured for marine particles in the NPSG. In contrast, the $\delta^{202}\text{Hg}$ values of the dissolved THg in the Arctic are considerably more negative ($\delta^{202}\text{Hg}$ average= $-2.08\pm 0.61\text{‰}$, 1SD) than particles in the NPSG. This is not surprising because the Canadian Arctic Archipelago not only has Hg inputs from precipitation but also from riverine discharge (Sunderland and Mason, 2007; Fisher et al., 2012; Cossa et al., 2018).

Measurements of the Hg isotopic composition of precipitation and marine particles allow a reasonable estimation of the Hg isotopic composition of the bioavailable Hg pool. In surface waters, Hg enters the foodweb when phytoplankton incorporate dissolved THg from passive uptake or when zooplankton graze on marine particles or phytoplankton. This results in $\Delta^{200}\text{Hg}$ and $\Delta^{204}\text{Hg}$ values in surface zooplankton that retain a positive $\Delta^{200}\text{Hg}$ and negative $\Delta^{204}\text{Hg}$ signature of Hg from precipitation (zooplankton: $\Delta^{200}\text{Hg}=0.11\pm 0.09\text{‰}$ and $\Delta^{204}\text{Hg}=-0.07\pm 0.08\text{‰}$, 1SD, n=6; precipitation: $\Delta^{200}\text{Hg}=0.13\pm 0.05\text{‰}$ and $\Delta^{204}\text{Hg}=-0.26\pm 0.17\text{‰}$, n=8; Figure S3). The THg isotopic composition of marine particles in surface waters likely represent the THg isotopic composition that is exported to the ocean interior. Below the mixed layer POM is the primary pathway by which Hg is transported to depth in the ocean, and is the source of Hg that is available to enter the pelagic foodweb (Figure 1; Zaferani et al., 2018; Sunderland et al., 2009; Lamborg et al., 2016). This is because metazoans rely on marine particles as food resources, and dissolved Hg would have to be either sorbed to particles or assimilated by phytoplankton in order to be transferred higher in the food-web as illustrated in Figure 1.

The size classes of particles we collected contain both phytoplankton biomass and other particles, such as marine snow and detritus, and both small and large particles have been identified as food sources for zooplankton and micronekton at station ALOHA (Choy et al., 2015; Gloeckler et al., 2018; Hannides et al., 2016). The $\delta^{202}\text{Hg}$ values show a small negative offset (0.18‰) between precipitation (n = 8) and small particles (n = 3)(Figure 2a,b); this offset is consistent with the MDF of Hg that occurs during binding to thiol functional groups associated with organic matter and sorption to particles (Wiederhold et al., 2010; Jiskra et al., 2012). The 0.18‰ offset in $\delta^{202}\text{Hg}$ is small compared to the offset observed in experimental sorption studies (Wiederhold et al., 2010; Jiskra et al., 2012), but this is not surprising because experiments used pure goethite or thiol

ligands, and Hg sorption experiments do not take into consideration the effects of the high ionic strength of seawater. The $\Delta^{199}\text{Hg}$ and $\Delta^{200}\text{Hg}$ values of precipitation overlap with those of the particles, however, the range of $\Delta^{199}\text{Hg}$ and $\Delta^{200}\text{Hg}$ is narrow suggesting that isotopic variability attributed to individual precipitation events may be homogenized in the surface ocean as Hg undergoes exchange with particles.

2.4.2.2. Hg stable isotope ratios in the lower epipelagic and upper mesopelagic (150-700 m depth)

Below the mixed layer even-MIF values support the idea that the main source of Hg to the marine foodweb is particulate Hg. The even-MIF isotopic composition of the particles is nearly the same throughout the water column and is similar to the surface water particulate matter isotopic signature (average, $\Delta^{200}\text{Hg}=0.06\pm 0.03\%$ and $\Delta^{204}\text{Hg}=-0.10\pm 0.06\%$, $n=9$; 1SD). The zooplankton have a very narrow range of even-MIF values below the mixed layer ($\Delta^{200}\text{Hg}=0.06\pm 0.07\%$ and $\Delta^{204}\text{Hg}=-0.06\pm 0.07\%$, $n=9$; 1SD) compared to precipitation, and the zooplankton overlap with the $\Delta^{200}\text{Hg}$ and $\Delta^{204}\text{Hg}$ values of the particles. This is because below the mixed layer metazoans primarily consume POM (Hannides et al., 2016). As a consequence, the average even-MIF of pelagic fish in NPSG ($\Delta^{200}\text{Hg}=0.07\pm 0.05\%$ and $\Delta^{204}\text{Hg}=-0.11\pm 0.06\%$, $n=9$; 1SD) is also similar to the particles and zooplankton.

The THg $\delta^{202}\text{Hg}$ values of the particles below the mixed layer also reflect significant changes in particulate Hg with depth. For example, at 150 m the THg to bulk particulate carbon ratio (THg/PC) increases abruptly (Table S4a,b; Umhau et al., 2016), which is indicative of preferential organic carbon degradation (Close et al., 2014, 2015) or an increase in THg sorption that results in an enrichment of THg in particles. At this depth, $\delta^{202}\text{Hg}$ values of marine particles were more negative than surface samples, which suggests that the particulate increase in THg

relative to PC is due to THg sorption to POM. (Figure 2a; Wiederhold et al., 2010; Jiskra et al., 2012). At greater depths (400-690 m), $\delta^{202}\text{Hg}$ values show seasonal differences that are likely driven by temporal changes in marine particle export at Station ALOHA (Umhau et al., 2016). Samples collected in May coincided with the beginning of a period of increased productivity, while samples collected in September coincided with the middle to end of the commonly observed seasonal bloom at ALOHA, which is marked by higher concentrations of PC and bulk nitrogen across small and large particle size classes and high particle export fluxes (Umhau et al., 2016; Church et al., 2013). The increase in $\delta^{202}\text{Hg}$ values of particles sampled at 400-690 m in May and September (Figure 2a) likely reflects this period of increased productivity at Station ALOHA (Umhau et al., 2016; Church et al., 2013). This interpretation agrees with the findings of Hannides et al. (2016), who provided evidence for increased microbial reworking of small particles in September and May relative to zooplankton grazing.

2.4.3 Methylation of Hg in the water column

The THg isotopic composition of marine particles serves as a marker of the Hg available for methylation and subsequent bioaccumulation, and as such, it can also be used as a proxy for examining Hg methylation. The specific mechanism for methylation of Hg(II) in the open ocean water column is uncertain, but is likely microbially mediated, as it is in freshwater and terrestrial ecosystems (Morel et al., 1998; Sunderland et al., 2009; Cossa et al., 2009,1997). There is, however, also evidence from filtered seawater experiments (Munson et al., 2018) for non-cellular or extracellular methylation in the water column in the oligotrophic Pacific. Methylation of Hg in the water column was also shown to be consistent with patterns of Hg isotope variation with the depth of marine fish feeding (Blum et al., 2013). Here, we use measured particle THg concentrations and isotopic compositions to infer the isotopic composition of MMHg available for

consumption. Although we lack direct measurements of particle MMHg abundance and isotopic composition, previous experimental work has shown that the MMHg produced has lower $\delta^{202}\text{Hg}$ values compared to that of reactant Hg(II) (Janssen et al., 2016; Rodriguez-Gonzalez et al., 2009). If the extent of methylation is high enough, residual Hg(II) will have detectably higher $\delta^{202}\text{Hg}$ than reactant Hg(II). Experimental studies have also demonstrated that methylation of Hg by microbial processes results in MDF but not MIF (Janssen et al., 2016; Rodriguez-Gonzalez et al., 2009).

In order to aid in the interpretation of Hg isotope measurements made in this study, within the context of Hg methylation in the water column, we have listed five assumptions that we have made based on previous research on the biological pump and Hg stable isotope behavior:

- 1) The difference in $\delta^{202}\text{Hg}$ values between precipitation and particles in surface waters results from MDF of Hg(II) during sorption to particles (Wiederhold et al., 2010; Jiskra et al., 2012) and equilibration with the existing pool of Hg(II) in the surface ocean.
- 2) The main zone of particle production at Station ALOHA is within the mixed layer and maximum particle remineralization occurs immediately below the deep chlorophyll maximum (Figure S1; Benitez-Nelson et al., 2001; Steinberg et al., 2008), which in this study was at ~125 m.
- 3) In the mesopelagic zone, large particles ($> 53 \mu\text{m}$) are exploited as a food resource by zooplankton during all seasons and small particles (1-53 μm) become an important source during the winter (Hannides et al., 2016).
- 4) MMHg accumulated in particles by methylation of Hg(II) is efficiently bioaccumulated by consumers and incorporated in the pelagic food web by zooplankton grazing. The Hg(II) that is not bioaccumulated is excreted as fecal pellets at depth (Mason et al., 1996) leading to a relative increase of Hg(II) in the large particles at depth. These large fecal pellets can

also be modified by sloppy feeding from zooplankton (Steinberg and Landry, 2017) resulting in an increase of Hg(II) in the small particles at depth.

- 5) Photochemical degradation of MMHg in sunlit surface water results in elevated $\Delta^{199}\text{Hg}$ values. Since there are no known mechanisms in aquatic systems for erasing that MIF, except by dilution with newly formed MMHg at depths below the euphotic zone that does not have elevated $\Delta^{199}\text{Hg}$ values, observed decreases in $\Delta^{199}\text{Hg}$ (and $\delta^{202}\text{Hg}$) values in marine organisms with depth requires Hg methylation below the euphotic zone (Cossa et al., 2009; Blum et al., 2013).

Evidence that newly methylated Hg carried by particles enters the pelagic marine food web is illustrated by the $\delta^{202}\text{Hg}$ values in Figure 2a. We observe significantly higher $\delta^{202}\text{Hg}$ values associated with particles collected in deeper waters (400-700 m, Figure 2a) relative to $\delta^{202}\text{Hg}$ values measured in particles from the upper 150 m around the period of the rapid particle export pulse below the mixed layer (150 m) typically observed at Station ALOHA (Karl et al. 2012, Böttjer et al. 2017). We propose that the increased productivity at these depths (Church et al., 2013; Hannides et al., 2016) may stimulate methylation of Hg resulting in an increase in $\delta^{202}\text{Hg}$ values at this depth between May and September. An increase in $\delta^{202}\text{Hg}$ values is supported by findings from microbial methylation experiments (Janssen et al., 2016, Rodriguez-Gonzalez et al., 2009) and the fact that below 150 m the concentration of particulate THg is similar regardless of the season (Fig S2), whereas the MMHg content has been observed to increase (Munson et al., 2014; Hammerschmidt and Bowman, 2012). For zooplankton and fish, lower $\delta^{202}\text{Hg}$ values are also observed with increasing depth (Figures 2a, Figure S4a). This is consistent with zooplankton preferentially bioaccumulating MMHg and discarding Hg(II) in their fecal matter (Mason et al., 1996); the newly formed MMHg with lower $\delta^{202}\text{Hg}$ values deeper in the water column is

preferentially assimilated leaving the residual particulate Hg(II) with increasingly higher $\delta^{202}\text{Hg}$ values. Residual Hg is continuously incorporated into the POM shifting the Hg isotopic composition to higher $\delta^{202}\text{Hg}$ values at depth. Our results are consistent with the argument by Blum et al (2013) that the decreasing $\delta^{202}\text{Hg}$ and $\Delta^{199}\text{Hg}$ values in predatory fish provides evidence that new MMHg formed at depth is incorporated into the foodweb.

While $\Delta^{199}\text{Hg}$ values of pelagic fish decrease with depth (indicating Hg methylation), the $\Delta^{199}\text{Hg}$ values of zooplankton collected at and below the chlorophyll maximum display minimal variation with depth or time of day (Figure 2b, Figure S4b). We suggest that the invariant $\Delta^{199}\text{Hg}$ values of zooplankton with depth are a result of diurnal migration and MMHg demethylation (See section 4.4.3). Zooplankton occupy an intermediate trophic position between marine particles and fish resulting in a mixture of Hg(II) and MMHg that may obscure any methylation or demethylation signal of Hg because both pools are represented in the THg isotope composition of the zooplankton, and they have complementary $\Delta^{199}\text{Hg}$ values. As such, the migration of zooplankton from greater depths to surface waters likely results in mixing of THg in the water column by predation and digestion. The mixed pool of Hg in the zooplankton and the continuous incorporation of surface material at depth, with $\Delta^{199}\text{Hg}$ values fractionated by photodegradation, obscures the relationship of $\Delta^{199}\text{Hg}$ and depth. An exception to constant $\Delta^{199}\text{Hg}$ values with depth is at 400 m for the intermediate and large zooplankton (Figure 2b, Figure S3b), where the $\Delta^{199}\text{Hg}$ value from the intermediate and large-size zooplankton collected at night is higher than the value measured in the sample collected during the day. This $\Delta^{199}\text{Hg}$ diurnal variation coincides with greater $\delta^{202}\text{Hg}$ values during the day for the large zooplankton size fraction (Figure 2b, Figure S4b). These diurnal isotope signatures at 400 m also coincide with elevated THg concentrations within the intermediate and large size fractions sampled at night (Figure 3b); and this is the depth

interval where there is elevated migrant biomass of zooplankton (Hannides et al., 2016). This indicates that the Hg isotopic composition of zooplankton in this depth range is likely affected by diurnal migration, but it is unclear how it results in greater $\Delta^{199}\text{Hg}$ values. A more complete understanding of Hg in zooplankton is needed to fully evaluate the pathways affecting these Hg isotope signatures. It is important to note that the large size fraction also contains some small fish (e.g., *Cyclothone*), which may further complicate isotope patterns, as small fish are likely to migrate differently than zooplankton.

2.4.4 Demethylation of MMHg in the water column

Demethylation occurs by either photochemical degradation, which leaves residual MMHg in the reactant pool with higher $\Delta^{199}\text{Hg}$ values and higher $\delta^{202}\text{Hg}$ values (Bergquist and Blum, 2007), or by microbial degradation, which also results in higher $\delta^{202}\text{Hg}$ values for residual MMHg but does not change $\Delta^{199}\text{Hg}$ values (Kritee et al., 2009). Although photo-demethylation is an important process, it only occurs in the upper euphotic zone where there is significant light penetration; microbial demethylation is expected to occur throughout the water column and is the dominant process that breaks down MMHg in deeper waters.

2.4.4.1 Photochemical demethylation within the mixed layer

In surface waters the photochemical degradation of MMHg is the dominant pathway for breakdown of MMHg to Hg(II) and Hg(0) (Mason et al., 2012), but the exact mechanism and rate controlling factors remain uncertain (Inoko, 1981; Suda et al., 1993; Hammerschmidt and Fitzgerald, 2006; Lehnherr and St. Louis, 2009; Zhang and Hsu-Kim, 2010; Black et al., 2012). Based on Hg stable isotope experimental and field data (Bergquist and Blum, 2007; Chandan et al., 2015) the $\Delta^{199}\text{Hg}/\Delta^{201}\text{Hg}$ ratio has been shown to be diagnostic of photochemical reactions of Hg mediated by a radical pair mechanism. For example, in experiments with natural organic

matter, photoreduction of Hg(II) produced $\Delta^{199}\text{Hg}/\Delta^{201}\text{Hg} = 1.00$ and photoreduction of MMHg produced $\Delta^{199}\text{Hg}/\Delta^{201}\text{Hg} = 1.36$ (Bergquist and Blum, 2007). Other Hg(II) photoreduction experiments with cysteine and serine showed that the ratio of $\Delta^{199}\text{Hg}$ to $\Delta^{201}\text{Hg}$ values is sensitive to the binding ligand, reaction conditions, and specifically to radical pair intermediates (Zheng and Hintelmann, 2010). For Station ALOHA the $\Delta^{199}\text{Hg}/\Delta^{201}\text{Hg}$ ratio (Figure 4a) for all samples measured, with the exception of precipitation, was 1.21 ± 0.003 (York Regression, 1SD). This slope from the NPSG samples is similar to other marine and estuary fish studies (1.23 ± 0.01 1SD; Senn et al., 2010; Gehrke et al., 2011; Kwon et al., 2015; Li et al., 2016; Sackett et al., 2017) suggesting that the MIF values were produced by similar MMHg photochemical degradation mechanisms. This is supported by the good correlation between $\Delta^{199}\text{Hg}$ and $\delta^{202}\text{Hg}$ with a slope of 2.68 ± 0.12 (Figure 4b, 1SD), which agrees with the experimentally derived photochemical degradation slope for MMHg of 2.43 ± 0.10 (Bergquist and Blum, 2007). The $\Delta^{199}\text{Hg}$ values reported here can be used to examine the photodegradation of MMHg available for uptake at the base of the food-web, but because we did not measure the Hg isotopic composition of dissolved MMHg we are unable to fully characterize the isotopic signature for degradation of dissolved MMHg. Many pathways for the photodegradation of MMHg have been identified but not all of these may represent the MMHg pool that is taken up by pelagic fish. For example, residual photodegraded MMHg associated with high molecular weight DOM is not available for passive uptake by phytoplankton (See Figure 1; Mason et al., 1996; Gorski et al., 2006; Lee and Fisher, 2017) and it is likely not representative of the THg isotopic signatures of the small zooplankton, which feed on phytoplankton in surface waters (Steinberg and Landry, 2012; Lee and Fisher, 2016).

$\Delta^{199}\text{Hg}$ values presented here can be used to track the photochemical degradation of biologically active MMHg that enters the marine food web in surface waters. The high $\delta^{202}\text{Hg}$ and

$\Delta^{199}\text{Hg}$ values measured in samples from each zooplankton size-class and in fish from the shallowest waters at Station ALOHA are consistent with the accumulation of Hg that has been photochemically modified in surface waters (Figure 2a,b). The $\Delta^{199}\text{Hg}$ values of surface (25 m) zooplankton display a clear diurnal pattern, where $\Delta^{199}\text{Hg}$ values are greater during the day than at night, and their isotopic composition is significantly higher than deeper samples (125-1250 m, Wilcoxon test, $W=15$, $p<0.01$). A diurnal cycle of $\Delta^{199}\text{Hg}$ values in zooplankton is expected given the recent reports that marine phytoplankton and bacterioplankton can photochemically degrade Hg (Grégoire and Poulain, 2016; Kritee et al., 2017; Lee and Fisher, 2018). We suggest the $\Delta^{199}\text{Hg}$ value in surface zooplankton represents the isotopic composition of photodegraded MMHg in phytoplankton or particle-associated MMHg that has been photo-demethylated before entering the food web. Elevated $\Delta^{199}\text{Hg}$ values of small zooplankton relative to the other size fractions are attributed to a tight linkage between zooplankton (0.06-0.2 and 0.2-0.5 mm) and primary productivity in surface waters at Station ALOHA, because surface water small zooplankton (e.g., copepods) obtain most of their MMHg from an algal dietary source (Lee and Fisher, 2017). Larger zooplankton may also exploit large POM as a dietary source resulting in lower $\Delta^{199}\text{Hg}$ values (Figure 1; Hannides et al., 2016), because the $\Delta^{199}\text{Hg}$ values associated with POM are very low. There is also a possibility that $\Delta^{199}\text{Hg}$ values at the surface are altered by diel migration, where migrant zooplankton bring to the surface new Hg with low $\Delta^{199}\text{Hg}$ values during the night resulting in day/night variations at the surface. However, a simple mixing model demonstrates that migrant associated Hg contributions would need to be about 53-55% and 95% of the total Hg in large and intermediate zooplankton, respectively. Such large contributions are unlikely given that at Station ALOHA night biomass is only about 1.7 times higher than the zooplankton biomass that is

measured during the day (Hannides et al., 2016; See supporting information and references therein for details).

2.4.4.2 Demethylation below the mixed layer

Patterns in $\Delta^{199}\text{Hg}$ values with depth for marine particles and zooplankton (Figure 2b) are consistent with active dark demethylation of Hg below the mixed layer, which was also suggested by Munson et al. (2018) based on an experimental study in the Pacific Ocean. The $\Delta^{199}\text{Hg}$ values of THg within particles is relatively constant with depth as expected in the absence of light, with the exception of samples from 400 m and one sample from 690 m. At these depths the particles have significantly higher $\Delta^{199}\text{Hg}$ values (by 0.26‰ in Feb, 0.37‰ in Sept and 0.18‰ in May) compared to all the samples collected at 25-150 m from all three seasons (average = $0.12 \pm 0.05\%$, 1SD, n=8). A possible explanation for the increase in $\Delta^{199}\text{Hg}$ values in marine particles with depth is demethylation of MMHg within the water column. MMHg is expected to have elevated $\Delta^{199}\text{Hg}$ values (relative to the Hg(II)) from photo-decomposition, as indicated by the THg isotopic composition of pelagic fish, which usually contain >95% MMHg. This suggests that the Hg(II) newly formed from MMHg will have elevated $\Delta^{199}\text{Hg}$ values compared to the Hg(II) derived from precipitation, and we propose that this product Hg(II) may be incorporated into marine particles with depth.

There is incomplete understanding of the sources and sinks of Hg at depth, and this makes it difficult to specify with certainty a single mechanism for demethylation. Migrating zooplankton may also contribute to the increase in $\Delta^{199}\text{Hg}$ values within particles by adding fecal pellets with elevated THg. It has been shown that zooplankton primarily bioaccumulate MMHg and discard Hg(II) in their fecal pellets, which are an important source to POM below the twilight zone (Figure 1; Mason et al., 1996). However, demethylation of MMHg to Hg(II) within the water column is

supported by the constant values for $\Delta^{199}\text{Hg}$ in zooplankton with depth (Figures 2b, S4b), since THg in zooplankton is a combination of MMHg and Hg(II), and the THg isotopic composition of zooplankton represents a weighted average of the two end members. The proportion of MMHg within zooplankton is expected to increase with depth, because dissolved MMHg and MMHg in pelagic fish has been shown to also increase with depth. The increasing MMHg concentrations with depth suggest that if only methylation and diel migration were altering the pool of Hg available to the food web, we would find lower values of $\Delta^{199}\text{Hg}$ with increasing depth in the zooplankton, as is the case with pelagic fish.

2.5. Conclusions

At Station ALOHA in the North Pacific Ocean, Hg stable isotope ratios and concentrations indicate that Hg from precipitation represents the major source of Hg to marine pelagic waters. After deposition, a portion of this Hg is sorbed to marine particles. This is supported by an overlap in $\Delta^{199}\text{Hg}$ values between precipitation and marine particles in surface waters and the consistent difference in $\delta^{202}\text{Hg}$ values between precipitation and particles, which we attribute to MDF accompanying sorption. The negative shift in $\delta^{202}\text{Hg}$ values in particles at 150 m compared to surface particles corresponds to a sharp increase in the ratio of THg to PC within marine particles (Umhau et al., 2016). $\Delta^{199}\text{Hg}$ values measured in particles between 400-700 m and the invariant $\Delta^{199}\text{Hg}$ values in zooplankton at various depths below the photic zone demonstrate that the production and degradation of MMHg occurs throughout the water column. The isotopic trends demonstrate a tight link in Hg uptake between particles and zooplankton and that the bioaccumulation of MMHg depends on particle formation and degradation as well as the activity of zooplankton (both vertically migrating and resident) that mobilize and modify the THg content

of sinking and suspended particles. The nearly constant $\Delta^{199}\text{Hg}/\Delta^{201}\text{Hg}$ ratios throughout the marine foodweb suggests that the pool of bioaccumulated MMHg is partially photochemically degraded by a process that includes radical pair formation and that is ubiquitous in marine ecosystems. Our results highlight the importance and impact that particles and zooplankton have in the marine biogeochemical cycle of Hg. Additional detailed studies of Hg isotope ratios in marine foodwebs are needed and should include seasonal studies as well as studies in non-oligotrophic environments. A more complete understanding of the mechanisms controlling Hg isotope variations in the pelagic ocean will allow better modeling of the biogeochemical cycle of Hg.

Acknowledgements

We thank S. Wakeham, E. DeLong and K. Maiti for providing McLane pumps and T. Shanahan of McLane Research Laboratories for providing 30 L min⁻¹ pump components. We also thank K. Miyano, A. Leitner, and C. Ka'apu-Lyons from the U. of Hawaii who helped with sample collection and McLane pump and MOCNESS deployments. Finally, thanks to the captain and crew of the *R/V Kilo Moana* and the UH Ocean Technology Group. This work was supported by National Science Foundation (NSF) grants OCE 1433710 (to J.D. Blum), OCE 1333734 (to J.C. Drazen., H.G.Close., B.N.Popp., C.C.S.Hannides.), OCE 1433846 (to B.N.Popp., J.C.Drazen., C.C.S.Hannides.) and OCE 1433313 (To C.R. Benitez-Nelson) and an NSF Graduate Fellowship to L. Motta. All THg and Hg stable isotope data is available in the supporting information table

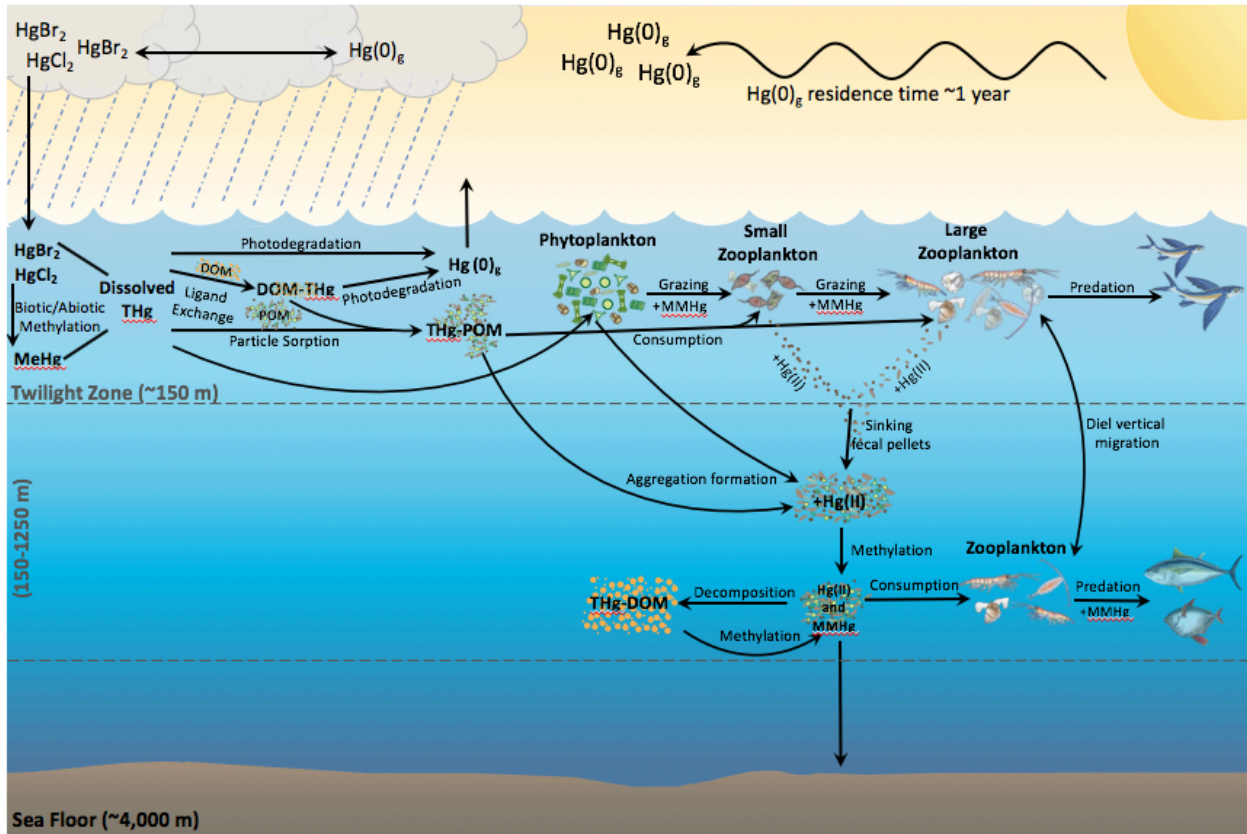


Figure 2.1. Biogeochemical cycle of Hg at Station ALOHA. The zooplankton and phytoplankton dynamics are explained in detail by Steinberg and Landry, 2012. The zooplankton and phytoplankton interactions with Hg are explained in Mason et al. (1995,1996), Watras and Bloom, (1992), Lee and Fisher, (2016). Particle and zooplankton dynamics at station ALOHA are explained in detail by Hannides et al., (2016), Umhau et al., (2016), Close et al., (2014,2015).

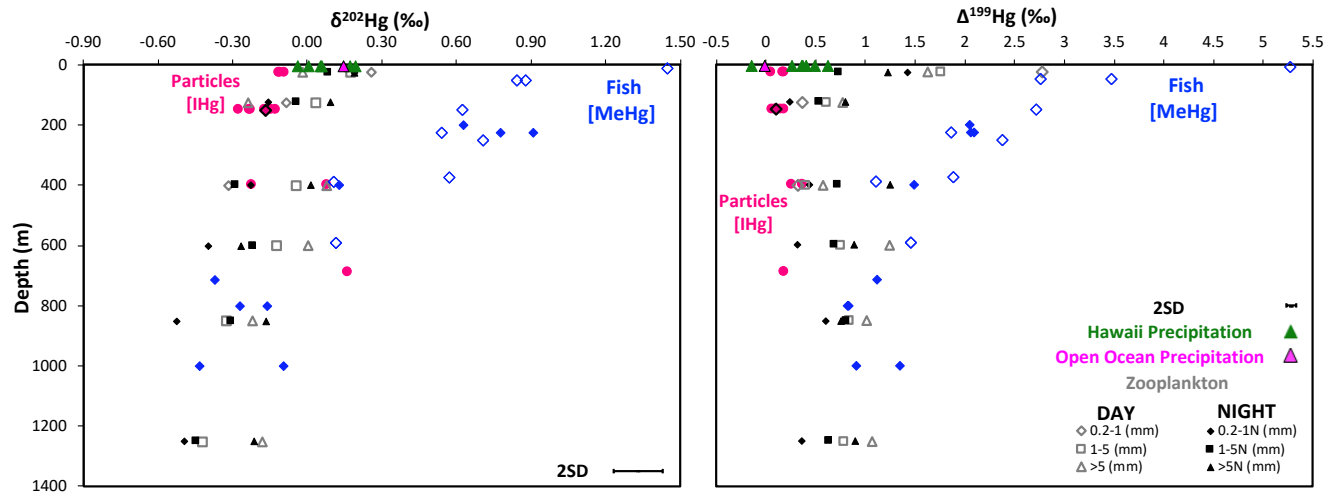


Figure 2.2. (A) $\delta^{202}\text{Hg}$ and (B) $\Delta^{199}\text{Hg}$ values of samples as a function of depth in meters. Green triangles are precipitation samples collected on the island of Hawaii and the pink triangle is a ship-board precipitation sample. The magenta circles are small particles and the diamonds are large particles. The open blue diamonds are pelagic fish from the NPSG near Hawaii published by Blum et al (2013) and the filled blue diamonds are additional samples from Station ALOHA. The open gray symbols are zooplankton collected during the day and the filled black symbols are zooplankton collected during the night. Measurement uncertainty Almaden $\Delta^{199}\text{Hg} \pm 0.05$ and TORT-2 $\delta^{202}\text{Hg} \pm 0.10$ 2SD)

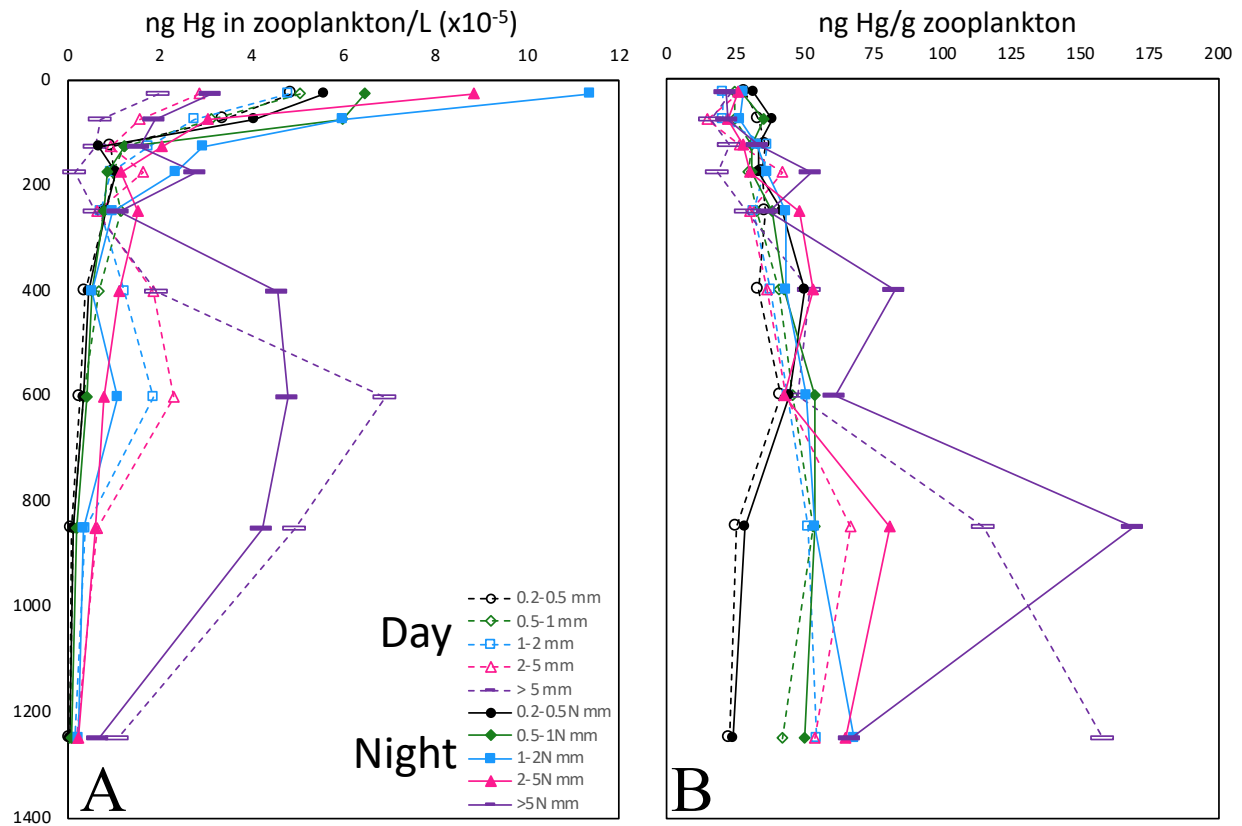


Figure 2.3. Vertical profiles of total Hg recovered from zooplankton biomass sampled during day (open symbols) and night (closed symbols). (A) normalized to zooplankton dry weight and (B) normalized to total water volume sampled by MOCNESS tows.

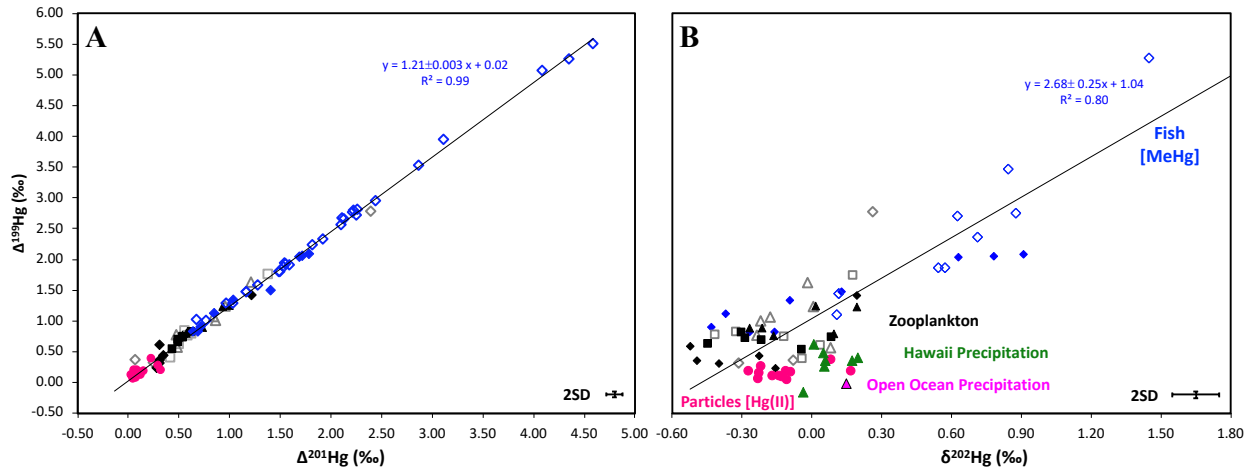


Figure 2.4. A) $\Delta^{201}\text{Hg}$ versus $\Delta^{199}\text{Hg}$ and B) $\delta^{202}\text{Hg}$ versus $\Delta^{199}\text{Hg}$ for samples analyzed in this study. The symbols and measurement uncertainty are the same as for Figure 2A,B.

References

1. Andersson, M., Sommar, J., Gårdfeldt, K., and Jutterström S. (2011). Air-sea exchange of volatile mercury in the North Atlantic Ocean. *Marine Chemistry*, 125, pp. 1-7
2. Black, F. J., Poulin, B. A., and Flegal, A. R. (2012). Factors controlling the abiotic photodegradation of monomethylmercury in surface waters. *Geochimica et Cosmochimica Acta*, 84, 492–507.
3. Bergquist, B., and Blum, J. D. (2007). Mass-dependent and independent fractionation of Hg isotopes by photoreduction in aquatic systems. *Science*, 318, 417–420.
4. Benitez-Nelson, C. R., K. O. Buesseler, D. M. Karl, J. E. Andrews (2001) A time-series study of particulate matter export in the North Pacific Subtropical Gyre based on ²³⁴Th:²³⁸U disequilibrium. *Deep-Sea Res. I*, 48, 2595-2611.
5. Bishop JKB, Lam PJ and Wood TJ (2012) Getting good particles: Accurate sampling of particles by large volume in-situ filtration. *Limnology and Oceanography – Methods* 10:681-710.
6. Biswas, A., Blum, J.D., Bergquist, B.A., Keeler, G.J., Xie, Z., 2008. Natural mercury isotope
7. variation in coal deposits and organic soils. *Environmental Science and Technology* 42, 8303–8309. doi:10.1021/es801444b
8. Blum, J. D., and Bergquist, B. A. (2007). Reporting of variations in the natural isotopic composition of mercury. *Analytical and Bioanalytical Chemistry*, 388(2), 353–359.
9. Blum, J. D., B. N. Popp, J. C. Drazen, C. A. Choy, and M. W. Johnson (2013), Methylmercury production below the mixed layer in the North Pacific Ocean, *Nature Geoscience*, 6, 879–884
10. Blum, J.D., Sherman, L.S., Johnson, M.W. (2014) Mercury isotopes in earth and environmental science. *Annual Review of Earth and Planetary Sciences* 42, 249-269
11. Blum J.D. and Johnson M.W. (2017) Recent Developments in Mercury Stable Isotope Analysis. *Non-traditional Isotope Geochemistry, Reviews in Mineralogy & Geochemistry* 82, 733-757.
12. Böttjer, D., Dore, J.E., Karl, D.M., Letelier, R.M., Mahaffey, C., Wilson, S.T., Zehr, J., Church, M.J., (2017). Temporal variability of nitrogen fixation and particulate nitrogen export at Station ALOHA. *Limnology and Oceanography*. 62, 200–216. doi:10.1002/lno.10386
13. Chandan, P., Ghosh, S., and Bergquist, B. A. (2015). Mercury Isotope Fractionation during Aqueous Photoreduction of Monomethylmercury in the Presence of Dissolved Organic Matter. *Environmental Science and Technology*. 49, 259–267.

14. Chen, J., Hintelmann, H., Feng, X., & Dimock, B. (2012). Unusual fractionation of both odd and even mercury isotopes in precipitation from Peterborough, ON, Canada. *Geochimica et Cosmochimica Acta*, 90, 33–46. <http://doi.org/10.1016/j.gca.2012.05.005>
15. Chen, H., Johnston, R. C., Mann, B. F., Chu, R. K., Tolic, N., Parks, J. M., and Gu, B. (2016). Identification of Mercury and Dissolved Organic Matter Complexes Using Ultrahigh Resolution Mass Spectrometry. *Environmental Science and Technology Letters*, 4, 59–65
16. Choy, C.A., Popp, B.N., Kaneko, J.J., Drazen, J.C., (2009). The influence of depth on mercury levels in pelagic fishes and their prey. *Proc. Natl. Acad. Sci.* 106, 13865–13869. doi:10.1073/pnas.0900711106
17. Choy, C.A., Popp, B.N., Hannides, C.C.S., Drazen, J.C., (2015). Trophic structure and food resources of epipelagic and mesopelagic fishes in the north pacific subtropical Gyre ecosystem inferred from nitrogen isotopic compositions. *Limnology and Oceanography*. 60, 1156-1171
18. Church, M.J., Lomas, M.W., Muller-karger, F., (2013). Deep-Sea Research II Sea change: Charting the course for biogeochemical ocean time-series research in a new millennium. *Deep. Res. Part II* 93, 2–15. doi:10.1016/j.dsr2.2013.01.035
19. Close, H.G., Hannides, C.S.; Popp, B.N., (2014) Compound-specific values as indicator of biosynthesis and degradation in marine particles, from submicron to sinking at Station ALOHA. *2014 Ocean Sciences Meeting (Honolulu, HI)*
20. Close, H.G., Hannides, C.S., Drazen, J.C., Popp, B.N., (2015) Degradative transformations of stable isotope ratios in sinking and suspended organic matter, from surface to upper bathypelagic depths, Station ALOHA. *2015 Aquatic Sciences Meeting (Granada, Spain)*
21. Cossa, D., J.-M. Martin, K. Takayanagi, and J. Sanjuan (1997), The distribution and cycling of mercury species in the western Mediterranean, *Deep Sea Res., Part II*, 44, 721–740, doi:10.1016/S0967-0645(96)00097-5.
22. Cossa, D., B. Averty, and N. Pirrone (2009), The origin of methylmercury in open Mediterranean waters, *Limnol. Oceanogr.*, 54, 837–844
23. Cossa, D., Heimbürger, L.E., Lannuzel, D., Rintoul, S.R., Bultler, E.C.V., Bowie, A.R., Averty, B., Watson, R.J., and Remenyi, T (2011), Mercury in the Southern Ocean, *Geochimica et Cosmochimica Acta*, 75, 4037-4052
24. Cossa, D., Heimbürger, L.E., Sonke, J.E., Planquette, H., Lherminier, P., García-Ibáñez, M.I., Pérez, F.F., and Sarthou, G., (2018). Sources, cycling and transfer of mercury in the Labrador Sea (Geotraces-Geovide cruise). *Marine Chemistry*, 198, 64-69

25. Fitzgerald, W. F., Lamborg, C. H., and Hammerschmidt, C. R. (2007). Marine Biogeochemical Cycling of Mercury. *Chem. Rev.*, *107*, 641–662.
26. Gratz, L. E., Keeler, G. J., Blum, J. D., & Sherman, L. S. (2010). Isotopic composition and fractionation of mercury in Great Lakes precipitation and ambient air. *Environmental Science and Technology*, *44*, 7764–7770. <http://doi.org/10.1021/es100383w>
27. Grégoire, D.S., Poulain, A.J., A physiological role for HgII during phototrophic growth. *Nature Geoscience*. *9*, 121
28. Gehrke G.E., Blum J.D., Marvin-DePasquale M. (2011). Sources of mercury to San Francisco Bay surface sediment as revealed by mercury stable isotopes. *Geochimica et Cosmochimica. Acta* *75*:691–705
29. Gloeckler, K. , Choy, C. A., Hannides, C. C., Close, H. G., Goetze, E. , Popp, B. N. and Drazen, J. C. (2018), Stable isotope analysis of micronekton around Hawaii reveals suspended particles are an important nutritional source in the lower mesopelagic and upper bathypelagic zones. *Limnology and Oceanography.*, *63*: 1168-1180.
doi:10.1002/lno.10762
30. Gosnell, K. J., Mason, R. P. (2015). Mercury and methylmercury incidence and bioaccumulation in plankton from the central Pacific Ocean. *Marine Chemistry*, *177*, 772–780.
31. Gorski, P.R., Armstrong, D.E., Hurley, J.P., and Shafer, M.M. (2006) Speciation of aqueous methylmercury influences uptake by freshwater alga (*Selenastrum Capricornutum*). *Environmental Toxicology and Chemistry*. *25*, 534-540
32. Hammerschmidt, C. R., K. L. Bowman (2012), Vertical methylmercury distributions in the subtropical North Pacific Ocean. *Marine Chemistry*, *132–133*, 77–82.
33. Hammerschmidt CR, Fitzgerald WF. (2006) Methylmercury cycling in sediments on the continental shelf of southern New England. *Geochimica et Cosmochimica. Acta* *70*, 918–930.
34. Hammerschmidt, C. R., Finiguerra, M. B., Weller, R. L., and Fitzgerald, W. F. (2013). Methylmercury Accumulation in Plankton on the Continental Margin of the Northwest Atlantic Ocean. *Environmental Science and Technology*, *47*, 3671–3677.
35. Hannides, C.C.S., Popp, B.N., Choy, C.A., Drazen, J.C., (2013). Midwater zooplankton and suspended particle dynamics in the North Pacific Subtropical Gyre: A stable isotope perspective. *Limnology and Oceanography*. *58*, 1931–1946.
doi:10.4319/lo.2013.58.6.1931

36. Hannides, C.C.S., Drazen, J.C., Popp, B.N., (2015). Mesopelagic zooplankton metabolic demand in the North Pacific Subtropical Gyre. *Limnology and Oceanography*. 60, 419–428. doi:10.1002/lno.10032
37. Hannides, C.C., Popp, B.N., Close, H.G., Benitez-Nelson, C.R., Ka'apu-Lyons, C.A., Gloecker, K., Wallsgrove, N., Umahu, B., Drazen, J. (2016) Midwater Zooplankton Response to Seasonality in Export Flux in the North Pacific Subtropical Gyre. *2016 Ocean Sciences Meeting (New Orleans, LA)*.
38. Heimbürger, L.-E., D. Cossa, J.-C. Marty, C. Migon, B. Averty, A. Dufour, and J. Ras (2010), Methyl mercury distributions in relation to the presence of nano and picophytoplankton in an oceanic water column (Ligurian Sea, North-western Mediterranean), *Geochimica et Cosmochimica Acta*, 74, 5549–5559.
39. Inoko M. (1981) Studies on the photochemical decomposition of organomercurials–methylmercury(II) chloride. *Environ. Pollut. B2*, 3–10.
40. Janssen, S. E., Schaefer, J. K., Barkay, T., Reinfelder, J. R. (2016). Fractionation of Mercury Stable Isotopes during Microbial Methylmercury Production by Iron- and Sulfate-Reducing Bacteria. *Environmental Science and Technology* 50, 8077–8083. article. <http://doi.org/10.1021/acs.est.6b00854>
41. Jiskra M, Wiederhold JG, Bourdon B, Kretzschmar R. (2012). Solution speciation controls mercury isotope fractionation of Hg(II) sorption to goethite. *Environmental Science and Technology* 46, 6654–62
42. Jonsson, S., Mazrui, N.M., Mason, R.P, (2016) Dimethylmercury formation mediated by inorganic and organic reduced sulfur surfaces. *Scientific Reports*, 6-27958
43. Karl, D.M., Church, M.J., Dore, J.E., Letelier, R.M., Mahaffey, C., (2012). Predictable and efficient carbon sequestration in the North Pacific Ocean supported by symbiotic nitrogen fixation. *Proc. Natl. Acad. Sci.* 109, 1842–9. doi:10.1073/pnas.1120312109
44. Kritee, K., Barkay, T., and Blum, J. D. (2009). Mass dependent stable isotope fractionation of mercury during mer mediated microbial degradation of monomethylmercury. *Geochimica et Cosmochimica Acta*, 73, 1285–1296.
45. Kritee, K., Motta, L.C., Blum, J.D., Tsui, M.T., Reinfelder, J.R., (2017) Photomicrobial visible light-induced magnetic mass independent fractionation of mercury in marine microalga. *Earth and Space Chemistry*, 2, 432-440

46. Kwon SY, Blum JD, Carvan MJ, Basu N, Head JA, et al. (2012). Absence of fractionation of mercury isotopes during trophic transfer of methylmercury to freshwater fish in captivity. *Environmental Science and Technology* 46:7527–34
47. Kwon, S.Y., Blum, J.D., Chen, CY, Meattley, DE, Mason R.P. (2015) Mercury isotope study of sources and exposure pathways of methylmercury in estuarine food webs in the Northeastern US. *Environmental Science and Technology* 48, 10089-10097
48. Lamborg, C. H., Damm, K. L. Von, Fitzgerald, W. F., Hammerschmidt, C. R., and Zierenberg, R. (2006). Mercury and monomethylmercury in fluids from Sea Cliff submarine. *Geophysical Research Letters*, 33, 18–21.
49. Lamborg, C. H., C. R. Hammerschmidt, C. R., Gill G. A., Mason R. P., and Gichuki S. (2012), An intercomparison of procedures for the determination of total mercury in seawater and recommendations regarding mercury speciation during GEOTRACES cruises, *Limnology and Oceanography Methods*, 10, 90–100.
50. Lamborg, C. H., Hammerschmidt, C. R., and Bowman, K. L (2016). An examination of the role of particles in oceanic mercury cycling. *Phil. Trans. R. Soc. A*, 374.
51. Landis, M. S., and G. J. Keeler (1997), Critical evaluation of a modified automatic wet-only precipitation collector for mercury and trace element determinations, *Environmental Science and Technology* 31, 2610–2615
52. Lauretta, D.S., Klaue, B., Blum, J.D., Buseck, P.R. 2001. Mercury abundances and isotopic compositions in the Murchison (CM) and Allende (CV) carbonaceous chondrites. *Geochimica et Cosmochimica Acta* 65:2807–18
53. Laurier, F. J. G., R. P. Mason, G. A. Gill, and L. Whalin (2004), Mercury distributions in the North Pacific Ocean—20 years of observations, *Marine Chemistry*, 90, 3–19.
54. Lee, C.S., Fisher, N.S., (2016) Methylmercury uptake by diverse marine phytoplankton. *Limnology and Oceanography*., 61, 1626-1639
55. Lee, C.S., Fisher, N.S., (2017) Bioaccumulation of methylmercury in a marine copepod. *Environmental toxicology and chemistry*., 36, 1287-1293
56. Lee, C.S., Fisher, N.S., (2018) Microbial generation of elemental mercury from dissolved methylmercury in seawater. *Limnology and Oceanography*., 00, 1-15
57. Lehnherr, I., and St. Louis, V. L. (2009). Importance of Ultraviolet Radiation in the Photodemethylation of Methylmercury in Freshwater Ecosystems. *Environmental Science and Technology*, 43, 5692–5698.
58. Li, M., Schartup, A. T., Valberg, A. P., Ewald, J. D., Krabbenhoft, D. P., Yin, R., ... Sunderland, E. M. (2016). Environmental Origins of Methylmercury Accumulated in

- Subarctic Estuarine Fish Indicated by Mercury Stable Isotopes. *Environmental Science and Technology*, 50, 11559–11568.
59. Mason, R. P., and Fitzgerald, W. F. (1993). The distribution and biogeochemical cycling of mercury in the equatorial Pacific Ocean. *Deep-Sea Research Part I*, 40, 1897–1924.
60. Mason, R. P., and Sheu, G. (2002). Role of the ocean in the global mercury cycle. *Global Biogeochemical Cycles*, 16, 1093.
61. Mason, R. P., Reinfelder, J. R., and Morel, F. M. M. (1995). Bioaccumulation of Mercury and Methylmercury. *Water, Air, and Soil Pollution*, 80, 915–921.
62. Mason, R. P., Reinfelder, J. R., and Morel, F. M. M. (1996). Uptake, Toxicity, and Trophic Transfer of Mercury in a Coastal Diatom. *Environmental Science and Technology*, 30, 1835–1845.
63. Mason, R.P., Choi, A.L., Fitzgerald, W.F., Hammerschmidt, C.R., Lamborg, C.H., Soerensen, A.L., and Sunderland, E.M. (2012) Mercury biogeochemical cycling in the ocean and policy implications. *Environ. Res.*, 119, 101-117
64. McGowan, J.A., Walker, P.W., (1979). Structure in the copepod community of the North Pacific central gyre. *Ecological Monographs*. 49, 195–226.
65. Mende, D.R., Bryant, J.A., Aylward, F.O., Eppley, J.M., Nielsen, T., Karl, D.M., Delong, E.F., (2017). Environmental drivers of a microbial genomic transition zone in the ocean's interior. *Nature Microbiology*. 2, 1367–1373. doi:10.1038/s41564-017-0008-3
66. Morel, F. M. M., Kraepiel, A. M. L., and Amyot, M. (1998). The chemical cycle and bioaccumulation. *Annual Review Ecology. Evolution, and Systematics*, 29, 543–566.
67. Monperrus, M., Martin-Doimeadios, R. C. R., Scancar, J., Amouroux, D., Donard, O. F. X., Adour, D. (2003). Simultaneous Sample Preparation and Species-Specific Isotope Dilution Mass Spectrometry Analysis of Monomethylmercury and Tributyltin in a Certified Oyster Tissue mance were carefully optimized both for species-specific. *Anal. Chem.*, 75(16), 4095–4102.
68. Monperrus, M., Tessier, E., Amouroux, D., Leynaert, A., Huonnic, P., Donard, O. F. X. (2007) Mercury methylation, demethylation and reduction rates in coastal and marine surface waters of the Mediterranean Sea, *Marine Chemistry*., 107, 49-63
69. Munson, K. M., D. Babi, and C. H. Lamborg (2014), Monomethylmercury determination from seawater using ascorbic-acid assisted direct ethylation, *Limnology and Oceanogr. Methods*, 12, 1–9, doi:10.4319/lom.2014.12.1.
70. Munson, K. M., C. H. Lamborg, G. J. Swarr, and M. A. Saito (2015), Mercury species concentrations and fluxes in the Central Tropical Pacific Ocean, *Global Biogeochem.*

Cycles, 29, doi:10.1002/ 2015GB005120.

71. Munson K.M., Lamborg C.H., Boiteau R.M., Saito M.A., (2018) Dynamic mercury methylation and demethylation in oligotrophic marine water. *Biogeosciences Discuss* 15, 6451-6460
72. Noble, A. E., Lamborg, C.H., Ohnemus, D.C., Lam, P.P., Goepfert, T.J., Measures, C.I., Frame, C.H., Casciotti, K.L., Ditullio, G.R., Jennings, J.C., and Saito, M.A (2012), Basin-scale plumes of cobalt, iron, and manganese emanating from the Benguela-Angola front in the South Atlantic Ocean, *Limnology and Oceanography*., 57, 989–1000.
73. Pasulka, A.L., Landry, M.R., Taniguchi, D.A.A., Taylor, A.G., and Church, M.J., (2013) Temporal dynamics of phytoplankton and heterotrophic protists at Station ALOHA, *Deep Sea Research Part II*, 93, 44-57
74. Rodriguez-Gonzalez, P.; Epov, V.N.; Bridou, R.; Tessier, E.; Guyoneaud, R.; Monperrus, M., Amouroux, D. (2009) Species specific stable isotope fractionation of mercury during Hg(II) methylation by an anaerobic bacteria (*Desulfobulbus propionicus*) under dark conditions. *Environmental Science & technology* 43, 9183– 9188 DOI: 10.1021/es902206j
75. Sackett, D.K., Drazen, J.C., Popp, B.N., Choy, C.A., Blum, J.D., Johnson, M.W., (2017) Carbon, Nitrogen, and Mercury Isotope Evidence for the Biogeochemical History of Mercury in Hawaiian Marine Bottomfish. *Environmental Science & technology* 51, 13976-13984
76. Senn D.B., Chesney E.J., Blum J.D., Bank M.S., Maage A., Shine J.P. (2010). Stable isotope (N, C, Hg) study of methylmercury sources and trophic transfer in the northern Gulf of Mexico. *Environmental Science and Technology* 44,1630–37
77. Fisher, J.A., Jacob, D.J., Soerensen, A.L., Amos, H.M., Steffen, A., Sunderland, E.M., (2012) Riverine source of Arctic Ocean mercury inferred from atmospheric observations. *Nature Geoscience*., 5, 499-504
78. Steinberg, D.K., Van Mooy., B.A.S., Buesseler, K.O., Boyd P.W., Kobari, T., and Karl, D.M., (2008) Microbial vs. zooplankton control of sinking particle flux in the ocean's twilight zone *Limnology and Oceanography*, 53, 1327-1338
79. Steinberg, D.K., Landry, M.R., (2017) Zooplankton and the Ocean carbon cycle. *Annual Reviews of Marine Science*. 9:413-44
80. Strode, S., Jaegle, L., Selin, N., Jacob D., Park, R., Yantosca, R., Mason, R., and Slemr, F. (2007) Air-sea exchange in the global mercury cycle. *Global Biogeochemical Cycles*., 21-GB1017
81. Štok, M., Baya, P.A., Hintelmann, H. (2015) The mercury isotope composition of Arctic

coastal seawater. *Comptes Rendus Geoscience*. 347(7-8), pp. 368-376

82. Suda I., Suda M. and Hirayama K. (1993) Degradation of methyl and ethyl mercury by singlet oxygen generated from sea water exposed to sunlight or ultraviolet light. *Arch. Toxicol.* 67, 365–368.
83. Sunderland, E.M., and Mason, R.P. (2007) Human impacts on open ocean mercury concentrations. *Global Biogeochemical Cycles* 21, GB4022
84. Sunderland, E. M., D. P. Krabbenhoft, J. W. Moreau, S. A. Strode, and W. M. Landing (2009), Mercury sources, distribution, and bioavailability in the North Pacific Ocean: Insights from data and models, *Global Biogeochemical. Cycle*, 23, GB2010, doi:10.1029/2008GB003425.
85. Talley, L. (1993), Distribution and formation of North Pacific Intermediate Water, *J. Phys. Oceanogr.*, 23, 517–537
86. Umhau, B., Motta, L.C., Benitez-Nelson, C.R., Close, H.G., Hannides, C.C.S., Popp, B.N., Blum, J.D., Drazen, J.C., Grabb, K.C., 2016. Characterization of Mercury Particle Flux Using ^{238}U : ^{234}Th Disequilibria in the North Pacific Subtropical Gyre. *2016 Ocean Sciences Meeting (New Orleans, LA)*.
87. Ueno, H., and I. Yasuda (2003), Intermediate water circulation in the North Pacific subarctic and northern subtropical regions, *J. Geophys. Res.*, 08(C11), 3348
88. Washburn, S. J., Blum, J. D., Demers, J. D., Kurz, A. Y., and Landis, R. C. (2017). Isotopic Characterization of Mercury Downstream of Historic Industrial Contamination in the South River, Virginia. *Environmental Science and Technology*, 51, 10965–10973.
89. Watras, C., and Bloom, N. (1992). Mercury and methylmercury in individual Implications for bioaccumulation zooplankton: *Limnology and Oceanography*, 37(6), 1313–1318.
90. Wiederhold JG, Cramer CJ, Daniel K, Infante I, Bourdon B, Kretzschmar R. (2010). Equilibrium mercury isotope fractionation between dissolved Hg(II) species and thiol-bound Hg. *Environmental Science and Technology*. 44, 4191–97
91. Wiebe, P.H., Morton A.W., Bradley A. M., Backus R.H., Craddock J.E., Barber V., Cowle T.J. and Flierl G.R. (1985). New developments in the MOCNESS, an apparatus for sampling zooplankton and micronekton. *Marine Biology*. 87, 313-323.
92. York, D. (1969) Least squares fitting of a straight line with correlated errors. *Earth Planet. Sci. Lett.* 5, 320–324.
93. Zhang T. and Hsu-Kim H. (2010) Photolytic degradation of methylmercury enhanced by binding to natural organic ligands. *Nature Geoscience*. 3, 473–476.

94. Zheng, W., & Hintelmann, H. (2010). Isotope Fractionation of Mercury during Its Photochemical Reduction by Low-Molecular-Weight Organic Compounds. *J. Phys. Chem. A*, *114*, 4246–4253.
95. Zaferani, S., Pérez-Rodríguez, M., and Biester, H. (2018) Diatom ooze – A large marine mercury sink. *Science*, *361*, 797-800

2.6 Supporting Information

2.6.1. Additional Methods

2.6.1.1. Dissolved Hg: Water samples were filtered on board *the R/V Kilo Moana* in a “clean area bubble” constructed from plastic sheeting inside laboratory designated space and supplied with HEPA-filtered air. All samples for dissolved Hg measurements were passed through acid cleaned (10% HCl wt/vol) 0.2 μm polyethersulfone filters (Supor). The seawater was filtered into acid-cleaned 2 L amber polycarbonate bottles for MeHg analysis and acid-cleaned 250 mL glass bottles (I-Chem) for THg analysis. The MeHg samples were acidified to 0.5% vol/vol with concentrated H_2SO_4 . The THg samples were immediately oxidized with 0.2 mL of BrCl solution ($\sim 0.09\text{M}$, Brooks Rand) after collection. Samples were stored at 4°C and analyzed at Woods Hole Oceanographic Institution (WHOI). Seawater samples for THg measurement were neutralized with $\text{NH}_2\text{OH}\cdot\text{HCl}$ (0.2 mL 30% wt/vol) and then reduced with SnCl_2 and analyzed by dual Au-amalgamation cold vapor atomic fluorescence spectrometry (Tekran 2600), using both gaseous Hg and aqueous standards (method adapted from Munson et al., 2015; Lamborg et al., 2012). The seawater samples for MeHg analysis were analyzed using ascorbic acid-assisted direct ethylation (Munson et al., 2014). All reagents were prepared according to U.S. EPA method 1630 (EPA, 1998).

2.6.1.2. Particulate Hg: Submersible pumps were deployed for 3-6 hours in order to filter up to 2500 L of seawater. In deployments where pumps malfunctioned (failed to turn on) filters were used as process blanks. Particles larger than $53\mu\text{m}$ were trapped on acid-cleaned synthetic nylon mesh (53 μm Nitex, Wildlife Supply Company) and smaller particles ranging down to 1 μm were collected on combusted (for minimum of 6 hours at 450°C) high purity quartz (SiO_2) microfiber filters (Whatman QMA). Additional 142 mm QMA filters used during the summer cruise were

acid cleaned (10% HCl wt/vol). On all cruises multiple pump-casts were employed to collect small particles. On the spring cruise, one pump was equipped with a pump head and motor with a maximum flow rate of 30 L min^{-1} , and only particles $> 53 \mu\text{m}$ were sampled. The increased flow rate plus the pooling of samples collected from the same depth using multiple pump-casts facilitated the collection of large particles from $>35,000 \text{ L}$ of seawater for Hg isotope measurement. The quartz microfiber filters and nylon mesh were prepared for deployment and sampled in a laminar flow hood in a “clean area bubble”. The samples were then stored at -80°C on board the *R/V Kilo Moana*, shipped frozen, and analyzed for THg concentrations and isotopic composition at the University of Michigan.

Digestion of small particles trapped on QMA filters for THg content was accomplished using microwave assisted acid digestion (MARS5, CEM Corporation). The lyophilized 142 mm diameter QMA filters were folded with acid cleaned tweezers into digestion vessels and submerged in reverse aqua regia (7 ml; HCl:HNO₃, 1:3, vol:vol) overnight, then digested for 35 minutes at a maximum pressure of 350 psi. Aliquots of the digestions were measured for THg by cold vapor atomic absorption spectroscopy (CV-AAS, MA-2000, Nippon Instruments). Calibration was obtained using dilutions of the standard NIST-SRM-3133, and it was also measured after every three samples. A Hg standard solution from Inorganic Ventures was also used as a secondary standard to further verify the calibration. The large particles collected on the nylon mesh were sonicated for 8 minutes in filtered seawater prior to concentration onto a pre-combusted 47 mm QMA filter by gravity filtration under clean room conditions. These filters were then lyophilized and Hg was released from the particle matrix by two-stage combustion and trapping into an oxidizing solution (1% KMnO₄ in 10% H₂SO₄ (wt/wt)) (Biswas et al., 2008). A small aliquot of the trap solution was measured for THg concentration by CV-AAS (Nippon MA-2000).

Combustion performance was monitored with procedural blanks and microfiber quartz filter blanks (Table S3a,b).

2.6.2. Discussion

2.6.2.1. Dissolved THg and MeHg Concentration Profiles: Vertical profiles of dissolved THg and MeHg that we measured at Station ALOHA (Figure S1) are similar to those of other N. Pacific Ocean profiles (Sunderland et al., 2009; Hammerschmidt and Bowman, 2012; Munson et al., 2015; Laurier et al., 2004). In our study the surface water MeHg concentrations (0.02 ng/L) were within the range of values reported by Sunderland et al (2009) at 23°N 155°W but were greater than the values reported by Munson et al (2015) at 17°N 155°W. This variability in MeHg concentration in the surface ocean is likely the result of spatial variation in MeHg production and degradation rates as well as differences in partitioning of dissolved MeHg between water and particle surfaces due to seasonal changes in productivity (Laurier et al., 2004; Sunderland et al., 2009).

Of all depths sampled at Station ALOHA, dissolved MeHg concentrations were most elevated at the surface and at 400 m (within the N. Pacific intermediate waters) as well as in the oxygen minimum zone (725–825 m). Previous studies have recorded enrichment in MeHg in oxygen depleted waters in many ocean basins and this has been attributed to enhanced methylation of Hg(II) by heterotrophic microorganisms in the water column (Cossa et al., 2009; Sunderland et al., 2009; Heimbürger et al., 2010). The reason for the MeHg maxima in NPIW is less clear, mostly because previous research has shown that particles add little Hg to NPIW at 140 ° W, 30°N (Hammerschmidt and Bowman, 2012) or to the Eastern North Pacific Ocean (Sunderland et al., 2009). It has been suggested that intermediate waters (300-700 m) transport THg by lateral circulation of the NPIW and may be an important source of THg to the North Pacific Ocean (Sunderland et al., 2009; Hammerschmidt and Bowman, 2012). NPIW originates when surface

waters at the convergence between the Oyashio and Kuroshio currents sink and are mixed with deeper waters, after which the NPIW travels eastward along a similar trajectory as the North Pacific current (Talley, 1993; Ueno et al., 2007). However, the importance of the horizontal transport of Hg is difficult to evaluate because the lifetimes of MeHg and Hg(II) appear to be relatively short (Munson et al., 2018; Monperrus et al., 2007), but recently it has been shown that a fraction of surface THg from the Canadian Arctic Archipelago is carried to the Labrador Sea by the Labrador Current, and at depth via the Western Boundary Current (Cossa et al., 2018).

Finally, dimethyl-Hg may play an important role in the dissolved THg content of the water column and degradation of dimethyl-Hg at depth may contribute to the pool of MeHg available for uptake. Although we did not measure dimethyl-Hg, it does not bioaccumulate in the food-web (Morel et al., 1997) and likely does not contribute to the Hg isotope signatures in marine organisms.

2.6.2.2 Marine particulate THg vertical profiles: Station AHOLA was once considered to be a relatively stable environment seasonally (McGowan and Walker, 1979), but recently it has been shown that in surface waters primary production varies on an annual cycle (Church et al, 2013). A consequence of periods of higher productivity is faster particle export below the mixed layer to the ocean interior, which is typically observed from mid-July to mid-August (Karl et al., 2012; Böttjer et al., 2017). Small particles (1-53 μm) collected at Station Aloha had the highest THg at the surface and declined with depth reaching an average of $4.57 \times 10^{-3} \pm 0.75 \times 10^{-3}$ ng/L (1SD, n=5; Fig S2). The surface THg was highest in September (1.75×10^{-2} ng/L), followed by February (1.43×10^{-2} ng/L), and then May (1.15×10^{-2} ng/L). Large particles (>53 μm) were orders of magnitude lower in THg than the smaller fraction at the same depths (150 m) with a THg of 1.70×10^{-4} ng/L in September and 6.66×10^{-4} ng/L in May. In February THg of large particles ranged

from 6.51×10^{-4} ng/L at 25 m to 2.84×10^{-4} ng/L at 400 m. (Fig S2). Umhau et al. (2016) normalized particle THg/ L_{seawater} to bulk particulate carbon (PC) content to determine differences in Hg bioaccumulation versus surface sorption. At Station ALOHA particulate inorganic carbon was minimal and only accounted for up to 10% of the PC. Thus, even though both Hg and PC decline with depth, the increase in the Hg/PC ratio right below the chlorophyll maximum is driven by a reduction in PC. THg/Th ratios do not appear to be driven by differences in volume to surface area ratio like PC/Th (Benitez-Nelson et al., 2001), but rather by aggregation and disaggregation processes (Umhau et al., 2016), similarly to what has been observed in the Atlantic Ocean (Lamborg et al., 2016).

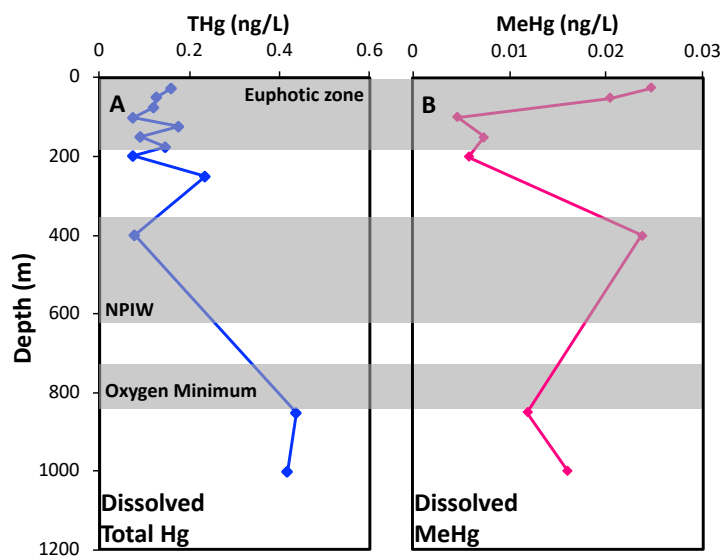


Figure S2.1 Vertical Profiles of (A) dissolved total Hg and (B) dissolved methylmercury. The concentrations are reported in ng/L. The euphotic zone, north Pacific intermediate water and oxygen minimum zone are shown as labeled grey regions. Seawater was collected for dissolved THg and MeHg analysis during the summer cruise.

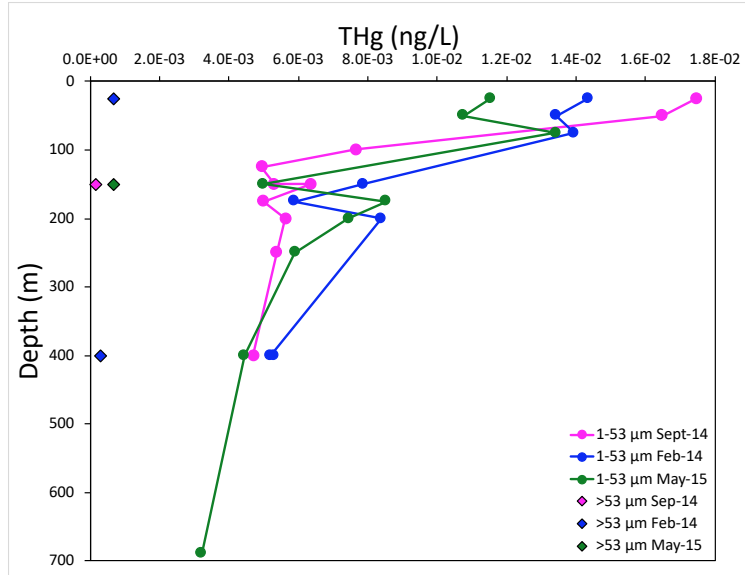


Figure S2.2. (A) Vertical profile of total Hg concentration in small (1-53 μm , circles) and large (>53 μm , diamonds) particles per liter of water filtered.

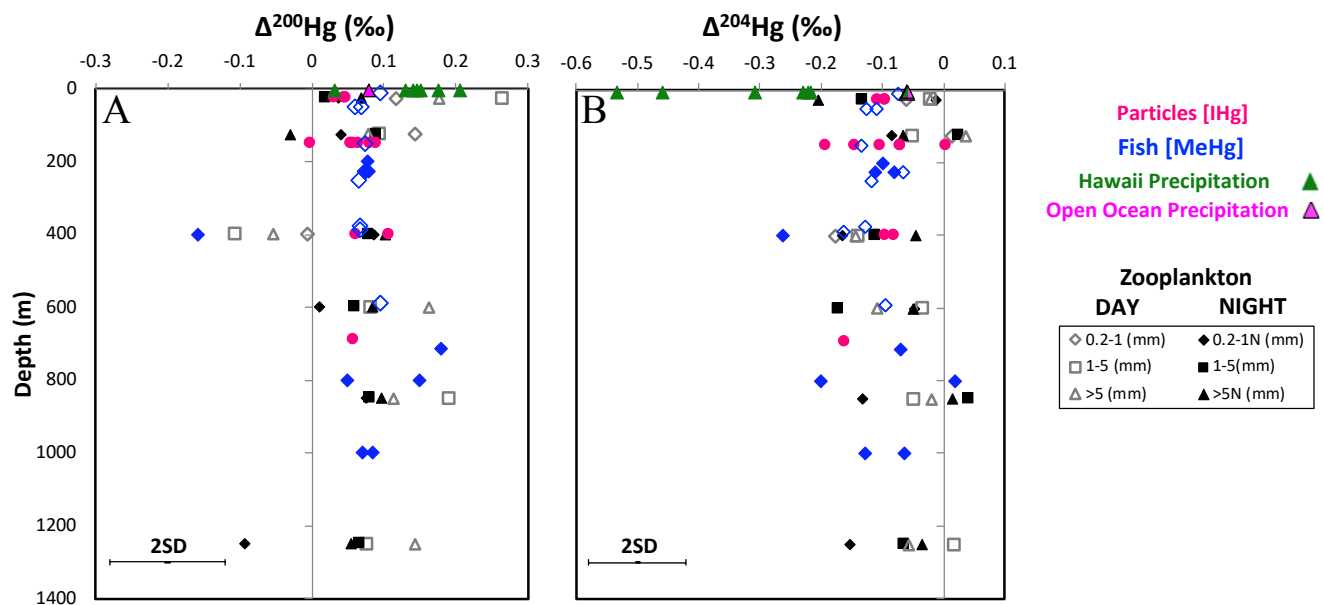


Figure S2.3. (A) $\Delta^{200}\text{Hg}$ and (B) $\Delta^{204}\text{Hg}$ values of samples as a function of depth in meters. Green triangles are precipitation samples collected on the island of Hawaii and the pink triangle is a ship-board precipitation sample. The magenta circles are small particles and the diamonds are large particles. The open blue diamonds are pelagic fish from the NPSG near Hawaii published by Blum et al (2013) and the filled blue diamonds are additional samples from Station ALOHA. The open gray symbols are zooplankton collected during the day and the filled black symbols are zooplankton collected during the night. Measurement uncertainty $\Delta^{200}\text{Hg} \pm 0.10$ and $\Delta^{204}\text{Hg} \pm 0.09$

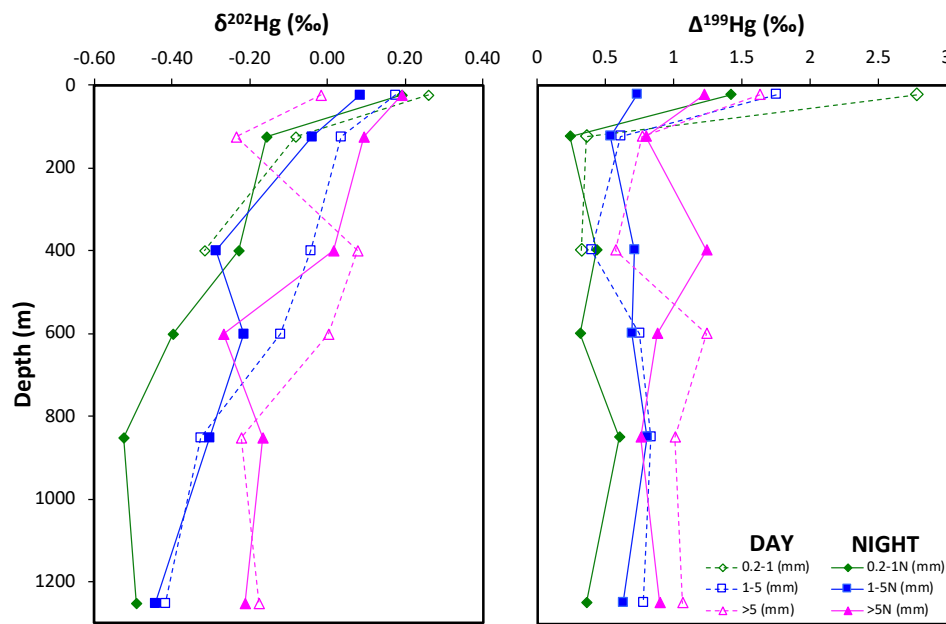


Figure S2.4 (A) $\delta^{202}\text{Hg}$ and (B) $\Delta^{199}\text{Hg}$ values of total Hg in zooplankton with depth. The magenta triangles are the large fraction (>5 mm), the blue squares are the intermediate fraction (1-5 mm), and the green diamonds are the small fraction (0.2-1 mm). The open symbols represent the samples collected during the day and the filled symbols during the night.

2.6.3 Isotope Mixing Models

Zooplankton-Marine particles mass balance for 400-700 m

A simple mass balance equation was used for determining the contribution of surface Hg to marine particles between 400-690 m by migrating zooplankton.

$$\begin{aligned} & \Delta^{199}\text{Hg}_{\text{Part.}(400-690\text{m})} \\ &= F_{\text{Part.}(25-150\text{m})}\Delta^{199}\text{Hg}_{\text{Part.}(25-150\text{m})} \\ &+ F_{\text{Zoop}(\text{Night}-25\text{m})}\Delta^{199}\text{Hg}_{\text{Zoop}(\text{Night}-25\text{m})} \end{aligned}$$

$$1 = F_{\text{Part.}(25-150\text{m})} + F_{\text{Zoop}(\text{Night}-25\text{m})}$$

The $\Delta^{199}\text{Hg}$ values used to calculate the percent contribution of surface derived THg mediated by zooplankton diel migration

$$\Delta^{199}\text{Hg}_{\text{part}(25-150\text{m})} = \text{Average: } 0.11\text{‰} \text{ (n=5)}$$

$$\Delta^{199}\text{Hg}_{\text{zoop}(\text{night}, >5\text{ mm}, 25\text{ m})} = 1.22\text{‰}$$

$$\Delta^{199}\text{Hg}_{\text{zoop}(\text{night}, 1-5\text{ mm}, 25\text{ m})} = 0.73\text{‰}$$

2.6.4 Supporting Tables

Table S2.1a Marine Fish Isotope Ratios and THg

Sample ID	Taxonomic ID	THg Run Solution (ng/g)	Feeding Depth (m)	Session Date	THg (ng/g)	$\delta^{202}\text{Hg}$	$\Delta^{204}\text{Hg}$	$\Delta^{201}\text{Hg}$	$\Delta^{200}\text{Hg}$	$\Delta^{199}\text{Hg}$
B-Opah-062	<i>Lampris</i> sp. (small-eye)	5.00	225	24-Jul-13	747	0.91	-0.08	1.78	0.07	2.09
B-Opah-063	<i>Lampris</i> sp. (small-eye)	5.00	225	24-Jul-13	946	0.79	-0.08	1.74	0.08	2.07
B-Opah-063	<i>Lampris</i> sp. (small-eye)	5.00	225	24-Jul-13	949	0.76	-0.13	1.71	0.08	2.05
Average Opah-063	<i>Lampris</i> sp. (small-eye)				948	0.78	-0.11	1.72	0.08	2.06
KM1407 BE Tuna 246 5ppb	<i>Thunnus obesus</i>	5.00	200	28-Jan-16	496	0.63	-0.10	1.69	0.08	2.04
Combined FIWF059+128+130 1.44ppb*	<i>Idiacanthus fasciola</i>	1.44	400	29-Jan-16		0.13	-0.26	1.40	-0.16	1.49
01-2-0035	<i>Anoplogaster cornuta</i>	1.80	713	24-Jul-13	233	-0.37	-0.07	0.85	0.18	1.12
04-3-0440A	<i>Cyclothone pallida</i>	3.90	800	24-Jul-13	603	-0.27	0.02	0.69	0.05	0.82
06-3-0847-B	<i>Cyclothone pallida</i>	3.90	800	24-Jul-13	367	-0.16	-0.20	0.64	0.15	0.83
FITF192 5ppb	<i>Melanocetus johnsonii</i>	5.00	1000	28-Jan-16	2058	-0.09	-0.13	1.04	0.09	1.34
FIWF030	<i>Melanocetus johnsonii</i>	5.00	1000	12-Apr-16	559	-0.43	-0.06	0.71	0.07	0.90
*Separate Muscle Tissue from Idiacanthus fasciola										
Sample ID	THg (ng/g)									
FIWF059	91									
FIWF128	34									
FIWF130	23									

Table S2.1b Mercury isotopic data for reference materials used for process quality control and evaluation

Reference Material	Range of Sessions	Average \pm 2SD	n*	$\delta^{202}\text{Hg}$	2SD	$\Delta^{204}\text{Hg}$	2SD	$\Delta^{201}\text{Hg}$	2SD	$\Delta^{200}\text{Hg}$	2SD	$\Delta^{199}\text{Hg}$	2SD
UM-Almaden	24Jul2013-12Dec2016	All	11	-0.56	0.07	0.00	0.04	-0.04	0.05	0.01	0.03	-0.02	0.05
		4.3-5 ng/g	8	-0.55	0.07	0.00	0.03	-0.03	0.05	0.00	0.03	-0.02	0.03
		1.9-3.3 ng/g	3	-0.59	0.06	0.02	0.01	-0.05	0.04	0.02	0.04	-0.03	0.10
DORM-3	24Jul2013-28Jan2016	All	2	0.44	0.09	-0.05	0.00	1.49	0.06	0.05	0.08	1.81	0.12
ERM-CE464	24Jul2013-12Dec2016	All	3	0.60	0.13	-0.10	0.04	1.99	0.04	0.09	0.09	2.43	0.08
NIST CRM1947	24-Jul-13	All	2	1.18	0.26	-0.18	0.08	4.30	0.01	0.10	0.00	5.47	0.03
TORT-2	9Jul2013-28Jan2016	All	12	0.09	0.10	-0.11	0.13	0.61	0.08	0.10	0.09	0.77	0.05
		5ng/g	4	0.08	0.04	-0.07	0.03	0.62	0.05	0.09	0.03	0.79	0.04
		1.4-3.7 ng/g	8	0.09	0.12	-0.13	0.14	0.61	0.09	0.10	0.11	0.76	0.05

n= the number of sessions; in each session on average the Almaden was analyzed 5 times

Table S2.1c Small and Large Particles THg Isotope Ratios

Mean Depth (m)	THg run solution (ng/g)	$\delta^{202}\text{Hg}$	$\Delta^{199}\text{Hg}$	$\Delta^{201}\text{Hg}$	$\Delta^{200}\text{Hg}$	$\Delta^{204}\text{Hg}$
1-53 μm						
Feb-14						
25	2.5	-0.09	0.17	0.16	0.03	-0.09
150	2.5	-0.23	0.06	0.08	0.00	-0.07
400	4.7	-0.22	0.26	0.3	0.06	-0.09
Sep-14						
25	3.6	-0.11	0.18	0.06	0.05	-0.11
150	4.3	-0.27	0.18	0.09	0.07	-0.10
150	4.3	-0.23	0.15	0.11	0.06	0.01
400	4.3	0.08	0.37	0.23	0.11	-0.08
May-15						
25	3.15	-0.11	0.05	0.06	0.05	-0.09
150	3.02	-0.14	0.11	0.12	0.09	-0.19
150	5.12	-0.13	0.10	0.05	0.06	-0.14
690	2.27	0.17	0.18	0.32	0.06	-0.16
>53 μm						
May-15						
150	3.7	-0.17	0.11	0.04	0.08	-0.07

Table S2.1d Zooplankton THg Isotope Ratios

Day Zooplankton ID	THg Run Solution (ng/g)	Mean Depth (m)	Size	$\delta^{202}\text{Hg}$	$\Delta^{204}\text{Hg}$	$\Delta^{201}\text{Hg}$	$\Delta^{200}\text{Hg}$	$\Delta^{199}\text{Hg}$
T6+10N9S.2+0.5 5ppb	5.00	25	0.5	0.26	-0.06	2.39	0.12	2.78
T6+10N9S1+2 4.1ppb	4.10	25	2	0.18	-0.02	1.38	0.26	1.75
T6+10N9S5 1.8ppb	1.80	25	5	-0.02	-0.02	1.21	0.18	1.63
T6+10N7S0.2+0.5 2.6ppb	2.60	125	0.5	-0.08	0.01	0.07	0.14	0.36
T6+10N7S1+2 3.3ppb	3.30	125	2	0.04	-0.05	0.50	0.09	0.61
T6+10N7S5 0.7ppb	0.70	125	5	-0.24	0.04	0.48	0.08	0.77
T6+10N4S0.2+0.5 3.3ppb	3.30	400	0.5	-0.32	-0.18	0.24	-0.01	0.32
T6+10N4S1+2 5ppb	5.00	400	2	-0.04	-0.14	0.42	-0.11	0.39
T6+10N4S5 5ppb	2.28	400	5	0.08	-0.14	0.48	-0.05	0.57
T6+10N3S1+2 2.28ppb	5.00	600	2	-0.12	-0.03	0.59	0.08	0.75
T6+10N3S5 5ppb	4.10	600	5	0.00	-0.11	0.95	0.16	1.24
T6+10N2S1+2 4.1ppb	5.00	850	2	-0.33	-0.05	0.55	0.19	0.83
T6+10N2S5 5ppb	5.00	850	5	-0.22	-0.02	0.86	0.11	1.01
T6+10N1S1+2 2.6ppb	2.60	1250	2	-0.42	0.02	0.63	0.08	0.78
T6+10N1S5 5ppb	5.00	1250	5	-0.18	-0.06	0.84	0.14	1.07
Night Zooplankton ID	THg Run Solution (ng/g)	Mean Depth (m)	Size	$\delta^{202}\text{Hg}$	$\Delta^{204}\text{Hg}$	$\Delta^{201}\text{Hg}$	$\Delta^{200}\text{Hg}$	$\Delta^{199}\text{Hg}$
T8+9N9S0.2+0.5 5ppb	5.00	25	0.5	0.19	-0.01	1.21	0.04	1.42
T8+9N9S1+2 5ppb	5.00	25	2	0.08	-0.13	0.54	0.02	0.73
T8+9N9S5 3.08ppb	3.08	25	5	0.19	-0.20	0.93	0.07	1.22
T8+9N7S0.2+0.5 2.28ppb	2.28	125	0.5	-0.16	-0.08	0.27	0.04	0.24
T8+9N7S1+2 5ppb	5.00	125	2	-0.04	0.03	0.44	0.09	0.53
T8+9N7S5 2.28ppb	2.28	125	5	0.09	-0.07	0.58	-0.03	0.80
T7-9N4S0.2+0.5 4.19ppb	4.19	400	0.5	-0.23	-0.16	0.35	0.09	0.43
T8+9N4S1+2 5ppb	5.00	400	2	-0.29	-0.11	0.54	0.08	0.72
T8+9N4S5 5ppb	2.28	400	5	0.02	-0.04	1.00	0.10	1.24
T6-10N3S0.2+0.5 2.28ppb	1.39	600	0.5	-0.40	-0.05	0.31	0.01	0.31
T7-9N3S1+2 1.39ppb	5.00	600	2	-0.21	-0.17	0.49	0.06	0.69
T7-9N3S5 5ppb	5.00	600	5	-0.27	-0.05	0.74	0.08	0.88
T6-10N2S0.2+0.5 1.39ppb	1.39	850	0.5	-0.52	-0.13	0.31	0.08	0.60
T7-9N2S1+2 2.28ppb	2.28	850	2	-0.30	0.04	0.63	0.08	0.81
T7-9N2S5 4.55ppb	4.55	850	5	-0.17	0.01	0.53	0.10	0.76
T6-10N1S0.2+0.5 1.39ppb	1.39	1250	0.5	-0.49	-0.15	0.31	-0.09	0.36
T7-9N1S1+2 4.19ppb	4.19	1250	2	-0.45	-0.06	0.49	0.07	0.63
T7-9N1S5 3.08ppb	3.08	1250	5	-0.21	-0.04	0.71	0.05	0.89

Table S2.1e Daytime zooplankton THg concentrations and Hg stable isotope ratios – May 2015

Sample ID (mean depth 600m)	THg Run Solution (ng/g)	Size Class	THg (ng/g)	$\delta^{202}\text{Hg}$	$\Delta^{204}\text{Hg}$	$\Delta^{201}\text{Hg}$	$\Delta^{200}\text{Hg}$	$\Delta^{199}\text{Hg}$
T1N2-8S0.2 2.16ppb	2.16	0.2	44	-0.26	-0.26	0.37	0.08	0.48
T1N2-8S0.5 3.1ppb	3.10	0.5	55	-0.3	-0.1	0.4	0.1	0.59
T1N2S1 4ppb	4.00	1	48	-0.17	-0.14	0.49	0.02	0.69
T1N4S1 5ppb	5.00	1	49	-0.21	-0.08	0.45	0.04	0.62
T1N6S1 4ppb	4.00	1	53	-0.13	-0.1	0.5	0.07	0.61
T1N8S1 5ppb	5.00	1	51	-0.06	-0.1	0.45	0.07	0.69
T1N2S2 5ppb	5.00	2	57	-0.19	-0.2	0.71	0.05	0.89
T1N4S2 5ppb	5.00	2	48	-0.13	-0.08	0.67	0.05	0.79
T1N6S2 5ppb	5.00	2	60	-0.23	-0.05	0.53	0.13	0.63
T1N8S2 5ppb	5.00	2	54	-0.18	-0.08	0.61	0.07	0.8
T1N2S5 5ppb	5.00	5	59	-0.04	-0.06	0.9	0.02	1.13
T1N4S5 5ppb	5.00	5	105	0.28	-0.11	1.13	0.05	1.42
T1N6S5 5ppb	5.00	5	58	-0.06	-0.11	0.66	0.06	0.97
T1N8S5 5ppb	5.00	5	72	-0.03	-0.15	0.71	0.03	0.91

Table S2.1f Precipitation THg concentrations and Hg isotope ratios

Sample ID	THg (ng/L)	THg run solution (ng/g)	$\delta^{202}\text{Hg}$	$\Delta^{204}\text{Hg}$	$\Delta^{201}\text{Hg}$	$\Delta^{200}\text{Hg}$	$\Delta^{199}\text{Hg}$	
Island of Hawaii								
HKL_41_2.32ppb_2005	15.7	2.3	0.17	-0.22	0.31	0.15	0.37	
HKL_42_2.32ppb_2005	21.7	2.3	0.05	-0.23	0.26	0.18	0.26	
HKL_5_1.22ppb_2005	20.7	1.2	0.20	-0.53	0.52	0.14	0.40	
PAH#1-2_1.0ppb_2014	5.4	1.0	0.06	-0.22	-0.03	0.13	0.35	
PAH#3-4_1.0ppb_2014	16.0	1.0	0.01	-0.31	0.41	0.15	0.62	
WAI#1-2_1.4ppb_2014	5.5	1.4	-0.04	-0.06	0.12	0.03	-0.15	
WAI#5-6_2.2ppb_2014	6.7	2.2	0.05	-0.46	0.64	0.21	0.49	
WAI#3-4_0.4ppb_2014	2.8	-	NOT ENOUGH PRECIPITATION					
Open Ocean Station Aloha								
Open_Ocean14_P1-2-3_1.0ppb	7.7	1.0	0.15	-0.06	0.10	0.08	-0.02	
Open_Ocean14_P4-5-6_0.4ppb*	11.4	-	N/A	N/A	N/A	N/A	N/A	

* Not enough precipitation for isotope analysis

Chapter 3 Mercury Stable Isotopes in Flying Fish as Flying Fish as a Monitor of Photochemical Degradation of Methylmercury in the Atlantic and Pacific Oceans

Co-authored with Joel D. Blum, Brian N. Popp, Jeffrey C. Drazen, and Hilary G. Close. Isotopes in Flying Fish as a Monitor of Photochemical Degradation of Methylmercury in the Atlantic and Pacific Oceans. *Marine Chemistry*. **In Revision**

Abstract: The photochemical degradation of the neurotoxin methylmercury (MeHg) in marine surface waters is of great interest because it reduces the amount of MeHg available for uptake and bioaccumulation in marine aquatic food webs. Studies have shown that the dominant cause of odd isotope mass independent fractionation (odd-MIF) of Hg in marine foodwebs is the photo-degradation of MeHg. Residual MeHg is then incorporated into low trophic level organisms and bio-accumulated without additional mass independent fractionation. Based on this understanding of Hg isotope fractionation we sought to use Hg isotope measurements of fish tissues containing Hg mostly as MeHg to assess the relative degree of photochemical decomposition across the world's oceans. In 19 samples of flying fish, the magnitude of odd-MIF varies by a factor of ~2. We estimate that 56 to 80% of MeHg was photo-degraded prior to entering the food web depending on location. The proportion of MeHg degradation does not correlate with latitude, solar radiation or estimates of the concentration of DOC or chlorophyll at the collection sites, but it does correlate with proxies for water clarity. The ratio of odd-MIF for ^{199}Hg compared to ^{201}Hg is constant in all flying fish sampled (1.20 ± 0.03) suggesting that there is a common mechanism for photo-degradation of MeHg in surface waters across oceans and hemispheres. The ratio of odd-MIF to mass dependent fractionation (MDF) is generally consistent with photochemical degradation but

is more variable (2.71 ± 0.14), suggesting that there is minimal internal demethylation of MeHg and that variable amounts of MDF occur at different locations in the ocean, likely driven by variable rates of methylation and demethylation of Hg in the water column.

3.1 Introduction

Methylmercury (MeHg) is a toxic form of the global pollutant Hg that poses a threat to human health because it biomagnifies in aquatic food webs, reaching elevated concentrations in predatory fish ¹. Despite decades of research on MeHg in marine waters there is still incomplete understanding of its biogeochemical cycle, including the process by which it degrades. The photochemical degradation of MeHg reduces the amount of MeHg available for bioaccumulation by transforming it into inorganic Hg(II) or gaseous elemental Hg(0) ². In this study, we used the Hg stable isotope composition in flying fish (*Exocoetidae*) in the South Atlantic (n=10), North Pacific (n=6), and coastal Pacific Oceans (n=3) to better understand MeHg photodegradation averaged over large areas of the ocean. Hg stable isotopes have previously proven to be an effective tool for investigating and estimating the relative photochemical degradation of MeHg in aquatic ecosystems ^{3,4}.

Experimental degradation of MeHg in the laboratory and in field incubations has demonstrated clear correlations between degradation rates of MeHg and both light intensity and wavelength ⁵⁻⁹. These studies have pointed to degradation of MeHg complexes by both direct and indirect photolysis reaction mechanisms. Direct photolysis occurs via the absorption of a photon by the Hg complex and homolytic cleavage of the Hg-C bond ^{6,10}. Indirect photolysis involves a secondary reaction with a photochemically generated reactive intermediate, such as reactive oxygen species, which attacks the MeHg complex ^{7,8,11}. The wide variety and number of reactions identified and proposed has led to the hypothesis that multiple reaction pathways for MeHg

degradation exist, and that their importance depends on the specifics of water chemistry and the wavelength of light that is present. However, there are well known drawbacks to applying laboratory and field incubation experiments to marine environments ⁹. First, in laboratory experiments it is difficult to fully simulate conditions in the open ocean to get a complete understanding of the parameters controlling MeHg degradation. Second, while *in situ* experiments are successful at estimating degradation rates and studying MeHg degradation under environmentally relevant conditions, it has been challenging to compare the results between different published experiments due to diverging environmental conditions and methods ⁹. These shortcomings have made it difficult to identify the key pathways for photodegradation of the pool of MeHg available for bioaccumulation, and have led to somewhat contradictory conclusions about the role of dissolved organic matter (DOM) ¹¹⁻¹³, photoactive trace metals ^{7,14}, reactive oxygen species ^{7,11,15-17}, and ultimately reaction mechanisms ^{6,7,11,18}.

In this study, we investigated the photochemistry of MeHg by analyzing organisms living in the surface ocean for their Hg stable isotopic composition. We utilized total Hg (THg) isotope signatures in flying fish (*Exocoetidae*) from the Atlantic and Pacific Oceans to examine photochemical pathways of MeHg degradation in the open ocean. We chose flying fish as a proxy because they live in the upper 10 meters of the ocean, and Hg in pelagic fish tissue is mostly MeHg (~95%; ¹⁹). Another advantage of the use of flying fish is that they only live for ~2 years ²⁰⁻²² and based on tagging studies ²⁰ they have a relatively small migratory range (~100-400 km) compared to other pelagic species. The flying fish habitats ranged from subtropical gyres to the equatorial ocean, including the Costa Rica dome, which is known for its high productivity ^{23,24}.

We had two overarching goals in this study. First, to estimate the proportion of MeHg that was photochemically degraded before being introduced to the base of the food web in large areas

of the world's oceans using Hg stable isotopic compositions. Second, to use Hg mass independent isotope signatures to elucidate important photochemical pathways in the degradation of MeHg. Hg stable isotope ratios have been shown to be effective for exploring physiochemical reactions relevant to changes in speciation within the water column, such as reduction, photodegradation, oxidation, and methylation²⁵⁻³⁰. This technique is enabled by the observation that the isotope fractionation of Hg in the environment displays mass dependent fractionation (MDF; represented by $\delta^{202}\text{Hg}$ values) during all abiotic and biotic chemical reactions that have been investigated. In contrast, large magnitude ($\geq 0.4\text{‰}$) mass independent fractionation of odd-mass isotope ratios (odd-MIF; represented by $\Delta^{199}\text{Hg}$ and $\Delta^{201}\text{Hg}$ values) has been observed exclusively during photochemical reduction and degradation of Hg^{25,28}. Thus biological processes (e.g., bioaccumulation, methylation, demethylation, trophic transfer) do not produce MIF of Hg and elevated MIF is believed to be generated only through a photochemical radical pair reaction mechanism^{25,26}.

3.2 Materials and Methods

Flying fish samples were collected from the decks of research ships, with surface net tows or at night by dipnet. Western Atlantic Ocean samples were collected on board the R/V Knorr and the Equatorial Pacific Ocean samples were collected on board the R/V Kilo Moana. The samples from the Gulf of California and the Costa Rica dome were provided by the University of Hawaii. North Pacific Subtropical Gyre (NPSG) fish analyses are from Blum et al (2013) and analysis of a single fish from the coast of eastern Japan is from Madigan et al. (2018). See Figure 1 for sample locations and supporting information for study details. Regression calculation used to examine isotopic relationships followed procedures described by York^{32,33}, which considers errors in both X and Y axes.

3.2.1 Flying fish sampling and preparation

Fish were either collected whole and frozen at -20°C until tissue sampling in the laboratory, or a small muscle tissue sample was taken from freshly-collected fish and frozen at -20°C shipboard. Samples were transferred to the laboratory frozen and were then lyophilized and measured for THg concentrations and Hg stable isotopic composition.

3.2.2 THg analysis

For THg determination, samples and a National Research Council Canada (NRCC) reference material DORM-3 were combusted in a two-stage furnace by placing them in the first stage and slowly heating to 750°C for over 6 hours while the second stage furnace was held at 1000°C. The released Hg(0) was trapped online into a solution of 1% KMnO₄ (w/w) in 10% H₂SO₄ (v/v)³⁴. For the flying fish samples, about 0.5-0.1 g of dried sample was combusted for a target solution concentration of 4-5 ng/g for Hg isotope analysis (Table S1). Aliquots of the KMnO₄ solution were analyzed for total Hg by cold vapor atomic absorption spectroscopy (CV-AAS; Nippon MA-2000). Calibration was obtained using NIST SRM 3133 as a standard, and it was checked every three samples. A Hg standard solution from Inorganic Ventures was also used as a secondary standard to verify the calibration. The THg concentrations of the flying fish could not be analyzed by other methods to check for combustion recoveries because there was not sufficient sample available, however, the DORM-3 reference material yielded an average recovery of 90% (n=6).

3.2.3 Hg stable isotope analysis

All the samples were pre-concentrated into 1% KMnO₄ solutions to be analyzed for Hg stable isotope composition using a multiple collector inductively coupled plasma mass spectrometer (MC-ICP-MS; Nu Instruments) with a continuous flow cold vapor generation inlet

system with SnCl₂ reduction^{25,35}. Prior to isotope analysis, the Hg concentrations of the samples were matched (within 5%) to bracketing standards (SRM NIST 3133) for each of the mass spectrometry run sessions.

MDF of Hg isotopes is reported as $\delta^{202}\text{Hg}$ in permil (‰) relative to NIST SRM 3133 (equation 1). MIF of Hg isotopes is calculated as the difference between the measured $\delta^{202}\text{Hg}$ value and that which would be predicted based on mass dependence for a given isotope, and is reported in $\Delta^{\text{xxx}}\text{Hg}$ notation in permil (‰) (equation 2), where xxx is the mass of each Hg isotope 199, 200, 201, 204 and β is the mass proportionality constant (0.252, 0.502, 0.752, 1.492, respectively²²).

$$\delta^{202}\text{Hg} = \left(\left(\frac{\left(\frac{^{202}\text{Hg}}{^{198}\text{Hg}} \right)_{\text{sample}}}{\left(\frac{^{202}\text{Hg}}{^{198}\text{Hg}} \right)_{\text{NIST3133}}} \right) - 1 \right) \times 1000 \quad (1)$$

$$\Delta^{\text{xxx}}\text{Hg} \approx \delta^{\text{xxx}} - (\delta^{202} \times \beta) \quad (2)$$

Procedural process blanks and standard reference materials (TORT-2 and DORM-3, NRCA) were processed alongside samples in an identical manner (Table S3). Recovery during the secondary purge and trap of the 1% KMnO₄ solution trap was 94±7% (1SD, n=16, minimum = 87%). The long-term analytical uncertainty of the Hg isotopic composition was characterized using UM-Almaden as a secondary standard during all analytical sessions (Table S1-3).

3.2.4 Environmental Modeled Satellite Data

Average annual surface solar irradiance³⁶ and ~10 m depth chlorophyll³⁷ data were retrieved from the Moderate Resolution Imaging Spectroradiometer (MODIS) satellite, and dissolved organic carbon content was estimated from the Massachusetts Institute of Technology ocean general circulation model (MITgcm model; Zhang et al., 2015). The *in-situ* % beam transmittance was obtained from a Seabird SBE 9/11plus CTD. Annual average water clarity was

estimated for each sample collection location (reported as equivalent Secchi Disk depth) from the global map of seasonal time series based on the semi-analytic algorithm from data retrieved from the Sea-Viewing Wide Field of View Sensor (SeaWiFS; He et al., 2017) satellite. The penetration of ultraviolet (UV) radiation was estimated for each sample collection location from the global map of the climatologically averaged period 1998-2009 in April at 305 nm (UVB) ⁴⁰. It is difficult to measure annual global UV penetration for the ocean because the current generation of ocean color satellites (e.g., SeaWiFS or MODIS) only estimate radiation in the visible part of the spectrum.

3.2.5 The Magnetic Isotope Effect: Theoretical Considerations

Hg undergoes several types of mass independent isotope fractionation that follow different physico-chemical mechanisms. These include nuclear volume effects, even-MIF during photochemical oxidation of Hg in the atmosphere (Chen et al., 2012; Gratz et al., 2010; represented as $\Delta^{200}\text{Hg}$ and $\Delta^{204}\text{Hg}$ values), and odd-MIF by the magnetic isotope effect during photochemical degradation or reduction in aquatic systems ^{25,27,43}. In this study we focus on odd-MIF. The magnetic isotope effect was first reported in Hg by Bergquist and Blum (2007) who measured large $\Delta^{199}\text{Hg}$ and $\Delta^{201}\text{Hg}$ values (>0.4‰) for the photochemical reduction of Hg(II) and MeHg. They also showed that MIF values were preserved during trophic transfer of MeHg in aquatic food webs. Subsequent studies ^{3,4,44}, have also observed that odd-MIF in living organisms is a signature inherited from MeHg dissolved in waters before it was incorporated into food webs. The preserved $\Delta^{199}\text{Hg}$ and $\Delta^{201}\text{Hg}$ values in biological tissues have been a powerful tool for studying the Hg cycle because they can track MeHg sources prior to bioaccumulation ⁴⁵.

Bergquist and Blum (2007) proposed the magnetic isotope effect (MIE) as a potential fractionation mechanism for odd-MIF. The unpaired neutron in the nucleus of odd isotopes

produces nonzero nuclear spin, nuclear magnetic moments, and hyperfine splitting--which are required for the MIE ⁴⁶. To fractionate odd from even isotopes a direct photochemical reaction is needed to produce a Hg-centered radical pair ^{46,47}; in this Hg radical pair the unpaired electron in the Hg fragment can couple with the Hg nucleus via hyperfine interactions. This electron-nucleus hyperfine interaction is selective to odd-isotopes and does not conserve the electron multiplicity of these radical pair intermediates. This means that hyperfine interactions can change the rates of direct photochemical reactions that discriminate the odd from even isotopes ⁴⁶.

Even though the mechanism for the MIE is not well understood, especially as it applies to heavy elements ⁴⁸, Hg stable isotope photochemical experiments have yielded results that allow odd-MIF measurements of natural materials to provide important new information. For example, it has been shown that $\Delta^{199}\text{Hg}$ and $\Delta^{201}\text{Hg}$ are sensitive to the Hg bonding environment ^{28,49}, ultraviolet and visible light conditions ⁴³, and types and amounts of DOM ²⁷. In this study we use measurements of $\Delta^{199}\text{Hg}$ and $\Delta^{201}\text{Hg}$ in flying fish as a proxy to investigate the photodecomposition of MeHg in surface waters. Our main objective is to explore the relative degree of photochemical reduction of MeHg across the world's oceans and to explore possible relationships with environmental factors that might affect the abundance and penetration of sunlight into the water column and thus influence the amount of photodegradation of MeHg.

A potential limitation of Hg stable isotopes as a proxy for photodecomposition of MeHg is that there are studies of photochemical reduction of MeHg in the literature that point to photochemical pathways that do not meet the requirements for MIE (for instance, secondary photolysis; Black et al., 2012; Zhang and Hsu-Kim, 2010). As a result MIE may not track all the photodegradation occurring in the water column ⁴³. However, MIE is an effective tool for investigating the relative extent of direct photolysis in the presence of UV light ⁴³, and it has been

suggested UV light accounts for up to 73% of the MeHg loss in marine waters ⁹.

3.3 Results and Discussion

3.3.1 The magnetic isotope effect and photochemical degradation of MeHg

High values of mass independent isotope fractionation of the odd isotopes of Hg (odd-MIF >0.4‰, $\Delta^{199}\text{Hg}$ and $\Delta^{201}\text{Hg}$) are only known to occur during the photochemical degradation of Hg in surface waters, particularly during the photodegradation of MeHg (e.g., Blum et al., 2014). The experimental photochemical degradation of MeHg with freshwater DOM has been shown to yield a $\Delta^{199}\text{Hg}/\Delta^{201}\text{Hg}$ slope of 1.36 ± 0.04 ^{25,27,43}, and a $\Delta^{199}\text{Hg}/\Delta^{201}\text{Hg}$ slope ranging from 1.27 to 1.33 has been recorded in living organisms in freshwater systems ^{50–53}. However, the majority of living organisms in a wide range of marine and estuarine food-webs have an average $\Delta^{199}\text{Hg}/\Delta^{201}\text{Hg}$ slope of 1.23 ± 0.02 (2SD). ^{3,4,31,44,54–56} The $\Delta^{199}\text{Hg}/\Delta^{201}\text{Hg}$ slope close to 1.2 likely represents the residual MeHg from photochemical degradation in marine waters, where the MeHg is preferably coordinated to thiol ligands. The experimental $\Delta^{199}\text{Hg}/\Delta^{201}\text{Hg}$ slope of 1.36 likely represents MeHg coordinated to O or N ligands in freshwater DOM ⁴⁹, while in marine waters, the elevated Cl concentrations would limit MeHg complexation to N or O ligands in DOM ⁵⁷. Consistent with these studies, the flying fish discussed here have a combined $\Delta^{199}\text{Hg}/\Delta^{201}\text{Hg}$ slope of 1.20 ± 0.03 (Fig. 2a, $R^2=0.99$) indicating MeHg photodegradation. This $\Delta^{199}\text{Hg}/\Delta^{201}\text{Hg}$ slope is likely not impacted by Hg(II) photoreduction because in marine waters Hg(II) speciation is likely dominated by HgCl_2 or Hg-thiol complexes due to the high Cl and DOM concentrations ⁵⁷. HgCl_2 that is not available for direct photolysis and photoreduction of Hg-thiol complexes yields negative MIF ²⁸. This is supported by the negative MIF from the photoreduction of Hg(II) in marine DOM derived from phytoplankton ⁵⁸. Negative MIF is not expected for MeHg-thiol complexes because the direct photolysis does not cleave the Hg-thiol bond, instead it cleaves the Hg-C bond⁵⁹; this is

in agreement with MeHg photodegradation experiments in marine plankton derived DOM that resulted in positive MIF⁵⁸. The potential photodecomposition of dimethylmercury in marine waters should not have any significant impact on the Hg isotopic composition of the flying fish because it is not available for direct photolysis in natural sunlight⁵⁹ and it is not incorporated in the food-web⁶⁰.

We suggest that the linear relationship of $\Delta^{199}\text{Hg}$ to $\Delta^{201}\text{Hg}$ across all of the samples discussed in this study, from both the Atlantic and Pacific Oceans (Fig. 2b), indicates that the MeHg being bioaccumulated in the flying fish was photodegraded by a common mechanism. The $\Delta^{199}\text{Hg}/\Delta^{201}\text{Hg}$ not only indicates a unique reaction pathway, but specifically points to primary photolysis mediated by a MeHg centered radical intermediate^{46–48,61}. After considering the theoretical framework for MIE (*see section 2.1 above*), we suggest that the $\Delta^{199}\text{Hg}/\Delta^{201}\text{Hg}$ slope of 1.2 is representative of the unique hyperfine interaction of ¹⁹⁹Hg and ²⁰¹Hg nuclei with the unpaired electron in the radical pairs generated from methylated Hg complexes during direct photodegradation. Therefore, the ratio of $\Delta^{199}\text{Hg}/\Delta^{201}\text{Hg}$ appears to be fingerprinting a specific primary photochemical reaction^{46,61}. Although MIE for heavy elements has not been well studied, there is experimental evidence indicating that odd-MIF is sensitive to reaction conditions (i.e., binding ligands, wavelength, and DOM; Rose et al., 2015; Zheng and Hintelmann, 2010, 2009).

The strong correlation between $\Delta^{199}\text{Hg}$ and $\Delta^{201}\text{Hg}$ found in flying fish across wide regions of the Atlantic and Pacific Oceans and in fish of a variety of species and feeding depths in the North Pacific Subtropical Gyre (NPSG; Blum et al., 2013), leads us to conclude that the role of solar irradiance, DOM, and water chemistry in the degradation of MeHg in surface marine waters may alter the reaction kinetics but not the reaction mechanism. This may suggest that the contradictory evidence about the rate controlling factors of the reaction^{7,14–16} is likely due to

reaction kinetics. For example, the kinetics of a radical pair mediated photochemical reaction are sensitive to photophysical quenching⁴⁶, which can increase or decrease the rate of reaction. DOM, molecular oxygen, and other reactive dissolved species are known radical pair quenchers that decrease reaction rates but do not change the reaction mechanisms^{6,12,47}. If there were multiple MeHg photodecomposition pathways in open ocean marine waters, we argue that flying fish would not display a strong correlation between $\Delta^{199}\text{Hg}$ to $\delta^{202}\text{Hg}$ (Fig 2), because $\delta^{202}\text{Hg}$ values would vary with the different decomposition pathways.

3.3.2 $\Delta^{199}\text{Hg}/\delta^{202}\text{Hg}$ spatial trends

Previous pelagic ocean studies have found a strong linear relationship between $\Delta^{199}\text{Hg}$ and $\delta^{202}\text{Hg}$ values with a slope of 2.68 ± 0.25 for zooplankton and other pelagic organisms that feed at a wide range of depths in the NPSG^{3,62}. Our results show that the ratio of $\Delta^{199}\text{Hg}$ to $\delta^{202}\text{Hg}$ for flying fish is 2.71 ± 0.21 (Fig 2, $R^2=0.62$), which is close to previous pelagic ocean studies. The fish collected near the eastern coast of Japan and at the Costa Rica Dome do not follow this trend and we suggest that these samples have higher $\delta^{202}\text{Hg}$ values relative to the open ocean samples due to an increase in microbial demethylation of Hg in these high productivity regions.^{26,31} The eastern coast of Japan is in the Oyashio Current, which has nutrient-rich waters⁶³, and the Costa Rica Dome is a nutrient rich upwelling zone.^{23,24} The $\Delta^{199}\text{Hg}$ and $\delta^{202}\text{Hg}$ relationship of the oceanic flying fish is within uncertainty of the photochemical degradation experimental $\Delta^{199}\text{Hg}/\delta^{202}\text{Hg}$ slope of 2.43 ± 0.10 ²⁵. Deviation of flying fish from the 2.71 slope has been suggested to be indicative of different relative amounts of biotic methylation and demethylation of Hg at each location superimposed onto the photochemical degradation signal³. The scatter around the slope of 2.7 can also be attributed to some internal demethylation of MeHg prior to incorporation into muscle tissue⁶⁴. However, this is unlikely to be a dominant factor because internal demethylation

would result in greater $\delta^{202}\text{Hg}$ values in the residual MeHg incorporated in the fish tissue resulting in a lower $\Delta^{199}\text{Hg}/\delta^{202}\text{Hg}$ slope. This is supported by the Hg isotopic composition of marine tilefish and tusk fish, which have a significantly depressed $\Delta^{199}\text{Hg}/\delta^{202}\text{Hg}$ slope consistent with potential demethylation^{65,66}.

Because the flying fish $\Delta^{199}\text{Hg}/\delta^{202}\text{Hg}$ is within uncertainty of the experimental photodegradation $\Delta^{199}\text{Hg}/\delta^{202}\text{Hg}$ slope, we can estimate the $\delta^{202}\text{Hg}$ values of MeHg prior to photochemical degradation, in a similar manner as has been done in previous fresh and seawater studies.^{44,45,55,67} We use the MeHg photodecomposition experimental slope of $\Delta^{199}\text{Hg}/\delta^{202}\text{Hg}$ at 1 mg/L DOC, because DOC in the sample sites was on average 0.89 ± 0.07 mg/L (Table S2). The $\delta^{202}\text{Hg}$ source values were calculated in the following way: 1) we determined the $\Delta^{199}\text{Hg}$ intercept from the $\Delta^{199}\text{Hg}/\delta^{202}\text{Hg}$ slope using the $\Delta^{199}\text{Hg}$ values in the muscle tissue of the flying fish by setting $\delta^{202}\text{Hg}$ to zero; and 2) the $\Delta^{199}\text{Hg}$ intercept values were then used to calculate the source $\delta^{202}\text{Hg}$ value at $\Delta^{199}\text{Hg}$ equal to zero. Our estimated values for $\delta^{202}\text{Hg}$ of MeHg prior to photochemical degradation are given in Table S2 and Figure 2b.

The estimated range in $\delta^{202}\text{Hg}$ values of MeHg available for uptake prior to photochemical degradation has average $\delta^{202}\text{Hg}$ of $-0.68\pm 0.23\%$, $n=17$, 1SD. The two samples from high productivity zones have more positive $\delta^{202}\text{Hg}$ values (Costa Rica Dome $\delta^{202}\text{Hg}=0.04$; Coast of Japan $\delta^{202}\text{Hg}=0.38$). The open ocean sample $\delta^{202}\text{Hg}$ values are more negative than average precipitation $\delta^{202}\text{Hg}$ values measured in the central Pacific Ocean⁶². It is generally assumed that precipitation is the major source of Hg to the surface pelagic ocean^{19,68,69} and we suggest that once Hg enters the ocean ligand exchange and/or sorption to DOM/POM imprints negative MDF fractionation on sorbed Hg(II)^{29,30}. In contrast to the pelagic ocean, high productivity zones likely

stimulate microbial demethylation resulting in sources of Hg to the marine food-web that have positive $\delta^{202}\text{Hg}$ values ^{70,71}; but additional work is needed to confirm this hypothesis.

3.3.3 Relative photochemical degradation of MeHg and controlling environmental factors

We used $\Delta^{199}\text{Hg}$ values in the flying fish to estimate the relative proportion of MeHg photochemically degraded prior to bioaccumulation, and investigated the correlation of $\Delta^{199}\text{Hg}$ values with environmental factors that have been mapped for the global oceans, including water clarity, solar irradiance, chlorophyll content, and DOM, to test whether the reaction pathway for photochemical degradation is dependent on specific environmental conditions. We find that $\Delta^{199}\text{Hg}/\Delta^{201}\text{Hg}$ ratios (Fig 2a) do not correlate well with environmental factors (including solar irradiance and primary productivity) at specific locations.

3.3.3.1 Relative degree of photochemical degradation of MeHg

To estimate the relative photochemical degradation of MeHg from the $\Delta^{199}\text{Hg}$ values in flying fish, we used the fractionation factor (in epsilon notation) for the photochemical degradation of MeHg ⁷² in 1 mg of DOC/L ($\epsilon = -3.33$). This fractionation factor was chosen because the $\Delta^{199}\text{Hg}/\delta^{202}\text{Hg}$ experimental slope for that reaction was in close agreement with the slope for the open ocean data in the NPSG ^{3,62}. Additionally, based on modeled annual average DOC at 0-10 meters, the concentration of DOC at the sample locations is expected to range from 0.77-1.00 mg C/L, which is consistent with the experimental conditions. The relative percentage of photochemical degradation of MeHg in the North Pacific and South Atlantic Oceans is estimated to range from 56-80%. The greatest values for the relative amount of photochemical degradation were found in the NPSG and the lowest relative percent degradation was near the equator in the Atlantic Ocean and in coastal samples (Fig 3a; Table S2).

A potential explanation for the higher percentage degradation of MeHg in oligotrophic waters of the S. Atlantic and N. Pacific subtropical gyres could be that surface waters in the subtropical gyres are more highly stratified in comparison with equatorial waters, affecting the residence time of MeHg in the water column ⁷³. Flying fish are expected to integrate seasonal variability because they live for about 2 years, reside in the upper 10 meters, and have a migratory range of only ~100-400 km ²⁰. Another possible explanation is that the $\Delta^{199}\text{Hg}$ values and the relative percent degradation of MeHg are a function of water clarity and UV penetration, as both variables are highest and least variable at the subtropical gyres ^{39,40}. A relationship between $\Delta^{199}\text{Hg}$ values and light penetration was observed by Sherman and Blum (2013) among multiple lakes in Florida, where they showed that fish inhabiting lakes with greater light penetration showed higher $\Delta^{199}\text{Hg}$ values.

3.3.3.2 Factors controlling the photochemical degradation of MeHg

Previous studies of photochemical degradation of MeHg in freshwater have suggested that the photochemical degradation of MeHg can be dependent on a range of factors including solar irradiance, water clarity (Secchi depth), DOM, reactive metals, and primary productivity ^{7,9,11}. Recently a study in the Pacific Ocean suggested that MeHg photodegradation is driven by UV instead of PAR, opposite to conclusions of studies of coastal and freshwater environments ⁹. Therefore, we tested for correlations between $\Delta^{199}\text{Hg}$ values of the flying fish and relevant variables for which data are available including water clarity, solar irradiance (PAR, Einsteins/m²/day), penetration depth of UV radiation (m), annual mean chlorophyll (mg/m³*10²), and annual mean dissolved organic carbon (mg/L) (Figure 3a-c, and Table S2). Some MeHg photodegradation experiments have shown that hydroxyl radicals formed from the photolysis of nitrate may degrade MeHg in solution. We did not, however, test for the concentrations of any

radical species or nitrate¹⁵ because secondary photochemical reactions that are mediated by reactive oxygen species are not expected to yield MIE anomalies based on the radical pair mechanism. There were no significant correlations between $\Delta^{199}\text{Hg}$ values and solar irradiance ($R^2=0.05$, $p=0.42$), annual mean chlorophyll ($R^2=0.21$, $p=0.05$), or annual mean dissolved organic carbon ($R^2=0.09$, $p=0.22$). There was, however, a significant relationship with water clarity ($y=0.09\pm 0.01$, $R^2=0.77$, $p<0.001$, $n=18$) and UV penetration at 305 nm wavelength, which is representative of UVB ($y=2.371\pm 0.22$, $R^2=0.77$, $p<0.001$, $n=18$). These results support our hypothesis that elevated $\Delta^{199}\text{Hg}$ values and the relative percent of MeHg photo-degradation at the subtropical gyres are due to the effects of light penetration in the water column. There was, however, one clear outlier sample collected off the coast of Brazil (Fig. 3c, FF02). The outlier is probably due to the low resolution of the SeaWiFs satellite near this seamount region, resulting in an overestimation of the Secchi depth^{74,75}. An overestimation of the water clarity is supported by the percent beam transmittance from CTD data from the cruises on which the open ocean samples were collected (Fig 3d). The lack of correlation between $\Delta^{199}\text{Hg}$ values with either PAR or DOC is probably because, unlike freshwater systems, the range of DOC and PAR in the surface ocean is relatively small (DOC= 0.89 ± 0.07 mg/L and PAR= 41.5 ± 2.96 Ein/m²/day) across the sample sites (Table S2). The poor negative correlation of $\Delta^{199}\text{Hg}$ values with chlorophyll may be due to the fact that primary productivity inhibits photodegradation of MeHg by attenuating light penetration⁹. For the sample locations where chlorophyll concentrations and $\Delta^{199}\text{Hg}$ values were low, we speculate that this was because water clarity was compromised by other factors such as high-water turbidity near the equatorial Atlantic (Fig 3b,d) and because surface satellite chlorophyll data is not a good predictor of productivity at depth⁷⁴. Additional experiments on Hg isotope fractionation in seawater with variable water quality parameters will be of benefit in

understanding the different controlling factors for photodegradation of MeHg in pelagic waters. We conclude that the Hg stable isotope composition of marine biological samples in surface waters may serve as a good avenue for investigating MeHg photochemical decomposition, because it avoids many drawbacks of traditional laboratory approaches since Hg stable isotope values reflect the natural conditions at the time of photodegradation.

Acknowledgements

We thank the captains, crew, and science parties of the R/V Kilo Moana for the Pacific Ocean samples and the R/V Knorr for the South Atlantic Samples. The South Atlantic cruise was funded by a grant from the U.S. National Science Foundation (OCE 1154320 to Elizabeth Kujawinski and Krista Longnecker). The Pacific cruises and laboratory analyses were supported by National Science Foundation (NSF) grants OCE 1433710 (to J.D. Blum), OCE 1333734 (to J.C.D., H.G.C., B.N.P), OCE 1433846 (to B.N.P., J.C.D) and an NSF Graduate Fellowship to L.C. Motta.

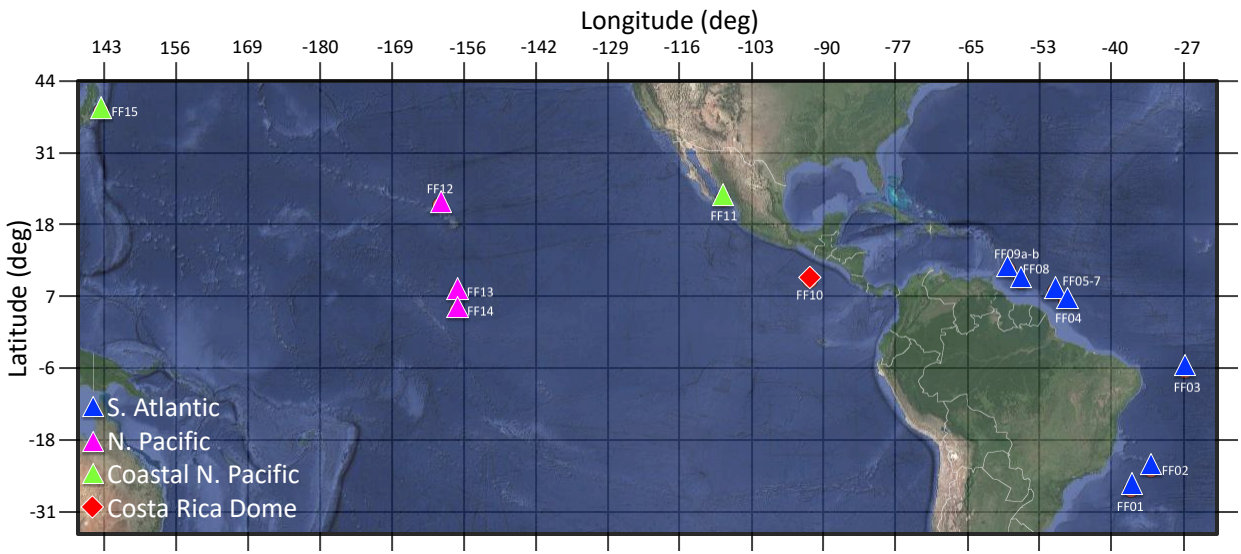


Figure 3.1. Sample locations.

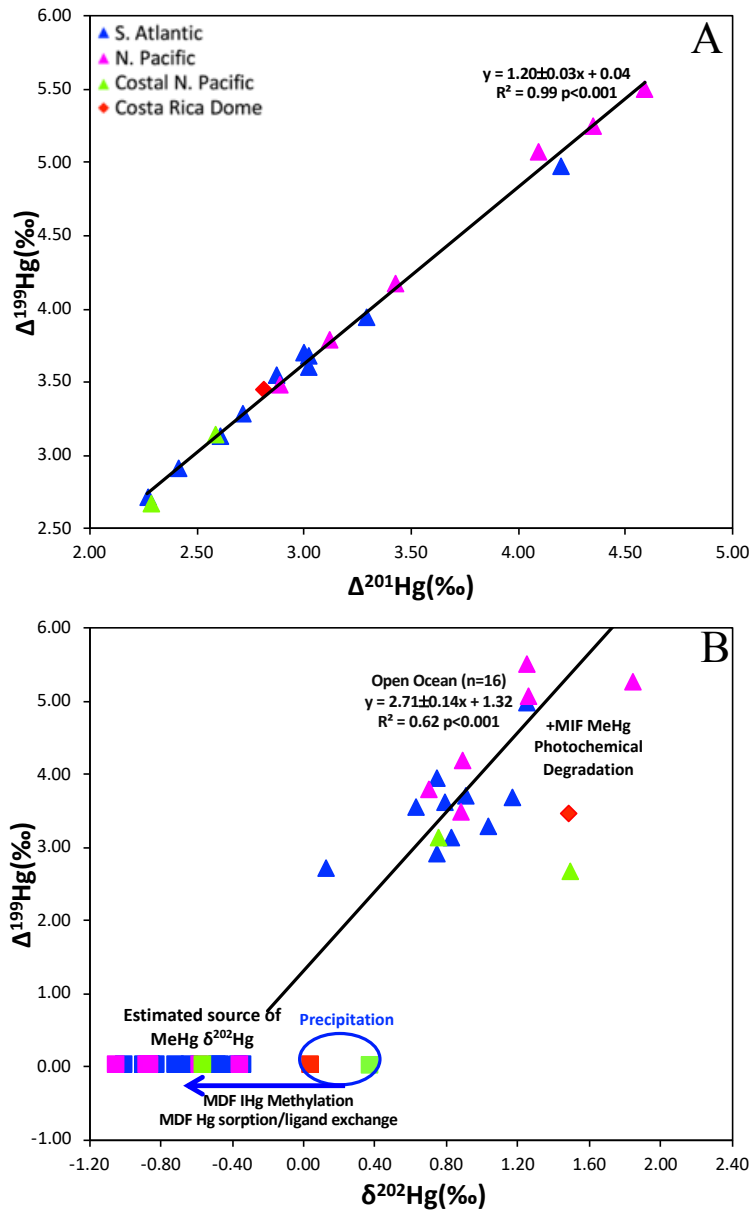


Figure 3.2 (a) Plot of $\Delta^{199}\text{Hg}$ versus $\Delta^{201}\text{Hg}$ (both are MIF) and (b) Plot of MIF ($\Delta^{199}\text{Hg}$) versus MDF ($\delta^{202}\text{Hg}$). The 2.71 slope was calculated using the open ocean flying fish (n=16); we excluded coastal fish (n=3) and the estimated MeHg $\delta^{202}\text{Hg}$ values from regressions. The triangles are the isotopic values for the biological tissue of the flying fish and the squares are the estimated isotopic values for the MeHg source prior to photochemical degradation. The magenta symbols are samples from the Pacific Ocean, the blue are from the Atlantic Ocean, the green from the coastal N. Pacific (Gulf of California and off Japan), and the red symbol is from the Costa Rica Dome. The oval shows the range of isotope values for precipitation from the open ocean at Station ALOHA and the Island of Hawaii (Motta et al., 2019)

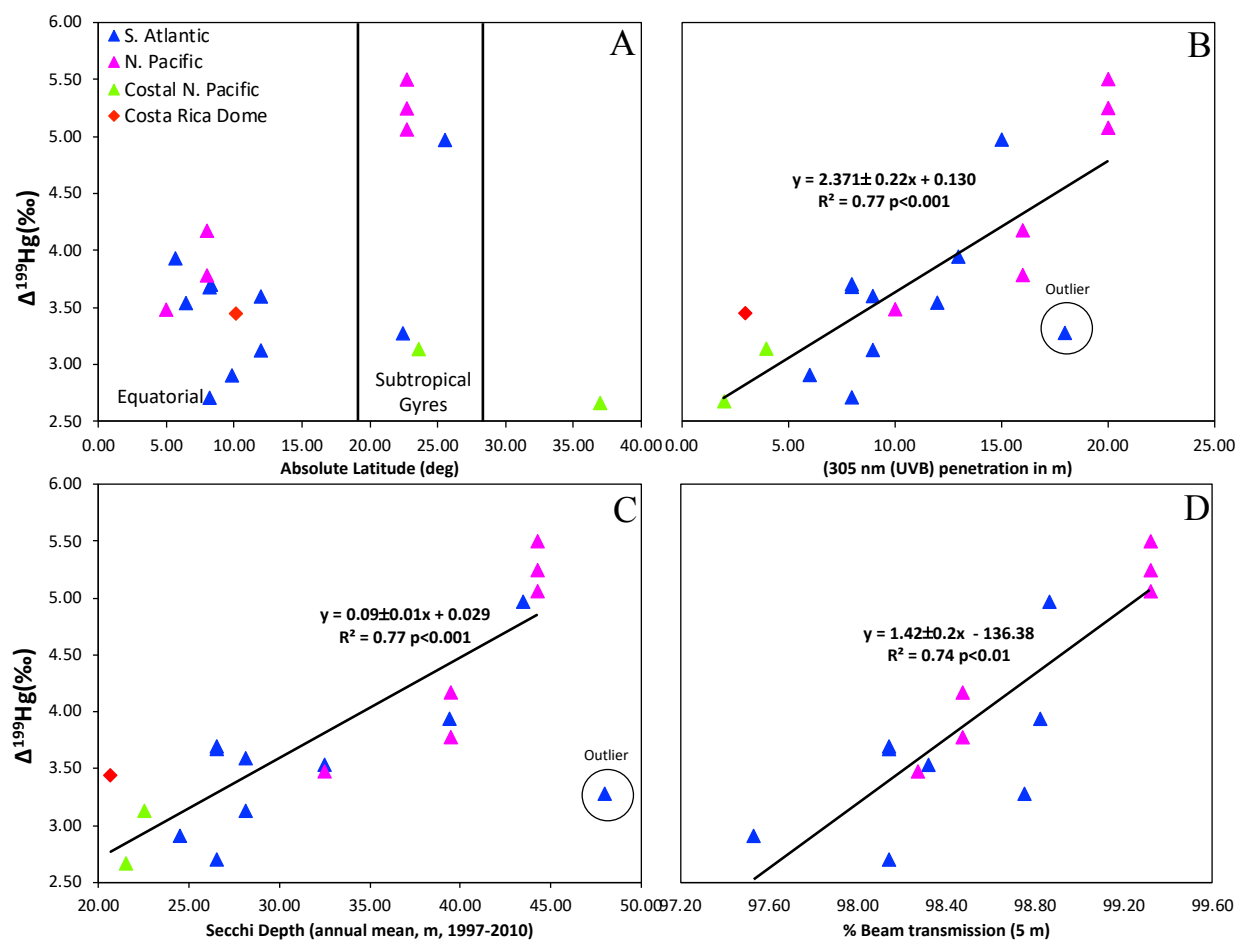


Figure 3.3. (a) $\Delta^{199}\text{Hg}$ plotted against absolute latitude (deg) and (b) $\Delta^{199}\text{Hg}$ plotted against UV penetration in meters at 305 nm wavelength, from the month of April (1998-2009). (c) $\Delta^{199}\text{Hg}$ plotted against modelled Secchi depth (SeaWiFs satellite). Sample FF02 is an outlier and is not included in the regression for (b) and (c). FF02 is located near the Vitoria-Trinidad seamounts, some of which rise close to the surface and alter primary productivity locally. Upwelling at these sites, if visited by flying fish in the region, would result in reduced $\Delta^{199}\text{Hg}$ and/or reductions in water clarity that might not be captured in the model used. (d) $\Delta^{199}\text{Hg}$ plotted against % beam transmission at 5 meters from CTD data. The CTD data was not available for the coastal samples or Costa Rica.

References

1. Mahaffey, K. R. *et al.* Balancing the benefits of n-3 polyunsaturated fatty acids and the risks of methylmercury exposure from fish consumption. *Nutr. Rev.* **69**, 493–508 (2011).
2. Mason, R. P. *et al.* Mercury biogeochemical cycling in the ocean and policy implications. *Environ. Res.* **119**, 101–117 (2012).
3. Blum, J. D., Popp, B. N., Drazen, J. C., Anela Choy, C. & Johnson, M. W. Methylmercury production below the mixed layer in the North Pacific Ocean. *Nat. Geosci.* **6**, 879–884 (2013).
4. Point, D. *et al.* Methylmercury photodegradation influenced by sea-ice cover in Arctic marine ecosystems. *Nat. Geosci.* **4**, 188–194 (2011).
5. Seller, P., Kelly, C. A., Rudd, J. W. M. & Mac Hutchon, A. R. Photodegradation of methylmercury in lakes. *Nature* **380**, 694–697 (1996).
6. Jeremiason, J. D. *et al.* Photoreduction of Hg(II) and photodemethylation of methylmercury: The key role of thiol sites on dissolved organic matter. *Environ. Sci. Process. Impacts* **17**, 1892–1903 (2015).
7. Black, F. J., Poulin, B. A. & Flegal, A. R. Factors controlling the abiotic photodegradation of monomethylmercury in surface waters. *Geochim. Cosmochim. Acta* **84**, 492–507 (2012).
8. Fernández-Gómez, C. *et al.* Towards universal wavelength-specific photodegradation rate constants for methyl mercury in humic waters, exemplified by a boreal lake-wetland gradient. *Environ. Sci. Technol.* **47**, 6279–6287 (2013).
9. DiMento, B. P. & Mason, R. P. Factors controlling the photochemical degradation of methylmercury in coastal and oceanic waters. *Mar. Chem.* **196**, 116–125 (2017).
10. Inoko, M. Studies on the Photochemical Decomposition of Organomercurials - Methylmercury (II) Chloride. *Environ. Pollut. (Series B)* **2**, 3–10 (1981).
11. Zhang, T. & Hsu-Kim, H. Photolytic degradation of methylmercury enhanced by binding to natural organic ligands. *Nat. Geosci.* **3**, 473–476 (2010).
12. Qian, Y. *et al.* Why Dissolved Organic Matter Enhances Photodegradation of Methylmercury. *Environ. Sci. Technol. Lett.* **1**, 426–431 (2014).
13. Tai, C. *et al.* Methylmercury photodegradation in surface water of the Florida everglades: Importance of dissolved organic matter-methylmercury complexation. *Environ. Sci. Technol.* **48**, 7333–7340 (2014).
14. Hammerschmidt, C. R. & Fitzgerald, W. F. Iron-mediated photochemical decomposition of methylmercury in an arctic Alaskan Lake. *Environ. Sci. Technol.* **44**, 6138–6143 (2010).
15. Chen, J., Pehkonen, S. O. & Lin, C. J. Degradation of monomethylmercury chloride by hydroxyl radicals in simulated natural waters. *Water Res.* **37**, 2496–2504 (2003).
16. Gårdfeldt, K., Sommar, J., Strömberg, D. & Feng, X. Oxidation of atomic mercury by hydroxyl radicals and photoinduced decomposition of methylmercury in the aqueous phase. *Atmos. Environ.* **35**, 3039–3047 (2001).
17. Suda, I., Suda, M. & Hirayama, K. Degradation of methyl and ethyl mercury by singlet oxygen generated from sea water exposed to sunlight or ultraviolet light. *Arch. Toxicol.* **67**, 365–368 (1993).

18. Kim, M. K. & Zoh, K. D. Effects of natural water constituents on the photo-decomposition of methylmercury and the role of hydroxyl radical. *Sci. Total Environ.* **449**, 95–101 (2013).
19. Fitzgerald, W. F., Lamborg, C. H. & Hammerschmidt, C. R. Marine Biogeochemical Cycling of Mercury. *Chem. Rev.* **107**, 641–662 (2007).
20. Oxenford, H. A. Movements of flyingfish (*Hirundichthys affinis*) in the eastern Caribbean. *Bull. Mar. Sci.* **54**, 49–62 (1994).
21. Oxenford, H. A., Mahon, R. & Hunte, W. Distribution and relative abundance of flyingfish (Exocoetidae) in the eastern Caribbean. 1. Adults. *Mar. Ecol. Prog. Ser.* **117**, 11–24 (1995).
22. Oxenford, H. A., Hunte, W., Deane, R. & Campana, S. E. Otolith age validation and growth-rate variation in flyingfish (*Hirundichthys affinis*) from the eastern Caribbean. *Mar. Biol.* **118**, 585–592 (1994).
23. Wyrтки, K. Upwelling in the Costa Rica Dome. *Fish. Bull.* **63**, 355–372 (1964).
24. Fiedler, P. C. The annual cycle and biological effects of the Costa Rica Dome. *Deep. Res. Part I Oceanogr. Res. Pap.* **49**, 321–338 (2002).
25. Bergquist, B. A. & Blum, J. D. Mass-dependent and -independent fractionation of hg isotopes by photoreduction in aquatic systems. *Science* **318**, 417–420 (2007).
26. Kritee, K., Barkay, T. & Blum, J. D. Mass dependent stable isotope fractionation of mercury during mer mediated microbial degradation of monomethylmercury. *Geochim. Cosmochim. Acta* **73**, 1285–1296 (2009).
27. Chandan, P., Ghosh, S. & Bergquist, B. A. Mercury isotope fractionation during aqueous photoreduction of monomethylmercury in the presence of dissolved organic matter. *Environ. Sci. Technol.* **49**, 259–267 (2015).
28. Zheng, W. & Hintelmann, H. Isotope Fractionation of Mercury during Its Photochemical Reduction by Low-Molecular-Weight Organic Compounds. *J. Phys. Chem. A* **114**, 4246–4253 (2010).
29. Wiederhold, J. G. *et al.* Equilibrium mercury isotope fractionation between dissolved Hg(II) species and thiol-bound Hg. *Environ. Sci. Technol.* **44**, 4191–4197 (2010).
30. Jiskra, M. *et al.* Kinetics of Hg(II) exchange between organic ligands, goethite, and natural organic matter studied with an enriched stable isotope approach. *Environ. Sci. Technol.* **48**, 13207–13217 (2014).
31. Madigan, D. J. *et al.* Mercury Stable Isotopes Reveal Influence of Foraging Depth on Mercury Concentrations and Growth in Pacific Bluefin Tuna. *Environ. Sci. Technol.* **52**, 6256–6264 (2018).
32. York, D. *et al.* Unified equations for the slope, intercept, and standard errors of the best straight line. **367**, 642–646 (2004).
33. York, D. Least Squares Fitting a Straight Line with Correlated Errors. *Earth Planet. Sci. Lett.* **5**, 320–324 (1969).
34. Biswas, A., Blum, J. D., Bergquist, B. A., Keeler, G. J. & Xie, Z. Natural mercury isotope variation in coal deposits and organic soils. *Environ. Sci. Technol.* **42**, 8303–8309 (2008).
35. Lauretta, D. S., Klaue, B., Blum, J. D. & Buseck, P. R. Mercury abundances and isotopic compositions in the murchison (CM) and Allende (CV) carbonaceous chondrites. *Geochim. Cosmochim. Acta* **65**, 2807–2818 (2001).
36. NASA. NASA Goddard Space Flight Center, Ocean Ecology Laboratory, Ocean Biology Processing Group. Moderate-resolution Imaging Spectroradiometer (MODIS) Aqua

- Photosynthetically Available Radiation Data. (2018).
37. NASA. NASA Goddard Space Flight Center, Ocean Ecology Laboratory, Ocean Biology Processing Group. Moderate-resolution Imaging Spectroradiometer (MODIS) Aqua Chlorophyll Data. (2018).
 38. Zhang, Y. *et al.* Biogeochemical drivers of the fate of riverine mercury discharged to the global and Arctic oceans. *Global Biogeochem. Cycles* **29**, 854–864 (2015).
 39. He, X. *et al.* Recent changes of global ocean transparency observed by SeaWiFS. *Cont. Shelf Res.* **143**, 159–166 (2017).
 40. Smyth, T. J. Penetration of UV irradiance into the global ocean. *J. Geophys. Res. Ocean.* **116**, 1–12 (2011).
 41. Gratz, L. E., Keeler, G. J., Blum, J. D. & Sherman, L. S. Isotopic composition and fractionation of mercury in Great Lakes precipitation and ambient air. *Environ. Sci. Technol.* **44**, 7764–7770 (2010).
 42. Chen, J., Hintelmann, H., Feng, X. & Dimock, B. Unusual fractionation of both odd and even mercury isotopes in precipitation from Peterborough, ON, Canada. *Geochim. Cosmochim. Acta* **90**, 33–46 (2012).
 43. Rose, C. H., Ghosh, S., Blum, J. D. & Bergquist, B. A. Effects of ultraviolet radiation on mercury isotope fractionation during photo-reduction for inorganic and organic mercury species. *Chem. Geol.* **405**, 102–111 (2015).
 44. Li, M. *et al.* Environmental Origins of Methylmercury Accumulated in Subarctic Estuarine Fish Indicated by Mercury Stable Isotopes. *Environ. Sci. Technol.* **50**, 11559–11568 (2016).
 45. Blum, J. D., Sherman, L. S. & Johnson, M. W. Mercury Isotopes in Earth and Environmental Sciences. *Annu. Rev. Earth Planet. Sci.* **42**, 249–269 (2014).
 46. Salikhov, K. *Magnetic Isotope Effect in Radical Reactions - Introduction.* (1996).
 47. Turro, N. J., Ramamurthy, V. & Scaiano, J. C. *Modern Molecular Photochemistry of Organic Molecules.* (University Science Book, 2010).
 48. Khudyakov, I. V., Serebrennikov, Y. A. & Turro, N. J. Spin-orbit coupling in free-radical reactions: on the way to heavy elements. *Chem. Rev.* **93**, 537–570 (1993).
 49. Zheng, W. & Hintelmann, H. Mercury isotope fractionation during photoreduction in natural water is controlled by its Hg/DOC ratio. *Geochim. Cosmochim. Acta* **73**, 6704–6715 (2009).
 50. Gantner, N., Hintelmann, H., Zheng, W. & Muir, D. C. Variations in stable isotope fractionation of Hg in food webs of Arctic lakes. *Environ. Sci. Technol.* **43**, 9148–9154 (2009).
 51. Sherman, L. S. & Blum, J. D. Mercury stable isotopes in sediments and largemouth bass from Florida lakes, USA. *Sci. Total Environ.* **448**, 163–175 (2013).
 52. Perrot, V. *et al.* Higher mass-independent isotope fractionation of methylmercury in the pelagic food web of Lake Baikal (Russia). *Environ. Sci. Technol.* **46**, 5902–5911 (2012).
 53. Pouilly, M., Bacarreza, N., Mayor, U. & Andre, D. S. Compositions of Fish and Human Hair in the Bolivian Amazon. *Environ. Sci. Technol.* 8985–8990 (2009).
 54. Senn, D. B. *et al.* Stable isotope (N, C, Hg) study of methylmercury sources and trophic transfer in the northern Gulf of Mexico. *Environ. Sci. Technol.* **44**, 1630–1637 (2010).
 55. Gehrke, G. E., Blum, J. D. & Marvin-DiPasquale, M. Sources of mercury to San Francisco Bay surface sediment as revealed by mercury stable isotopes. *Geochim. Cosmochim. Acta* **75**, 691–705 (2011).

56. Kwon, S., Blum, J. D., Nadelhoffer, K. J., Dvonch, J. T. & Tsui, M. T. Science of the Total Environment Isotopic study of mercury sources and transfer between a freshwater lake and adjacent forest food web. *Sci. Total Environ.* **532**, 220–229 (2015).
57. Zhong, H. & Wang, W. X. Controls of dissolved organic matter and chloride on mercury uptake by a marine diatom. *Environ. Sci. Technol.* **43**, 8998–9003 (2009).
58. Kritee, K., Motta, L. C., Blum, J. D., Tsui, M. T. & Reinfelder, J. R. Photo-microbial visible light-induced magnetic mass independent fractionation of mercury in a marine microalga. *Earth Sp. Chem.* (2017). doi:10.1021/acsearthspacechem.7b00056
59. Baughman, G. ., Gordon, J. ., Lee Wolfe, N. & Zepp, R. G. Chemistry of Organomercurials in Aquatic Systems. *Epa-660/3-73- 012-Ecological Res. Ser.* (1973).
60. Mason, R. P., Reinfelder, J. R. & Morel, F. M. M. Uptake , Toxicity , and Trophic Transfer of Mercury in a Coastal Diatom. *Environ. Sci. Technol.* **30**, 1835–1845 (1996).
61. Turro, N. J. Influence of nuclear spin on chemical reactions: Magnetic isotope and magnetic field effects (A Review). *Proc. Natl. Acad. Sci.* **80**, 609–621 (1983).
62. Motta, L. C. *et al.* Mercury cycling in the North Pacific Subtropical Gyre as revealed by mercury stable isotope ratios. *Global Biogeochem. Cycles* 2018GB006057 (2019). doi:10.1029/2018GB006057
63. Tomczak, M. & Godfrey, J. S. *Regional Oceanography: An Introduction.* (Daya Publishing House, 2004).
64. Kwon, S. Y., Blum, J. D., Chirby, M. A. & Chesney, E. J. Application of mercury isotopes for tracing trophic transfer and internal distribution of mercury in marine fish feeding experiments. *Environ. Toxicol. Chem.* **32**, 2322–2330 (2013).
65. Perrot, V., Landing, W. M., Grubbs, R. D. & Salters, V. J. M. Mercury bioaccumulation in tilefish from the northeastern Gulf of Mexico 2 years after the Deepwater Horizon oil spill: Insights from Hg, C, N and S stable isotopes. *Sci. Total Environ.* **666**, 828–838 (2019).
66. Rua-Ibarz, A. *et al.* Tracing Mercury Pollution along the Norwegian Coast via Elemental, Speciation, and Isotopic Analysis of Liver and Muscle Tissue of Deep-Water Marine Fish (Brosme brosme). *Environ. Sci. Technol.* **53**, 1776–1785 (2019).
67. Donovan, P. M., Blum, J. D., Yee, D., Gehrke, G. E. & Singer, M. B. An isotopic record of mercury in San Francisco Bay sediment. *Chem. Geol.* **350**, 87–98 (2013).
68. Sunderland, E. M., Krabbenhoft, D. P., Moreau, J. W., Strode, S. A. & Landing, W. M. Mercury sources, distribution, and bioavailability in the North Pacific Ocean: Insights from data and models. *Global Biogeochem. Cycles* **23**, 1–14 (2009).
69. Mason, R. P. & Sheu, G. Role of the ocean in the global mercury cycle. *Global Biogeochem. Cycles* **16**, 1093 (2002).
70. Janssen, S. E., Schaefer, J. K., Barkay, T. & Reinfelder, J. R. Fractionation of Mercury Stable Isotopes during Microbial Methylmercury Production by Iron- and Sulfate-Reducing Bacteria. *Environ. Sci. Technol.* **50**, 8077–8083 (2016).
71. Rodríguez-González, P. *et al.* Species-specific stable isotope fractionation of mercury during Hg(II) methylation by an anaerobic bacteria (*Desulfobulbus propionicus*) under dark conditions. *Environ. Sci. Technol.* **43**, 9183–9188 (2009).
72. Blum, J. D. & Bergquist, B. A. Reporting of variations in the natural isotopic composition of mercury. *Anal. Bioanal. Chem.* **388**, 353–359 (2007).
73. Karl, D. M. & Church, M. J. Microbial oceanography and the Hawaii Ocean Time-series programme. *Nat. Rev. Microbiol.* **12**, 699–713 (2014).

74. Gregg, W. W. & Casey, N. W. Global and regional evaluation of the SeaWiFS chlorophyll data set. *Remote Sens. Environ.* **93**, 463–479 (2004).
75. Gregg, W. W. & Casey, N. W. Sampling biases in MODIS and SeaWiFS ocean chlorophyll data. *Remote Sens. Environ.* **111**, 25–35 (2007).

3.4 Supporting Information

Table S3.1 Flying Fish collection data, THg concentration, and THg isotope ratios

Location	Sample ID	Figure ID	Species	Length (cm)	Length Type	Latitude	Longitude	THg (ng/g)	Solution THg (ng/g) ^a	1/THg	$\delta^{202}\text{Hg}$	$\Delta^{199}\text{Hg}$	$\Delta^{200}\text{Hg}$	$\Delta^{204}\text{Hg}$	$\Delta^{201}\text{Hg}$
S. Atlantic	FF01		<i>E. volitans</i>	11.2	FL	-25.6	-36.5	20.5	4.3	0.049	1.25	4.97	0.05	-0.34	4.20
	FF02		<i>C. comatus</i>	11.1	FL	-22.5	-33.0	27.0	4.3	0.037	1.03	3.28	0.04	-0.60	2.71
	FF03		<i>H. speculiger</i>	22.6	FL	-5.7	-27.0	532.0	4.0	0.002	0.75	3.94	0.01	-0.07	3.29
	FF04		<i>C. exsiliens</i>	18	FL	6.5	-48.0	57.6	4.0	0.017	0.63	3.54	0.06	-0.04	2.87
	FF05		<i>C. exsiliens</i>	23.9	FL	8.2	-50.0	217.2	5.0	0.005	0.13	2.71	0.08	-0.13	2.27
	FF06		<i>E. volitans</i>	16.4	FL	8.2	-49.9	60.0	5.0	0.017	1.17	3.68	0.05	-0.26	3.02
	FF07		<i>P. hillianus</i>	12.7	FL	8.3	-49.9	73.5	4.3	0.014	0.91	3.70	0.08	-0.09	3.00
	FF08		Not identified	22.4	FL	9.9	-55.9	72.7	5.0	0.014	0.75	2.91	0.07	-0.11	2.41
	FF09a		Not identified	20.5	FL	12.0	-58.2	76.3	4.0	0.013	0.83	3.13	0.09	-0.11	2.61
	FF09b		Not identified	19.4	FL	12.0	-58.2	220.7	4.3	0.005	0.79	3.60	0.04	-0.15	3.02
Gulf of California	FIMBTF0076		<i>C. dorsomaculata</i>	20.4	SL	23.7	-108.3	294.3	5.0	0.003	0.75	3.13	0.05	-0.10	2.58
	GROSS-01*	FF12a*	<i>Exocoetus</i> sp.	16.5	FL	22.8	-158.0	16.9	1.0	0.059	1.25	5.50	0.07	0.02	4.59
N. Pacific	SFM-08*	FF12b*	<i>Exocoetus</i> sp.	15.4	FL	22.8	-158.0	18.1	1.0	0.055	1.26	5.07	0.12	-0.19	4.09
	87R12-01*	FF12c*	<i>Exocoetus</i> sp.	16	FL	22.8	-158.0	51.8	5.0	0.019	1.84	5.25	0.10	-0.05	4.35
	M102	FF13a	<i>Paraxocoetus</i>	10.5	TL	8.0	-155.0	22.3	4.3	0.045	0.70	3.79	0.13	-0.33	3.11
	M102-b	FF13b	<i>Exocoetus</i> sp.	13.9	TL	8.0	-155.0	41.4	5.0	0.024	0.89	4.17	0.12	-0.26	3.43
	M1010	FF14	<i>H. speculiger</i>	8	TL	5.0	-155.0	13.0	1.0	0.077	0.88	3.48	0.15	-0.55	2.89
	Costa Rica Dome	100710-002	FF10	<i>P. mento</i>	14.4	FL	10.1	-93.0	33.4	4.3	0.030	1.48	3.45	0.10	-0.18
Coast of Japan	Not identified**	FF15**	Not identified	-	-	37.0	142.4	-	1.0	-	1.49	2.67	0.08	-	2.29

* Samples from Blum et al., 2013

** Sample from Madigan et al., 2018

^a THg (ng/g) run solution for isotope analysis

Table S3.2 Calculated photochemical parameters, modeled environmental variables, and reference materials

Location	Sample ID	Figure ID	Species	Relative % Photodegradation	$\Delta^{199}\text{Hg}$ y- intercept	Calculated MeHg source $\delta^{202}\text{Hg}$	PAR ^a (annual mean, e ¹⁹ /m ² /day)	DOC ^b (annual mean, mg/L)	GH ^c (annual mean, 0-10 m (mg * m ⁻³) 10 ⁵)	Secchi Depth ^d (annual mean, 1997-2010)	UV penetration at 305 nm (m) ^e	%Beam Transmittance ^f
S. Atlantic	FF01		<i>E. voltans</i>	77.43	1.97	-0.82	35.67	0.82	0.59	43.5	15	98.86
	FF02		<i>C. comatus</i>	62.59	0.81	-0.34	41.71	0.84	0.00	48	18	98.75
	FF03		<i>H. speculiger</i>	69.29	2.14	-0.89	45.38	0.91	18.17	39.4	13	98.82
	FF04		<i>C. exiliens</i>	65.39	2.03	-0.85	41.92	0.89	10.23	32.5	12	98.31
	FF05		<i>C. exiliens</i>	55.63	2.40	-1.00	43.14	0.92	11.44	26.5	8	98.14
	FF06		<i>E. voltans</i>	67.01	0.87	-0.36	43.14	0.92	11.44	26.5	8	98.14
	FF07		<i>P. hillianus</i>	67.00	1.52	-0.63	43.14	0.92	11.44	26.5	8	98.14
	FF08		Not identified	58.21	1.11	-0.46	43.64	0.98	19.76	24.5	6	97.53
	FF09a		Not identified	61.00	1.14	-0.47	45.13	0.97	8.37	28.125	9	-
	FF09b		Not identified	66.01	1.70	-0.71	45.13	0.97	8.37	28.125	9	-
	FF11		<i>C. dorsomaculata</i>	60.99	1.33	-0.55	37.75	0.91	1.94	22.5	4	-
Gulf of California	FIMBT0076		<i>C. dorsomaculata</i>	80.07	2.50	-1.04	42.85	0.89	0.14	44.25	20	99.32
	CROSS-01*		<i>Exocetus</i> sp.	78.09	2.05	-0.85	42.85	0.89	0.14	44.25	20	99.32
	SFM-08*		<i>Exocetus</i> sp.	79.24	0.83	-0.35	42.85	0.89	0.14	44.25	20	99.32
	8TR12-01*		<i>Exocetus</i> sp.	67.88	2.10	-0.87	36.88	0.78	20.43	39.50	16	98.47
	M102		<i>Paratexocetus</i>	71.33	2.04	-0.85	36.88	0.78	20.43	39.50	16	98.47
N. Pacific	M102-b		<i>Exocetus</i> sp.	64.76	1.37	-0.57	39.03	0.77	25.66	32.50	10	98.27
	M1010		<i>H. speculiger</i>	64.45	-0.10	0.04	40.32	1.00	11.14	20.65	3	-
	100710-002		<i>P. mento</i>	55.5	-0.91	0.38	-	-	-	21.50	2	-
Costa Rica Dome	100710-002		Not identified	-	-	-	-	-	-	-	-	
Coast of Japan	Not identified**		Not identified	-	-	-	-	-	-	-	-	
FF15		Not identified	Not identified	-	-	-	-	-	-	-	-	

* Samples from Blum et al., 2013

** Sample from Madigan et al., 2018

Reference Material	Range of Sessions	n	$\delta^{202}\text{Hg}$	2SD	$\Delta^{199}\text{Hg}$	2SD	$\Delta^{200}\text{Hg}$	2SD	$\Delta^{199}\text{Hg}$	2SD		
UM-Almaden	02Feb2014-28Jan2016	21	-0.58	0.13	-0.02	0.15	-0.04	0.08	0.01	0.06	-0.01	0.08
ERM-CE464	02Feb2014-28Jan2016	6	0.71	0.13	-0.17	0.24	1.96	0.06	0.08	0.04	2.41	0.08

- Average annual surface solar irradiance was retrieved from the Moderate Resolution Imaging Spectroradiometer (MODIS) satellite³⁶
- Dissolved organic carbon content was estimated from the Massachusetts Institute of Technology ocean general circulation model (MITgcm model; Zhang et al., 2015)
- Average annual chlorophyll was retrieved from the Moderate Resolution Imaging Spectroradiometer (MODIS) satellite³⁷
- Annual average water clarity was estimated for each sample collection location (reported as equivalent Secchi Disk depth) from the global-map of seasonal time series based on the semi-analytic algorithm from data retrieved from the Sea-Viewing Wide Field of View Sensor (SeaWiFS) satellite³⁹
- UV depth (m) penetration at 305 nm representative of UVB radiation of the month of April averaged over 1999-2009 (error ± 1.5 m)⁴⁰
- The *in-situ* % beam transmittance was obtained from a Seabird SBE 9/1plus CTD, from the research cruises where the flying fish samples were collected.

Chapter 4 Mercury Isotope Fractionation During the Photochemical reduction of Hg(II) Coordinated with Organic Ligands

Co-authored with K. Kritee, Joel D. Blum, Martin Tsz-Ki Tsui, and John Reinfelder. Mercury Isotope Fractionation During the Photochemical Reduction of Hg(II) Coordinated With Organic Ligands. *Journal of Physical Chemistry A*. **In revision**

Abstract: The photochemical reduction of Hg(II) is an important pathway in the environmental Hg cycle because it competes with Hg methylation and potentially limits the formation of neurotoxic methylmercury. Hg stable isotope systematics have been proven to be an effective tool for investigating the transport, transformation, and bioaccumulation of Hg, and the dominant cause of mass independent isotope fractionation (MIF) of Hg in nature is the photochemical reduction of various species of Hg(II). However, it is difficult to fully interpret Hg stable isotope signatures in natural samples due to the lack of mechanistic information about which Hg compounds are susceptible to MIF, and why. This study investigated Hg isotope fractionation during the photochemical reduction of Hg(II) complexed to organic ligands representative of the available binding sites in natural dissolved organic matter. Mass dependent isotope fractionation (MDF) of specific Hg(II)–organic complexes followed the same relationship regardless of pH, wavelength of light, or dissolved oxygen content, while MIF varied with all of these variables. The photochemical reduction of Hg(II) in the presence of cysteine resulted in both negative and positive MIF in residual Hg(II), where the sign depended on pH and dissolved oxygen. In the presence of serine, either nuclear volume or magnetic isotope effects were observed depending on the wavelength of light and the extent of Hg(II) complexation by serine. In the presence of

ethylenediamine, MIF was negative. Our Hg stable isotope results suggest that MDF and MIF are induced at different steps in the overall photochemical reduction reaction, and that MIF does not depend on the rate determining step but on photophysical aspects of the reaction, such as intersystem crossing and hyperfine coupling. The behavior of Hg isotopes reported here will allow for a better understanding of the underlying reaction mechanisms controlling the Hg isotope signatures recorded in natural samples.

4.1 Introduction

Mercury (Hg) is a toxic global pollutant that is strongly retained at each trophic level in aquatic food webs, reaching high concentrations in fish and leading to public health concerns¹. Despite decades of research there is still an incomplete understanding of the transformations of Hg that may limit its uptake and bioaccumulation in food webs, due to the complexity of its biogeochemical cycle. Hg stable isotopes have been an effective tool for investigating Hg, but there is limited experimental and theoretical information on isotope fractionation mechanisms that result in mass independent isotope anomalies in the odd isotopes of Hg (MIF; measured as $\Delta^{199}\text{Hg}$ and $\Delta^{201}\text{Hg}$). These MIF signatures have only been recorded during photochemical reactions of Hg complexes, and existing experimental studies have suggested that the isotope fractionation pattern is consistent with the magnetic isotope effect (MIE)²⁻⁴. Of the photochemical reactions of Hg that exhibit MIE, the photochemical reduction of inorganic Hg(II) complexes is among the most important pathways in natural waters because it may compete with Hg methylation, limiting the amount of bioavailable and neurotoxic methylmercury. In the present work we focus our attention on various aspects of photochemical reduction of Hg(II) complexed to low molecular weight organic ligands (LMWOL) representative of different dissolved organic matter (DOM) binding sites that may alter the MIE. The limited understanding of the controlling factors of MIE

hinder the interpretation of Hg isotopic composition in natural environments, specifically in marine environments where the composition and availability of DOM is significantly different from freshwaters.

It is difficult to interpret MIE in the environment because the reaction mechanisms involved in the photochemical reduction of Hg(II) in natural waters are uncertain, and both direct and indirect photolysis reactions have been proposed³⁻⁸. Direct photolysis occurs via the absorption of a photon by Hg complexes and leads to homolytic cleavage of Hg–ligand bonds. In contrast, indirect photolysis involves the reaction of a Hg complex with a photochemically generated reactant, such as reactive oxygen species. Since Hg(II) is largely complexed by dissolved organic matter (DOM) in natural waters, the role of such complexation in the photochemical reduction of Hg(II) has received special attention^{3,4,6-10}. Hg(II) is primarily bound to thiol groups in DOM, but in excess will also bind to O and N binding sites such as carboxylic acid and amine functional groups¹¹⁻¹⁵. It has been demonstrated that Hg stable isotope signatures associated with Hg(II) photoreduction depend largely on the complexing ligand³, but the isotopic signatures may also vary with reaction conditions, such as wavelength of light, pH, and dissolved oxygen (DO), because these may alter the pathways or mechanisms of direct and indirect photochemical reactions.

To investigate the mechanisms of MDF and MIF of Hg isotopes during photochemical reduction of Hg(II), we broke down the reaction into constituent parts including photophysical, photochemical, and thermally induced processes¹⁶. *Photophysical processes* are interactions of light with molecules resulting in net physical changes, such as a change in electronic multiplicity of an excited state. *Photochemical processes*, on the other hand, involve the interaction of light with molecules that results in net chemical changes, like bond dissociation and formation of

radicals. Lastly, *thermal processes* occur when photochemically generated reactive species like radical pairs, undergo conventional chemical processes to produce the observed product without interactions with light; typically these reactions are known as secondary thermal or secondary (indirect) photochemical processes¹⁶.

Because MIE depends directly on the reactivity and spin multiplicity of reactive intermediates, and since MIE arises from the formation of radical pairs^{17,18}, we hypothesize that photophysical aspects of the reaction control the rate and extent of MIE during the photoreduction of Hg(II). The essential features of these photophysical effects are illustrated in Figure 1, and are as follows:

1. A ground state precursor “XHgX (X= O, S, or N ligand)” is photoexcited to produce an excited state with the same multiplicity as the ground state. All Hg complexes have a singlet ground state multiplicity.
2. The singlet excited state can undergo intersystem crossing to a triplet state mediated by spin-orbit coupling common to heavy elements.
3. The excited triplet (singlet) state will evolve into a correlated triplet (singlet) radical pair (RP) whose electron spins will be well-defined in an overall spin-state inside a solvent cage.
4. A portion of the triplet (singlet) RPs can interconvert to singlet (triplet) RPs by an intramolecular magnetic field arising from hyperfine coupling (HFC) between the unpaired electron and magnetic nuclei (e.g. ¹⁹⁹Hg, ²⁰¹Hg).
5. The newly formed singlet RPs can undergo spin-selective recombination to the ground state precursor, which competes with the HFC mediated interconversion T↔S. Triplet RPs cannot undergo recombination to the ground state because it is spin forbidden.

6. A competing step is the escape or diffusion of the triplet (singlet) RPs from the solvent cage to free radicals. Once the RPs have escaped, all spin correlation is lost and HFC can no longer have an effect.
7. The free radicals can then undergo secondary thermal reactions to the products.

The MIE originates from the preferential spin interconversion of the separated RPs containing odd mass isotopes induced by HFC (step 4). However, the sign of MIE in residual Hg(II) will depend on the efficiency of intersystem crossing of the excited singlet state (step 2), because efficient intersystem crossing will result in a RP in a triplet state (step 3), where HFC will induce preferential spin interconversion of the magnetic isotopes to a singlet state, increasing the population of RPs with ^{199}Hg and ^{201}Hg isotopes. These newly formed singlet RPs, enriched in magnetic isotopes, have a greater probability of geminate recombination to the ground state precursor because the ground state has a singlet character (Figure 1; + MIE). Meanwhile, if there is not efficient intersystem crossing (step 2), the RP will evolve in the singlet state and HFC will induce selective spin interconversion of the magnetic isotopes to the triplet state, as indicated in parentheses in the outlined steps. This will result in RPs with singlet character to be depleted in magnetic isotopes, resulting in preferential geminate recombination of RPs to the ground state resulting in depletion in the magnetic isotopes (Figure 1; (-) MIE).

Within the theoretical framework outlined here, reaction conditions such as DO, wavelength of light, and pH may alter the rate and sign of MIE. Molecular oxygen is a known triplet state radical quencher^{16,19,20} and it has been reported to affect the rate of photochemical decomposition of monomethylmercury (MeHg) complexes^{5,21}. The wavelength of light may affect MIE because the excitation of the ground state precursor of the Hg(II) complex depends directly on it, and the pH may alter the solvent cage altering the efficiency of spin interconversion by HFC.

All the photochemical reactions of Hg investigated to date also exhibit kinetic mass dependent isotope fractionation (MDF: measured as $\delta^{202}\text{Hg}$). Traditionally, kinetic isotope theory (producing MDF) describes exclusively thermally induced processes, because it was derived from transition state theory with the assumption that the reaction takes place in a single potential energy surface defined by equilibrium statistical mechanisms²². The assumptions for MDF do not apply to photochemical reactions in which the excitation of an electron by a photon involves the jump from a ground state to an excited state described by the RP mechanism^{17,18,22}. This excited reactive intermediate RP will occupy a different potential energy surface that is far from equilibrium (Figure 1)¹⁸ and cannot be described within equilibrium statistical mechanics²². Kinetic isotope theory involving heavy elements is also not well understood, and it has been suggested that the net effect will depend on both the nuclear volume effect (NVE) and the masses of the isotopes²³⁻²⁵. The kinetic theory for the NVE has not been developed, but it has been proposed to be analogous to NVE equilibrium exchange reactions^{23,24}. When NVE arises from the interaction of electrons with the nucleus, nuclei with large volumes will overlap with a greater share of the electron density than nuclei with small volumes, resulting in electrons being more weakly bound by large rather than small nuclei. The effects of the nuclear volume on the binding energy of the electron results in a relatively small MIF of Hg isotopes ($\Delta^{199}\text{Hg} < 0.5\%$), because the mean square radius of the nucleus does not scale linearly with the number of neutrons²⁶.

Based on these theoretical considerations about MDF and MIF, there are still many open questions about the photochemical transformations of Hg(II) that occur in the environment and exhibit MIF (NVE and MIE). To improve our ability to catalog MIF signatures in nature, we examined the effects of pH, DO, and wavelength of light (UV and Visible) on Hg stable isotope fractionation during the photochemical reduction of Hg(II) coordinated to the LMWOLs L-serine,

L-cysteine, and ethylenediamine, representative of binding sites in natural DOM. A more in depth understanding of the controlling factors of the Hg stable isotope fractionation during photoreduction of Hg(II) will facilitate the identification of key reaction mechanisms and organic ligands involved in the reduction of Hg(II) in natural waters prior to methylation and incorporation into aquatic foodwebs.

4.2 Materials and Methods

4.2.1 Experimental materials

All photochemical reduction experiments were performed in 1 L, UV-transparent fluorinated ethylene propylene (FEP, Nalgene Teflon), narrow-mouth bottles (which transmit 66% UVB, 82% UVA and 99% visible light²⁷) under natural sunlight at Rutgers University, New Brunswick, New Jersey, USA (40.4769 N 74.4387 W). Aqueous stock solutions of Hg(II) (100 µg/g) were made from powdered Sigma-Aldrich mercuric nitrate monohydrate or mercuric chloride. The mercuric chloride stock was used for all anoxic experiments to avoid the oxidant nitrate. Purified (≥99%, HPLC-grade Sigma Aldrich) L-serine, L-cysteine, and ethylenediamine were used to prepare solutions of LMWOL, and are referred to as ser, cys, and en, respectively. The experimental reactors were continuously purged with ultra-pure N₂ (AirGas, NJ) or Hg-free air from a zero gas generator (Tekran model 1100, ON Canada) to remove gaseous Hg(0) (See Table S1 for experiment dates and details).

4.2.2 Photochemical Reduction of Hg(II)

All photochemical reduction experiments were conducted during clear days (no cloud cover) and the average outdoor temperature ranged from 24 to 30 °C, with the exception of the May experiments when temperatures were cooler (as low as 18 °C). Most incubations were exposed to the full spectrum of natural sunlight. In some incubations (referred to as “Vis”), UV

radiation was blocked using Lee 226 filters, which absorb 96–100% of light at wavelengths below 378 nm. The experiments in which reactor bottles were exposed to both UV and Vis radiation are referred to as UV–Vis.

The experiments were conducted with an initial average Hg(II) concentration of 0.17 ± 0.04 μM in about 700 mL of deionized water. The Hg(II) was incubated in the dark with the corresponding organic compounds, 0.4 mM cysteine, 4 and 0.4 mM serine, and 4 mM ethylenediamine in ultra-pure deionized water for 12 hours to let the Hg(II) fully equilibrate with each organic ligand, while being purged with ultra-pure air or N_2 to remove any potential trace amounts of Hg(0) produced in the dark. The LMWOL concentrations were chosen to ensure that Hg speciation was dominated (90% to >99%) by complexation to the LMOWL, and an additional experimental condition (with 0.4 mM serine) was employed to allow a direct comparison with the results of Zheng and Hintelmann (2010)³. Low pH incubations of Hg(II) with serine and cysteine were conducted at pH 3.8 and 3.2, respectively, and additional experiments were conducted with cysteine and serine in which the pH was adjusted to 7.2 with a phosphate buffer (sodium phosphate salts, Sigma Aldrich). Ethylenediamine experiments were only conducted at pH 7.4. For anoxic experiments bottles were purged with ultra-pure Ar, while for oxic experiments bottles were purged with Hg-free air.

The speciation of Hg(II) in each treatment was estimated using a thermodynamic modelling program (ChemEQL²⁸; see Table S2 for calculation details). In the incubations with 0.4 mM cysteine at both pH 3.2 and 7.2, Hg(II) was estimated to have been present as $\text{Hg}(\text{HCys})_2$ (96%), $\text{Hg}(\text{Cys})_2^{2-}$ (3.5%), $\text{Hg}(\text{Cys})_3^{4-}$ (<1%), and $\text{Hg}(\text{Cys})_4^{6-}$ (<1%). For the incubations with 4 mM serine at pH 3.8, Hg(II) was estimated to have been present as $\text{Hg}(\text{Ser})_2^{2-}$ (50%), and HgSer (40%) and at pH 7.2 was 99.9% $\text{Hg}(\text{Ser})_2$. The speciation of Hg(II) in the incubations with 0.4 mM serine

was estimated to have included HgSer (19.4%, 91.3%) and Hg(Ser)₂ (2.3%, 0.3%), at pH 3.8 and 7.2, respectively. In oxic treatments, the balance of Hg(II) was estimated to have been present as Hg(OH)₂, while in anoxic treatments, the balance of Hg(II) was estimated to have been present as Hg(OH)₂ and Hg(Cl)₂. For incubations with 4 mM ethylenediamine, Hg(II) was estimated to have been present as [Hg(en)₂]⁺² (70.6%), [HgOH(en)₂]⁺² (29%), and [HgH(en)₂]⁺² (0.3%).

For incubations longer than 10 hours, reactors were purged in the dark at 18 °C during the night and exposed to sunlight the next day at 7:30 am; no detectable change in the concentration of Hg(II) occurred during the night. Samples taken of the reactant Hg(II) from each reactor were immediately weighed and preserved with 10% wt/vol BrCl, to avoid any Hg(II) losses and breakdown any matrix effects²⁹. See Table S1 for complete reaction conditions.

4.2.3 Hg concentration and Isotope Analysis

The Hg concentrations in the aliquots of preserved experimental solutions were analyzed for total Hg by cold vapor atomic absorption spectroscopy (CV-AAS, MA-2000, Nippon Instruments). Calibration was obtained using NIST-SRM-3133 as a standard, which was also measured as a check standard after every third sample. An additional Hg standard solution from Inorganic Ventures was used as a secondary standard to verify the calibration.

For Hg stable isotope analysis all the samples were neutralized with hydroxylamine, further reduced with SnCl₂, and purged and trapped into 1% KMnO₄ in 10% H₂SO₄ (wt/wt) solution to remove matrix interferences for isotope analysis (Blum and Johnson, 2017). Trapping recovery in 1% KMnO₄ was 96.8±5% (1SD, minimum = 87%). The 1% KMnO₄ solutions were analyzed for Hg stable isotope composition using a multiple collector inductively coupled plasma mass spectrometer (MC-ICP-MS; Nu Instruments) with a continuous flow cold vapor generation inlet system with SnCl₂ reduction (Lauretta et al., 2001; Blum and Bergquist, 2007). Prior to isotope

analysis, the Hg concentrations of the samples were adjusted and matched to the bracketing standard within 5% (SRM NIST 3133). Instrumental mass discrimination was corrected using a Tl internal standard and sample standard bracketing³⁰.

Mass dependent fractionation (MDF) of Hg isotopes is reported as $\delta^{202}\text{Hg}$ values in per mil (‰) relative to NIST SRM 3133 (equation 1). Mass independent fractionation (MIF) of Hg isotopes is calculated as the difference between the measured $\delta^{\text{xxx}}\text{Hg}$ value and that which would be predicted based on mass dependence for a given isotope, and is reported in $\Delta^{\text{xxx}}\text{Hg}$ notation in ‰ (equation 2), where xxx is the mass of each Hg isotope 199, 200, 201, 204 and β is the mass proportionality constant (0.2520, 0.5024, 0.7520, 1.493, respectively)³⁰.

$$\delta^{202}\text{Hg} = \left(\left(\frac{\left(\frac{^{202}\text{Hg}}{^{198}\text{Hg}} \right)_{\text{sample}}}{\left(\frac{^{202}\text{Hg}}{^{198}\text{Hg}} \right)_{\text{NIST3133}}} \right) - 1 \right) \times 1000 \quad (1)$$

$$\Delta^{\text{xxx}}\text{Hg} \approx \delta^{\text{xxx}} - (\delta^{202} \times \beta) \quad (2)$$

Procedural process blanks and a standard reference material (UM–Almadén) were processed alongside samples in an identical manner. The long–term analytical uncertainty of the Hg isotopic composition was characterized using UM–Almadén as a secondary standard during all isotope analysis sessions. All the stable isotope data from this study are listed on Table S3a–e.

The Hg isotope fractionation throughout the experiments was quantified as the difference between reactant and instantaneous product at any given time by isotopic fractionation factors (ϵ) in ‰ units assuming Rayleigh fractionation³⁰ using the Hg stable isotope composition of the Hg(II) remaining in solution. Here we did not measure the Hg stable isotope composition of the gaseous product given that previous work with microbial reduction of Hg(II) in similar reactors has shown that the results (i.e., fractionation factors) based on isotopic composition of the Hg remaining in

the reactor versus on the isotopic composition of the Hg vapor product trapped in KMnO_4 oxidizing solutions are similar even when there is some loss of $\text{Hg}(0)^{29}$. Also, KMnO_4 base traps do not maintain their oxidizing function over a few hours and the majority of the experiments ran for several hours to days. Isotopic fractionation caused by MDF was quantified by the isotope enrichment factor ($\epsilon^{\text{MDF}}\text{Hg}_{\text{reactant/product}}$) in units of ‰, where ϵ is related to fractionation factors ($\alpha = R_{\text{reactant}}/R_{\text{product}}$) by $(\alpha-1)\times 1000$. The ϵ^{MDF} factor was calculated from the slope between $\delta^{202}\text{Hg}_{\text{final}} - \delta^{202}\text{Hg}_{\text{initial}}$ of the residual $\text{Hg}(\text{II})$ and $\ln(f)$, where f is the fraction of $\text{Hg}(\text{II})$ remaining following Rayleigh distillation. Rayleigh distillation is a reasonable assumption because the instantaneous product (gaseous Hg) is continuously being purged from the reaction^{3,29,31}. The $\epsilon^{\text{MIE}}\text{Hg}_{\text{reactant/product}}$ factor caused by MIE was quantified in a similar manner as MDF from a plot of $\Delta^{199}\text{Hg}_t - \Delta^{199}\text{Hg}_{\text{initial}}$ versus $\ln(f)$, in units of ‰. The Rayleigh plot slopes and standard errors were calculated using least squares regression, and for the three isotope relationships we used York regressions with correlated errors³² to account for errors in both axes.

4.3 Results

4.3.1 Reaction Kinetics

All $\text{Hg}(\text{II})$ reduction rates followed pseudo-first order kinetics and there were no statistical differences in the rate constants between different dates of experiments with the same ligands (Table S1). In the cysteine experiments, there was no reduction of $\text{Hg}(\text{II})$ in the dark or in incubations exposed only to visible light. The lack of reduction of $\text{Hg}(\text{HCys})_2$ under visible light results from the thermodynamic stability of this complex^{11,14}, which is only subject to direct photolysis near its absorption maxima in the UVB-C region at 245–310 nm⁵. With cysteine, the $\text{Hg}(\text{II})$ reduction rate was on average greater in the neutral treatment (pH=7; oxic, $1.13\pm 0.21 \text{ day}^{-1}$,

1SD, n=3, outlier 0.18 day⁻¹; anoxic, 0.59±0.04 day⁻¹ 1SD, n=2) compared to the acidic ones (pH=3.2; oxic, 0.24±0.06 day⁻¹ 1SD, n=2; anoxic 0.49±0.14 day⁻¹ 1SD, n=3).

Unlike with cysteine, Hg(II) in the presence of serine was degraded under visible light, but in all cases the reduction was faster with UV light than with only visible light. The highest rate of Hg(II) reduction was recorded for pH 7 with high DO conditions and the full sunlight spectrum (UV-Vis, oxic=29.94±4.23 day⁻¹, n=2 1SD), but there was a significant reduction in the rate after 3 hours (>3 hours, oxic, 1.27±0.29 day⁻¹, n=3 1SD), to rates comparable to those in the cysteine incubations. The reduction rates at these pH's were also affected by the presence of DO (anoxic = 6.10, n=2), but there was no effect on reduction rates with two different serine concentrations (0.4 mM and 4 mM). There also were no significant effects of DO or UV light on the degradation rates of Hg(II) in the pH=3 treatments.

The photochemical reduction rate of Hg(II) with ethylenediamine was about twice that in the cysteine experiments (pH 7 oxic, 2.80±0.36 day⁻¹, n=2 1SD), but lower than all the serine experiments.

4.3.2 Mercury stable isotope fractionation during photochemical reduction of Hg(II) in the presence of cysteine

Under all conditions, the photochemical reduction of Hg(II) in the presence of cysteine resulted in MDF (Figure 2a; $\delta^{202}\text{Hg}$ versus $\ln(f)$; Table S4) that followed a Rayleigh fractionation pattern. The resulting fractionation factor for this reaction ($\epsilon^{\text{MDF}}=1.04\pm 0.09\%$, n=5) is lower than the previously reported value ($\epsilon^{\text{MDF}}=1.32\pm 0.07\%$, n=1)³. However, at pH 7 and under oxic conditions, MDF was suppressed after about 42% of the Hg(II) had been reduced, indicating that the initial rate limiting step was no longer causing the fractionation of Hg isotopes; no suppression of MDF was recorded in the pH 3 experiments.

The ϵ^{MIF} and sign (\pm) of MIF as recorded by $\Delta^{199}\text{Hg}$ versus $\ln(f)$, varied depending on pH and DO (Figure 2d). For example, under acidic and anoxic conditions, $\Delta^{199}\text{Hg}$ values were negative and in close agreement with the previously reported Rayleigh fractionation factor ($\epsilon^{\text{MIF}}=-0.90\pm 0.2\%$), while under neutral anoxic conditions, $\Delta^{199}\text{Hg}$ values were positive with a fractionation factor of $\epsilon^{\text{MIF}}=1.15\pm 0.11\%$. For the neutral oxic experiments, significant negative MIF was only recorded after about 42% of the Hg(II) had been reduced and this coincided with the suppression of MDF, resulting in a very small MIF fractionation factor of $\epsilon^{\text{MIF}}=-0.25\pm 8\times 10^{-2}\%$.

Because the reduction of Hg(II) with cysteine under acidic and oxic conditions was very slow, it was difficult to accurately determine the extent of Hg isotope fractionation in this treatment. Results for the only sample in which Hg was significantly fractionated indicate that under these reaction conditions Hg(II) reduction followed the same MDF Rayleigh fractionation as in the other treatments and exhibited positive $\Delta^{199}\text{Hg}$ similar to that in the incubation at pH 7 under anoxic conditions.

4.3.3 Mercury stable isotope fractionation during photochemical reduction of Hg(II) in the presence of serine

The photochemical reduction of Hg(II) in the presence of serine resulted in MDF of Hg isotopes that followed a similar $\delta^{202}\text{Hg}$ fractionation relative to $\ln(f)$ regardless of experimental conditions (Figure. 2b). The average fractionation factor for these reactions was $\epsilon^{\text{MDF}}=1.81\pm 0.04\%$, which was slightly higher than the previously reported value ($\epsilon=1.71\pm 0.03\%$ ³). For the UV-Vis neutral conditions there was a clear suppression of MDF after 74% of Hg(II) was reduced with 4 mM serine, and after 58% was reduced with 0.4 mM serine, resulting in an average ϵ^{MDF} of $0.43\pm 0.3\%$.

In the serine experiments, DO had no effect on Hg stable isotope values, but two types of MIF were recorded depending on the wavelength of light. The experiments that were only exposed to visible light resulted in relatively small negative $\Delta^{199}\text{Hg}$ values in the remaining reactant (Figure 2e; average $\Delta^{199}\text{Hg} = -0.11 \pm 0.06\text{‰}$, $n=34$). However, while incubations exposed to UV-Vis had small negative $\Delta^{199}\text{Hg}$ values ($\sim \Delta^{199}\text{Hg} = -0.20\text{‰}$) during the first few hours, after 3–5 hours, when a significant amount of the Hg(II) had been reduced (41–74%), large positive MIF values were recorded in the residual Hg(II) ($\Delta^{199}\text{Hg} > 0.4\text{‰}$). The extent of Hg(II) reduction that occurred at the change in MIF varied with serine concentration and pH. For example, in the anoxic experiment with 4 mM serine at pH 3 the MIF change started after 41% of the Hg had been reduced, while at pH 7 it was after 76% reduction (See Table S3e for details).

4.3.4 Mercury stable isotope fractionation during photochemical reduction of Hg(II) in the presence of ethylenediamine

The photochemical reduction of Hg(II) in the presence of ethylenediamine resulted in a $\delta^{202}\text{Hg}$ fractionation factor of $\epsilon^{\text{MDF}} = 2.11 \pm 0.2\text{‰}$, and there was suppression of MDF after ~50% of the Hg(II) had been reduced (Figure 2c;). During these incubations, $\Delta^{199}\text{Hg}$ values of the remaining reactant Hg(II) were negative by up to -0.52‰ with a fractionation factor of $\epsilon^{\text{MIE}} = -0.16 \pm 0.03\text{‰}$ (Figure 2f).

4.4 Discussion

The limited understanding of Hg isotope effects during photochemical reactions makes it difficult to interpret Hg MDF and MIF and their relationship to each other (e.g. $\Delta^{199}\text{Hg}$ to $\delta^{202}\text{Hg}$ and $\Delta^{199}\text{Hg}$ to $\Delta^{201}\text{Hg}$) in natural samples. Based on the experimental results presented here, it appears that MDF and MIF are controlled by different physical and chemical factors, which may explain why values for ϵ^{MDF} were similar for all the reactions with the same ligand while ϵ^{MIF}

varied depending on reaction conditions including DO and wavelength of light (Figure 2). Our results also demonstrate that the sign and rate of MIE does not directly depend on the binding ligand and negative MIE is not exclusive to thiol ligands. Here we discuss the Hg stable isotope signatures during photochemical reduction of Hg(II) bound to various LMWOLs, the possible relationship between MDF and MIF, and the environmental importance of these results.

4.4.1 Photochemical reduction of Hg(II) in the presence of LMWOL

4.4.1.1 Cysteine experiments

The Hg stable isotope fractionation photoreduction experiments with $\text{Hg}(\text{HCys})_2$ demonstrate that negative MIF does not depend on the binding ligand, but instead depends on the reaction conditions. The $\text{Hg}(\text{HCys})_2$ complex was estimated to be dominant under all experimental conditions, but MIF varied in sign and rate with pH and DO (Figure 2d). MIF was negative for anoxic pH=3 and oxic pH=7 conditions, whereas it was positive for anoxic pH=7 conditions. The elevated $\Delta^{199}\text{Hg}$ values are a clear indication that the dominant isotope effect was MIE, as NVE can only result in small $\Delta^{199}\text{Hg}$ values ($<0.4\text{‰}^3$). The sign of MIE represents the spin multiplicity of the excited state precursor such that (-) MIE indicates that the radical pair was formed in the singlet state, whereas (+) MIE indicates radical pair formation in the triplet state¹⁷ (See Figure. 1).

For Hg cysteine complexes at pH=7, it appears that DO may have quenched the excited triplet state to a singlet before the evolution of the RP (step 2, Figure 1) in the neutral experiments, and therefore caused a change in sign of MIE (Figure 2d). Molecular oxygen is a known triplet state radical quencher that photophysically changes the multiplicity of the electronically excited state, and it has been reported to alter the rate of photodecomposition of methylmercury–thiol complexes^{5,21}. For the oxic pH 7 experiment there was also a strong suppression of MDF concomitant with an increase in MIE after 42% of the Hg had been reduced. The change in isotope

fractionation (both MDF and MIF) did not correlate with a change in reduction rates, suggesting that a change in reaction mechanism is unlikely. Instead, the suppression of MDF indicates that the initial rate limiting step was no longer causing the fractionation of Hg isotopes; this may suggest a change in the availability of the reactive intermediate species for the *thermal process* that may induce MDF. The suppression of MDF is not expected to have any effects on the MIE because these two isotope effects are not expected to be induced in the same reaction step based on theoretical considerations outlined herein.

An opposite effect of DO was observed for the photoreduction of cysteine-bound Hg(II) at pH=3; under anoxic conditions it yielded negative MIE. As such, the role of pH remains unclear in the photochemical degradation of cysteine-bound Hg. However, based on the changes in the sign of MIE, pH likely alters the photophysical aspects of the reaction resulting in changes in the dynamics of the RP. A plausible explanation for this behavior is that solvent polarity and pH alter the efficiency of the solvent cage and hyperfine coupling constants^{33–35}; but more research is needed to test this hypothesis.

Even though ϵ^{MIE} values and the sign of MIE varied with experimental conditions, MDF remained unchanged (Figure 2a). A potential explanation for this is that the pathway that leads to MIE is not a major pathway of photodegradation, as suggested by Chandan et al. (2015)³¹ for the degradation of monomethylmercury (MeHg) with different concentrations of DOM. Chandan et al. reported variable slopes (ϵ^{MIE}) of $\Delta^{199}\text{Hg}$ versus $\ln(f)$, but constant ϵ^{MDF} values from $\delta^{202}\text{Hg}$ versus $\ln(f)$. Based on these results, they concluded that photodegradation of MeHg likely did not involve a RP intermediate, and that indirect photolysis was likely the dominant photochemical pathway. However, in our Hg(II) photoreduction experiments the results indicate that pH and DO did not affect the rate-limiting step, but changed the rate and sign of MIE. This may reflect the

fact that the evolution of a coherent RP and interconversion of spin multiplicity between triplet and singlet states are photophysical effects, where no bond is broken or created^{17,18,36,37}. Indirect photolysis is also unlikely for our experimental conditions because there was no DOM to initiate the reaction, and cysteine does not absorb light in the UVA/B or visible region (absorption maximum=190 nm, tail=260 nm³⁸). As such, we demonstrate that DO and pH affect the sign and extent of MIE, but not MDF, and the overall reaction mechanism is similar for all conditions. The differential dependence of the magnitude of mass independent fractionation (ϵ^{MIE}) on the aqueous chemical environment indicates that the MIE is induced at a different reaction step than MDF (See section 4.2; Figure 1).

4.4.1.2 Serine experiments

The rate of Hg(II) reduction in the presence of serine varied with the speciation of Hg(II), the pH, and the wavelength of light (See Table S1). Reduction rates were greatest in all experiments exposed to the full spectrum of sunlight (UV–Vis) compared to only visible light. This was expected as UV light has been reported to enhance the photochemical transformation of Hg species in solution^{8,39,40}. The reduction of Hg(II) was also faster at pH 7, where the Hg was 99.9% Hg(Ser)₂²⁻, in comparison to acidic conditions (50% Hg(Ser)₂²⁻ and 40% HgSer with 4 mM serine and 2.3% Hg(Ser)₂²⁻ and 19% HgSer with 0.4 mM serine); this may suggest that Hg(Ser)₂²⁻ complexes are more likely to undergo direct photolysis. There was also a sudden decrease in reaction rates in the pH 7 UV–Vis experiments after significant Hg(II) had been reduced. This suggests a change in reaction mechanism, as was previously demonstrated³, but this sudden change in kinetics was not apparent in the pH 3 experiments with UV–Vis.

A change in reaction mechanism in the course of the experiments with UV light is supported by the Hg isotope signatures. The Hg(II) experiments with serine resulted in two

different MIF effects. NVE was observed under all reaction conditions, whereas MIE was only exhibited in experiments with UV light after significant Hg(II) had been reduced (Figure 2e; Table S3e), and where the onset of MIE was also dependent on pH. We agree with the hypothesis from a previous study³ that the change in kinetics and MIF suggests that the dominant reaction mechanism changed from indirect photoreduction by reactive radicals to direct photolysis of the Hg complex. We observe that the change in MIF from NVE to MIE seems to depend on multiple factors, such as, pH, DO, and the speciation of Hg(II) in solution (Table S3b). For example, at pH=3 under anoxic conditions and with 4 mM serine, MIE was induced after 40% of the Hg(II) had been reduced, while at pH=7 under anoxic conditions MIE was induced after 76% reduction (Figure 2e; Table S3b). We do not have a clear explanation for the effects of pH on the onset of MIE in the reaction, but we suggest that it may correlate with the dissolved Hg(II) species in solution at different pH values (See Table S2). MIE may be limited by the availability of Hg-serine complexes in solution, which can undergo direct photolysis favoring indirect photolysis and resulting in fast reduction rates in the early stages of the reaction. This is supported by Zheng and Hintelmann (2010)³, where MIE was only observed after a much larger proportion of Hg(II) had been reduced (~98%) compared to any of our experiments. This may have been due to excess Cl⁻, low pH, or low serine concentration (0.4 mM), all of which could have limited complexation of Hg(II) by serine compared to our experiments.

During the phase of the UV-Vis experiments characterized by large positive $\Delta^{199}\text{Hg}$ values, the ϵ^{MDF} and ϵ^{MIE} also appear to depend on pH and by inference, the speciation of Hg in solution. For the pH=7 experiments there was a suppression of MDF concomitant with the onset of MIE, while this was not recorded in the pH=3 experiments. Differential timing of ϵ^{MDF} and ϵ^{MIE} may indicate that MDF and MIE do not arise from the same steps in the photochemical reaction. By

inspecting the relationship between $\Delta^{199}\text{Hg}$ and $\delta^{202}\text{Hg}$ values, we report that both pH 3 and 7 experiments plot within uncertainty of the same slope (1.84 ± 0.11 ; Figure 3 inset(a)). It is unclear why both experimental conditions have similar $\Delta^{199}\text{Hg}/\delta^{202}\text{Hg}$ slopes, but the overlap suggests that the direct photolysis of Hg(II)–serine complexes has a similar reaction mechanism at pH 3 and 7. We suggest that $\Delta^{199}\text{Hg}$ reflects the photophysical aspects of the reaction, while $\delta^{202}\text{Hg}$ reflects the rate limiting step of the thermal aspects. More research is needed to fully determine the significance of the $\Delta^{199}\text{Hg}$ to $\delta^{202}\text{Hg}$ relationship in these experiments.

In the Vis experiments and the early hours of the UV–Vis experiments the slightly negative $\Delta^{199}\text{Hg}$ and $\Delta^{201}\text{Hg}$ values (up to -0.3% , Figure 2e inset) but positive $\delta^{199}\text{Hg}$ and $\delta^{201}\text{Hg}$ values are a clear sign of NVE by indirect photolysis of Hg(II) by reactive radicals³. The fractionation factors with δ values (Table S5) also showed the characteristic odd–even staggering of NVE^{3,41}. Despite the variable reduction rates of Hg(II) in these experiments, the ϵ^{MDF} values were the same for all the reactions (Figure 2b) suggesting that the indirect photolysis mechanism was similar for all reaction conditions. The ϵ^{MDF} fractionation factor was identical even for solutions where HgCl_2 was the dominant species of Hg in solution (pH 3, anoxic, 0.4 mM serine). This further supports our hypothesis that the Hg stable isotope values during this part of the reaction may represent indirect photolysis, because HgCl_2 does not absorb light in the natural sunlight spectrum^{42,43} and cannot exhibit MIE in natural sunlight. This suggests that the isotopic signatures of indirect photolysis are insensitive to the complexing ligand (Figure 2b and 2e–inset). However, it is difficult to ascertain the radical precursor for the indirect photolysis because serine, with an absorption maxima of 168 nm, does not absorb natural sunlight³⁸.

4.4.1.3 Ethylenediamine experiments

Hg has a high affinity for organic thiols, however, when thiols are saturated, Hg will bind to N ligands preferentially to O ligands in DOM^{13,14}. Hg-en complexes are thermodynamically very stable¹¹ resulting in photoreduction rates that are slightly faster than those for Hg-cysteine complexes, but slower than in all of our experiments with Hg-serine complexes. The slow reaction rate and the absence of NVE suggests that there was no secondary photolysis. Moreover, the large negative $\Delta^{199}\text{Hg}$ values (Figure 2f), which are characteristic of MIE, may indicate direct photolysis during the reduction of en-bound Hg(II). The (-) sign of MIE may indicate that the excited state precursor was formed in a singlet state (See Figure. 1¹⁷). In this case, it is possible that molecular oxygen quenched the excited triplet state to a singlet state as proposed for the photoreduction of cysteine-bound Hg(II) in the presence of oxygen, however, no ethylenediamine experiments were conducted under anoxic conditions. Similarly to the cysteine experiments there was an apparent suppression of MDF after 74% of the Hg had been reduced. The suppression suggests that the initial rate limiting step was no longer fractionating the Hg isotopes in the *thermal* stage of the reaction likely due to the availability of a reactive intermediate. As in the cysteine experiments the suppression of MDF should not affect the extent of MIE because these two isotope effects are not expressed in the same reaction step.

4.4.2 Photophysical control of MIE during the photochemical reduction of Hg(II) complexes

Based on our results and the theoretical frameworks for MDF and MIE, we suggest that these isotope effects may not occur in the same reaction step during the photochemical reduction of Hg(II). $\Delta^{199}\text{Hg}$ values are expected to arise from intersystem crossing of the solvent separated RP (Figure 1, step 4), with no significant $\delta^{202}\text{Hg}$. And $\delta^{202}\text{Hg}$ values are expected to arise from the rate limiting step of a thermally induced process, with no significant $\Delta^{199}\text{Hg}$. This explains why MDF Rayleigh plots for the incubations of Hg(II)-cysteine followed the same slope (ϵ^{MDF})

regardless of pH prior to any MDF suppression (Figure 2a). Yet in the same experiments, ϵ^{MIE} varied with reaction conditions (Figure 2d) resulting in variable MIE rates and sign. The variable ϵ^{MIE} with different pH and DO may be a result of changes in the solvation and reactivity of the RP intermediate. It has been demonstrated that MIE enrichment factors for C, S, and Si may change with varying viscosity^{44–46}, triplet sensitizers^{17,47}, excited state quenchers⁴⁶, and the bonding environment^{31,36,45} for the same reaction mechanism. As such, the interaction of photophysical factors likely determines the sign and extent of MIE during light-driven reduction of Hg(II). In the serine experiments, photophysical effects on the MIE were obscured by large differences in Hg(II) speciation in the UV–Vis experiments.

4.4.3 Environmental implications

Hg isotope measurements in natural samples have been proven to be effective tools for elucidating important transformations of Hg in the environment^{2,48,49}, and MIF signatures from photochemical reduction of Hg(II) have served as a useful way to track Hg in the environment^{31,50,51}. This is because once Hg is incorporated into higher trophic level organisms it is not available for photochemical degradation⁵². The Hg isotope trends reported here allow for an enhanced interpretation of Hg MIF signatures in the environment (Figure 4). For example, our experiments where HgCl₂ was the major species in solution suggest that in marine environments, where more than 50% of Hg(II) may be complexed to Cl⁵³, photochemical reduction will be dominated by indirect photolysis resulting in NVE effects with small negative $\Delta^{199}\text{Hg}$ values (Figure 4). The photolysis of HgCl₂ cannot yield MIE because it is not available for direct photolysis in natural sunlight. In contrast, in surface freshwaters where most Hg(II) is expected to be complexed to DOM^{12–14}, our results indicate that the photoreduction of Hg(II) may preferentially result in negative MIE, because in surface oxygenated waters Hg will preferentially

bind to S- or N- type functional groups in DOM. This contradicts the results of previous experiments with Hg(II) and DOM^{2,4}, which resulted in large (+) $\Delta^{199}\text{Hg}$ values in residual Hg(II). This difference may be due to the elevated Hg concentrations used in previous experiments. Elevated Hg to DOM ratios favor Hg(II) complexation to O-type ligands, which have greater reduction rates and exhibit positive $\Delta^{199}\text{Hg}$ values.⁴ Recent experiments with DOM derived from marine phytoplankton exhibited negative MIF similar to our cysteine experiments²⁷.

Finally, it has been suggested that the $\Delta^{199}\text{Hg}/\Delta^{201}\text{Hg}$ (Figure 5) slope could be used to determine whether inorganic Hg(II) or MeHg is the substrate of photochemical reactions leading to MIF in the environment. However, the $\Delta^{199}\text{Hg}$ and $\Delta^{201}\text{Hg}$ values reported here indicate that the slope is sensitive to the complexing ligand and that it does not exclusively discriminate between MeHg and Hg(II) type complexes. We have shown that the $\Delta^{199}\text{Hg}/\Delta^{201}\text{Hg}$ ratio for MIE can range from 0.85 to 1.46, with serine, ethylenediamine, and neutral cysteine experiments having a $\Delta^{199}\text{Hg}/\Delta^{201}\text{Hg}$ ratio close to 1 (0.85–1.11), while acidic cysteine experiments have a $\Delta^{199}\text{Hg}/\Delta^{201}\text{Hg}$ ratio of 1.30 in this study and 1.46 in the previous study³. This contradicts the assumption that Hg(II) photochemical reduction may exclusively yield a $\Delta^{199}\text{Hg}/\Delta^{201}\text{Hg}$ ratio of 1.00 ± 0.01 ². In addition to the $\Delta^{199}\text{Hg}/\Delta^{201}\text{Hg}$ ratio for MIE, the deviation from the hypothesized NVE 1.6 slope⁴¹ in the serine visible experiments indicates that NVE may vary depending on reactions conditions and dissolved Hg species in solution (Figure 4, inset). This is supported by $\Delta^{199}\text{Hg}/\Delta^{201}\text{Hg}$ NVE slopes ranging from 1.5–1.6 for nonphotochemical degradation of Hg coordinated to natural DOM⁴¹, 1.64 during the photochemical oxidation of gaseous Hg by Br radicals⁵⁴, and 2.0 for Hg liquid–vapor equilibrium⁵⁵. We propose that examining even–odd patterns in the fractionation factors of the Hg isotopes is a better indicator of NVE⁴¹ than the $\Delta^{199}\text{Hg}/\Delta^{201}\text{Hg}$ slope.

In summary, we demonstrate that during the photoreduction of Hg(II) bound to various LMWOLs, the occurrence of Hg stable isotope fractionation by the NVE or MIE mechanisms depends on Hg(II) speciation and wavelength of light, while the sign and rate of MIE depends on the complexing ligand, DO, and pH (Figure 4). MDF and MIE are induced at different steps in the reactions and specifically highlight the potential role of photophysical processes on MIE. However, to better interpret MIF signatures preserved in aquatic organisms additional experiments are needed to explore the role of pH and photophysical quenchers on MIE and investigate the relationships between $\Delta^{199}\text{Hg}$ and $\delta^{202}\text{Hg}$ in photochemical transformations of Hg, particularly concentrating on potential implications of excited state non-equilibrium isotope effects⁵⁶.

ABBREVIATIONS

Ser, Serine; Cys, Cysteine; En, Ethylenediamine; MDF, Mass dependent isotope fractionation; MIF, Mass independent isotope fractionation; NVE, Nuclear volume effects; MIE, Magnetic isotope effect, MIE.

ACKNOWLEDGEMENTS

The authors would like to thank Tamar Barkay for her involvement in the conception of this project, Sarah Janssen for all her help with the experiments during very sunny days at Rutgers University, and Marcus Johnson for all his valuable help with mass spectrometry. This work was supported by National Science Foundation (NSF) grants OCE 1433710 and EAR-0952108 to JDB, EAR-0952291 to JRR, a Hatch/McIntyre-Stennis grant through the New Jersey Agricultural Experiment Station, and a NSF Graduate Fellowship to L.C. Motta.

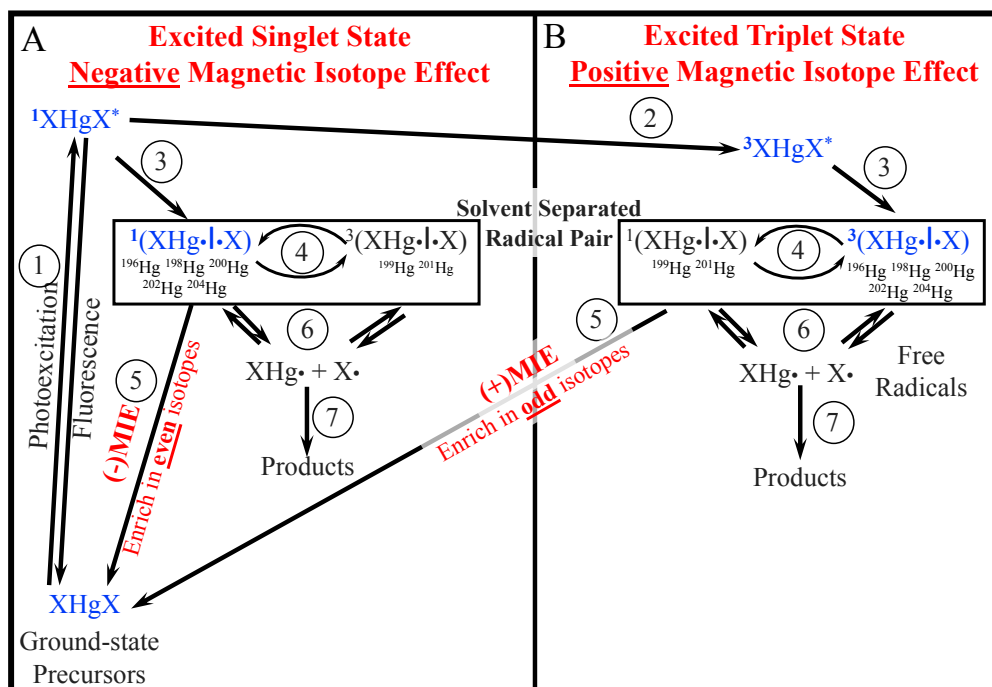


Figure 4.1. Radical Pair mechanism for magnetic isotope effect for the XHgX complex, where X=–S, –N, or –O bearing ligand^{17,37}. The steps are described in the introduction. Briefly, MIE arises from the nonzero nuclear spin and nuclear magnetic moment produced by the presence of an unpaired neutron in the nucleus of odd mass isotopes that results in hyperfine splitting. The origin of MIE comes from the spin coherent evolution of the correlated solvent separated radical pair in step 3, where hyperfine coupling affects the rate of spin state interconversion T↔S (step 4). The correlated radical pair must be solvent separated for electron exchange interactions to be minimized (step 4), and the magnitude and preference for odd to even isotope enrichment in the ground state will be determined by the spin multiplicity of the excited state precursor prior to the evolution of the RP (step 3–5)^{17,18}

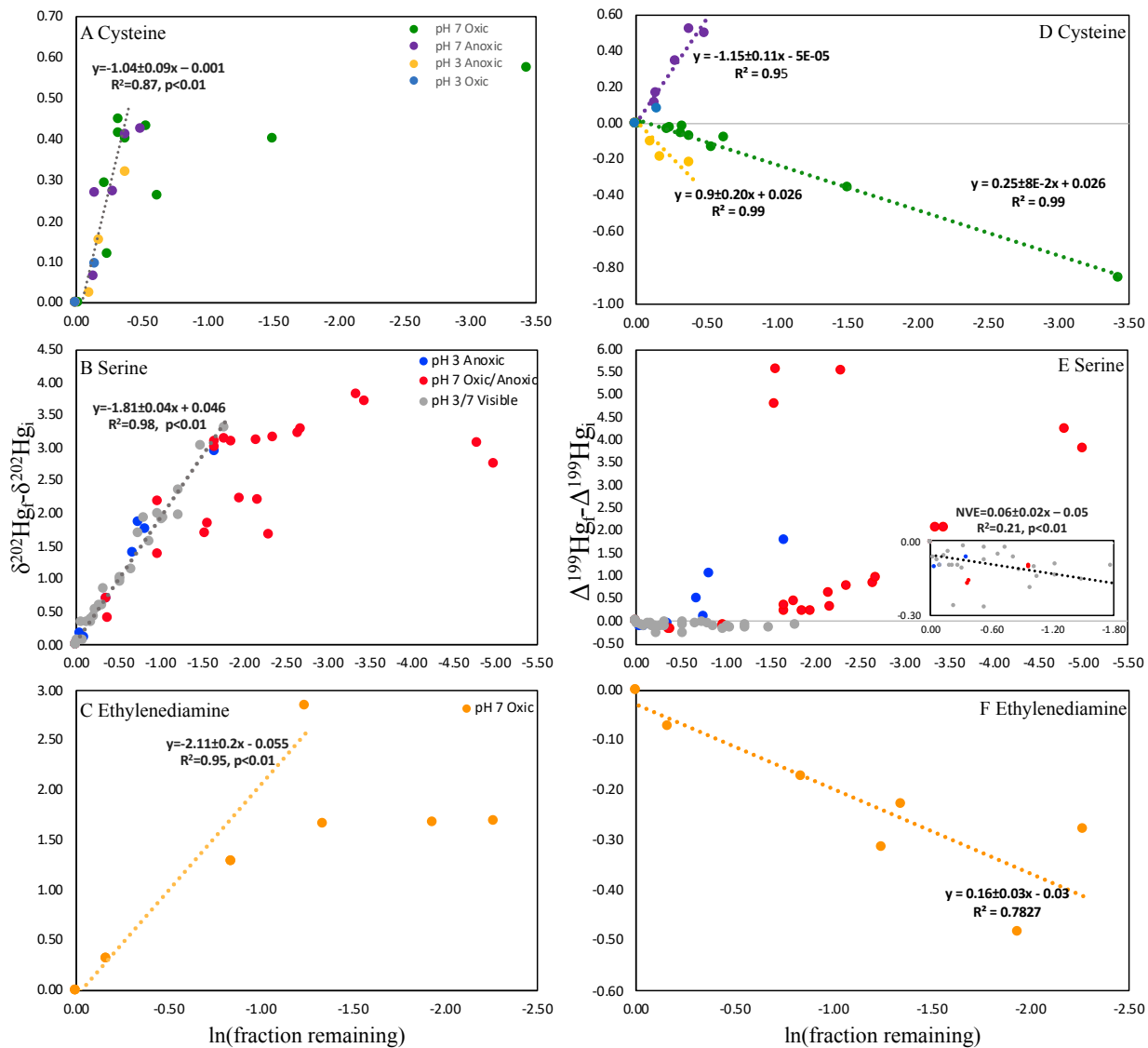


Figure 4.2. Rayleigh distillation plots of the mass–dependent (MDF, A–C) and mass–independent fractionation (MIF, D–F) of Hg stable isotopes during the photochemical reduction of Hg(II) bound to various ligands. For the reduction of Hg(II) in the presence of cysteine (A and D), circles are results from the present study. For the serine experiments (B and E), grey circles are for all of the experiments with only visible light, blue circles are for the pH 3 anoxic treatments, and red circles are for the pH 7 anoxic/oxic treatments. For ethylenediamine (C and E), yellow circles represent the two pH 7 oxalic experiments. The inset in panel E shows the small extent of (–)MIF by NVE.

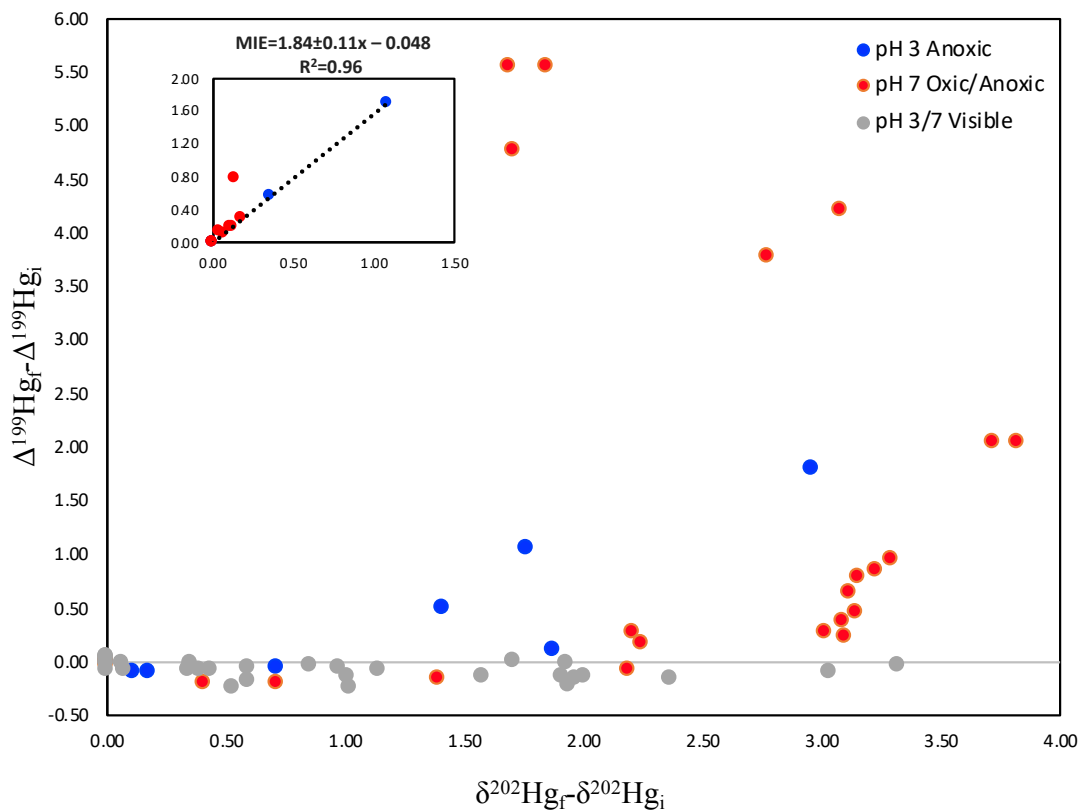


Figure 4.3. Three-isotope plots illustrating correlations between MIF ($\Delta^{199}\text{Hg}$) and MDF ($\delta^{202}\text{Hg}$) for the serine experiments. The symbols are the same as in Figure 2. Inset the values were normalized to the onset of MIE (see text section 4.1.2 for details).

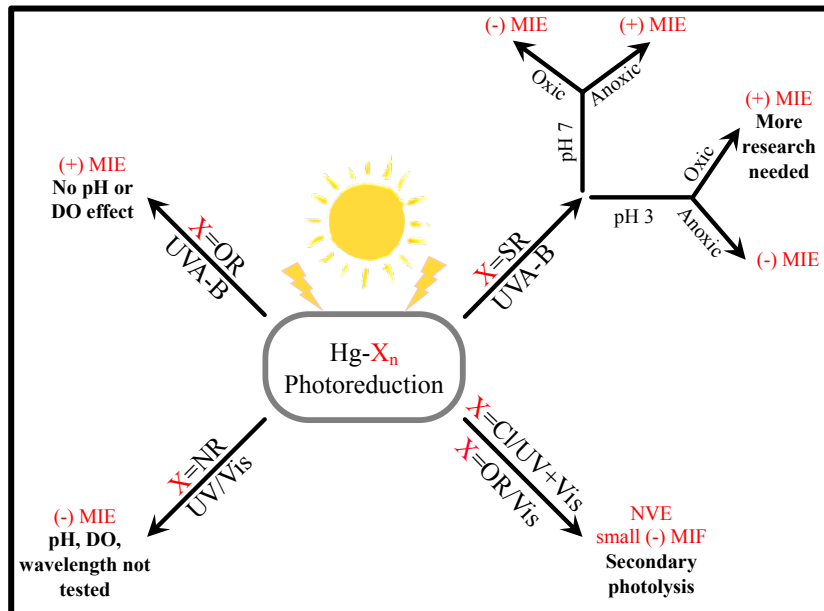


Figure 4.4. Summary diagram showing the expected effects of environmental factors (wavelength of light, pH, and dissolved oxygen) on the type (nuclear volume effect, NVE or magnetic isotope effect, MIE) and sign of MIF in residual Hg(II) during the photochemical reduction of Hg–X_n (n is the number of ligands; X=SR, OR, NR organic ligands, or Cl). Briefly, when Hg(II) is complexed with thiol ligands, the sign of MIE will depend on pH and DO, but more observations are needed to verify that pH3/oxic conditions yields (+) MIE in residual Hg(II). The photoreduction of Hg(II) complexed to OR type ligands with UVA–B radiation will yield (+) MIE regardless of pH or DO. The MIE of residual photoreduced Hg(II)–NR complexes will yield negative MIE at pH7 with UV–Vis radiation, but other pH values, DO concentrations, or wavelengths of light were not examined with this ligand. Lastly, the photochemical reduction of Hg(II) complexed to Cl under UV–Vis or to OR under visible light will only yield small, negative ($\Delta^{199}\text{Hg} > -0.4\text{‰}$) extents of MIF in residual Hg(II) indicative of NVE.

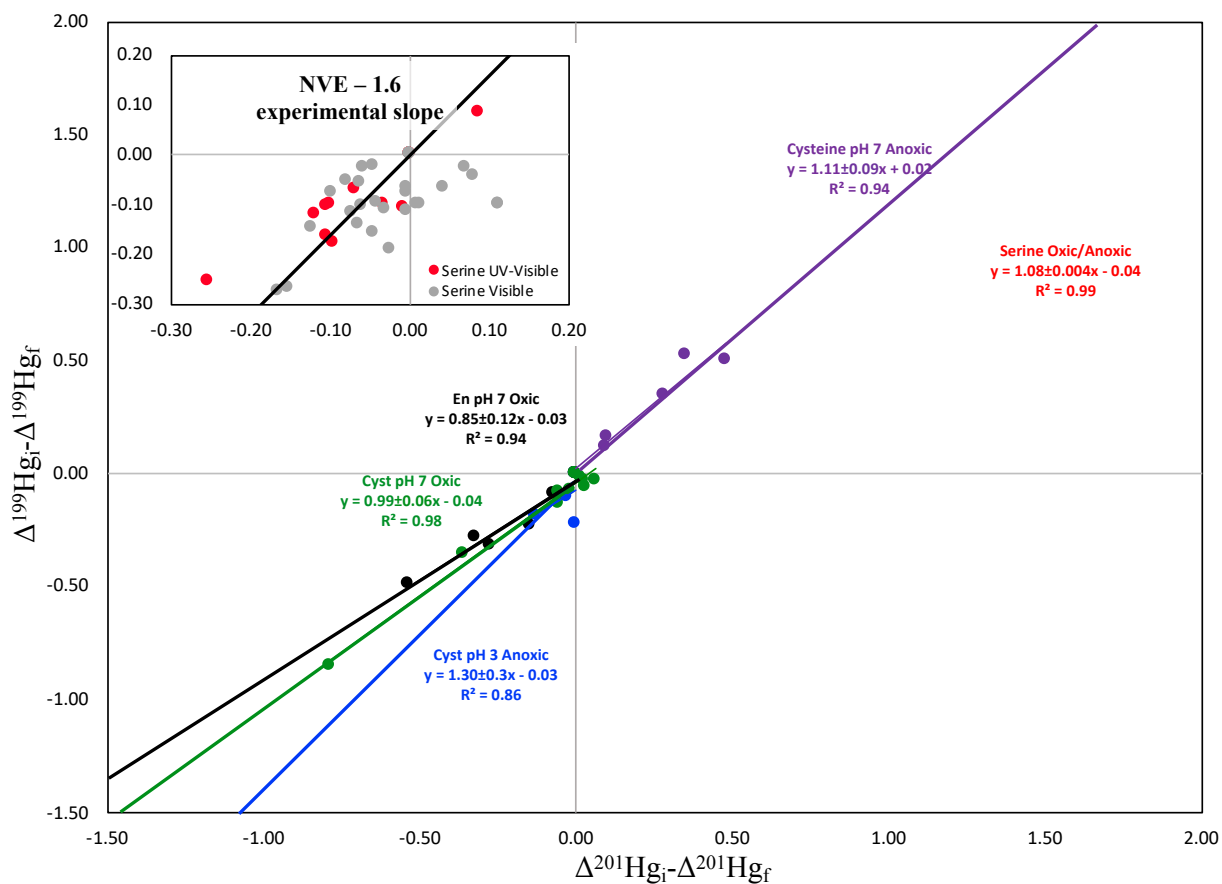


Figure 4.5. Three isotope plot illustrating correlation between $\Delta^{199}\text{Hg}$ and $\Delta^{201}\text{Hg}$ (both MIF). The purple circles are for the cysteine pH 7 anoxic experiments, red circles are for the serine UV-Visible oxidic and anoxic experiments, black circles are for the ethylenediamine pH 7 oxidic experiments, green circles are for the cysteine pH 7 oxidic experiments, and blue circles are for the pH 3 anoxic experiments. The inset shows the small extent of (-) MIF due to NVE during the early stages of the serine experiments in the presence of visible (grey circles) or UV-visible (red circles) light.

References

- (1) Mahaffey, K. R.; Sunderland, E. M.; Chan, H. M.; Choi, A. L.; Grandjean, P.; Mariën, K.; Oken, E.; Sakamoto, M.; Schoeny, R.; Weihe, P.; et al. Balancing the Benefits of N-3 Polyunsaturated Fatty Acids and the Risks of Methylmercury Exposure from Fish Consumption. *Nutr. Rev.* **2011**, *69* (9), 493–508.
<https://doi.org/10.1111/j.1753-4887.2011.00415.x>.
- (2) Bergquist, B. a; Blum, J. D. Mass-Dependent and -Independent Fractionation of Hg Isotopes by Photoreduction in Aquatic Systems. *Science* **2007**, *318* (5849), 417–420.
<https://doi.org/10.1126/science.1148050>.
- (3) Zheng, W.; Hintelmann, H. Isotope Fractionation of Mercury during Its Photochemical Reduction by Low-Molecular-Weight Organic Compounds. *J. Phys. Chem. A* **2010**, *114*, 4246–4253.
- (4) Zheng, W.; Hintelmann, H. Mercury Isotope Fractionation during Photoreduction in Natural Water Is Controlled by Its Hg/DOC Ratio. *Geochim. Cosmochim. Acta* **2009**, *73* (22), 6704–6715. <https://doi.org/10.1016/j.gca.2009.08.016>.
- (5) Jeremiason, J. D.; Portner, J. C.; Aiken, G. R.; Hiranaka, A. J.; Dvorak, M. T.; Tran, K. T.; Latch, D. E. Photoreduction of Hg(II) and Photodemethylation of Methylmercury: The Key Role of Thiol Sites on Dissolved Organic Matter. *Environ. Sci. Process. Impacts* **2015**, *17* (11), 1892–1903. <https://doi.org/10.1039/c5em00305a>.
- (6) Zheng, W.; Liang, L.; Gu, B. Mercury Reduction and Oxidation by Reduced Natural Organic Matter in Anoxic Environments. *Environ. Sci. Technol.* **2012**, *46* (1), 292–299.
<https://doi.org/10.1021/es203402p>.

- (7) Amyot, M.; Southworth, G.; Lindberg, S. E.; Hintelmann, H.; Lalonde, J. D.; Ogrinc, N.; Poulain, A. J.; Sandilands, K. A. Formation and Evasion of Dissolved Gaseous Mercury in Large Enclosures Amended with 200 HgCl₂. *Atmos. Environ.* **2004**, *38* (26), 4279–4289. <https://doi.org/10.1016/j.atmosenv.2004.05.002>.
- (8) Amyot, M.; Mierle, G.; Lean, D.; Mcqueen, D. J. Effect of Solar Radiation on the Formation of Dissolved Gaseous Mercury in Temperate Lakes. *Geochim. Cosmochim. Acta* **1997**, *61* (5), 975–987. [https://doi.org/10.1016/S0016-7037\(96\)00390-0](https://doi.org/10.1016/S0016-7037(96)00390-0).
- (9) Allard, B.; Arsenie, I. Abiotic Reduction of Mercury by Humic Substances in Aquatic System – an Important Process for the Mercury Cycle. *Water, Air, Soil Pollut.* **1991**, *56* (1), 457–464. <https://doi.org/10.1007/BF00342291>.
- (10) Alberts, J. J.; Schindler, J. E.; Miller, R. W. Elemental Mercury Evolution Mediated by Humic Acid. *Science* (80-.). **1974**, *184* (4139), 895–898.
- (11) Berthon, G. The Stability Constants of Metal Complexes of Amino Acids With Polar Side Chains. *Pure Appl. Chem.* **1995**, *67* (7), 1117–1240. <https://doi.org/10.1351/pac199567071117>.
- (12) Drexel, R. T.; Haitzer, M.; Ryan, J. N.; Aiken, G. R.; Nagy, K. L. Mercury(II) Sorption to Two Florida Everglades Peats: Evidence for Strong and Weak Binding and Competition by Dissolved Organic Matter Released from the Peat. *Environ. Sci. Technol.* **2002**, *36* (19), 4058–4064. <https://doi.org/10.1021/es0114005>.
- (13) Haitzer, M.; Aiken, G. R.; Ryan, J. N. Binding of Mercury(II) to Dissolved Organic Matter: The Role of the Mercury-to-DOM Concentration Ratio. *Environ. Sci. Technol.* **2002**, *36* (16), 3564–3570. <https://doi.org/10.1021/es025699i>.

- (14) Song, Y.; Jiang, T.; Liem–Nguyen, V.; Sparrman, T.; Björn, E.; Skyllberg, U. Thermodynamics of Hg(II) Bonding to Thiol Groups in Suwannee River Natural Organic Matter Resolved by Competitive Ligand Exchange, Hg L III –Edge EXAFS and ¹H NMR Spectroscopy. *Environ. Sci. Technol.* **2018**, *52* (15), 8292–8301.
<https://doi.org/10.1021/acs.est.8b00919>.
- (15) Chen, H.; Johnston, R. C.; Mann, B. F.; Chu, R. K.; Tolic, N.; Parks, J. M.; Gu, B. Identification of Mercury and Dissolved Organic Matter Complexes Using Ultrahigh Resolution Mass Spectrometry. *Environ. Sci. Technol. Lett.* **2016**, No. 4, 59–65.
<https://doi.org/10.1021/acs.estlett.6b00460>.
- (16) Turro, N. J.; Ramamurthy, V.; Scaiano, J. C. *Modern Molecular Photochemistry of Organic Molecules*; University Science Book: Sausalito, California, 2010.
- (17) Salikhov, K. *Magnetic Isotope Effect in Radical Reactions – Introduction*; 1996.
- (18) Hore, P. J.; Mouritsen, H. The Radical–Pair Mechanism of Magnetoreception. *Annu. Rev. Biophys.* **2016**, *45* (1), 299–344.
<https://doi.org/10.1146/annurev-biophys-032116-094545>.
- (19) Wilkinson, F.; McGarvey, D. J.; Olea, A. F. Excited Triplet State Interactions with Molecular Oxygen: Influence of Charge Transfer on the Bimolecular Quenching Rate Constants and the Yields of Singlet Oxygen [O*(1.Δ.g)] for Substituted Naphthalenes in Various Solvents. *J. Phys. Chem.* **2005**, *98* (14), 3762–3769.
<https://doi.org/10.1021/j100065a035>.
- (20) Grewer, C.; Brauer, H. D. Mechanism of the Triplet–State Quenching by Molecular Oxygen in Solution. *J. Phys. Chem.* **1994**, *98* (16), 4230–4235.

<https://doi.org/10.1021/j100067a006>.

- (21) Baughman, G. .; Gordon, J. .; Lee Wolfe, N.; Zepp, R. G. Chemistry of Organomercurials in Aquatic Systems. *Epa-660/3-73- 012-Ecological Res. Ser.* **1973**.
- (22) Bigeleisen, J.; Wolfsberg, M. Theoretical and Experimental Aspects of Isotope Effects in Chemical Kinetics. *Adv. Chem. Phys.* **1958**, *1*, 15–76.
- (23) Bopp IV, C. J.; Lundstrom, C. C.; Johnson, T. M.; Glessner, J. J. G. Variations in $^{238}\text{U}/^{235}\text{U}$ in Uranium Ore Deposits: Isotopic Signatures of the U Reduction Process? *Geology* **2009**, *37* (7), 611–614. <https://doi.org/10.1130/G25550A.1>.
- (24) Andersen, M. B.; Stirling, C. H.; Weyer, S. Uranium Isotope Fractionation. *Rev. Mineral. Geochemistry* **2017**, *82* (1), 799–850. <https://doi.org/10.2138/rmg.2017.82.19>.
- (25) Basu, A.; Sanford, R. A.; Johnson, T. M.; Lundstrom, C. C.; Löffler, F. E. Uranium Isotopic Fractionation Factors during U(VI) Reduction by Bacterial Isolates. *Geochim. Cosmochim. Acta* **2014**, *136*, 100–113. <https://doi.org/10.1016/j.gca.2014.02.041>.
- (26) Dauphas, N.; Schauble, E. A. Mass Fractionation Laws , Mass-Independent Effects , and Isotopic Anomalies. *Annu. Rev. Earth Planet. Sci.* **2016**, *44*, 709–783. <https://doi.org/10.1146/annurev-earth-060115-012157>.
- (27) Kritee, K.; Motta, L. C.; Blum, J. D.; Tsui, M. T.; Reinfelder, J. R. Photo-Microbial Visible Light-Induced Magnetic Mass Independent Fractionation of Mercury in a Marine Microalga. *Earth Sp. Chem.* **2017**. <https://doi.org/10.1021/acsearthspacechem.7b00056>.
- (28) Müller, B. ChemEQL, User's Guide to Application. Swiss Federal Institute of Environmental Sciences and Technology: Dübendorf, Switzerland 2015.
- (29) Kritee, K.; Blum, J. D.; Johnson, M. W.; Bergquist, B. A.; Barkay, T. Mercury Stable

- Isotope Fractionation during Reduction of Hg(II) to Hg(0) by Mercury Resistant Microorganisms. *Environ. Sci. Technol.* **2007**, *41* (6), 1889–1895.
<https://doi.org/10.1021/es062019t>.
- (30) Blum, J. D.; Bergquist, B. A. Reporting of Variations in the Natural Isotopic Composition of Mercury. *Anal. Bioanal. Chem.* **2007**, *388* (2), 353–359.
<https://doi.org/10.1007/s00216-007-1236-9>.
- (31) Chandan, P.; Ghosh, S.; Bergquist, B. A. Mercury Isotope Fractionation during Aqueous Photoreduction of Monomethylmercury in the Presence of Dissolved Organic Matter. *Environ. Sci. Technol.* **2015**, *49* (1), 259–267. <https://doi.org/10.1021/es5034553>.
- (32) York, D.; Evensen, N. M.; López, M.; Delgado, J. D. B.; York, D.; Evensen, N. M.; Lo, M. Unified Equations for the Slope, Intercept, and Standard Errors of the Best Straight Line. **2004**, *367* (2004), 642–646. <https://doi.org/10.1119/1.1632486>.
- (33) Autschbach, J.; Ziegler, T. Nuclear Spin–Spin Coupling Constants from Regular Approximate Relativistic Density Functional Calculations. I. Formalism and Scalar Relativistic Results for Heavy Metal Compounds. *J. Chem. Phys.* **2000**, *113* (3), 936–947.
<https://doi.org/10.1063/1.481874>.
- (34) Saracino, G. A. A.; Tedeschi, A.; D’Errico, G.; Improta, R.; Franco, L.; Ruzzi, M.; Corvaia, C.; Barone, V. Solvent Polarity and PH Effects on the Magnetic Properties of Ionizable Nitroxide Radicals: A Combined Computational and Experimental Study of 2,2,5,5–Tetramethyl–3–Carboxypyrrolidine and 2,2,6,6–Tetramethyl–4–Carboxypiperidine Nitroxides. *J. Phys. Chem. A* **2002**, *106* (44), 10700–10706. <https://doi.org/10.1021/jp026492e>.

- (35) Schwartz, R. N.; Peric, M.; Smith, S. A.; Bales, B. L. Simple Test of the Effect of an Electric Field on the ^{14}N -Hyperfine Coupling Constant in Nitroxide Spin Probes. *J. Phys. Chem. B* **2002**, *101* (43), 8735–8739. <https://doi.org/10.1021/jp970555p>.
- (36) Turro, N. J. Influence of Nuclear Spin on Chemical Reactions: Magnetic Isotope and Magnetic Field Effects (A Review). *Proc. Natl. Acad. Sci. U. S. A.* **1983**, *80* (2), 609–621. <https://doi.org/10.1073/pnas.80.2.609>.
- (37) Kattnig, D. R.; Evans, E. W.; Déjean, V.; Dodson, C. A.; Wallace, M. I.; Mackenzie, S. R.; Timmel, C. R.; Hore, P. J. Chemical Amplification of Magnetic Field Effects Relevant to Avian Magnetoreception. *Nat. Chem.* **2016**, No. February. <https://doi.org/10.1038/nchem.2447>.
- (38) Goto, T.; Ikehata, A.; Morisawa, Y.; Ozaki, Y. Electronic Transitions of Protonated and Deprotonated Amino Acids in Aqueous Solution in the Region 145–300 nm Studied by Attenuated Total Reflection Far-Ultraviolet Spectroscopy. *J. Phys. Chem. A* **2013**, *117* (12), 2517–2528. <https://doi.org/10.1021/jp4008416>.
- (39) Lehnherr, I.; Louis, V. L. S. Importance of Ultraviolet Radiation in the Photodemethylation of Methylmercury in Freshwater Ecosystems. *Environ. Sci. Technol.* **2009**, *43* (15), 5692–5698.
- (40) Rose, C. H.; Ghosh, S.; Blum, J. D.; Bergquist, B. A. Effects of Ultraviolet Radiation on Mercury Isotope Fractionation during Photo-Reduction for Inorganic and Organic Mercury Species. *Chem. Geol.* **2015**, *405*, 102–111.
- (41) Zheng, W.; Hintelmann, H. Nuclear Field Shift Effect in Isotope Fractionation of Mercury during Abiotic Reduction in the Absence of Light. *J. Phys. Chem. A* **2010**, *114* (12),

- 4238–4245. <https://doi.org/10.1021/jp910353y>.
- (42) Griffiths, T. R.; Anderson, R. A. Structure of Mercury(II) Halides in Solution and Assignment of Their Resolved Electronic Spectra. *J. Chem. Soc. Faraday Trans. 2 Mol. Chem. Phys.* **1979**, *75*, 957–970. <https://doi.org/10.1039/F29797500957>.
- (43) Sitkiewicz, S. P.; Rivero, D.; Oliva–Enrich, J. M.; Saiz–Lopez, A.; Roca–Sanjuán, D. Ab Initio Quantum–Chemical Computations of the Absorption Cross Sections of HgX₂ and HgXY (X, y = Cl, Br, and I): Molecules of Interest in the Earth’s Atmosphere. *Phys. Chem. Chem. Phys.* **2019**, *21* (1), 455–467. <https://doi.org/10.1039/c8cp06160b>.
- (44) Turro, N. J.; Weed, G. C. Micellar Systems as “Supercages” for Reactions of Geminate Radical Pairs. Magnetic Effects. *J. Am. Chem. Soc.* **1983**, *105* (7), 1861–1868. <https://doi.org/10.1021/ja00345a031>.
- (45) Turro, N. J. From Boiling Stones to Smart Crystals: Supramolecular and Magnetic Isotope Control of Radical–Radical Reactions in Zeolites. *Acc. Chem. Res.* **2000**, *33* (9), 637–646. <https://doi.org/10.1021/ar980103a>.
- (46) Buchachenko, A. L. Magnetic Isotope Effect: Nuclear Spin Control of Chemical Reactions. *J. Phys. Chem. A* **2001**, *105* (44), 9995–10011. <https://doi.org/10.1021/jp011261d>.
- (47) Step, E. N.; Tarasov, V. F.; Buchachenko, A. L. ²⁹Si Magnetic Isotope Effects in the Photolysis of Silyl Ketones. *Chem. Phys. Lett.* **1988**, *144* (5–6), 523–526. [https://doi.org/10.1016/0009–2614\(88\)87308–1](https://doi.org/10.1016/0009–2614(88)87308–1).
- (48) Kritee, K.; Barkay, T.; Blum, J. D. Mass Dependent Stable Isotope Fractionation of Mercury during Mer Mediated Microbial Degradation of Monomethylmercury. *Geochim.*

- Cosmochim. Acta* **2009**, 73 (5), 1285–1296. <https://doi.org/10.1016/j.gca.2008.11.038>.
- (49) Li, M.; Schartup, A. T.; Valberg, A. P.; Ewald, J. D.; Krabbenhoft, D. P.; Yin, R.; Balcom, P. H.; Sunderland, E. M. Environmental Origins of Methylmercury Accumulated in Subarctic Estuarine Fish Indicated by Mercury Stable Isotopes. *Environ. Sci. Technol.* **2016**, 50 (21), 11559–11568. <https://doi.org/10.1021/acs.est.6b03206>.
- (50) Point, D.; Sonke, J. E.; Day, R. D.; Roseneau, D. G.; Hobson, K. a.; Vander Pol, S. S.; Moors, a. J.; Pugh, R. S.; Donard, O. F. X.; Becker, P. R. Methylmercury Photodegradation Influenced by Sea–Ice Cover in Arctic Marine Ecosystems. *Nat. Geosci.* **2011**, 4 (3), 188–194. <https://doi.org/10.1038/ngeo1049>.
- (51) Blum, J. D.; Popp, B. N.; Drazen, J. C.; Anela Choy, C.; Johnson, M. W. Methylmercury Production below the Mixed Layer in the North Pacific Ocean. *Nat. Geosci.* **2013**, 6 (10), 879–884. <https://doi.org/10.1038/ngeo1918>.
- (52) Kwon, S. Y.; Blum, J. D.; Carvan, M. J.; Basu, N.; Head, J. a; Madenjian, C. P.; David, S. R. Absence of Fractionation of Mercury Isotopes during Trophic Transfer of Methylmercury to Freshwater Fish in Captivity Absence of Fractionation of Mercury Isotopes during Trophic Transfer of Methylmercury to Freshwater Fish in Captivity School of Natural R. *Environ. Sci. Technol.* **2012**, 46, 7527–7534.
- (53) Lamborg, C. H.; Tseng, C. M.; Fitzgerald, W. F.; Balcom, P. H.; Hammerschmidt, C. R. Determination of the Mercury Complexation Characteristics of Dissolved Organic Matter in Natural Waters with “Reducible Hg” Titrations. *Environ. Sci. Technol.* **2003**, 37 (15), 3316–3322. <https://doi.org/10.1021/es0264394>.
- (54) Sun, G.; Sommar, J.; Feng, X.; Lin, C. J.; Ge, M.; Wang, W.; Yin, R.; Fu, X.; Shang, L.

- Mass-Dependent and -Independent Fractionation of Mercury Isotope during Gas-Phase Oxidation of Elemental Mercury Vapor by Atomic Cl and Br. *Environ. Sci. Technol.* **2016**, *50* (17), 9232–9241. <https://doi.org/10.1021/acs.est.6b01668>.
- (55) Estrade, N.; Carignan, J.; Sonke, J. E.; Donard, O. F. X. Mercury Isotope Fractionation during Liquid-Vapor Evaporation Experiments. *Geochim. Cosmochim. Acta* **2009**, *73* (10), 2693–2711. <https://doi.org/10.1016/j.gca.2009.01.024>.
- (56) Spörkel, L.; Cui, G.; Koslowski, A.; Thiel, W. Nonequilibrium H/D Isotope Effects from Trajectory-Based Nonadiabatic Dynamics. *J. Phys. Chem. A* **2014**, *118* (1), 152–157. <https://doi.org/10.1021/jp4120749>.

4.5 Supporting Information

Table S4.1. Experimental details of Hg(II) photoreduction experiments in the presence of serine, cysteine, and ethylenediamine

Ligand	Date	Treatment	Expt. Duration (hr)	%Reduction	Rate Constant (day ⁻¹)	Secondary Reaction Rate (day ⁻¹)	Avg. T (°C)	Max T (°C)
Cysteine 0.4 mM	Jun-30-2011	pH 7 Oxic	10.82	31.54	0.84		24	30
		pH 7 Oxic Vis	10.81	0.04	0.00			
	May-18-2012	pH 7 Oxic	18.28	13.91	0.18		18	23
		pH 7 Anoxic	18.35	39.04	0.62			
		pH 3 Oxic	18.23	21.09	0.27			
		pH 3 Anoxic	18.38	31.73	0.39			
	Jul-17-2013	pH 7 Oxic	7.03	46.54	1.19		30	34
		pH 7 Anoxic	6.55	13.75	0.56			
		pH 3 Oxic	15.03	13.53	0.21			
		pH 3 Anoxic	6.55	16.10	0.59			
Aug-23-2012	pH 7 Oxic	60.45	96.78	1.36		25	30	
Serine 0.4 mM	Sept-10-2011	low- pH 7 Oxic	8.72	89.95	Not Determined	Not Determined	24	27
		low-pH 7 Anoxic	8.62	79.11	6.10	0.064 ^a		
		low-pH 7 Oxic Vis	8.92	27.51	0.87			
		low-pH 7 Anoxic Vis	8.80	52.23	2.05			
		low pH 3 Anoxic	8.50	80.92	4.81			
		low pH 3 Anoxic Vis	8.68	5.62	0.16			
Serine 4.0 mM	Jun-30-2011	pH 7 Oxic	10.83	93.20	32.94	1.61	24	30
		pH 7 Oxic Vis	10.82	83.09	4.21	Not Determined		
	Sept-10-2011	pH 7 Oxic	7.70	87.25	26.95	1.11	24	27
		pH 7 Anoxic	6.73	81.66	6.10	0.064 ^a		
		pH 7 Oxic Vis	8.13	70.45	3.69			
		pH 7 Anoxic Vis	7.93	70.57	3.43			
		pH 3 Anoxic	7.68	55.85	2.62			
		pH 3 Anoxic Vis (nitrate)	8.15	19.23	0.65			
Aug-23-2012	pH 7 Oxic	26.87	99.41	Not Determined	1.08	25	30	
Ethylenediamine 4.0 mM	May-18-2012	pH 7 Oxic	18.22	71.17	2.54		18	23
		pH 7 Oxic	17.53	89.66	3.06			

a the secondary reduction rate was determined as an average of both experiments

Table S4.2 Dissolved Hg(II) species in solution

Ligand	Hg Species	Treatment (%Hg Species)			
		pH 7 Oxidic	pH 7 Anoxic	pH 3 Oxidic	pH 3 Anoxic
0.4 mM Cysteine	Hg(HCys) ₂	96.5	96.5	96.5	96.5
	[Hg(Cys) ₂] ⁻²	3.5	3.5	3.5	3.5
	[Hg(Cys) ₃] ⁻⁴	2.6x10 ⁻¹⁰	2.6x10 ⁻¹⁰	1.1x10 ⁻¹⁷	1.1x10 ⁻¹⁷
	Hg(Cys) ₄	4.6x10 ⁻¹⁷	4.6x10 ⁻¹⁷	8.5x10 ⁻³²	8.5x10 ⁻³²
	HgCys	1.3x10 ⁻²¹	1.31x10 ⁻²¹	2.64x10 ⁻¹⁴	2.64x10 ⁻¹⁴
	HgCl ₂	0	1.9x10 ⁻³⁵	0	6.3x10 ⁻⁰⁶
	Hg(OH) ₂	8.0x10 ⁻²⁰	8.0x10 ⁻²⁰	1.7x10 ⁻¹²	1.7x10 ⁻¹²
	Hg(NO ₃) ₂	1.9x10 ⁻³⁵	0	1.0x10 ⁻¹⁷	0
0.4 mM Serine	HgSer	0.3	0.3		19.4
	[Hg(Ser) ₂] ⁻²	91.3	91.3		2.3
	HgCl ₂	0	1.2		76.8
	Hg(OH) ₂	8.37	8.27		0.2
	Hg(NO ₃) ₂	2.02x10 ⁻¹⁵	0		0
4 mM Serine	HgSer	3.3x10 ⁻²	3.3x10 ⁻²		40
	[Hg(Ser) ₂] ⁻²	99.9	99.9		50
	HgCl ₂	0	1.3x10 ⁻²		16
	Hg(OH) ₂	9.1x10 ⁻²	9.1x10 ⁻²		4.0x10 ⁻²
	Hg(NO ₃) ₂	2.0x10 ⁻¹⁷	0		0
4 mM Ethylenediamine	Hg(en) ⁺²	2.3x10 ⁻²			
	[Hg(en) ₂] ⁺²	70.6			
	[HgOH(en) ₂] ⁺²	29			
	[HgH(en) ₂] ⁺²	0.3			
	HgCl ₂	0			
	Hg(OH) ₂	4.7x10 ⁻³			
Hg(NO ₃) ₂	1.2x10 ⁻¹⁸				

Stock Hg(II) solutions

HgCl ₂ , preserved in 1 % BrCl	250 ppm
Hg(NO ₃) ₂ , preserved in 2% HNO ₃	100 ppm

Table S4.3a. Hg stable isotope values for cysteine experiments

Date	Treatment	time(hrs)	[Hg] ng/g	[Hg] uM	f	$\delta^{202}\text{Hg}$	$\delta^{204}\text{Hg}$	$\delta^{200}\text{Hg}$	$\delta^{201}\text{Hg}$	$\delta^{199}\text{Hg}$	$\Delta^{199}\text{Hg}$	$\Delta^{201}\text{Hg}$
Jun-30-2011	pH 7 Oxid Vis	0.00	39.40	0.20	1.00							
		10.81	39.20	0.20	0.99							
Aug-23-2012		0.00	48.62	0.24	1.00	-0.66	-0.97	-0.35	-0.58	-0.22	-0.05	-0.08
		9.95	34.96	0.17	0.72	-0.21	-0.38	-0.06	-0.22	-0.12	-0.06	-0.06
		15.28	28.26	0.14	0.58	-0.23	-0.29	-0.12	-0.31	-0.24	-0.18	-0.13
		36.02	10.82	0.05	0.22	-0.26	-0.32	-0.14	-0.63	-0.47	-0.40	-0.44
		60.45	1.56	0.01	0.03	-0.09	-0.16	-0.04	-0.93	-0.92	-0.90	-0.86
Jul-17-2013	pH 7 Oxid	0.00	38.68	0.19	1.00	-0.46	-0.69	-0.21	-0.37	-0.12	0.00	0.00
		0.54	38.06	0.19	0.98							
		2.21	33.32	0.17	0.86							
		4.38	34.35	0.17	0.89							
		7.03	28.18	0.14	0.73							
		12.30	20.68	0.10	0.53	-0.20	-0.15	-0.13	-0.07	0.24	-0.08	-0.06
May-18-2012	pH 7 Oxid	0.00	42.55	0.21	1.00							
		1.42	40.47	0.20	0.95							
		10.15	38.60	0.19	0.91							
		15.28	37.26	0.19	0.88							
		18.28	36.63	0.18	0.86							
Jun-30-2011	pH 7 Oxid	0.00	39.00	0.19	1.00							
		1.33	38.40	0.19	0.98	-0.84	-1.25	-0.45	-0.67	-0.17	0.04	-0.04
		4.87	30.60	0.15	0.78	-0.72	-1.09	-0.34	-0.54	-0.17	0.02	0.02
		6.33	31.20	0.16	0.80	-0.55	-0.81	-0.25	-0.43	-0.12	0.01	-0.02
		9.42	28.20	0.14	0.72	-0.42	-0.63	-0.18	-0.33	-0.12	-0.01	-0.01
		10.82	26.70	0.13	0.68	-0.44	-0.69	-0.18	-0.39	-0.14	-0.03	-0.06
Jul-17-2013	pH 7 Anoxic	0.00	43.36	0.22	1.00	-0.46	-0.69	-0.21	-0.37	-0.12	0.00	0.00
		0.46	43.00	0.21	0.99							
		2.13	41.68	0.21	0.96							
		4.30	38.99	0.19	0.90							
		6.55	37.40	0.19	0.86	-0.19	-0.22	-0.11	-0.04	0.12	0.168	0.10
May-18-2012	pH 7 Anoxic	0.00	38.24	0.19	1.00	-0.91	-1.36	-0.43	-0.68	-0.22	0.01	0.01
		5.22	33.35	0.17	0.87	-0.85	-1.36	-0.46	-0.53	-0.08	0.133	0.11
		10.30	30.81	0.15	0.81							
		12.75	28.76	0.14	0.75	-0.64	-1.01	-0.35	-0.19	0.20	0.37	0.29
		15.47	26.10	0.13	0.68	-0.50	-0.79	-0.22	-0.02	0.41	0.54	0.36
		18.35	23.31	0.12	0.61	-0.49	-0.64	-0.16	0.12	0.39	0.52	0.49
Jul-17-2013	pH 7 Anoxic	0.00	44.87	0.22	1.00	-0.46	-0.69	-0.21	-0.37	-0.12	0.00	0.00
		2.15	42.47	0.21	0.95							
		6.55	37.65	0.19	0.84	-0.30	-0.39	-0.17	-0.36	-0.26	-0.182	-0.131
May-18-2012	pH 3 Anoxic	0.00	39.95	0.20	1.00	-0.93	-1.45	-0.48	-0.75	-0.16	0.07	-0.06
		5.08	36.05	0.18	0.90	-0.91	-1.38	-0.50	-0.77	-0.26	-0.03	-0.08
		10.25	32.70	0.16	0.82							
		15.40	30.40	0.15	0.76							
		18.38	27.27	0.14	0.68	-0.61	-0.98	-0.29	-0.52	-0.30	-0.147	-0.06
Jul-17-2013	pH 3 Oxid	0.00	40.50	0.20	1.00	-0.44	-0.97	-0.29	-0.44	-0.15	0.01	0.02
		0.51	40.30	0.20	0.99							
		2.21	39.80	0.20	0.98							
		4.28	39.10	0.19	0.97							
		7.03	38.50	0.19	0.95							
		15.03	35.02	0.17	0.86	-0.34	-0.81	-0.27	-0.34	-0.05	0.10	0.08
May-18-2012	pH 3 Oxid	0.00	43.00	0.21	1.00							
		0.58	42.67	0.21	0.99							
		5.08	41.80	0.21	0.97							
		10.25	36.87	0.18	0.86							
		15.37	35.11	0.18	0.82							
		18.23	33.93	0.17	0.79							

Table S4.3b Hg stable isotope values for the serine experiments at 400 mM and low serine at 0.4 mM

Date	Treatment	time(hrs)	[Hg] ng/g	[Hg] uM	f	$\delta^{202}\text{Hg}$	$\delta^{204}\text{Hg}$	$\delta^{200}\text{Hg}$	$\delta^{201}\text{Hg}$	$\delta^{199}\text{Hg}$	$\Delta^{199}\text{Hg}$	$\Delta^{201}\text{Hg}$
Jun-30-2011	pH 7 Oxid	0.00	33.80	0.17	1.00	-0.46	-0.69	-0.25	-0.43	-0.11	0.00	-0.08
		1.35	5.30	0.03	0.16	2.64	4.03	1.34	2.24	0.89	0.23	0.25
		3.03	3.90	0.02	0.12	2.65	3.93	1.32	2.56	1.31	0.64	0.56
		4.88	3.20	0.02	0.09	2.69	4.04	1.32	2.73	1.45	0.78	0.71
		9.40	2.40	0.01	0.07	2.77	4.17	1.36	2.78	1.54	0.84	0.70
		10.83	2.30	0.01	0.07	2.83	4.26	1.42	2.82	1.66	0.95	0.69
Aug-23-2012	pH 7 Oxid	0.00	37.45	0.19	1.00	-0.26	-0.40	-0.14	-0.26	-0.10	-0.04	-0.07
		5.27	1.32	0.01	0.04	3.56	5.28	1.78	4.58	2.93	2.03	1.91
		6.70	1.20	0.01	0.03	3.45	5.23	1.68	4.55	2.91	2.04	1.96
		15.95	0.31	0.00	0.01	2.82	4.33	1.51	5.83	4.92	4.21	3.71
		21.20	0.25	0.00	0.01	2.51	3.90	1.21	5.24	4.40	3.77	3.35
		26.87	0.22	0.00	0.01							
Jun-30-2011	pH 7 Oxid Vis	0.00	33.70	0.17	1.00	-0.52	-0.88	-0.19	-0.44	-0.09	0.04	-0.05
		3.07	24.60	0.12	0.73	0.07	0.07	0.03	0.04	-0.01	-0.07	-0.06
		4.88	15.00	0.07	0.45	1.40	2.08	0.75	1.00	0.28	-0.02	-0.01
		6.37	12.70	0.06	0.38	1.48	2.28	0.74	1.04	0.22	-0.15	-0.08
		8.12	7.60	0.04	0.23	2.51	3.80	1.25	1.79	0.52	-0.11	-0.10
		10.82	5.70	0.03	0.17	2.79	4.19	1.37	2.06	0.65	-0.06	-0.04
Sept-10-2011	pH 7 Oxid	0.00	17.80	0.09	1.00	0.80	1.12	0.46	0.52	0.14	-0.06	-0.09
		0.42	12.40	0.06	0.70	1.21	1.91	0.54	0.72	0.08	-0.22	-0.19
		0.82	7.10	0.04	0.40	2.19	3.27	1.09	1.56	0.39	-0.17	-0.09
		3.15	2.80	0.01	0.16	3.04	4.53	1.47	2.49	0.93	0.16	0.20
		7.70	2.27	0.01	0.13	3.01	4.47	1.50	2.42	1.01	0.25	0.16
	low pH 7 Oxid	0.00	28.27	0.14	1.00	-0.59	-0.95	-0.31	-0.48	-0.14	0.01	-0.04
		8.72	2.84	0.01	0.10	1.10	1.67	0.57	5.28	5.09	5.54	5.18
	pH 7 Anoxic	0.00	26.21	0.13	1.00	-0.12	-0.19	-0.02	-0.13	-0.01	0.02	-0.04
		0.88	9.95	0.05	0.38	2.07	3.15	1.02	1.48	0.45	-0.08	-0.07
		3.10	5.02	0.03	0.19	2.89	4.38	1.43	2.481	0.98	0.25	0.30
		4.92	4.47	0.02	0.17	3.03	4.53	1.47	2.73	1.27	0.45	0.51
		6.73	5.02	0.03	0.19	2.97	4.31	1.50	2.52	1.10	0.36	0.29
	low pH 7 Anoxic	0.00	23.94	0.12	1.00	-0.56	-0.87	-0.29	-0.48	-0.17	-0.03	-0.06
		0.92	16.70	0.08	0.70	0.15	0.32	0.07	-0.04	-0.17	-0.21	-0.16
		3.98	5.10	0.03	0.21	1.14	1.68	0.55	5.32	5.04	4.75	4.46
	pH 7 Oxid Vis	0.00	17.60	0.09	1.00	0.42	0.67	0.16	0.28	0.02	-0.08	-0.03
		1.43	13.40	0.07	0.76	1.01	1.54	0.49	0.67	0.07	-0.18	-0.09
		2.75	10.40	0.05	0.59	1.43	2.17	0.75	0.95	0.20	-0.16	-0.13
		5.73	6.20	0.03	0.35	2.36	3.55	1.16	1.62	0.37	-0.23	-0.16
		8.13	5.20	0.03	0.30	2.39	3.57	1.21	1.72	0.42	-0.18	-0.08
	low pH 7 Oxid Vis	0.00	26.90	0.13	1.00	-0.56	-0.70	-0.34	-0.43	-0.17	-0.03	-0.01
		8.92	19.50	0.10	0.72	0.30	0.40	0.15	0.17	0.02	-0.05	-0.05
	pH 7 Anoxic Vis	0.00	35.00	0.17	1.00	-0.79	-1.20	-0.37	-0.63	-0.24	-0.04	-0.03
		1.52	20.70	0.10	0.59	0.51	0.75	0.26	0.30	0.07	-0.06	-0.09
		2.80	18.00	0.09	0.51	0.69	1.01	0.29	0.41	0.09	-0.09	-0.11
		4.27	14.70	0.07	0.42	1.12	1.65	0.53	0.74	0.13	-0.15	-0.10
		5.77	12.60	0.06	0.36	1.45	2.21	0.72	1.03	0.22	-0.14	-0.06
	low pH 7 Anoxic Vis	7.93	10.30	0.05	0.29	1.90	2.84	0.91	1.34	0.305	-0.18	-0.09
		0.00	27.63	0.14	1.00	-0.62	-1.02	-0.29	-0.43	-0.14	0.01	-0.10
		2.53	22.10	0.11	0.80	-0.09	-0.14	-0.01	-0.32	-0.28	-0.25	-0.26
		5.47	16.40	0.08	0.59	0.40	0.50	0.16	0.03	-0.16	-0.26	-0.27
	pH 3 Anoxic	8.80	13.20	0.07	0.48	1.09	1.59	0.58	0.81	0.26	-0.01	-0.03
		0.00	31.03	0.15	1.00	-0.45	-0.74	-0.22	-0.37	-0.12	-0.01	-0.03
		0.82	28.30	0.14	0.91	-0.34	-0.59	-0.19	-0.37	-0.19	-0.11	-0.10
		3.10	21.80	0.11	0.70	0.26	0.44	0.15	0.17	-0.01	-0.08	-0.02
		5.87	15.70	0.08	0.51	0.95	1.49	0.50	1.13	0.72	0.48	0.41
	low pH 3 Anoxic	7.68	13.70	0.07	0.44	1.31	1.89	0.66	1.94	1.37	1.04	0.96
		0.00	30.67	0.15	1.00	-0.70	-1.04	-0.31	-0.51	-0.18	0.00	0.01
		0.83	29.50	0.15	0.96	-0.53	-0.81	-0.26	-0.50	-0.24	-0.10	-0.10
		4.27	14.50	0.07	0.47	1.17	1.67	0.57	0.95	0.38	0.09	0.07
		8.50	5.85	0.03	0.19	2.26	3.39	1.15	3.50	2.36	1.79	1.80
	pH 3 Anoxic Vis (nitrate)	0.00	28.86	0.14	1.00	-0.39	-0.54	-0.18	-0.39	-0.08	0.01	-0.09
		3.15	26.50	0.13	0.92	-0.31	-0.45	-0.13	-0.22	-0.17	-0.09	0.02
		4.62	24.10	0.12	0.84	0.00	0.01	0.01	-0.07	-0.02	-0.09	0.02
		5.98	24.30	0.12	0.84	-0.04	-0.01	0.03	-0.04	-0.04	-0.03	-0.01
		8.15	23.31	0.12	0.81	0.05	0.17	0.03	-0.05	-0.08	-0.09	-0.09
	low pH 3 Anoxic Vis	0.00	33.80	0.17	1.00	-0.86	-1.30	-0.43	-0.66	-0.18	0.03	-0.02
		4.08	33.30	0.17	0.99	-0.79	-1.12	-0.38	-0.61	-0.23	-0.03	-0.02
		8.68	31.90	0.16	0.94	-0.51	-0.77	-0.28	-0.40	-0.17	-0.04	-0.02

Table S4.3c Hg stable isotope values for the ethylenediamine experiments. Reference standard Hg isotope data. Percent of Hg reduced at the shift between NVE to MIE in the serine experiments

Date	Treatment	time(hrs)	[Hg] ng/g	[Hg] uM	f	$\delta^{202}\text{Hg}$	$\delta^{204}\text{Hg}$	$\delta^{200}\text{Hg}$	$\delta^{201}\text{Hg}$	$\delta^{199}\text{Hg}$	$\Delta^{198}\text{Hg}$	$\Delta^{201}\text{Hg}$								
May-18-2012	pH 7 Oxic	0.0	15.91	0.08	1.00	-0.22	-0.38	-0.05	-0.11	-0.02	0.04	0.06								
		3.5	6.06	0.03	0.38															
		10.63	4.58	0.02	0.29															
		18.22	4.59	0.02	0.29	2.63	3.89	1.30	1.76	0.39	-0.28	-0.22								
		0.00	22.19	0.11	1.00	0.17	0.15	0.07	0.05	0.01	-0.03	-0.08								
		0.50	18.90	0.09	0.85	0.48	0.48	0.32	0.28	0.02	-0.11	-0.08								
		3.00	9.58	0.05	0.43	1.46	2.21	0.79	1.01	0.16	-0.20	-0.08								
		10.00	5.80	0.03	0.26	1.84	2.76	0.89	1.16	0.20	-0.26	-0.22								
		11.98	3.20	0.02	0.14	1.85	2.49	0.83	0.77	-0.05	-0.52	-0.61								
		17.53	2.29	0.01	0.10	1.86	2.85	0.95	1.00	0.16	-0.31	-0.40								
Sessions	Total Replicates	Average	δ^{204}	2SD	δ^{202}	2SD	δ^{201}	2SD	δ^{199}	2SD	Δ^{204}	2SD	Δ^{201}	2SD	Δ^{200}	2SD	Δ^{199}	2SD		
16	90		-0.86	0.08	-0.57	0.07	-0.47	0.06	-0.28	0.04	-0.16	0.05	0.00	0.10	-0.04	0.02	0.01	0.02	-0.02	0.04
Date	Treatment	% Reduced (onset of MIE)																		
Jun-30-2011	pH 7 Oxic	73.69																		
Aug-23-2012	pH 7 Oxic	70.83																		
Sept-10-2011	pH 7 Oxic	76.44																		
	pH 7 Anoxic	75.92																		
	low pH 7 Oxic	57.73																		
	low pH 7 Anoxic	57.73																		
	pH 3 Anoxic	40.52																		
	low pH 3 Anoxic	58.79																		

Table S4.4 MDF and MIF Fractionation factors for all experiments

Ligand	Treatment	ϵ^{MDF} (‰)	ϵ^{MIF} (‰)
Cysteine	pH 7 Oxic	1.04±0.09	1.15±0.11
	pH 7 Anoxic		0.25±8E-2
	pH 3 Oxic		0.09±0.20
	pH 3 Anoxic	Not enough reduction of Hg(II)	
Serine	pH 7 Oxic	1.81±0.04	
	pH 7 Anoxic		
	pH 7 Oxic Vis		
	pH 7 Anoxic Vis		
	pH 3 Anoxic Vis (nitrate)		
Ethylenediamine	pH 7 Oxic	2.11±0.2	0.16±0.03

Table S4.5 Summary of fractionation factors for visible serine experiments.

Isotope Pair	ϵ^{MDF}	Standard Deviation	R^2
199/198	0.39	0.03	0.86
200/198	0.93	0.03	0.96
201/198	1.41	0.04	0.96
202/198	1.81	0.04	0.98
204/198	2.94	0.08	0.97

Chapter 5 Methylmercury Photodecomposition and Incorporation in Marine Plankton

Co-authored with Joel D. Blum, Brian N. Popp, John R. Reinfelder, Paul M. Zimmerman, and Marcus W. Johnson. Methylmercury photodecomposition and incorporation in marine plankton. *Nature Geoscience*. **Submitted**

Abstract: Monomethylmercury (MeHg) is a highly toxic form of mercury (Hg) that accumulates in marine food webs reaching high enough levels in fish to be a public health concern. Despite decades of research, there is still an incomplete understanding of the marine biogeochemical cycle of MeHg, including how it enters and accumulates in pelagic food webs. Here we use *ab initio* methods to investigate the photoreactivity of MeHg complexes in seawater, together with mercury stable isotope ratios from laboratory and shipboard photodegradation experiments and in zooplankton from the central tropical and subtropical North Pacific Ocean. We trace the pathways by which MeHg is incorporated into planktonic organisms at the base of pelagic marine food webs. Significant differences in the Hg stable isotope composition ($\delta^{202}\text{Hg}$, $\Delta^{199}\text{Hg}$, and $\Delta^{201}\text{Hg}$) between small versus intermediate and large size classes are documented for zooplankton from the upper layer of the photic zone (25 m) of the N. Pacific Ocean. Our results suggest that much of the MeHg accumulated by phytoplankton and small zooplankton in the upper layers of the ocean's photic zone is not transferred to large consumers, while MeHg accumulated by phytoplankton and zooplankton living at the base of the euphotic zone is retained in the planktonic food web and effectively transferred to higher trophic level consumers. These results illuminate a critical link in

the accumulation of MeHg in oceanic food webs and inform efforts to trace the accumulation of pollutant Hg in marine seafood.

5.1 Introduction

Seafood is the primary route of human exposure to MeHg and consumption advisories for fish with the highest levels of MeHg are currently in place around the world¹. Concentrations of MeHg in marine fish are controlled in part by the accumulation of dissolved MeHg in planktonic marine organisms, which represents the largest enrichment step in marine food webs^{2,3}. Understanding the environmental and biological controls of MeHg in fish therefore depends on tracing the uptake of MeHg in marine plankton. This is challenging because of incomplete knowledge concerning the transformations and bioavailability of various forms of dissolved MeHg in seawater and the complexity of marine planktonic food webs. Some of these challenges may be overcome through the use of Hg stable isotopes to trace the transformations and bioaccumulation of Hg in the marine environment.⁴⁻¹⁰

Hg stable isotopes display mass dependent fractionation (MDF; represented by $\delta^{202}\text{Hg}$ values) during a wide range of abiotic and biotic chemical reactions. Hg also undergoes odd-isotope mass independent fractionation (MIF, represented by $\Delta^{199}\text{Hg}$ values) caused by the nuclear volume effect or the magnetic isotope effect. Photochemical reactions involving Hg result in large $\Delta^{199}\text{Hg}$ and $\Delta^{201}\text{Hg}$ values ($>0.4\%$) in products or reactants via the magnetic isotope effect (MIE).⁶ It has been demonstrated that $\Delta^{199}\text{Hg}$ and $\Delta^{201}\text{Hg}$ values in fish are inherited from the partial photodecomposition of MeHg in surface waters prior to incorporation at the base of aquatic food webs.^{4,5,11} This suggests that $\Delta^{199}\text{Hg}$ values preserved in marine fish may be used to identify the bioavailable pools and therefore the sources of MeHg to marine organisms. However, the isotopic compositions of various complexes of MeHg are currently unknown, and all of the Hg stable

isotope photochemistry experiments carried out prior to this study used fresh water, terrestrial DOM, and relatively high concentrations of MeHg, which may not accurately represent photochemical degradation in marine ecosystems.

Here we investigate the mechanisms of MeHg photochemical decomposition in pelagic marine waters by: 1) performing high level electronic structure calculations^{12,13} of environmentally relevant MeHg complexes to determine their photochemical reactivities; 2) conducting photodegradation experiments in seawater; and 3) analyzing the Hg isotopic compositions of zooplankton from the Central North Pacific Ocean. Our results provide insight into the mechanisms by which various chemical forms of MeHg undergo photodecomposition in marine waters, and in so doing, identify the bioavailable forms of MeHg and the dominant pathways by which MeHg is accumulated in planktonic organisms at the base of pelagic marine food webs.

5.2 Photochemically reactive complexes of MeHg in seawater

In our efforts to understand the accumulation of MeHg by marine organisms it is important to understand the dominant photochemical mechanism(s) that degrade(s) the pool of available MeHg. The photodecomposition of MeHg has been thought to be mediated by DOM, especially the thiol binding sites, but residual photodegraded MeHg coordinated with DOM is not readily taken up by phytoplankton.¹⁴⁻¹⁸ In marine waters the elevated ionic strength, salinity, and low DOM concentrations may inhibit Hg coordination to DOM¹⁹ and the photodecomposition may be controlled by low molecular weight (LMW) MeHg species. In seawater, the majority of MeHg may be in the MeHgCl form,¹⁹ but fast ligand exchange of MeHg complexes^{20,21} may result in equilibrium with MeHgOH, MeHg⁺, MeHgBr and MeHgOH₂⁺. Experimental and environmental observations show that the photodegradation of aqueous complexes of MeHg results in odd-MIF due to the magnetic isotope effect (MIE), however, there is a lack of information about the

photophysics of relevant complexes of MeHg in seawater. MeHg complexes may be degraded by either direct or indirect photolysis. Indirect photolysis involves a secondary reaction with a photochemically generated reactive intermediate, such as singlet oxygen²², while direct photolysis occurs via the absorption of a photon by the MeHg complex leading to homolytic cleavage of the Hg-C bond.^{23,24} Theoretical considerations and experimental results^{6,25} show that direct photolysis leading to the formation of correlated solvent-separated radical pair intermediates^{26,27} is required to produce the large extents of odd-MIF (>0.04 ‰) associated with MIE during photochemical transformations of Hg, while other reaction pathways (e.g. NVE) do not produce such large odd-MIF signatures.^{27,28} Using high level electronic structure simulations^{12,13} we determined the absorption energies of various MeHg complexes (Table 1) to examine the plausibility of their reaction by direct photolysis.

The results of these simulations demonstrate that MeHgX halides (X=Cl or Br) and MeHgOH₂⁺ are not available for direct photolysis because they do not absorb light in the natural sunlight spectrum (290-780 nm) and will not result in the MIE. While MeHgOH and MeHg⁺ are available for direct photolysis, these complexes have peak excitation energies to the singlet state (210 and 226 nm, respectively) slightly outside of the range of natural sunlight, but it has been documented that the absorption peaks of MeHgOH and MeHg⁺ complexes in water are broad (± 45 nm²⁴). In addition, the triplet states (227 and 366 nm, respectively) of these complexes are within or close to the UVA region and may mix with the singlet state, due to high spin-orbital coupling predicted for Hg.^{29,30} These results are supported by recent experiments that demonstrated fast photodegradation of MeHg in deionized water with 280-320 nm wavelengths.³¹

Our electronic structure simulations also demonstrate that MeHg-thiols are available for direct photolysis in natural sunlight. The excitation energies of MeHg complexed to a single

cysteine are slightly outside the range of sunlight (singlet 263 nm and triplet 270 nm), however, due to extensive peak broadening it has been shown that the absorption tail of MeHg-thiol complexes extends to >290 nm.²⁴ Using SCH₃ as a truncated thiol model of cysteine, we find that the singlet and triplet transitions of MeHg(SCH₃)₂ and MeHg(SCH₃)₃ are within the natural light spectrum (Table 1). There is very limited information about the complexation constants of MeHg to multiple thiol ligands, but there is strong evidence that, at elevated thiol concentrations and alkaline conditions, Hg will tend to form higher coordination complexes.³² It is unlikely that there is a high enough thiol concentration or sufficient S moieties in natural waters for MeHg to form higher coordination number complexes with DOM. However, marine phytoplankton have elevated intracellular thiol concentrations^{33,34} and this may produce appropriate conditions to mediate photodegradation.

5.3 Photochemical MeHg decomposition experiments

To apply our theoretic predictions of which complexes of MeHg are likely to produce large odd-MIF effects, we investigated MeHg photodecomposition kinetics and isotope fractionation in a series of photochemistry experiments conducted in synthetic seawater on a rooftop at Rutgers University and in natural seawater on the deck of a research vessel in the North Pacific Ocean. All experiments were carried out in 1L UV-transparent Teflon bottles (fluorinated ethylene propylene, FEP) under natural sunlight conditions on cloudless days. For each experiment MeHg was added to either synthetic seawater, freshly collected natural seawater, or ultrafiltered surface seawater in which dissolved organic carbon (DOC) was only present as low molecular weight (LMW) DOC (<1 KDa). For the synthetic seawater experiments specific LMW organic ligands were also added to the experimental solutions. Finally, experiments in the dark and with ultrapure deionized water were included as controls.

The photodecomposition of MeHg followed pseudo first order kinetics with reaction rate constants (range 0.092 to 0.40 d⁻¹; Table S1a,b) similar to those for freshwaters³⁵⁻³⁷ (0.17 to 0.59 d⁻¹), and to that previously measured in the North Pacific Ocean³⁸ (0.87 d⁻¹). The $\Delta^{199}\text{Hg}$ and $\delta^{202}\text{Hg}$ values (Table S2) from these experiments plot along two different lines with slopes of 4.1 ± 0.9 ($R^2=0.69$; $p<0.01$) and 11.3 ± 1.18 , ($R^2=0.74$; $p<0.01$) (Fig 1a). We interpret this to mean that there were two distinct pools of MeHg available for photochemical decomposition in our experiments, and by inference in marine waters. The group of experiments with a $\Delta^{199}\text{Hg}/\delta^{202}\text{Hg}$ ratio of 4.1 includes all of those in synthetic seawater with added ligands, plus an experiment with unfiltered natural surface seawater and an elevated concentration of MeHg, where MeHgCl was likely the dominant dissolved MeHg species. The photochemical degradation of intracellular MeHg in marine phytoplankton also yielded a similar slope of $\Delta^{199}\text{Hg}/\delta^{202}\text{Hg}$ slope of 6.3³⁹ (Fig. 1b). We suggest that $\Delta^{199}\text{Hg}$ and $\delta^{202}\text{Hg}$ values for all of the experiments in which MeHg was complexed by LMW-organic ligands (e.g., cysteine, serine) likely follow the same slope because homolytic cleavage of the Hg-C bond proceeds by the same mechanism during the direct photolysis of these MeHg complexes regardless of the ligand.^{23,24} Our results with MeHg-organic ligands are consistent with those showing that photodecomposition of MeHg complexed with HMW freshwater DOM under natural sunlight⁶ also plot along a slope of 4.1 (Fig 1b).

The group of experiments with a $\Delta^{199}\text{Hg}/\delta^{202}\text{Hg}$ slope of 11.3 includes those in unfiltered natural surface seawater with a relatively low concentration of added MeHg, those in natural seawater with LMW-DOC, and those in deionized water. This much higher slope represents the photochemical decomposition of photochemically reactive inorganic complexes of MeHg (MeHg⁺ and MeHgOH) because the other major dissolved MeHg species present in deionized water cannot undergo photochemical decomposition under natural sunlight (See Table 1²³). This is in agreement

with the arguments that MeHg will not bind marine DOC due to the elevated Cl or that MeHg-DOM reacts by a different mechanism that does not yield high levels of odd-MIF. Thermodynamic equilibrium calculations using ChemEQL⁴⁰ indicate that ~18% of MeHg in the deionized water was in the form of free MeHg⁺ and ~2% was present as MeHgOH. While it is difficult to determine the hydration of MeHg⁺ in seawater or deionized water based on *ab initio* calculations, it was recently reported that MeHg⁺ interacts with only one H₂O in solution forming a bond slightly stronger than a water-water hydrogen bond⁴¹.

For convenience will refer to the two groups of photochemically reactive MeHg species as **MeHg-ligand** for those with a slope of 4.1 and **reactive MeHg_i** (MeHgOH or MeHg⁺) for those with a slope of 11.3.

5.4 MeHg uptake and bioaccumulation at the base of oceanic marine food webs

Based on the large difference in odd-MIF of Hg isotopes between the reactive MeHg_i and MeHg-ligands pools of MeHg, we can use the extent of odd-MIF to identify the MeHg species accumulated by plankton at the base of the pelagic marine food web. This assumes minimal mixing of isotopic signatures between reactive-MeHg_i and MeHg-ligand pools prior to uptake by phytoplankton, which is reasonable given that uptake of MeHg⁺ and MeHgOH is likely faster than the dissociation of MeHg-DOC complexes, as is generally the case for transition metals⁴², and MeHg will preferentially bind Cl over DOM give the low concentrations of DOM in natural seawater.¹⁹

To assess the relative accumulation of the two pools of MeHg at the base of pelagic marine food webs, we compared Hg stable isotope compositions in various size classes of zooplankton from the tropical and subtropical N. Pacific Ocean (Fig. 2; Table S2c). Zooplankton were collected in day and night net tows through the upper mixed layer (<50 m) at 5°N, 155°W and 8°N, 155°W

in August and September, 2015 on board the R/V Kilo Moana. Additional Hg stable isotope measurements in zooplankton from surface and deep tows in the North Pacific Subtropical Gyre at Station ALOHA (22°45'N, 158°W) are from Motta et al.⁴³ The nighttime and larger surface zooplankton (>1 mm) plot within the region of all previously published N. Pacific marine organisms (Fig 2), while the small surface day zooplankton (0.2-1 mm) have statistically higher $\Delta^{199}\text{Hg}$ values (Wilcoxon test, $p < 0.01$). It is important to point out that although MeHg accounts for 6-60% of the total Hg (THg = Hg(II)+MeHg; Table S3) in surface zooplankton from the North Pacific^{38,44}, $\Delta^{199}\text{Hg}$ values in oceanic zooplankton are largely controlled by the large, positive $\Delta^{199}\text{Hg}$ signature of MeHg. This is because the photochemical reduction of HgCl_2 (~50% of dissolved Hg(II)^{19,45}) does not result in large, positive $\Delta^{199}\text{Hg}$ values, and the slower photoreduction of Hg(II) complexed by organic ligands (most of the remainder), results in large, negative $\Delta^{199}\text{Hg}$ values.^{25,39} As such, $\Delta^{199}\text{Hg}$ values for THg in zooplankton reflect the signature of MeHg photodegradation that is partially diluted by lower values associated with the photoreduction of Hg(II).

To evaluate the $\Delta^{199}\text{Hg}$ values in surface zooplankton associated with MeHg, we performed a mass balance calculation using the MeHg concentration in the surface zooplankton and the Hg isotopic composition of precipitation from the open ocean (and Hawai'i) as the Hg(II) source (Fig 2). This is a good assumption given that Motta et al⁴³ found (using Hg stable isotopes) that Hg from precipitation was incorporated into surface marine zooplankton at Station ALOHA. The estimated $\Delta^{199}\text{MeHg}$ values of the small surface zooplankton are statistically different from the larger and deeper zooplankton (Wilcoxon test, $p < 0.005$), which plot within the range of all published N. Pacific marine organisms. The surface zooplankton from the NPSG

have the highest $\Delta^{199}\text{MeHg}$ values due to the elevated MeHg photodegradation in the subtropical gyres compared to the equatorial ocean.⁴⁶

The elevated $\Delta^{199}\text{Hg}/\delta^{202}\text{Hg}$ ratios recorded in the daytime zooplankton (0.2-5 mm) compared to deeper-living zooplankton and fish are likely due to differences in MeHg photochemistry. To evaluate this hypothesis, we compared $\Delta^{199}\text{Hg}/\Delta^{201}\text{Hg}$ slopes, which record differences in reaction mechanism²⁰, for our MeHg photodegradation experiments with those preserved in zooplankton and pelagic fish (Fig. 3). The photochemical transformation of the **MeHg-ligand** pool of MeHg had a similar slope ($\Delta^{199}\text{Hg}/\Delta^{201}\text{Hg}$; 1.19 ± 0.001) to that in all marine and estuarine organisms analyzed to date ($\Delta^{199}\text{Hg}/\Delta^{201}\text{Hg}$; 1.23 ± 0.02).^{4,5,10,11,43,47,48} In contrast, the reactive **MeHg_i** pool of MeHg had a significantly lower slope of 1.11 ± 0.003 ($p<0.01$). This adds additional support to our hypothesis that there are two distinct pools of photochemically reactive MeHg in marine surface waters, and confirms that MeHg accumulated in marine food webs originates from the residual MeHg produced during the photochemical decomposition of MeHg complexed to LMW organic ligands. We specify LMW because the $\Delta^{199}\text{Hg}/\Delta^{201}\text{Hg}$ slope for the **MeHg-Ligand** experiments is statistically from experiments where MeHg was complexed to freshwater high molecular weight DOM ($\Delta^{199}\text{Hg}/\Delta^{201}\text{Hg}$ 1.38 ± 0.01 $n=95$).^{6,8,49}

The $\Delta^{199}\text{Hg}/\Delta^{201}\text{Hg}$ slope for small surface-dwelling zooplankton (1-50 m; 0.2-5 mm; Fig 3b $\Delta^{199}\text{Hg}/\Delta^{201}\text{Hg}$ 1.11 ± 0.03) indicates the accumulation of MeHg from the reactive MeHg_i pool. In contrast, large, surface-dwelling zooplankton (>5 mm; slope= 1.27 ± 0.02) and zooplankton from the lower euphotic zone (50-100 m; 0.2-5 mm; slope= 1.20 ± 0.02) plot within uncertainty of the slope for the photodegradation of MeHg in the MeHg-ligand pool (1.19 ± 0.001) or that of intracellular MeHg in marine phytoplankton (1.18 ± 0.013). While DOM

and thiol concentrations in seawater are likely too low⁵⁰ to form the most photochemically active, high coordination number complexes of MeHg, such complexes are expected to form in phytoplankton cells where much higher concentrations of thiols are found^{33,34}. These observations strongly indicate that large size classes of zooplankton and pelagic fish accumulate and preserve the odd-MIF signature produced during the photoreduction of intracellular MeHg complexed to LMW, thiol ligands. It is unlikely that the Hg isotopic signatures of zooplankton and pelagic fish are produced during the photochemical degradation of MeHg coordinated with HMW marine DOM, which is unavailable to phytoplankton.^{15,16,18} In addition, even if intermediate and large zooplankton have access to other sources of Hg than marine phytoplankton through consumption of marine particles, marine particles have minimal values of MIF and thus cannot significantly affect the $\Delta^{199}\text{Hg}/\Delta^{201}\text{Hg}$ ratio.⁴³

5.5 Conclusions

Based on the Hg stable isotope values associated with residual photodegraded MeHg and the Hg isotopic composition of small and large zooplankton from the central North Pacific Ocean, we have developed a conceptual model for Hg cycling in pelagic marine ecosystems (Fig. 3). The Hg isotope data shown here indicates that the pool of MeHg complexed to marine DOM is not available for incorporation into the marine foodweb; this is supported by the fact that the $\Delta^{199}\text{Hg}/\Delta^{201}\text{Hg}$ slope of MeHg complexed to HMW-DOM (1.38)^{6,8,44} has never been measured in marine organisms. Therefore, the photodegradation of MeHg-DOM does not reduce the pool of bioavailable MeHg that can be taken up by the marine foodweb and photodecomposition rates of MeHg-DOM are inadequate to account for the MeHg in pelagic fish. We suggest that small MeHg species (e.g. MeHgCl, MeHgOH, MeHg⁺) are the main source of MeHg to the marine foodweb. This is because in the upper 50 m of the ocean the $\Delta^{199}\text{Hg}/\Delta^{201}\text{Hg}$ slope of the **reactive**

MeHg_i pool (1.11±0.03) is preserved in the small daytime non-migrating zooplankton. Presumably motile larger zooplankton feed at depths greater than UVB penetration and deeper-dwelling migrating zooplankton are in the upper 50 m only at night. The photolysis of the **reactive-MeHg_i** pool is limited by UVB penetration (~33 m) inhibiting MIF in deeper waters. Small non-migrating zooplankton have a tight trophic link with phytoplankton in the euphotic zone (Hannides et al., in review). It has been shown that copepods may also uptake MeHg from the dissolved phase¹⁸ and this may also be the case for small zooplankton. Below the UVB penetration depth (50-100 m) the photolysis of MeHg is likely dominated by intracellular photolysis of phytoplankton, where the **reactive-MeHg_i** species that are available to phytoplankton do not have significant $\Delta^{199}\text{Hg}$ values. Elevated intracellular thiol concentrations facilitate the complexation of MeHg in phytoplankton cells by sulfur-bearing ligands, which leads to high extents of odd-MIF during photodegradation and a $\Delta^{199}\text{Hg}/\Delta^{201}\text{Hg}$ slope (1.19) that is identical to that of the **MeHg-ligand** reactions (1.19) and is preserved in large surface-living zooplankton (>5 mm), deep-dwelling zooplankton (50-100 m) and pelagic marine fish. Since it has been shown that visible light can lead to MIE during the photodegradation of MeHg in phytoplankton⁴⁸, we propose that the $\Delta^{199}\text{Hg}/\Delta^{201}\text{Hg}$ slope of 1.19 is preserved in the marine food web because, as shown by experiment and theoretical calculations (Table 1), MeHg complexed to multiple thiol ligands can be photodegraded by visible light. Visible light reaches greater depths in the water column than UV light, while reactive MeHg_i can only be degraded by UVB.

In summary, our results show that the **MeHg-ligand** isotopic signature by phytoplankton dominates biomass and it is the most important mechanism for MeHg decomposition in marine environments. **Reactive MeHg_i** is important in the upper-most ocean and is probably limited by

UVB light penetration. Understanding the environmental and biological factors that control these processes are critical for predicting the accumulation of pollutant Hg in pelagic marine food webs and the seafood they produce.

5.6 Methods

5.6.1 Rooftop Experiments. We performed rooftop experiments at Rutgers University in Brunswick NJ, USA. Photoreduction of MeHg was studied in synthetic seawater in the presence of synthetic low molecular weight (LMW) ligands including cysteine, serine, and ethylenediamine, which are representative of binding sites in seawater, and corresponding dark controls. We conducted the following control experiments: synthetic seawater without additional ligands (to mimic MeHgCl) and dark experiments in synthetic seawater with the corresponding LMW ligands. All of these experiments had an average starting MeHg concentration of 2.62 ± 0.33 mM.

5.6.2 Shipboard Experiments. These experiments were performed on the R/V Kilo Moana in the central North Pacific Ocean at Station ALOHA ($22^{\circ} 45'N$, $158^{\circ} 00'W$) in unfiltered surface seawater (from 10 m depth; with $7.9 \times 10^{-2} \pm 3.0 \times 10^{-3}$ mM DOC) and in ultrafiltered surface seawater where the only dissolved organic carbon (DOC) was marine LMW-DOC (DOM <1 KDa; with $6.4 \times 10^{-2} \pm 3.0 \times 10^{-3}$ mM DOC). Most marine DOM (60-90%) is LMW, and readily permeates through the ultrafiltration system⁵¹. All the experiments had an average MeHg concentration of 2.62 ± 0.33 mM. We also conducted the following control experiments: dark control in unfiltered seawater (0.07 mM MeHg), elevated MeHg concentration in unfiltered seawater (6.49 mM MeHg) to mimic the photochemical degradation of MeHg, and an ultra-pure water deionized water experiment (with 1.80 mM MeHg).

5.6.3 Zooplankton Analyses. We analyzed Hg concentrations and Hg stable isotope compositions of zooplankton from the Central Pacific for three different size fractions (0.5-1 mm), (1-5 mm)

and (>5 mm) (Fig 3b). Zooplankton Hg stable isotope measurements from Station ALOHA are from Motta et al.⁴³, and surface zooplankton (<50 m) from 8°N, 155°W and 5°N, 155°W were collected between August-September 2015 on board the R/V Kilo Moana using the same methods outlined by Motta et al.⁴³.

5.6.4 Electronic Structure Simulations. To identify the plausible MeHg species that may undergo primary photolysis in the photochemical experiments and marine zooplankton, we conducted high level electronic structure simulations^{13,52} of possible MeHg complexes in solution to determine excitation energies (Table 1).

Acknowledgements

We would like to give a special thanks to C.C.S. Hannides and J. C. Drazen for the zooplankton samples, the captain and crew of the *R/V Kilo Moana*, the UH Ocean Technology Group, and Alan Rask for all the helpful discussions about the excited states of Hg complexes. This work was supported by National Science Foundation (NSF) grants OCE 1433710 (to J.D. Blum), OCE 1333734 (to J.C. Drazen., H.G.Close., B.N.Popp., C.C.S.Hannides.), OCE 1433846 (to B.N.Popp., J.C.Drazen., C.C.S.Hannides.), OCE 1634154 (to J.R. Reinfelder) and an NSF Graduate Fellowship to L. Motta.

Table 5.1 Vertical excitation energies using the first principles EOM-CCSD^{12,47} level of theory and corrected for water solvation using TDDFT. The T1 state of MeHg⁺ was confirmed using incremental Full Configuration Interaction¹³ (iFCI). (See Supporting Information for full computational details)

Molecule	S (EOM-CCSD)	T (EOM-CCSD)	T (iFCI)	λ_{max}	λ_{tail}
CH ₃ HgCl	191(1.56E-02)	210	-	206 ⁴⁸	240 ⁴⁸
CH ₃ HgBr	209(2.21E-02)	217	-	210 ⁴⁸	246 ⁴⁸
CH ₃ Hg ⁺	226(3.71E-01)	366	338	208 ²⁴	260 ²⁴
CH ₃ HgOH ₂ ⁺	178(4.96E-01)	235	-	-	-
CH ₃ HgOH	210(2.77E-02)	227	-	202 ²⁴	260 ²⁴
CH ₃ HgCysteine	263(1.20E-03)	270	-	-	300 ²⁴
CH ₃ HgSCH ₃	270(8.76E-05)	275	-	-	-
CH ₃ Hg(SCH ₃) ₂	287(4.99E-02)	296	-	-	-
CH ₃ Hg(SCH ₃) ₃	343(2.78E-02)	343	-	-	-
Sunlight Spectrum (nm)					
UVB	290-315				
UVA	315-380				
Visible	380-780				

EOM-CCSD - Equation of motion coupled cluster with singlets and doublets

TDDFT-Time depended density functional theory

iFC incremental full configuration interaction

λ experimental absorption wavelengths

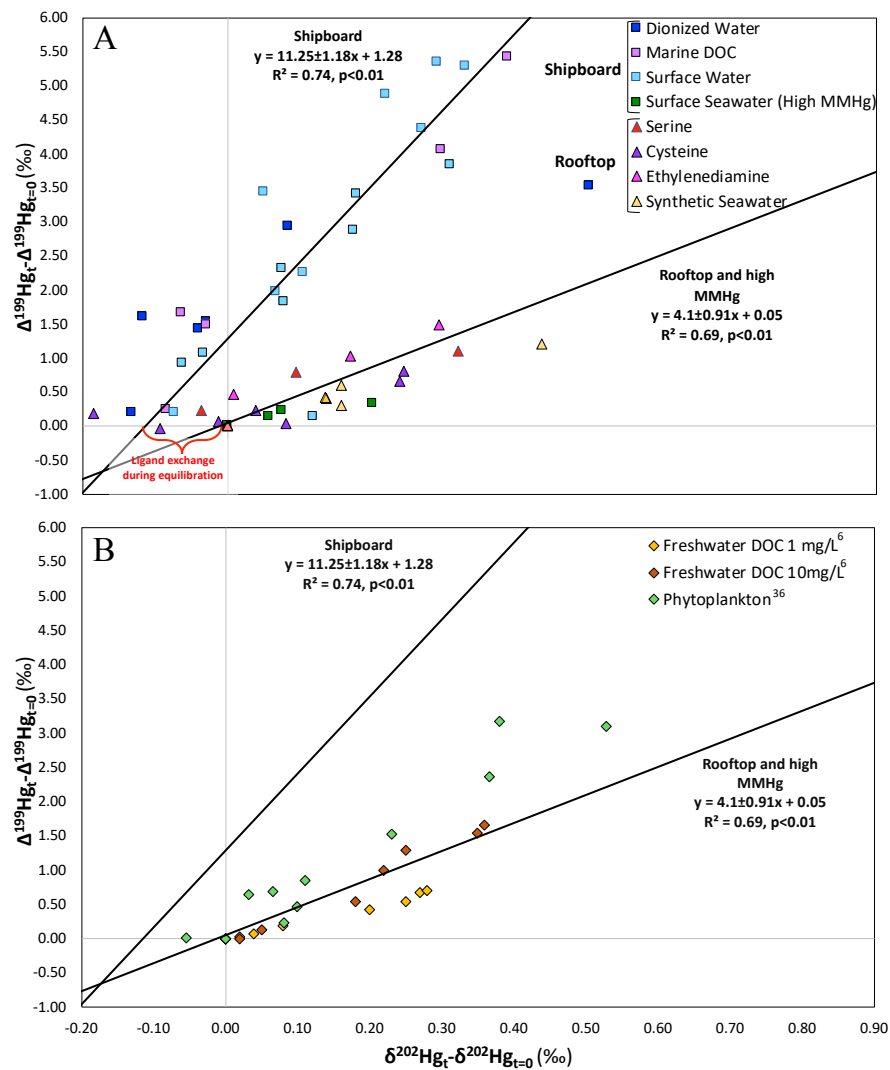


Figure 5.1. Plot of $\Delta^{199}\text{Hg}_t - \Delta^{199}\text{Hg}_{t=0}$ versus $\delta^{202}\text{Hg}_t - \delta^{202}\text{Hg}_{t=0}$. **A)** Shipboard: deionized water control, marine DOC is ultrafiltered surface seawater (>1KDa); surface water= unfiltered seawater; unfiltered seawater with high MeHg. Rooftop: synthetic seawater with low molecular weight organic ligands. The negative $\delta^{202}\text{Hg}$ at the beginning of the photodecomposition of MeHg in the shipboard experiments was observed during the dark incubation period and likely corresponds to ligand exchange during equilibration⁴⁹. This was not observed in the rooftop experiments **B)** High MW, freshwater DOC photochemistry MeHg experiments⁶, and phytoplankton experiments for reference³⁷

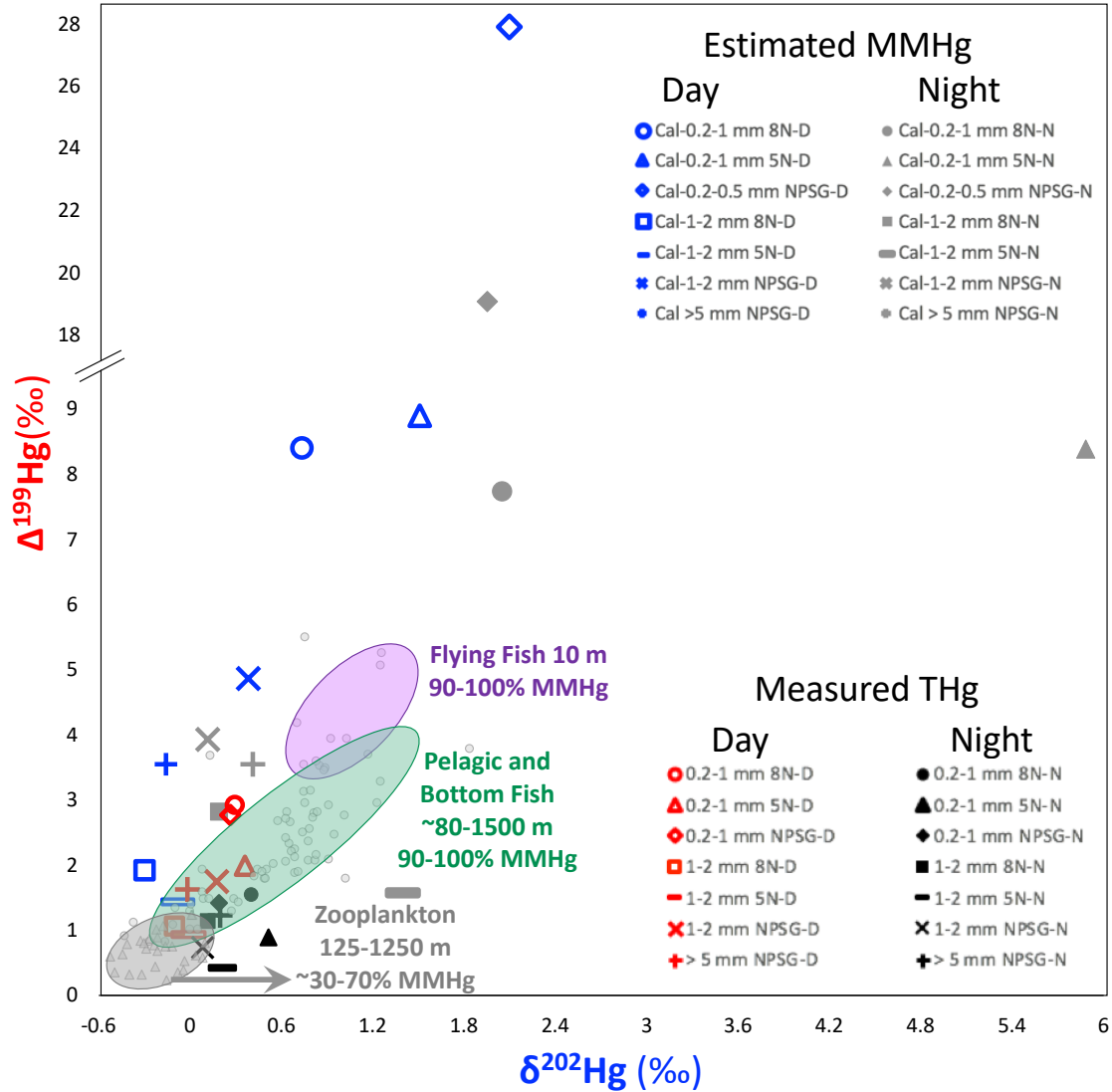


Figure 5.2. Plot of $\Delta^{199}\text{Hg}$ versus $\delta^{202}\text{Hg}$. Flying fish⁵⁰, pelagic and bottom fish^{10,41,51}, zooplankton from Station Aloha⁴¹, and zooplankton from the North Pacific Ocean. The red and black symbols are the measured THg isotopic composition of the surface water zooplankton. The blue and grey symbols are the calculated MeHg isotopic composition of the surface zooplankton. Refer to text for calculation details.

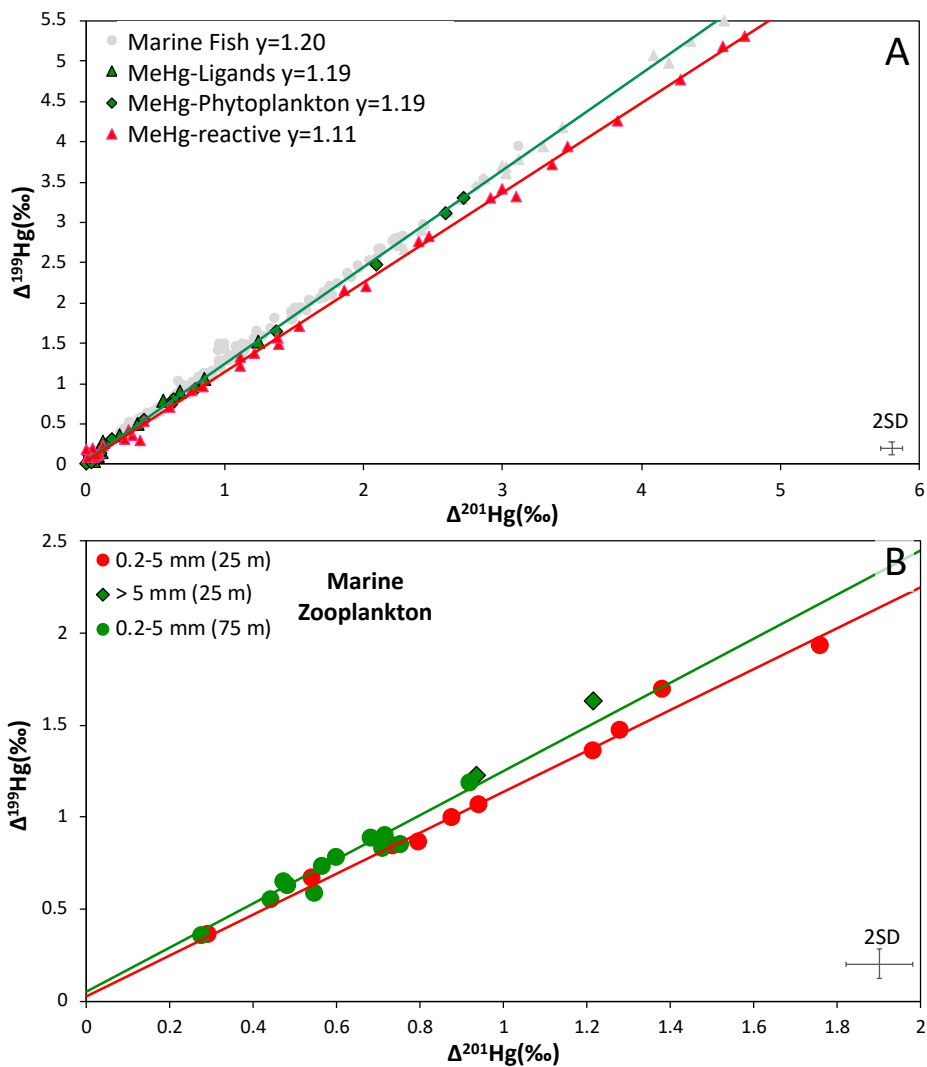


Figure 5.3. A) Plot of $\Delta^{199}\text{Hg}_t - \Delta^{199}\text{Hg}_{t=0}$ versus $\Delta^{201}\text{Hg}_t - \Delta^{201}\text{Hg}_{t=0}$. The black circles and black dotted line are the MeHg photochemistry experiments with freshwater DOC^{6,8,44}. The green triangles and green dotted line are the rooftop experiments from this study. The red circles and red dotted line are the shipboard experiments and deionized water. B) Plot of $\Delta^{199}\text{Hg}$ versus $\Delta^{201}\text{Hg}$ and the dashed lines represent the MeHg experiments from plot A. The green diamonds are the phytoplankton experiments³⁷; the red diamonds are the surface small zooplankton; the yellow circles are surface large zooplankton; the green circles are the mesopelagic zooplankton from Station ALOHA⁴¹.

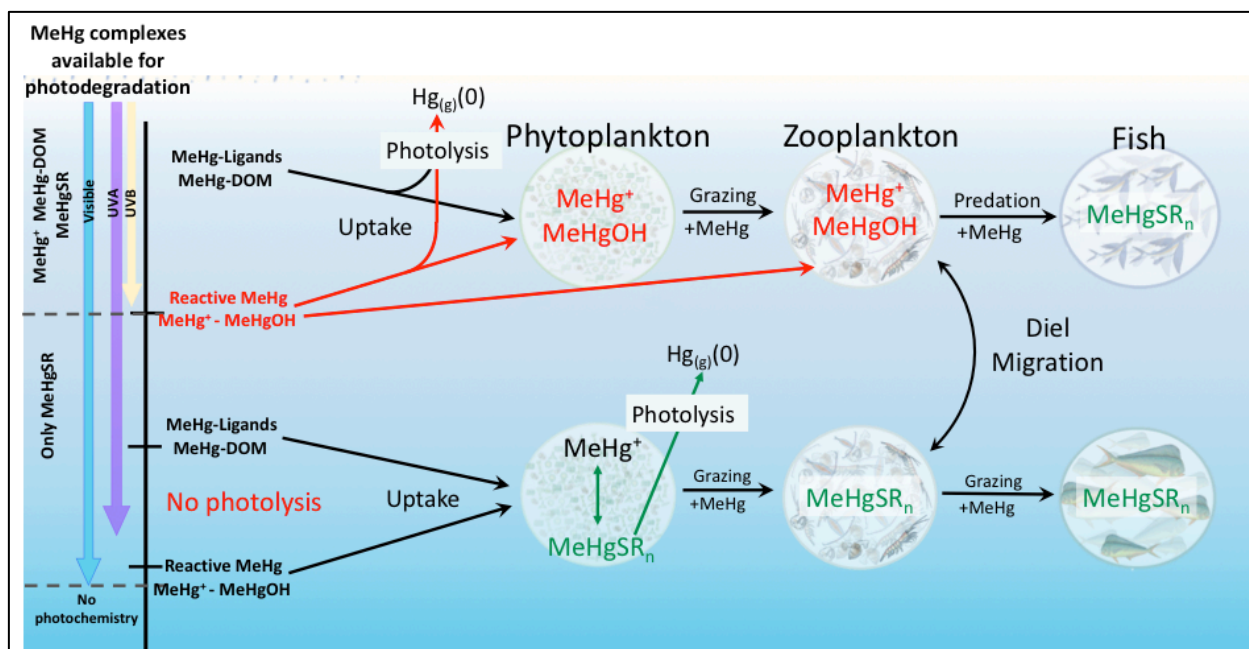


Figure 5.4. Diagram of MeHg photodecomposition, uptake, and incorporation of MeHg in the marine food web. In the diagram the MeHg systematics have been simplified to emphasize incorporation of the MIF Hg signatures (see conclusion). Not shown is that MeHgCl and MeHgOH₂⁺ are also available for uptake and incorporation into the foodweb, but these complexes are not available for photodecomposition under natural sunlight and will not exhibit any considerable MIF. There is no significant MIF associated with the photodegradation of MeHg in natural waters with limited UV light⁴⁴, while marine phytoplankton can photodegrade MeHg intracellularly in visible light and that results in significant MIF³⁷. Marine zooplankton also have access to particulate matter as a source for Hg, but it has been shown that marine particles do not have significant MIF⁴¹. The Hg isotopic composition of zooplankton with depth at station ALOHA are detailed in Motta et al., (2019)⁴¹

References

1. Sunderland, E. M., Li, M. & Bullard, K. Decadal Changes in the Edible Supply of Seafood and Methylmercury Exposure in the United States. *Environ. Health Perspect.* **126**, 029003 (2018).
2. Hammerschmidt, C. R., Finiguerra, M. B., Weller, R. L. & Fitzgerald, W. F. Methylmercury accumulation in plankton on the continental margin of the northwest atlantic ocean. *Environ. Sci. Technol.* **47**, 3671–3677 (2013).
3. Lee, C. S. & Fisher, N. S. Bioaccumulation of methylmercury in a marine diatom and the influence of dissolved organic matter. *Mar. Chem.* **197**, 70–79 (2017).
4. Li, M. *et al.* Environmental Origins of Methylmercury Accumulated in Subarctic Estuarine Fish Indicated by Mercury Stable Isotopes. *Environ. Sci. Technol.* **50**, 11559–11568 (2016).
5. Senn, D. B. *et al.* Stable isotope (N, C, Hg) study of methylmercury sources and trophic transfer in the northern Gulf of Mexico. *Environ. Sci. Technol.* **44**, 1630–1637 (2010).
6. Bergquist, B. A. & Blum, J. D. Mass-dependent and -independent fractionation of hg isotopes by photoreduction in aquatic systems. *Science* **318**, 417–420 (2007).
7. Kritee, K., Barkay, T. & Blum, J. D. Mass dependent stable isotope fractionation of mercury during mer mediated microbial degradation of monomethylmercury. *Geochim. Cosmochim. Acta* **73**, 1285–1296 (2009).
8. Chandan, P., Ghosh, S. & Bergquist, B. A. Mercury isotope fractionation during aqueous photoreduction of monomethylmercury in the presence of dissolved organic matter. *Environ. Sci. Technol.* **49**, 259–267 (2015).
9. Point, D. *et al.* Methylmercury photodegradation influenced by sea-ice cover in Arctic marine ecosystems. *Nat. Geosci.* **4**, 188–194 (2011).
10. Blum, J. D., Popp, B. N., Drazen, J. C., Anela Choy, C. & Johnson, M. W. Methylmercury production below the mixed layer in the North Pacific Ocean. *Nat. Geosci.* **6**, 879–884 (2013).
11. Kwon, S., Blum, J. D., Nadelhoffer, K. J., Dvonch, J. T. & Tsui, M. T. Science of the Total Environment Isotopic study of mercury sources and transfer between a freshwater lake and adjacent forest food web. *Sci. Total Environ.* **532**, 220–229 (2015).
12. Kowalski, K. & Piecuch, P. New coupled-cluster methods with singles, doubles, and noniterative triples for high accuracy calculations of excited electronic states. *J. Chem. Phys.* **120**, 1715–1738 (2004).
13. Zimmerman, P. M. Strong correlation in incremental full configuration interaction. *J. Chem. Phys.* **146**, (2017).
14. Mason, R. P., Reinfelder, J. R. & Morel, F. M. M. Bioaccumulation of Mercury and Methylmercury. *Water, Air, Soil Pollut.* **80**, 915–921 (1995).
15. Mason, R. P., Reinfelder, J. R. & Morel, F. M. M. Uptake , Toxicity , and Trophic Transfer of Mercury in a Coastal Diatom. *Environ. Sci. Technol.* **30**, 1835–1845 (1996).
16. Gorski, P. R., Armstrong, D. E., Hurley, J. P. & Shafer, M. M. Speciation of aqueous methylmercury influences uptake by a freshwater alga (*Selenastrum capricornutum*). *Environ. Toxicol. Chem.* **25**, 534–540 (2006).
17. Lee, C. S. & Fisher, N. S. Methylmercury uptake by diverse marine phytoplankton. *Limnol. Oceanogr.* **61**, 1626–1639 (2016).
18. Lee, C. S. & Fisher, N. S. Bioaccumulation of methylmercury in a marine copepod.

- Environ. Toxicol. Chem.* **36**, 1287–1293 (2017).
19. Zhong, H. & Wang, W. X. Controls of dissolved organic matter and chloride on mercury uptake by a marine diatom. *Environ. Sci. Technol.* **43**, 8998–9003 (2009).
 20. Raycheba, J. M. T. & Geier, G. Methylmercuriation of Carbon-Donor Ligands. A Kinetic Preference for Methylmercury(II) Transfer over Proton Transfer. *Inorg. Chem.* **18**, 2486–2491 (1979).
 21. Erni, I. & Geier, G. Kinetics of Extremely Fast Ligand Exchange Reactions with Methylmercury (II)-complexes of 1-Methylpyridine-2-thione and 1-Methyl- quinaldine-4-thione: Rate-Equilibria Correlations. *Helv. Chim. Acta* **62**, 18–19 (1979).
 22. Zhang, T. & Hsu-Kim, H. Photolytic degradation of methylmercury enhanced by binding to natural organic ligands. *Nat. Geosci.* **3**, 473–476 (2010).
 23. Inoko, M. Studies on the Photochemical Decomposition of Organomercurials - Methylmercury (II) Chloride. *Environ. Pollut. (Series B)* **2**, 3–10 (1981).
 24. Baughman, G. ., Gordon, J. ., Lee Wolfe, N. & Zepp, R. G. Chemistry of Organomercurials in Aquatic Systems. *Epa-660/3-73- 012-Ecological Res. Ser.* (1973).
 25. Zheng, W. & Hintelmann, H. Isotope Fractionation of Mercury during Its Photochemical Reduction by Low-Molecular-Weight Organic Compounds. *J. Phys. Chem. A* **114**, 4246–4253 (2010).
 26. Salikhov, K. *Magnetic Isotope Effect in Radical Reactions - Introduction.* (1996).
 27. Hore, P. J. & Mouritsen, H. The Radical-Pair Mechanism of Magnetoreception. *Annu. Rev. Biophys.* **45**, 299–344 (2016).
 28. Turro, N. J. Influence of nuclear spin on chemical reactions: Magnetic isotope and magnetic field effects (A Review). *Proc. Natl. Acad. Sci.* **80**, 609–621 (1983).
 29. Sitkiewicz, S. P. *et al.* Ab initio quantum-chemical computations of the electronic states in HgBr₂ and IBr: Molecules of interest on the Earth's atmosphere. *J. Chem. Phys.* **145**, (2016).
 30. Sitkiewicz, S. P., Rivero, D., Oliva-Enrich, J. M., Saiz-Lopez, A. & Roca-Sanjuán, D. Ab initio quantum-chemical computations of the absorption cross sections of HgX₂ and HgXY (X, y = Cl, Br, and I): Molecules of interest in the Earth's atmosphere. *Phys. Chem. Chem. Phys.* **21**, 455–467 (2019).
 31. Gu, B., Lu, X. I. A., Johs, A. & Pierce, E. M. Mercury in Water. in 1–41 (Wiley, 2018).
 32. Jalilehvand, F., Leung, B. O., Izadifard, M. & Damian, E. Mercury(II) cysteine complexes in alkaline aqueous solution. *Inorg. Chem.* **45**, 66–73 (2006).
 33. Ahner, B. A., Wei, L., Oleson, J. R. & Ogura, N. Glutathione and other low molecular weight thiols in marine phytoplankton under metal stress. *Mar. Ecol. Prog. Ser.* **232**, 93–103 (2002).
 34. Morelli, E. *et al.* Changes in the non-protein thiol pool and production of dissolved gaseous mercury in the marine diatom *Thalassiosira weissflogii* under mercury exposure. *Sci. Total Environ.* **408**, 286–293 (2009).
 35. Black, F. J., Poulin, B. A. & Flegal, A. R. Factors controlling the abiotic photo-degradation of monomethylmercury in surface waters. *Geochim. Cosmochim. Acta* **84**, 492–507 (2012).
 36. Lehnerr, I. & Louis, V. L. S. Importance of Ultraviolet Radiation in the Photodemethylation of Methylmercury in Freshwater Ecosystems. *Environ. Sci. Technol.* **43**, 5692–5698 (2009).
 37. Hammerschmidt, C. R. & Fitzgerald, W. F. Iron-mediated photochemical decomposition

- of methylmercury in an arctic Alaskan Lake. *Environ. Sci. Technol.* **44**, 6138–6143 (2010).
38. DiMento, B. P. & Mason, R. P. Factors controlling the photochemical degradation of methylmercury in coastal and oceanic waters. *Mar. Chem.* **196**, 116–125 (2017).
 39. Kritee, K., Motta, L. C., Blum, J. D., Tsui, M. T. & Reinfelder, J. R. Photo-microbial visible light-induced magnetic mass independent fractionation of mercury in a marine microalga. *Earth Sp. Chem.* (2017). doi:10.1021/acsearthspacechem.7b00056
 40. Müller, B. ChemEQL, User's Guide to Application. (2015).
 41. Flórez, E., Maldonado, A. F., Aucar, G. A., David, J. & Restrepo, A. Microsolvation of methylmercury: Structures, energies, bonding and NMR constants (199Hg, 13C and 17O). *Phys. Chem. Chem. Phys.* **18**, 1537–1550 (2016).
 42. Hudson, R. J. M. Which aqueous species control the rates of trace metal uptake by aquatic biota? Observations and predictions of non-equilibrium effects. *Sci. Total Environ.* **219**, 95–115 (1998).
 43. Motta, L. C. *et al.* Mercury cycling in the North Pacific Subtropical Gyre as revealed by mercury stable isotope ratios. *Global Biogeochem. Cycles* 2018GB006057 (2019). doi:10.1029/2018GB006057
 44. Gosnell, K. J. & Mason, R. P. Mercury and methylmercury incidence and bioaccumulation in plankton from the central Pacific Ocean. *Mar. Chem.* **177**, 772–780 (2015).
 45. Lamborg, C. H., Tseng, C. M., Fitzgerald, W. F., Balcom, P. H. & Hammerschmidt, C. R. Determination of the mercury complexation characteristics of dissolved organic matter in natural waters with 'reducible Hg' titrations. *Environ. Sci. Technol.* **37**, 3316–3322 (2003).
 46. Motta, L. C., Blum, J. D., Popp, B. N., Drazen, J. C. & Close, H. Mercury Stable Isotopes in Flying Fish as a Monitor of Photochemical Degradation of Methylmercury in the Atlantic and Pacific Oceans. *Environ. Sci. Technol.*
 47. Madigan, D. J. *et al.* Mercury Stable Isotopes Reveal Influence of Foraging Depth on Mercury Concentrations and Growth in Pacific Bluefin Tuna. *Environ. Sci. Technol.* **52**, 6256–6264 (2018).
 48. Sackett, D. K., Drazen, J. C., Choy, C. A., Popp, B. & Pitz, G. L. Mercury sources and trophic ecology for Hawaiian bottomfish. *Environ. Sci. Technol.* **49**, 6909–6918 (2015).
 49. Rose, C. H., Ghosh, S., Blum, J. D. & Bergquist, B. A. Effects of ultraviolet radiation on mercury isotope fractionation during photo-reduction for inorganic and organic mercury species. *Chem. Geol.* **405**, 102–111 (2015).
 50. Swarr, G. J., Kading, T., Lamborg, C. H., Hammerschmidt, C. R. & Bowman, K. L. Dissolved low-molecular weight thiol concentrations from the U.S. GEOTRACES North Atlantic Ocean zonal transect. *Deep. Res. Part I Oceanogr. Res. Pap.* **116**, 77–87 (2016).
 51. Benner, R. & Amon, R. M. W. The Size-Reactivity Continuum of Major Bioelements in the Ocean. *Ann. Rev. Mar. Sci.* **7**, 185–205 (2014).
 52. Piecuch, P., Kowalski, K., Pimienta, I. S. O. & McGuire, M. J. *Recent advances in electronic structure theory: Method of moments of coupled-cluster equations and renormalized coupled-cluster approaches. International Reviews in Physical Chemistry* **21**, (2002).
 53. Gowenlock, B. G. & Trotman, J. Ultraviolet Absorption Spectra of Some Mercury Compounds. *J. Chem. Soc.* 1454–1458 (1955).

54. Jiskra, M. *et al.* Kinetics of Hg(II) exchange between organic ligands, goethite, and natural organic matter studied with an enriched stable isotope approach. *Environ. Sci. Technol.* **48**, 13207–13217 (2014).

5.7 Supporting Information

5.7.1 Rooftop experiments

All experiments were conducted on clear days (no cloud cover) with average temperatures for the September 2012 experiments of $19\pm 1^\circ\text{C}$, and for the May 2013 experiments of $28.5\pm 0.5^\circ\text{C}$. All the experiments (except controls) were exposed to the full spectrum of sunlight on the roof of Foran Hall at Rutgers University, Brunswick NJ. A stock solution made from powdered Crescent Chemical company methylmercury chloride was used for all the experiments and purified ($\geq 99\%$, HPLC-grade Sigma Aldrich) L-serine, L-cysteine, and ethylenediamine were used in the experiments. MMHg was incubated separately with the corresponding organic compound: 0.4 mM cysteine, 4 mM serine, and 4 mM ethylenediamine in synthetic ocean water (SOW).

The speciation of MMHg in each treatment was estimated using the thermodynamic modelling program ChemEQL¹. In the incubations with 0.4 mM cysteine MMHg was estimated to be predominately complexed to cysteine as MMHg(HCyst) (97%) and MMHg(Cyst)⁻¹ (2%), for the incubations with 400 mM serine, MMHg was estimated to be present as MMHgHSer (90%) and MMHgCl (10%), finally for the incubations with 400 mM ethylenediamine, MMHg was estimated to be present as MMHg(en)⁺ (22.18%), MMHg(Hen)²⁺ (23.88%), and MMHgCl (53.81%). As a control experiment we used SOW where the dominant species was estimated to be MMHgCl (99%). Once the solutions were prepared the reactors were placed in the dark for 12-20 hours to let the MMHg fully equilibrate with each organic ligand, while being purged with pure air to remove any Hg(0) that might have been produced in the dark. For incubations longer than 10 hours, reactors were purged in the dark during the night and exposed to sunlight the next day at 7:30 am. There were no detectible changes in the total Hg concentrations during the night. See Table S1 for all reaction conditions

5.7.2 Shipboard experiments at Station ALOHA

Similar to the laboratory experiments, all the experiments were conducted during clear days in February 2014 and September 2014 onboard of the R/V Kilo Moana. The average temperature was 25 ± 1.5 °C in February and 28 ± 2.0 °C in September, and all experimental conditions were conducted with MMHgCl stock solution from Brooks Rand Instruments. There is no definitive information about MMHg complexation in open marine waters or to marine organic matter, but it has been hypothesized that in coastal marine waters Hg(II) is not fully complexed to DOC due to the elevated concentrations of Cl in the water². For the ultra-pure deionized water experiment MMHg was estimated to be present as MMHgCl (75-80%), MMHg⁺ (18%), and MMHgOH (2%), and in the high MMHg experiment we expect most of MMHg to be complexed to Cl due to the high concentration of MMHg to DOC. The experimental solutions were prepared as described above for the rooftop laboratory experiments.

5.7.3 Marine zooplankton samples

Marine zooplankton Hg stable isotope measurements from Station ALOHA are from Motta et al., (2019)³, and the surface zooplankton from 8N-155W and 5N-155W were collected between August-September 2015 on board of the R/V Kilo Moana using the same methods outlined previously by Motta et al., (2019)³. Briefly, zooplankton were collected using a 1 m² Multiple Opening/Closing Net and Environmental Sensing System⁴ equipped with nine sampling nets. Each tow collected material from 0-50 m depth and all samples were lyophilized and homogenized using an acid cleaned agate mortar and pestle.

The limited availability of bulk material necessitated pooling of samples for measurement of THg stable isotopic compositions, where four zooplankton size fractions were combined in pairs to produce samples representing small (0.2-1 mm) and intermediate (1-5 mm) size zooplankton.

The pooled zooplankton samples were placed in ceramic boats in a two-stage combustion system, where the Hg was released from the biotic matrix into an oxidizing solution (1% KMnO₄ in 10% H₂SO₄ (wt/wt))⁵. A small aliquot of the trap solution was measured for THg concentration by CV-AFS (Nippon MA-2000). Combustion performance was monitored with procedural blanks, microfiber quartz filter blanks and combustion blanks. Prior to measurement of Hg stable isotope ratios additional purification and pre-concentration of the Hg was accomplished by reduction with SnCl₂, and purging into a reducing trap with 1% KMnO₄ trap.

5.7.4. Hg stable isotope analysis

Samples from a secondary 1% KMnO₄ trap used for pre-concentration and purification⁶ were analyzed for Hg stable isotope composition using a multiple collector inductively coupled plasma mass spectrometer (MC-ICP-MS; Nu Instruments) with a continuous flow cold vapor generation inlet system with SnCl₂ reduction^{7,8}. The concentrations of the samples were matched to the bracketing standard (SRM NIST 3133) within 5% for each of the mass spectrometry sessions.

Mass dependent fractionation (MDF) of Hg isotopes is reported as δ²⁰²Hg values in permil (‰) relative to NIST SRM 3133 (equation 1). Mass independent fractionation (MIF) of Hg isotopes is calculated as the difference between the measured δ²⁰²Hg value and that which would be predicted based on mass dependence for a given isotope and is reported in Δ^{xxx}Hg notation in ‰ (equation 2), where xxx is the mass of each Hg isotope 199, 200, 201, 204 and β is the mass proportionality constant (0.2520, 0.5024, 0.7520, 1.493, respectively (Blum and Bergquist, 2007).

$$\delta^{xxx}\text{Hg}(\text{‰}) = \left(\frac{(^{202}\text{Hg}/^{198}\text{Hg})_{\text{unknown}}}{(^{202}\text{Hg}/^{198}\text{Hg})_{\text{SRM3133}}} - 1 \right) \times 1000 \quad (1)$$

$$\Delta^{xxx}\text{Hg} = \delta^{xxx}\text{Hg} - (\delta^{202}\text{Hg} \times \beta) \quad (2)$$

Procedural process blanks and standard reference materials (TORT-3 for the zooplankton samples, and UM-Almadén for the photochemistry experiments) were processed alongside

samples in an identical manner (Table S2). Process yields from secondary purge and trap of the 1% KMnO_4 trap solutions averaged $94\% \pm 5\%$ (1SD, minimum = 84%). The long-term analytical uncertainty of Hg isotopic composition of the samples, most of which could be measured only once, was estimated as 2SD of the results from UM-Almadén (measured multiple times in each mass-spectrometry session) or reference material (TORT-3) processed multiple times (Table S2). All the linear regressions for this study were completed using York regressions⁹ which consider errors in both the X and Y axes. It is important to note that to accurately evaluate the $\Delta^{199}\text{Hg}/\delta^{202}\text{Hg}$ or $\Delta^{199}\text{Hg}/\Delta^{201}\text{Hg}$ relationship for the photochemistry experiments fully correlated errors have to be considered. This is because a specific reaction with a known starting Hg isotopic composition is being evaluated. All Hg stable isotope data is available in TableS2a-c

5.7.5. Zooplankton MeHg Concentration analysis

MeHg in the marine zooplankton was determined by digesting a minimum of 4.0 mg of freeze-dried zooplankton in a maximum 3 ml of trace metal clean 30% HNO_3 (wt/vol) for 11.5 hours in a heated bath at 60° C. A maximum aliquot of 0.3 ml from the digested zooplankton was used for MeHg analysis by derivatization using cold sodium tetraethylborate by CV-AFS (MERX-M, Brooks Rand Instruments) as described by Bloom¹⁰. Standard reference material TORT-3 was processed alongside samples in an identical manner with process yields of 85-105%.

5.7.6. Computational Details

We investigated the excitation energies of environmentally relevant MMHg complexes to determine the species of MMHg available for photochemical decomposition under natural sunlight. All our calculations were conducted using the double zeta, polarized def2-VPD basis sets and the corresponding pseudo-potential for Hg. Geometries were optimized using second order Møller-Plesset perturbation theory method (Table S5a-i) and the low-lying singlet and triplet state

energies were determined by high level electronic structure simulations using Equation-of-Motion-Coupled-Cluster with singles and doubles (EOM-CCSD)^{11,12} as implemented in GAMESS^{13,14}. Due to the absence of detailed experimental information about the excited states of Hg compounds, ground triplet energies of MMHg⁺ were calculated using incremental Full Configuration Interaction,¹⁵ a benchmark level of theory that provides high accuracy confirmation of the EOM-CCSD results.

To get accurate vertical excitation energies of Hg compounds we estimated the influence of the solvent using the polarizable continuum model (PCM) with time-dependent density functional theory (TDDFT) using the LRC- ω PBE functional, which has been shown to be very accurate for the calculation of vertical excitation energies¹⁶. To estimate the solvent effects in vertical excitations, we must consider non-equilibrium solvation because during the electronic transition the solute undergoes a sudden change in its charge distribution. To describe this non-equilibrium solvent effects, we used the linear response and state specific approach pt(LR+SS), which has been shown to be the most accurate when considering charge transfer transitions¹⁶. See Table S6 for solvation effects.

Additional Results and Discussion

5.8.7. MMHg photochemical decomposition kinetics

All the MMHg decomposition rates followed pseudo first order kinetics. For the **MMHg-shipboard** experiments at Station ALOHA there were no statistical differences between the duplicate surface water experimental reduction rates (average 0.092 d⁻¹; n=2), and the rates were very similar to the high MMHg experiment from September (0.094 d⁻¹). The photochemical decomposition of MMHg was fastest with isolated LMW-DOC (0.30 d⁻¹). For the **MMHg-Rooftop** experiments the reduction rates for all the experiments were statistically similar

regardless of the day or complexing ligand (range 0.14-0.22 d⁻¹), with the exception of the serine experiment where the photodecomposition rate constant was 0.40 d⁻¹. The photochemical decomposition rates with SOW were faster than the surface seawater experiments, but, similar to the isolated DOC experiment. The reaction rate constants in this study were similar to the reaction rates in freshwaters¹⁷⁻¹⁹ (0.17-0.59d⁻¹), and close to the Pacific Ocean photodecomposition rate of MMHg²⁰ (0.87 d⁻¹). (See Table S1 for summary of degradation rate constants).

5.8.8. The $\Delta^{199}\text{Hg}$ and fraction remaining of MMHg relationship

It is important to note that there was not a trend in the plot of $\Delta^{199}\text{Hg}$ versus the fraction remaining in the reactor (f_{Hg} ; Fig S1), in contrast to the $\Delta^{199}\text{Hg}$ versus $\delta^{202}\text{Hg}$ values (Fig 1). This is because $\Delta^{199}\text{Hg}$ values do not depend on the overall rate limiting step of the reaction as has been observed for $\delta^{202}\text{Hg}$ ²¹. The fractionation of magnetic isotopes (¹⁹⁹Hg and ²⁰¹Hg) is driven by the radical pair mechanism, where the fractionation is mediated by intersystem crossing²². Intersystem crossing induced by hyperfine coupling is a photophysical effect, which does not alter the chemical composition of the radical species and depends on properties such as magnetic field, photosensitizers, and solvent cage effects²²⁻²⁵. It has been demonstrated that for the same photochemical reaction, changes in the aforementioned properties will alter the MIE fractionation factor^{22,24,26-29}. As such, the MIE as a function of f_{Hg} is not a good indicator of reaction mechanisms and, therefore, is not discussed further in this paper.

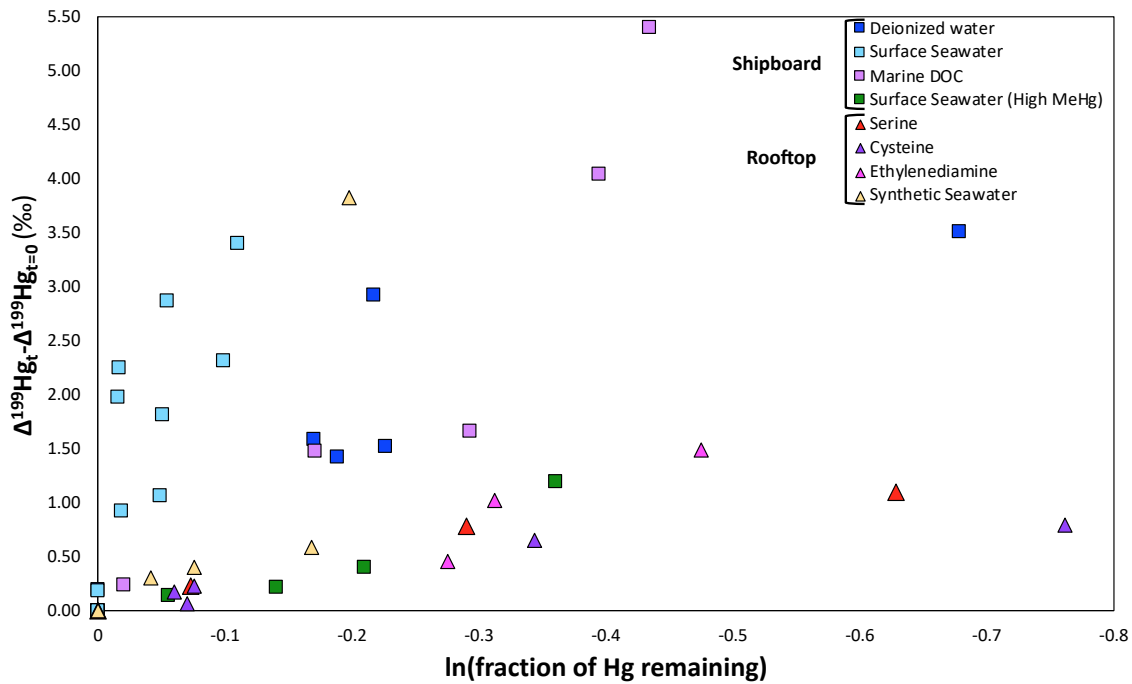


Figure S5.1. Plot of $\Delta^{199}\text{Hg}_t - \Delta^{199}\text{Hg}_{t=0}$ versus $\ln(\text{fraction remaining})$ for all the MMHg photochemistry experiments.

Table S5.1 Experimental details and environmental conditions

Location	Experiment	Expt. Duration (hr)	%Reduction	Rate Constant (day ⁻¹)	Avg. T (°C)	Max T (°C)
Shipboard Natural Seawater	Unfiltered Seawater #1	47.92	16.30	0.08	24.5±0.5	28±0.8
	Unfiltered Seawater #2	56.75	17.91	0.08	24.5±0.5	28±0.8
	Surface LMW-DOC	35.75	35.23	0.25	24.5±0.5	28±0.8
	Unfiltered Seawater High MMHg	59.83	23.24	0.09	28±1.1	31.7±0.9
	Deionized ultra-pure water	59.92	49.59	0.20	24.5±0.5	28±0.8
Rooftop Synthetic Seawater	Cysteine #1	42.83	29.03	0.15	27±1	31±0.5
	Cysteine #2	75.38	53.29	0.81	26.3±0.5	29.5±1.1
	Serine	38.32	46.62	0.40	27±1	31±0.5
	Ethylenediamine	42.83	37.76	0.22	26.3±0.5	29.5±1.1
	Synthetic Seawater	42.83	30.22	0.21	26.3±0.5	29.5±1.1

Table S5.2a Shipboard experiments Hg stable isotope data and concentrations

Treatment	Hours of Sunlight	[Hg] w/o BrCl (ng/g)	fraction remaining	ln(f)	$\delta^{202}\text{Hg}$	$\Delta^{199}\text{Hg}$	$\Delta^{201}\text{Hg}$	$\Delta^{204}\text{Hg}$	$\Delta^{200}\text{Hg}$
Surface Seawater #1	Dark	5.44			-0.95	-0.11	-0.03	0.00	-0.11
	0.00	5.19	1.00	0.00	-1.02	0.08	0.06	0.02	-0.01
	3.09	5.09	0.98	-0.02					
	7.75	5.11	0.98	-0.02	-0.88	1.87	1.65	-0.02	0.01
	10.58	5.11	0.98	-0.02	-0.84	2.15	1.86	-0.05	0.00
	13.92	5.09	0.98	-0.02					
	17.09	5.41	1.04	0.04	-0.90	3.32	3.10	0.03	0.00
	23.00	4.72	0.91	-0.10	-0.68	4.26	3.83	0.02	-0.06
	26.33	4.46	0.86	-0.15	-0.73	4.77	4.28	-0.07	0.01
	30.30	4.79	0.92	-0.08					
	35.58	4.86	0.94	-0.07	-0.62	5.17	4.58	0.03	-0.02
	39.00	4.64	0.89	-0.11					
	46.25	4.59	0.88	-0.12	-0.66	5.24	4.70	0.01	0.00
47.92	4.35	0.84	-0.18	-0.44	5.94	5.34	-0.11	-0.06	
Surface Seawater #2	Dark	5.54			-0.95	-0.11	-0.03	0.00	-0.11
	0.00	5.25	1.00	0.00	-0.83	0.03	-0.04	0.104	0.07
	7.37	5.24	1.00	0.00	-1.01	0.82	0.72	-0.01	0.05
	10.58	4.93	0.98	-0.02	-0.98	0.96	0.84	-0.02	0.03
	13.83	4.94	0.95	-0.05	-0.87	1.72	1.54	-0.03	0.00
	19.75	4.92	0.95	-0.05	-0.87	2.21	2.01	-0.04	-0.05
	23.08	4.77	0.91	-0.10					
	32.33	4.80	0.95	-0.05	-0.77	2.76	2.40	-0.07	0.10
	35.75	4.65	0.90	-0.11	-0.77	3.30	2.91	-0.03	0.00
	56.75	4.02	0.82	-0.20	-0.64	3.72	3.36	0.03	-0.07
LMW-DOC (<1KDa)	Dark	7.44			-0.95	-0.11	-0.03	0.00	-0.11
	0.00	7.63	1.00	0.00	-1.04	0.13	0.10	-0.01	0.01
	4.50	6.81	0.89	-0.11					
	7.37	6.44	0.84	-0.17	-0.98	1.37	1.21	-0.06	-0.02
	10.67	5.70	0.75	-0.29	-1.01	1.56	1.38	-0.01	0.04
	19.75	5.94	0.78	-0.25					
	23.08	5.15	0.67	-0.39	-0.65	3.95	3.47	0.02	-0.02
	32.33	5.31	0.70	-0.36					
	35.75	4.94	0.65	-0.43	-0.56	5.30	4.74	0.05	-0.02
Surface Seawater High MMHg	Dark								
	0.00	30.12	1.00	0.00	-1.05	0.09	0.01	0.00	0.01
	12.33	30.03	1.00	0.00					
	22.25	29.35	0.97	-0.03	-1.00	0.24	0.12	0.00	0.04
	36.17	29.33	0.97	-0.03					
	48.00	26.95	0.89	-0.11	-0.98	0.32	0.28	0.06	-0.03
59.83	23.12	0.77	-0.26	-0.85	0.42	0.31	0.01	-0.01	
Deionized ultra-pure water	Dark	8.39			-0.95	-0.11	-0.03	0.00	-0.11
	0.00	8.34	1.00	0.00	-1.08	0.09	0.06	-0.01	0.01
	7.75	6.70	0.80	-0.23	-0.98	1.42	1.61	0.00	0.04
	8.58	7.08	0.84	-0.17	-1.07	1.49	1.39	0.07	0.00
	13.83	6.96	0.83	-0.19	-0.99	1.32	1.16	0.03	0.01
	22.67	6.76	0.81	-0.22	-0.87	2.83	2.47	0.06	0.06
	38.33	6.34	0.76	-0.28					
	51.00	5.54	0.66	-0.42					
	59.92	4.23	0.50	-0.69	-0.45	3.41	2.99	-0.08	-0.08
Surface Seawater - Dark Control	0.0	3.26	1.00	0.00					
	81.2	3.22	0.99	-0.01					
	108.8	3.25	1.00	0.00					

Table S5.2b Laboratory experiments Hg stable isotope data and Hg

Treatment	Hours of Sunlight	[Hg] w/o BrCl (ng/g)	fraction remaining	ln(f)	$\delta^{202}\text{Hg}$	$\Delta^{199}\text{Hg}$	$\Delta^{201}\text{Hg}$	$\Delta^{204}\text{Hg}$	$\Delta^{200}\text{Hg}$
Cysteine #1	0.00	12.65	1.00	0.00	-1.07	0.12	0.02	0.03	0.02
	7.17	12.69	1.00	0.00	-0.99	0.15	0.12	0.05	0.02
	14.00	12.43	0.98	-0.02					
	20.00	12.20	0.93	-0.07	-1.08	0.19	0.10	0.01	0.02
	38.33	11.71	0.93	-0.07	-1.03	0.35	0.24	0.05	0.02
	42.83	8.84	0.71	-0.34	-0.83	0.78	0.56	-0.03	0.03
Cysteine #2	0.00	11.62	1.00	0.00	-0.88	0.11	0.08	-0.06	0.04
	5.88	11.50	0.99	-0.01					
	7.55	11.43	0.98	-0.02	-0.97	0.07	-0.02	-0.11	0.07
	40.38	10.95	0.94	-0.06	-1.06	0.28	0.12	0.03	-0.01
	75.38	5.43	0.47	-0.76	-0.63	0.90	0.68	-0.04	0.02
Serine	0.00	11.21	1.00	0.00	-0.88	0.12	0.10	-0.12	0.04
	0.83	11.10	0.99	-0.01					
	6.67	10.42	0.93	-0.07	-0.92	0.35	0.33	0.03	0.11
	17.83	8.39	0.75	-0.29	-0.79	0.91	0.76	0.09	0.03
	38.32	5.98	0.53	-0.63	-0.56	1.22	1.11	-0.02	0.04
Ethylenediamine	0.00	14.27	1.00	0.00	-1.07	0.03	0.06	0.07	0.02
	7.17	11.29	0.79	-0.23					
	14.00	10.84	0.76	-0.28	-1.06	0.50	0.37	0.04	0.03
	20.00	10.45	0.73	-0.31	-0.90	1.06	0.86	0.03	0.03
	28.33	10.63	0.74	-0.30					
	42.83	8.88	0.62	-0.47	-0.78	1.52	1.25	-0.02	0.03
Synthetic Seawater	0.00	12.13	1.00	0.00	-1.15	0.12	0.08	-0.03	0.01
	7.17	11.64	0.96	-0.04	-0.99	0.42	0.31	0.06	0.00
	14.00	11.25	0.93	-0.08	-1.01	0.53	0.42	0.01	-0.02
	17.17	10.26	0.85	-0.17	-0.99	0.71	0.61	0.02	0.04
	20.00	9.84	0.81	-0.21	-1.01	0.53	0.42	0.03	0.02
	28.33	9.43	0.78	-0.25					
	42.83	8.46	0.70	-0.36	-0.71	1.32	1.11	0.00	-0.01
Cysteine Dark Control	0.00	13.25	1.00	0.00					
	10.00	13.20	1.00	0.00					
	50.00	13.22	1.00	0.00					
Serine Dark Control	0.00	12.32	1.00	0.00					
	12.50	12.27	1.00	0.00					
	20.00	12.29	1.00	0.00					
Synthetic Seawater Dark Control	0.00	13.10	1.00	0.00					
	32.00	13.03	1.00	0.00					

Table S5.2c Zooplankton Hg stable isotope data and bulk Hg concentrations

Location	Time of Day	[Hg] Bulk (ng/g)	Size (mm)	$\delta^{202}\text{Hg}$	$\Delta^{199}\text{Hg}$	$\Delta^{200}\text{Hg}$	$\Delta^{201}\text{Hg}$	$\Delta^{204}\text{Hg}$
8 N	Day	46	0.2-1	0.29	2.93	0.11	2.54	-0.17
8 N		77	2.0-5.0	-0.10	1.06	0.12	0.88	-0.04
5N		40	0.2-1	0.36	1.99	0.06	1.76	-0.16
5N		59	2.0-5.0	-0.01	0.92	0.17	0.80	-0.32
8 N	Night	50	0.2-1	0.41	1.53	0.08	1.28	-0.11
8 N		54	2.0-5.0	0.12	1.13	0.13	0.94	0.00
5N		55	0.2-1	0.52	0.90	0.11	0.73	-0.14
5N		99	2.0-5.0	0.21	0.42	0.11	0.29	-0.17

Table S5.3 Surface zooplankton THg and MeHg concentrations and calculated MeHg isotopic composition

Location	Time of Day	Size (mm)	[Hg] Bulk (ng/g)	[MeHg] (ng/g)	Percent MeHg	$\delta^{202}\text{MeHg}$	$\Delta^{199}\text{MeHg}$
NPSG	Day	0.2-1	24*	2.1	9%	2.09	27.92
NPSG		2.0-5.0	21*	6.7	32%	0.38	4.87
NPSG		>5.0	23*	9.3	41%	-0.16	3.55
8 N		0.2-1	46	15.0	33%	0.73	8.39
8 N		2.0-5.0	77	36.0	47%	-0.30	1.92
5N		0.2-1	40	8.0	20%	1.51	8.90
5N		2.0-5.0	59	32.7	55%	-0.07	1.43
NPSG	Night	0.2-1	29*	1.8	6%	1.94	19.10
NPSG		2.0-5.0	21*	3.7	12%	0.12	3.94
NPSG		>5.0	19*	6.6	34%	0.41	3.04
8 N		0.2-1	50	8.3	17%	2.05	7.72
8 N		2.0-5.0	54	17.7	33%	0.19	2.82
5N		0.2-1	55	4.1	8%	5.88	8.39
5N		2.0-5.0	99	9.9	10%	1.40	1.56
Precipitation*	Avg. $\delta^{202}\text{Hg}$	SD $\delta^{202}\text{Hg}$	Avg. $\Delta^{199}\text{Hg}$	SD $\Delta^{199}\text{Hg}$			
	0.08	0.08	0.29	0.24			

*Data from Motta et al., 2019

Tables S5.4 – Hg complexes optimized geometries

Table S4a: Cartesian coordinates of MeHgCl in angstroms

ATOM	X	Y	Z
Hg	0.0382261760	0.0001272781	0.0001842408
C	2.1025587875	-0.0000243404	0.0000096174
H	2.4629030056	-0.5878792006	0.8535624868
H	2.4631629235	-0.4450989191	-0.9357577874
H	2.4632761173	1.0329047999	0.0825560939
Cl	-2.3012482922	0.0005362453	-0.0001649229

Table S4b: Cartesian coordinates of MeHgBr

ATOM	X	Y	Z
Hg	0.0350873974	0.0006288249	0.0002208685
C	2.1081154296	-0.0001033105	-0.0000914816
H	2.4676362234	-0.5893769397	0.8529083832
H	2.4674081895	-0.4443707327	-0.9369199140
H	2.4680571459	1.0331231448	0.0835970463
Br	-2.4234186126	0.0016174157	0.0006034577

Table S4c: Cartesian coordinates of MeHg⁺

ATOM	X	Y	Z
Hg	-0.2945432510	-0.4939307889	0.0948812275
C	1.7368736652	0.0261728114	-0.2998891979
H	1.6403769483	0.7117143731	-1.1489046573
H	2.1863033059	-0.9471203140	-0.5252633953
H	2.0474281776	0.4839611058	0.6456917736

Table S4d: Cartesian coordinates of MeHgOH₂⁺

ATOM	X	Y	Z
Hg	0.1236992833	0.0046817119	0.2313890604
C	2.0487693774	-0.3019850337	-0.4405783924
H	2.1444290752	0.2708607273	-1.3695850459
H	2.1495000725	-1.3811547907	-0.6002636942
H	2.7111321298	0.0685397370	0.3495909260
O	-1.9705750883	0.3251312873	0.9632136657
H	-2.7704989518	0.3217947641	0.4156069257
H	-2.2264642045	0.5673033532	1.8663644597

Table S4e: Cartesian coordinates of MeHgOH

ATOM	X	Y	Z
Hg	0.0084415323	0.0053563011	0.2425074630
C	1.9338524565	-0.2870415828	-0.4134700186
H	2.0941409825	0.2617393331	-1.3506550906
H	2.1107908564	-1.3567104298	-0.5852066565
H	2.6395921448	0.0794333569	0.3436366653
O	-1.8371931936	0.2992600325	1.0033746730
H	-2.5131688807	0.3058313920	0.3091864098

Table S4f: Cartesian coordinates of MeHgCysteine

ATOM	X	Y	Z
C	6.6315054436	0.1203937439	1.9750885468
C	8.0594304289	-0.0006845034	2.4941939558
C	9.0188302200	0.6947867576	1.5359142987
O	10.1778568589	1.0269296957	2.1575849201
O	8.8260283504	0.8900009962	0.3521754681
S	5.4626463070	-0.5776262091	3.2221871983
H	6.5403871711	-0.4222505912	1.0230667260
H	6.4113803783	1.1787466353	1.7826520846
N	8.4243685819	-1.4030219430	2.6732025231
H	8.1374140484	0.4899204229	3.4759147173
H	9.3359180115	-1.5066675771	3.1134061132
H	8.4362400489	-1.9005190245	1.7836503219
HG	3.4801630873	0.4904782497	2.4919905825
C	1.7203055375	1.4212825158	1.8700412158
H	10.7661567030	1.4072058545	1.4829467223
H	1.4274019671	1.0422492887	0.8818347748
H	1.8735569496	2.5072421512	1.8129901868
H	0.9203694757	1.2068732945	2.5915041263

Table S4g: Cartesian coordinates of MeHgSCH₃

ATOM	X	Y	Z
Hg	-0.2990659617	0.2941402756	-0.0213292977
C	-2.3767145643	0.4811139345	0.0009670757
H	-2.7345167725	0.5520111048	1.0368239184
H	-2.8287322817	-0.3972732156	-0.4794957961
H	-2.6736359323	1.3844144417	-0.5489117439
S	2.0535028942	0.0464009569	-0.0490621489
C	2.5762994989	1.8100416303	0.0070007766
H	3.6738899243	1.8141214618	0.0020981651
H	2.2329988961	2.3077209107	0.9227304826
H	2.2249744817	2.3670383778	-0.8708189763

Table S4h: Cartesian coordinates of MeHg(SCH₃)₂

ATOM	X	Y	Z
C	1.9229823174	-2.0704201912	-0.9468109523
C	-2.9297784731	-0.2048017679	0.6442802948
S	-2.3996584214	-0.9213209176	-0.9631575858
C	-0.6918047143	2.1675898329	0.3463506076
S	0.4922229982	0.9175963669	0.9941997025
Hg	0.0126462425	-1.1782149718	-0.6473232387
H	-3.5053553771	-0.9490631748	1.2125613657
H	-2.0524153046	0.1032721022	1.2308893495
H	-0.1482761384	3.0427854428	-0.0396619576
H	-1.3018100010	1.7492947129	-0.4694851297
H	-3.5678804611	0.6725540096	0.4624719381
H	-1.3727347292	2.5125714783	1.1408071830
H	1.8642152312	-3.0570639104	-1.4283526026
H	2.4104701017	-2.1693742298	0.0338529229
H	2.5278962259	-1.3963034663	-1.5705011709

Table S4i: Cartesian coordinates of MeHg(SCH₃)₃

ATOM	X	Y	Z
C	1.2042943822	-2.0168712828	-1.5809522533
C	1.8342819990	2.7979042308	0.1276330138
S	1.7906453788	1.3899356785	1.3091647486
C	-1.7696044533	1.8989370812	-0.0877508439
S	-0.9622025215	1.3130304664	-1.6357331312
C	-2.1504368665	-1.9900801397	-0.0639581107
S	-1.1644413092	-1.5499168296	1.4291529357
Hg	0.7786749020	-0.3755906509	-0.2211488606
H	2.7535454136	2.7861833656	-0.4807807060
H	0.9710014642	2.7414670183	-0.5546605344
H	-2.0447735033	1.0407047512	0.5463150578
H	-1.0796317217	2.5268265455	0.5005873078
H	-2.3394371288	-1.0947376903	-0.6781828041
H	-1.6093224050	-2.7146132367	-0.6957725981
H	1.8020357651	3.7482600858	0.6861162975
H	-2.6729038921	2.4898585261	-0.3165137022
H	-3.1163129396	-2.4406669368	0.2220639080
H	2.1860355117	-1.9111757960	-2.0705787819
H	0.4165883356	-2.0241561400	-2.3494399107
H	1.1774470211	-2.9614556239	-1.0151517512

Table S5.5. Vertical excitation energies of Hg complexes in nm. In the gas phase at the EOM-CCSD level of theory and energy correction in nm for non-equilibrium solvation effects using the TDDFT/pt(SS+LR)-PCM method.

Molecule	Gas phase - EOM-CCSD		Non-equilibrium TDDFT/pt(SS+LR)-PCM	
	S	T	S	T
CH ₃ HgCl	189	209	2.6	0.8
CH ₃ HgBr	205	216	3.2	0.6
CH ₃ Hg ⁺	220	358	5.6	7.6
CH ₃ HgO ₂ H ⁺	174	233	4.1	2.0
CH ₃ HgOH	209	225	0.6	1.8
CH ₃ HgCysteine	259	268	4.4	2.8
CH ₃ HgSCH ₃	265	272	4.6	2.9
CH ₃ Hg(SCH ₃) ₂	281	294	5.9	2.0
CH ₃ Hg(SCH ₃) ₃	338	343	4.6	0.6

All the energies are in nm

T triplet state

S singlet state

References

1. Müller, B. ChemEQL, User's Guide to Application. (2015).
2. Lamborg, C. H., Tseng, C. M., Fitzgerald, W. F., Balcom, P. H. & Hammerschmidt, C. R. Determination of the mercury complexation characteristics of dissolved organic matter in natural waters with 'reducible Hg' titrations. *Environ. Sci. Technol.* **37**, 3316–3322 (2003).
3. Motta, L. C. *et al.* Mercury cycling in the North Pacific Subtropical Gyre as revealed by mercury stable isotope ratios. *Global Biogeochem. Cycles* 2018GB006057 (2019). doi:10.1029/2018GB006057
4. Wiebe, P. H. *et al.* New development in the MOCNESS, an apparatus for sampling zooplankton and micronekton. *Mar. Biol.* **87**, 313–323 (1985).
5. Biswas, A., Blum, J. D., Bergquist, B. A., Keeler, G. J. & Xie, Z. Natural mercury isotope variation in coal deposits and organic soils. *Environ. Sci. Technol.* **42**, 8303–8309 (2008).
6. Blum, J. D. & Johnson, M. W. Recent Developments in Mercury Stable Isotope Analysis. *Rev. Mineral. Geochemistry* **82**, 733–757 (2017).
7. Lauretta, D. S., Klaue, B., Blum, J. D. & Buseck, P. R. Mercury abundances and isotopic compositions in the murchison (CM) and Allende (CV) carbonaceous chondrites. *Geochim. Cosmochim. Acta* **65**, 2807–2818 (2001).
8. Blum, J. D. & Bergquist, B. A. Reporting of variations in the natural isotopic composition of mercury. *Anal. Bioanal. Chem.* **388**, 353–359 (2007).
9. York, D. *et al.* Unified equations for the slope, intercept, and standard errors of the best straight line. **367**, 642–646 (2004).
10. Bloom, N. Determination of picogram levels of methylmercury by aqueous phase ethylation, followed by cryogenic gas chromatography, with cold vapour atomic fluorescence detection. *Can. J. Fish. Aquat. Sci.* **46**, 1131–1140 (1989).
11. Piecuch, P., Kowalski, K., Pimienta, I. S. O. & McGuire, M. J. *Recent advances in electronic structure theory: Method of moments of coupled-cluster equations and renormalized coupled-cluster approaches. International Reviews in Physical Chemistry* **21**, (2002).
12. Kowalski, K. & Piecuch, P. New coupled-cluster methods with singles, doubles, and noniterative triples for high accuracy calculations of excited electronic states. *J. Chem. Phys.* **120**, 1715–1738 (2004).
13. Schmidt, M. W. *et al.* General Atomic and Molecular Electronic Structure System. **14**, 1347–1363 (1993).
14. Gordon, M. S. & Schmidt, M. W. Theory and Applications of Computational Chemistry: the first forty years. in *Theory and Applications of Computational Chemistry* (eds. Dykstra, C. ., Frenking, G., Kim, K. . & Scuseria, G. E.) 1167–1189 (Elsevier, 2005). doi:10.1016/B978-044451719-7/50072-X
15. Zimmerman, P. M. Strong correlation in incremental full configuration interaction. *J. Chem. Phys.* **146**, (2017).
16. Mewes, J. M. *et al.* Experimental benchmark data and systematic evaluation of two a posteriori, polarizable-continuum corrections for vertical excitation energies in solution. *J. Phys. Chem. A* **119**, 5446–5464 (2015).
17. Black, F. J., Poulin, B. A. & Flegal, A. R. Factors controlling the abiotic photo-degradation of monomethylmercury in surface waters. *Geochim. Cosmochim. Acta* **84**, 492–507 (2012).

18. Lehnherr, I. & Louis, V. L. S. Importance of Ultraviolet Radiation in the Photodemethylation of Methylmercury in Freshwater Ecosystems. *Environ. Sci. Technol.* **43**, 5692–5698 (2009).
19. Hammerschmidt, C. R. & Fitzgerald, W. F. Iron-mediated photochemical decomposition of methylmercury in an arctic Alaskan Lake. *Environ. Sci. Technol.* **44**, 6138–6143 (2010).
20. DiMento, B. P. & Mason, R. P. Factors controlling the photochemical degradation of methylmercury in coastal and oceanic waters. *Mar. Chem.* **196**, 116–125 (2017).
21. Motta, L. C., Kritee, K., Blum, J. D., Tsui, M. T. & Reinfelder, J. R. Hg Isotope Fractionation During the Photochemical Reduction of Hg(II) Coordinated With Organic Ligands. *J. Phys. Chem. A*
22. Salikhov, K. *Magnetic Isotope Effect in Radical Reactions - Introduction*. (1996).
23. Buchachenko, A. L. Magnetic isotope effect: Nuclear spin control of chemical reactions. *J. Phys. Chem. A* **105**, 9995–10011 (2001).
24. Turro, N. J. Influence of nuclear spin on chemical reactions: Magnetic isotope and magnetic field effects (A Review). *Proc. Natl. Acad. Sci.* **80**, 609–621 (2006).
25. Turro, N. J., Ramamurthy, V. & Scaiano, J. C. *Modern Molecular Photochemistry of Organic Molecules*. (University Science Book, 2010).
26. Step, E. N., Buchachenko, A. L. & Turro, N. J. Magnetic effects in the photolysis of micellar solutions of phenacylphenylsulfone. *Chem. Phys.* **162**, 189–204 (1992).
27. Turro, N. J. & Kraeutler, B. Magnetic Isotope and Magnetic Field Effects on Chemical Reactions. Sunlight and Soap for the Efficient Separation of, ¹³C and ¹²C Isotopes. *J. Am. Chem. Soc.* **100**, 7432–7434 (1978).
28. Turro, N. J. & Mattay, J. Photochemistry of Some Deoxybenzoins in Micellar Solutions. Cage Effects, Isotope Effects, and Magnetic Field Effects. *J. Am. Chem. Soc.* **103**, 4200–4204 (1981).
29. Turro, N. J., Zimmt, M. B. & Gould, I. R. Dynamics of Micellized Radical Pairs. Measurement of Micellar Exit Rates of Benzylic Radicals by Time-Resolved Flash CIDNP and Optical Spectroscopy. *J. Am. Chem. Soc.* **105**, 6347–6349 (1983).

Chapter 6 Mercury Magnetic Isotope Effect: A Plausible Photochemical Mechanism

Co-authored with Alan D. Chien, Alan S. Rask, and Paul M. Zimmerman. Mercury Magnetic Isotope Effect: A Plausible Photochemical Mechanism. **In prep** for *Journal of American Chemical Society Communication*

“Those who are in love with practice without theoretical knowledge are like a sailor who goes onto a ship without rudder or compass and who never can be certain whither he is going – Practice must always be founded on sound theory” Leonardo Da Vinci (1510 – Leonardo’s Notebooks)

Abstract: Large mass-independent fractionation signatures in Hg have been observed in the laboratory and the environment, prompting deep questions about the chemical reasons behind these signatures. Since the relative lack of mechanistic information about Hg chemistry in the environment has precluded explanations of these isotope effects, the present study uses high-level electronic structure methods to evaluate possible photochemical mechanisms for mass-independent isotope effects in HgX_2 and CH_3HgX ($\text{X} = \text{Cl}, \text{Br}, \text{I}, \text{SCH}_3$). The results show that spin-orbit coupling wipes out the potential of mass-independent isotope effects (MIE) for Hg bound to Br or I, but that complexes involving lighter elements, HgX_2 and CH_3HgX ($\text{X} = \text{Cl}$ and SCH_3) have relatively small spin-orbit couplings upon photolysis. This unexpected finding shows that magnetic isotope fractionation due to hyperfine coupling is possible, depending on the identity of the Hg complex. By examination of the photolysis potential energy profiles, this study shows that HgX_2 complexes can have positive or negative MIEs (depending on reaction conditions), while CH_3HgX complexes exclusively result in positive MIE. These findings agree with MIE recorded in natural samples, demonstrating a plausible mechanism for the surprising mass-independent fractionation of Hg in the environment.

6.1 Introduction

A growing number of studies over the last decade have shown that isotope signatures can provide useful information to inform Hg transformations in the environment.¹⁻³ More specifically, Hg compounds have been shown to have anomalous fractionation of the odd isotopes (¹⁹⁹Hg and ²⁰¹Hg), and these signatures are preserved in biologic tissue of pelagic fish from around the world.¹ The ubiquity of Hg compounds in the aquatic food web gives these signatures paramount importance towards understanding the Hg cycle in the environment. The interpretation of these isotopic signatures is difficult, however, due to the limited information about the possible transformations of the relevant Hg compounds in nature. Though the mechanisms that control the fractionation remain unclear, they are postulated to occur during photochemical decomposition,⁴ with the isotope signatures being measured in the residual, undecomposed Hg species.

Experimental studies suggest the isotope fractionation patterns follow the magnetic isotope effect.⁴⁻⁶ Magnetic isotope effects typically arise from the formation of long-lived, solvent-separated radical pair intermediates upon direct photolysis, mediated by the radical pair mechanism.⁷⁻⁹ While magnetic isotope effects are considered the cause of the isotopic signatures of photolysis, it is unclear how it applies to heavy elements like Hg, because elevated spin-orbit coupling (SOC) may induce spin relaxation or phosphorescence that inhibits the formation of a separated radical pair at dissociation.^{10,11} It is also difficult to evaluate the source of isotope effects because the photochemical reaction mechanism for Hg compounds in natural waters remains uncertain. For example, while hydroxyl radicals were implicated as photochemical initiators for decomposition of Hg complexes,¹² singlet oxygen was later proposed as the reaction initiator because the concentration of hydroxyl radicals in natural waters is too low.¹³ Recently Black et al.¹⁴ reported that neither singlet oxygen nor hydroxyl radicals were involved in the photochemical

decomposition of CH₃Hg compounds in natural waters by employing various reactive oxygen species scavengers. This uncertainty has led to the hypothesis that multiple reaction pathways for Hg-compound photodegradation are operative, with somewhat contradictory conclusions about the role of dissolved organic matter,^{13,15,16} photoactive trace metals,^{14,17} and ultimately, reaction mechanism.^{13,14,18–20}

The magnetic isotope effect arises from the radical pair mechanism, which depends directly on the formation, reactivity, and spin multiplicity of the radical pair intermediates.⁹ In this mechanism the two electronic states of radical pairs (excited and ground state) become quasi-degenerate as the two radical centers separate, and the spin state of the radical pair will control the sign of MIE in the residual Hg compound.⁷ The essential features of these photophysical effects are illustrated in Figure 1. The magnetic isotope effect arises from the spin coherent evolution of a solvent-separated radical pair where hyperfine coupling (HFC) effects alter the rate of intersystem crossing (ISC) T↔S for odd isotopes. When separated radical pairs are generated in a singlet state, the magnetic isotopes (e.g. ¹⁹⁹Hg, ²⁰¹Hg) induce HFC to convert these into a triplet state (Fig 1a). The resulting triplet radical pairs cannot recombine to remake their photolyzed bond, but the singlet radical pairs (e.g. from non-magnetic isotopes) may recombine. The triplet Hg complexes thus degrade, while the singlet Hg survives photolysis. For radical pairs initially generated as singlet states, the overall effect will result in odd isotope depletion (– MIE). In the reverse case, radical pairs generated in the triplet state will experience HFC in magnetic isotopes, resulting in return to the singlet state and positive MIE (Fig 1b). The relevance of the MIE mechanism depends on low SOC in the dissociated complexes, where high SOC would otherwise overwhelm the HFC interactions.

6.2 Results and Discussion

In natural waters Hg tends to form divalent linear complexes with dissolved ions in solution or with dissolved organic matter,^{21–25} where the speciation is dominated by HgX_2 and to a lesser extent by CH_3HgX where $\text{X} = \text{OH}$, halides, or organic S, N, or O ligands. The CH_3Hg species in particular are of major importance since they bioaccumulate in aquatic foodwebs, and ultimately are environmental toxins. Despite the importance of the photodecomposition of CH_3Hg species in the biogeochemical cycle of Hg, there have been no experimental or theoretical studies on the electronic structure of the low-lying excited states of CH_3Hg complexes.^{26,27} Therefore we employed a range of high-level electronic structure methods to investigate the plausibility of magnetic isotope effects in CH_3Hg and HgX_2 complexes, to inform whether MIE could be due to photolysis of Hg in natural waters.

CH_3HgCl has a C_{3v} symmetry and the ground state (1^1A_1) has a valence orbital configuration ($1a_1^2, 1e_{nb}^4, 2a_{1nb}^2, 3a_1^{*0}, 2e^{*0}, 4a_1^{*0}$). CH_3HgCl has a manifold of ligand to metal charge transfer (LMCT; Figure 2 and Table S1) states, where the lowest singlet is a LMCT transition from the Cl to the Hg ($\pi\sigma^* 1^1\text{E}$) and the lowest triplet LMCT transition from the C to Hg ($\sigma\sigma^* 1^3\text{A}_1$) is degenerate with the Cl to Hg ($\pi\sigma^* 1^3\text{E}$) triplet transition. Photodissociation of CH_3HgCl prefers to cleave the Hg-C bond, which is energetically more favorable by 17 kcal/mol compared to Hg-Cl cleavage (SI section 4; Fig S1 and 2). This agrees with photodecomposition studies of CH_3Hg halides that show the same preference.²⁰ As the Hg-C bond breaks, the triplet $\sigma\sigma^*$ transition becomes quasi-degenerate with the singlet ground state (Figure 2). A cross-section of the potential energy surface as a function of the C-Hg-Cl bond angle (Fig 1b) from C_{3v} (180°) to C_1 (70°) demonstrates that excited states involving transitions to the σ^* prefer nonlinear geometries,^{28,29} resulting in the triplet $\sigma\sigma^*$ state having a bent equilibrium geometry (Table S2).

For CH₃HgCl photolysis to result in magnetic isotope effects the triplet $\sigma\sigma^*$ state needs to be populated near the time of initial photoexcitation of the complex. Marcus theory^{30,31} (see SI section 3 for details), predicts that after photoexcitation of CH₃HgCl to the lowest singlet state ($\pi\sigma^*$) there is efficient ISC ($\tau = 0.12$ ps, SOC 528.4 cm⁻¹; Figure 3) to the triplet $\pi\sigma^*$ 1^3E state, which is degenerate with the triplet $\sigma\sigma^*$. Internal conversion to the lower triplet state is therefore highly plausible, allowing dissociation of CH₃HgCl into a radical pair on the triplet $\sigma\sigma^*$ manifold.

Although the Hg-C dissociation via the triplet $\sigma\sigma^*$ state results in a separated radical pair, it has been suggested that there is no spin barrier to recombination when heavy elements are involved, and thus the reactivity of these species will be independent of the spin state.³² While this argument relies on the SOC being high in the radical pair, Figure 3a shows that the SOC between the triplet $\sigma\sigma^*$ and the ground state rapidly decrease as the Hg-C dissociates. Spin relaxation to other states is also unlikely because as the Hg-C ruptures there is an increasing energy gap between these states (Fig 2). Thus there are only two states available at dissociation for CH₃HgCl, and these are uncoupled by SO effects, making it unlikely that SO interactions will completely suppress the radical pair formation necessary for magnetic isotope effects.

The separated triplet radical pair, $^3[\text{ClHg}\cdot \cdot\text{CH}_3]$, can undergo HFC-mediated ISC to the singlet radical pair whenever magnetic isotopes of Hg are involved. The resulting singlet radical pairs will then undergo recombination to the ground state, resulting in (+) MIE (Fig 1b).

Having investigated methyl-Hg complexes, the photolysis of HgCl₂^{28,29,33} was examined to elucidate possible magnetic isotope effects by HgX₂ species (Fig 4a,b) with the $\sigma_g^{+2}\pi_u^{nb4}\pi_g^{nb4}\sigma_u^{+nb2}\sigma_g^{+*0}\pi_u^{*0}\sigma_u^{+*0}$ orbital configuration. The lowest singlet excited state of HgCl₂ is the dark $1^1\Pi_g(\pi_u\sigma_g^*)^1$ state and the lowest bright state is $1^1\Pi_u(\pi_u\sigma_u^*)^1$, which is degenerate with the $1^3\Sigma_u^+(\sigma_u\sigma_g^*)^3$ state (Fig 4). As the Hg-Cl bond ruptures, the $1^{1,3}\Pi_g(\pi_u\sigma_g^*)^{1,3}$, $1^3\Sigma_u^+(\sigma_u\sigma_g^*)^3$,

and the ground state become degenerate, indicating the possibility of dissociation into a triplet or singlet radical pair. Although the $1^{1,3}\Pi_g (\pi_u\sigma^*_g)^{1,3}$ and $1^3\Sigma^+_u (\sigma_u\sigma^*_g)$ transitions are symmetry or spin forbidden, there is considerable SOC between the first bright singlet state $1^1\Pi_u$ and $1^3\Pi_u$ (598.19 cm^{-1}) with estimated ISC average time constants of 0.65 ps. $1^3\Pi_u$ and $1^3\Sigma^+_u$ states cross near the Frank-Condon region, allowing a route for population of the $1^3\Sigma^+_u$ state (Fig 4).

Since triplet and singlet states are degenerate for the separated radical pair, the photolysis of HgCl_2 may result in either (+) or (-) MIE. The sign of MIE will therefore depend on specifics of the recombination and degradation kinetics. Though quantifying these relative rates is beyond the scope of the present study, triplet state quenchers could selectively deactivate the $1^3\Pi_g$ and $1^3\Sigma^+_u$ states, and MIE would then only be possible via the singlet ($1^1\Pi_g$) channel. This is in contrast to CH_3HgCl , where the only decay channel available for MIE is a triplet state. Therefore (+) or (-) MIE may in principle be seen for HgCl_2 , the (-) MIE channel may be operative under triplet state quenching conditions.

While photolysis of HgCl_2 is plausible via triplet and singlet radical pair states, dissociation of CH_3HgCl occurs primarily from the triplet radical pair ($^3\sigma\sigma^*$). The difference between the two lies in the accessibility and availability of lone pair orbitals for charge transfer, in the separated radical pair structure. The vertical electronic transitions of CH_3HgCl (Fig 6) include LMCT from the lone pair Cl π orbitals to the antibonding Hg-C σ^* ($1^{1,3}E$) and connect to four-fold degenerate separated radical pair states (two triplet, one excited singlet, and the ground state singlet), similar to HgCl_2 (Fig 4a). The four-fold degeneracy only occurs with rupture of the Hg-Cl bond, however, since the Hg-C bond dissociation is preferred (Fig 2) the Cl $\pi\sigma^*$ LMCT transitions are too high in energy to be relevant. The $\pi\sigma^*$ LMCT states therefore are photo physically most relevant in the absence of the CH_3 group, which does not contribute to π LMCT. Instead CH_3HgCl has only the triplet $\sigma\sigma^*$

LMCT state available upon dissociation of the Hg-C bond, because the singlet $\sigma\sigma^*$ is not dissociative (Fig 2a). This qualitative difference in electronic states upon photolysis of Hg complexes is therefore a function of ligand (Cl vs CH₃) electronic structure, and dictates the possible channels for magnetic isotope effects.

The results so far have examined photolysis of CH₃HgCl and HgCl₂, but these are model systems for Hg photochemistry in the sense that they do not absorb solar photons, and cannot be responsible for the MIE recorded in natural samples. In natural waters, however, Hg will preferentially complex with thiol ligands due to their high affinities. Since it is known that Hg(thiol)₂ and CH₃Hg(thiol) complexes absorb in the sunlight spectrum, they are good candidates for control of Hg photolysis in natural waters.^{13,18,34} To determine the likelihood that Hg-thiol complexes may be responsible for MIE in natural samples, the low-lying excited states for CH₃HgSCH₃ and Hg(SCH₃)₂ were thus investigated.

Hg pseudohalides, such as Hg-thiol complexes, have similar physical properties^{27,35-37} and HOMO and LUMO molecular orbital configurations^{27,36} as Hg halides. Their ground state configurations are similar to the chloride counterparts, for CH₃HgSCH₃ it is ($\pi^2, \sigma^2, \sigma^2, \pi_{nb}^2, \pi^{0*} \sigma^{0*} \pi^{0*} \sigma^{0*}$) and for Hg(SCH₃)₂ it is ($\pi^4, \sigma^2, \sigma_{nb}^2, \pi_{nb}^4, \sigma^{0*}, \pi^{0*}, \sigma^{0*}$). Computed lowest singlet states for CH₃HgSCH₃ and Hg(SCH₃)₂ have energies that match the absorption maxima of Hg thiol complexes in the UVB/A region (Figure 6).^{18,34,38,39} At dissociation of the Hg-S bond in Hg(SCH₃)₂ the ^{1,3} $\pi\sigma^*$ and ³ $\sigma\sigma^*$ states are degenerate with the ground state, similar to the case of HgCl₂ photolysis. For CH₃HgSCH₃ only the ³ $\sigma\sigma^*$ state is degenerate with the ground state, just as in CH₃HgCl. Since these are the states available (Fig 7) for potential radical-radical recombination and subsequent magnetic isotope effects, it is interesting to see that they closely parallel the Hg halides, except for being accessible via excitation within the solar spectrum.

Just as the excited state character of $\text{CH}_3\text{HgSCH}_3$ resembles CH_3HgCl , the mechanism for photolysis is also similar. During photolysis of $\text{CH}_3\text{HgSCH}_3$, the T_4 $^3\sigma\sigma^*$ state can be populated through internal conversion and ISC near the Frank-Condon geometry (Fig 7). This is supported by the large SOC between the bright S_1 state and T_3 (884.8 cm^{-1}), and T_3 is quasi-degenerate with T_4 and therefore accessible through internal conversion. Since the T_4 state rapidly drops in energy as the Hg-C bond ruptures, it is likely that it becomes the dominantly populated state for the resulting radical pair (Fig 2,7). At dissociated Hg-C bond distances, the SO $^3\sigma\sigma^*$ states have minimal SOC with the ground state. Just like CH_3HgCl , these findings suggest that the photolysis of $\text{CH}_3\text{HgSCH}_3$ may yield a (+) MIE.

The lowest bright singlet state of $\text{Hg}(\text{SCH}_3)_2$ ($\pi\sigma^*$) leads directly to photodissociation and also is close in energy with the lowest triplet state ($\pi\sigma^*$), which can be populated through ISC (SOCME = 71.6 cm^{-1} , $\Delta E = 0.08\text{ eV}$). And as the Hg-S bond ruptures, the $(\pi\sigma^*)^{1,3}$ states become degenerate with T_2 ($\sigma\sigma^*$), so all these states are likely populated and may result in the formation of the separated radical pair. The probability of mixing between these states is affirmed by the SOC between $(\pi\sigma^*)^3$ and $(\pi\sigma^*)^1$, which is 171.5 cm^{-1} at the Hg-S separated geometry (4.0 \AA). Like HgCl_2 , $\text{Hg}(\text{SCH}_3)_2$ may therefore yield (+) or (-) MIE depending on the reaction conditions. This agrees with recent experiments showing $\text{Hg}(\text{cysteine})_2$ yielded (-) MIE in the presence of dissolved oxygen, while in anoxic conditions it resulted in (+) MIE.⁴⁰ Dissolved oxygen is a well-known triplet state quencher and may inhibit the formation of radical pairs in the triplet state, resulting instead in MIE via HFC of the singlet.

The electronic structure simulations indicate that photolysis of CH_3HgX complexes can result in (+) MIE, while the photolysis of HgX_2 may yield (+) or (-) MIE depending on reaction conditions ($X = \text{Cl}$ and SCH_3). To further test this hypothesis, the low-lying excited states of two

additional CH₃Hg and Hg halides (Br and I) were investigated to determine if they follow similar mechanisms. The complexes share with their chlorides and thiols counterparts with the same vertical transitions at the Frank-Condon geometry and similar dissociation profiles. SOC with the ground state, however, is much higher for these complexes, being on average 670 cm⁻¹ for CH₃HgBr and HgBr₂ and 2060 cm⁻¹ on average for CH₃HgI and HgI₂. These couplings will result in significant triplet-singlet mixing compared to mercuric chloride counterparts (see Table S4,5, and 6), and these complexes are unlikely to exhibit magnetic isotope effects due to the inhibition of radical pair formation. This inhibition is supported by time-resolved liquid X-Ray diffraction experiments, which found that over 60% of excited HgBr₂ or HgI₂ decay to the ground state on 10 ps time scales.^{41,42}

Having examined the detailed electronic structure for photolysis of Hg complexes, the results suggest that photolysis in natural waters may result in magnetic isotope effects, which in turn can explain isotope signatures recorded in natural samples. By specifically measuring the degree of SOC in various Hg complexes, it is clear that complexes containing Br or I are unlikely to exhibit MIE due to strong SOC, but Cl and SCH₃ complexes have small SOC at separated radical pair geometries, permitting nuclear magnetic effects to come into play. For the potentially magnetic isotope effect-active complexes, HgX₂ may exhibit (+) or (-) MIE due to the availability of 4 degenerate electronic states in the radical pair, while CH₃HgCl only has 2 such states, which give rise to a (+) MIE. This explains the observed fractionation of natural samples of ¹⁹⁹Hg and ²⁰¹Hg, including why HgX₂ type complexes have significantly smaller anomalous isotope effects than CH₃HgX complexes.¹ The (+) MIE will be most obvious in CH₃Hg complexes because the ³σσ* LMCT state is energetically separated from other excited states in the radical pair, and therefore is prevented from transition to competing electronic states that may inhibit magnetic

isotope effects. As such, photolysis of the C-Hg of CH₃Hg maximizes magnetic isotope effects and results exclusively in (+) MIE, explaining why (-) MIE has never been recorded in natural samples of CH₃Hg.¹

6.3 Environmental Implications

Finally, the anomalous (+) MIE that has been recorded in biological tissue of pelagic fish from around the world can likely be explained by photolysis of CH₃Hg(thiol) complexes.¹ It has been suggested that CH₃Hg in natural waters is predominately coordinated to thiol ligands²¹⁻²⁵ and the lowest singlet transition of CH₃HgSCH₃ is available for photolysis in the UVB/A range.^{18,34,38,39} The magnetic isotope effect mechanism substantiated herein therefore can be used as a lens to examine the Hg cycle in the environment, providing deep insight into how biological samples of CH₃Hg are fractionated to mass-independent distributions.

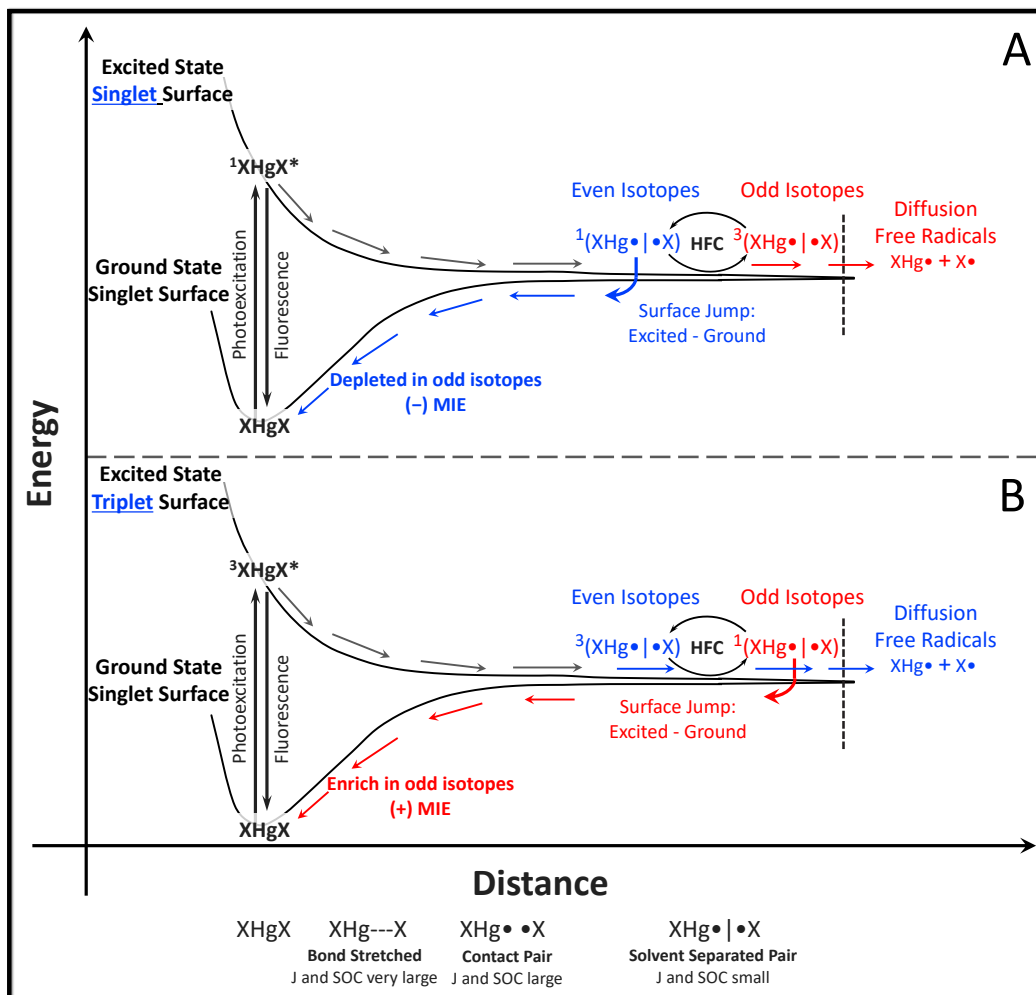


Figure 6.1. The radical pair mechanism for the magnetic isotope effect. The origin of MIE comes from the spin coherent evolution of the correlated solvent separated RP where hyperfine coupling affects may alter the rate of spin interconversion $T \leftrightarrow S$ of odd isotopes. At separated distances, SOC is not sufficient to induce $T \leftrightarrow S$ ISC because it requires some orbital overlap of the two radical centers to induce relaxation to the ground state, but when electron exchange (J) is close to zero at the dissociation the overlap is also close to zero.⁴³

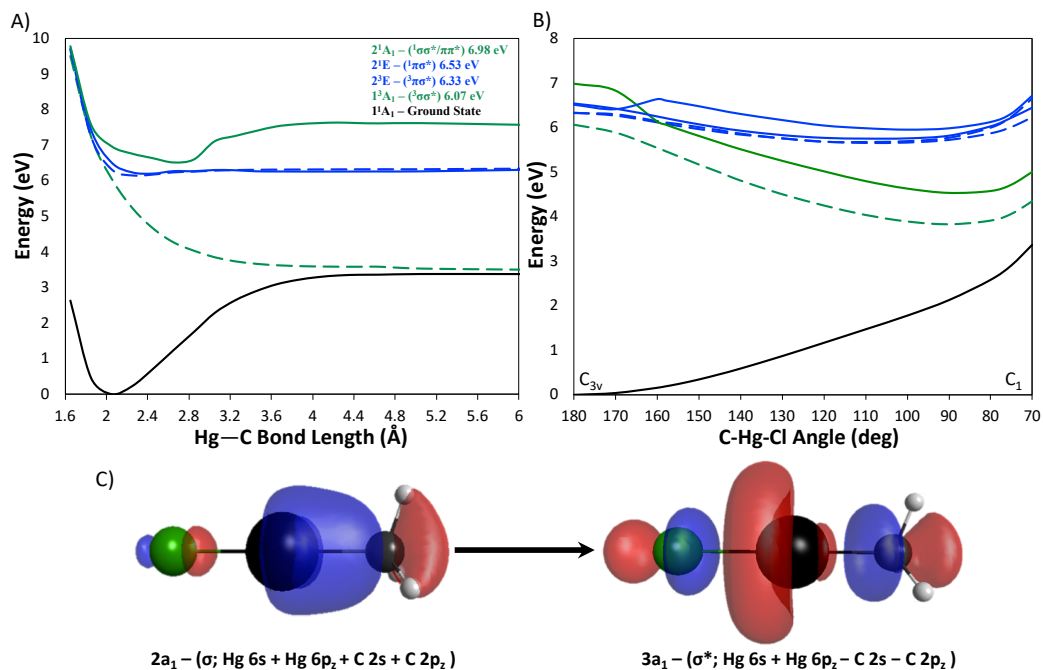


Figure 6.2. Potential energy curves of low-lying excited states of CH_3HgCl . The solid lines represent the singlet states and the dash lines the triplet states A) PEC as a function of the Hg-C bond length in C_{3v} symmetry. B) PEC as a function of C-Hg-Cl bending angle. As the C-Hg-Cl bends the $\pi\sigma^*$ will split into two states. Calculations at the MS-CASPT2(8,8)-IPEA(0.25 a.u)/ANO-RCC-VTZP level of theory from the ground state equilibrium geometry calculated at the MP2 level of theory. C) CASSCF orbitals for the triplet state dissociation transition ${}^32a_1 \rightarrow {}^33a_1^*$ (${}^3\sigma\sigma^*$).

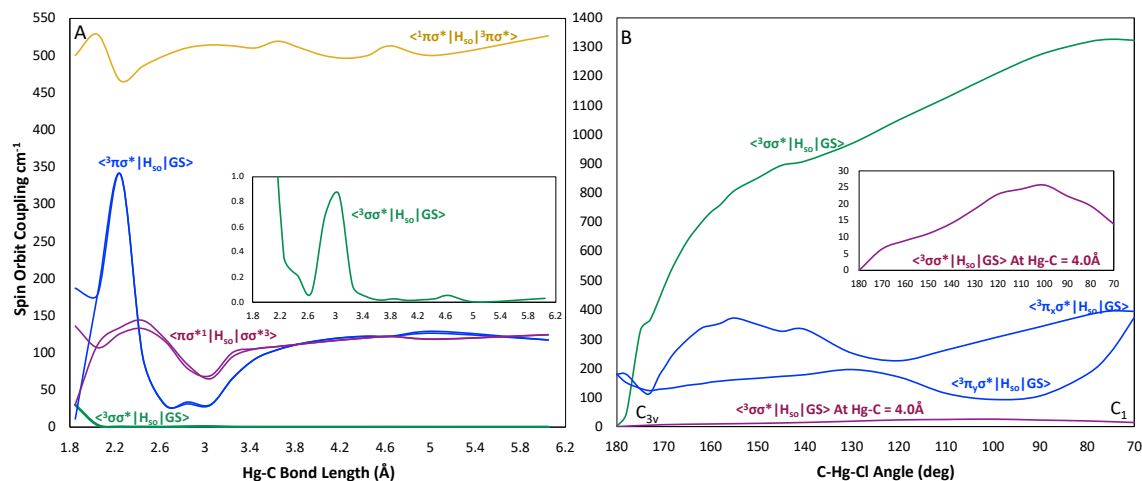


Figure 6.3. Absolute values of complex SO-Hamiltonian matrix elements over spin components of spin-free eigenstates (RASSI/MS-CASPT2) for CH₃HgCl. A) Matrix elements between the low-lying excited states and also the ground state as a function of Hg-C bond distance. B) Matrix elements between the low-lying triplet states and the ground states as a function of bond angle C-Hg. Inset matrix elements between the ³σσ* transition and the ground state with bending angle at dissociated Hg-C bond distances (4.0 Å)

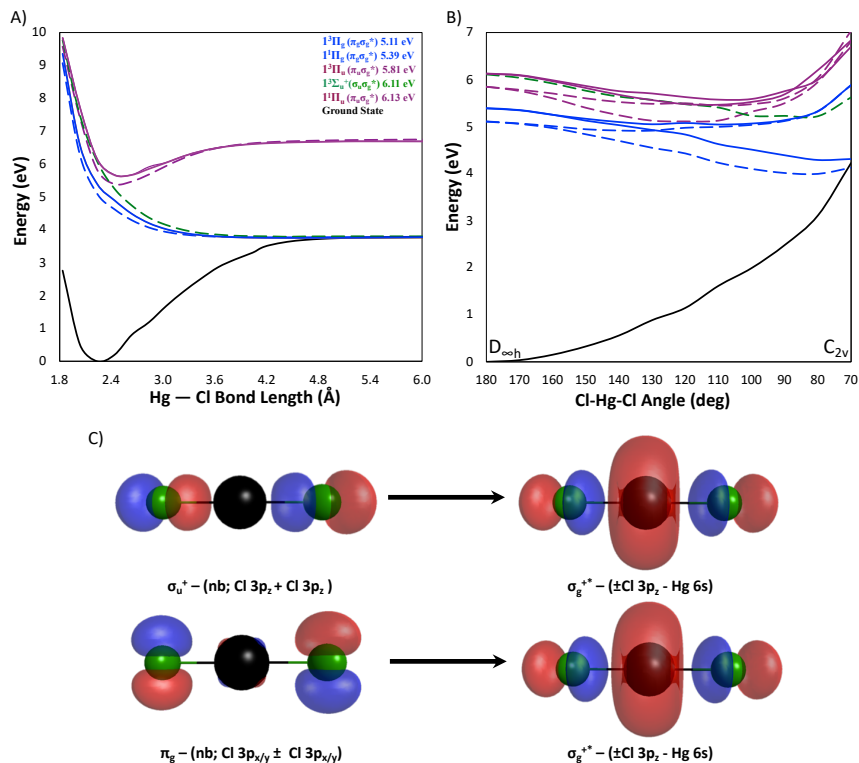


Figure 6.4. Potential energy curves of low-lying excited states of HgCl₂. The solid lines represent the singlet states and the dash lines the triplet states. A) PEC as a function of the Hg-Cl bond length. Excitation to the lowest singlet state (solid blue, $^1\pi_g\sigma_g$) is symmetry forbidden, the lowest bright singlet state is $^1\pi_u\sigma_g$ (solid purple). B) PEC as a function of Cl-Hg-Cl bending angle. As the Cl-Hg-Cl bends the $\pi\sigma_g^*$ states will split into two states. Calculations at the MS-CASPT2(8,8)-IPEA(0.25 a.u)/ANO-RCC-VTZP level of theory from the ground state equilibrium geometry calculated at the MP2 level of theory. C) CASSCF orbitals for the triplet and singlet dissociation transitions $^3\sigma_u\sigma_g^*$ and $^1,^3\pi_g\sigma_g^*$.

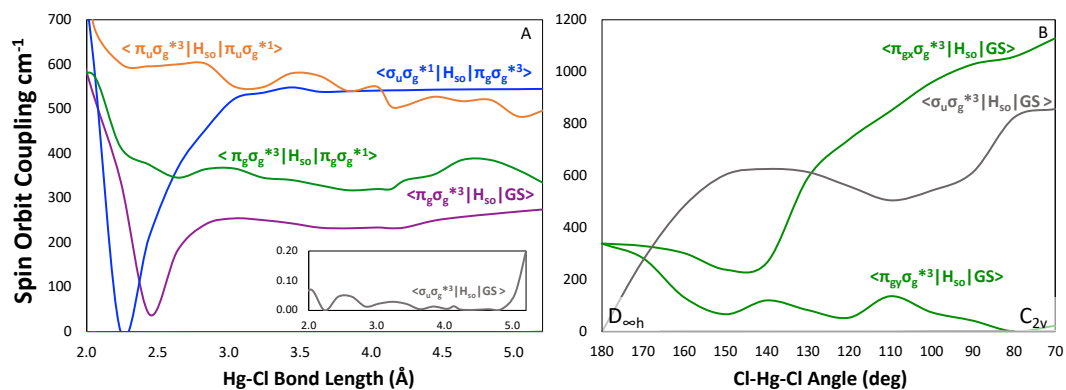


Figure 6.5. Absolute values of complex SO-Hamiltonian matrix elements over spin components of spin-free eigenstates (RASSI/MS-CASPT2) for HgCl₂. A) Matrix elements between the of low-lying excited states and also the ground state as a function of Hg-Cl bond distance. B) Matrix elements between triplet dissociative states and the ground states as a function of bond angle Hg-Cl.

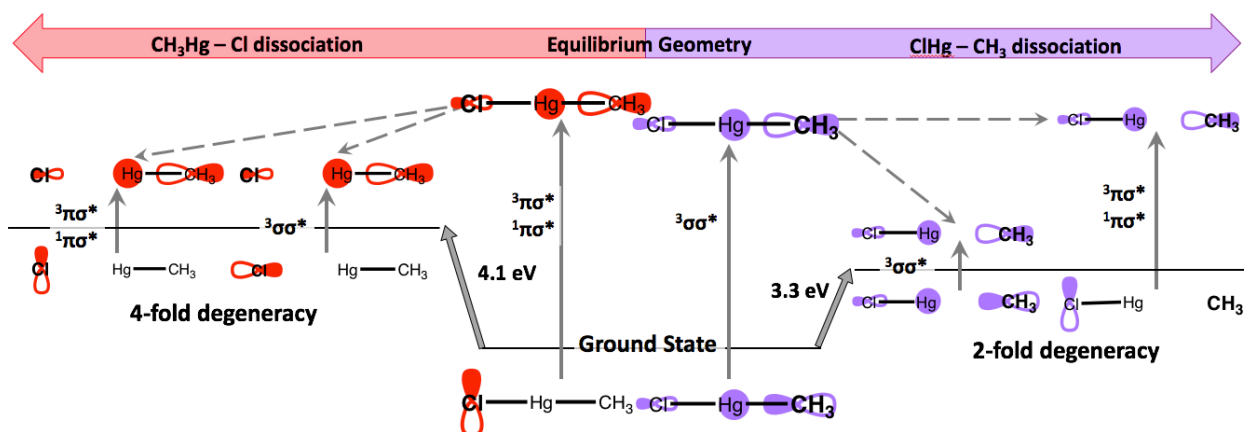


Figure 6.6. Low lying electronically excited states during Hg-Cl dissociation for CH_3HgCl . Left: Hg-Cl bond breaking. Middle: ground state equilibrium geometry. Right: Hg-C dissociation 4.0 \AA . Energies for dissociated states are based on 4.0 \AA separation.

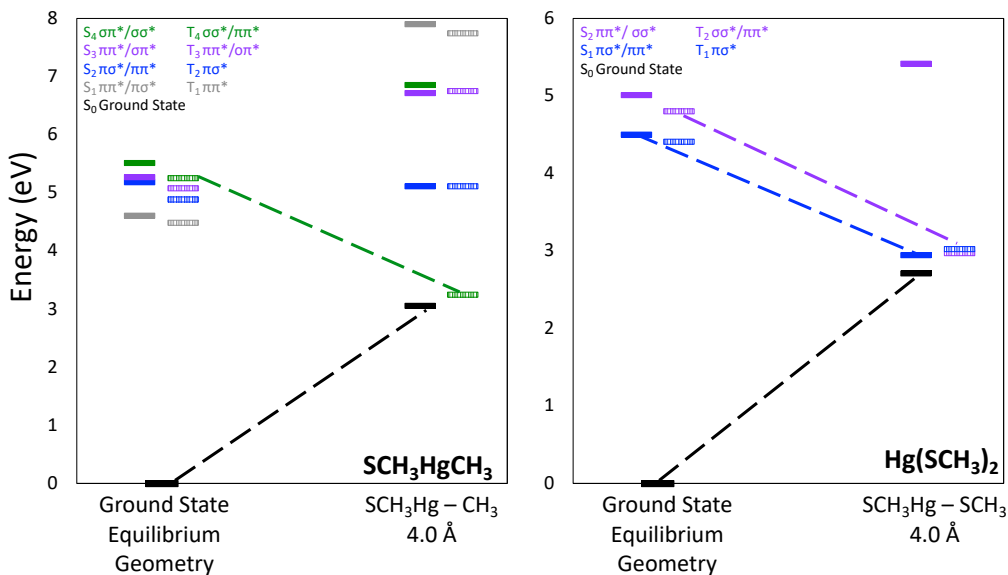


Figure 6.7. Vertical excitation energies at the ground state equilibrium geometry and at bond dissociated distances (4.0 \AA) for A) $\text{SCH}_3\text{HgCH}_3$ and B) $\text{Hg}(\text{SCH}_3)_2$. Calculated at the MS-CASPT2(8,8)-IPEA(0.25 a.u)/ANO-RCC-VTZP level of theory from the ground state equilibrium geometry calculated at the MP2 level of theory.

6.4 Supporting Information

6.4.1 Computational Details

The CASSCF¹/MS-CASPT2^{2,3}/SO-RASSI⁴ with the third order Douglas-Kroll and Hess (DKH3)^{5,6} Hamiltonian and the atomic-natural-orbital relativistic-correlation-consistent (ANO-RCC) basis set of valence triple- ζ plus polarization quality (ANO-RCC-VTZP) as implemented in OPENMOLCAS were used to investigate the photodissociation of the low-lying excited states of HgX₂ and CH₃HgX (X = Cl, Br, I, and SCH₃). For the HgX₂ calculations an active space of 12 active electrons over 10 natural orbitals (CAS, 12,10) $\sigma_g^{+2} \pi_u^{nb4} \pi_g^{nb4} \sigma_u^{+nb2} \sigma_g^{+*0} \pi_u^{*0} \sigma_u^{+*0}$, which was shown to be effective for describing their excited states in previous studies.⁷ For the CH₃Hg calculations a CAS(8,8) with the following configuration $1a_1^2, 1e_{nb}^4, 2a_{1nb}^2, 3a_1^{*0}, 2e^{*0}, 4a_1^{*0}$ was chosen and the performance was compared with that of a CAS(12,10) taking into account additional 5d occupied orbitals of Hg.

For the state-average CASSCF computations of HgX₂ at the equilibrium geometry 8 average roots in all irreps of the subgroup of D_{∞h} group D_{2h} were calculated to get an accurate description of the singlet-triplet mixing and overall Spin-Orbit (SO) states. Upon breaking or bending the Cl-Hg-Cl bond 25 singlet and 25 triplets were calculated without symmetry. For the CH₃Hg complexes 25 singlets and 25 triplets were calculated without symmetry because C_{3v} is a non-abelian symmetry point group. 30 average roots were also tested for CH₃Hg to analyze possible contributions of higher-energy states. Finally, dynamic electron correlation was computed using the CASPT2 method with an imaginary level shift of 0.2 a.u to avoid any intruder states and ionization potential electron affinity (IPEA) shift of 0.25 a.u as suggested by previous studies of the Hg halide excited states. The interaction between the individual CASPT2 states was evaluated with the MS-CASPT2 method. To account for spin-orbit effects an all-electron basis set was used

with the third-order Douglas-Kroll and Hess Hamiltonian was used. To SOC matrix elements (SOCMEs) and SO excited states were evaluated with the restricted-active-space state-iteration (RASSI) method using the atomic mean-field approximation (AMFI).

The ground-state equilibrium geometries were optimized at MP2 level using DKH3 and ANO-RCC-VTZP basis sets imposing the constraints of D_{2h} for the mercuric halides and the experimental C_{3v} geometries were used as reference for the CH_3Hg halides.

6.4.2 Non-equilibrium water solvation

To get accurate vertical excitation energies of the Hg complexes we estimated the influence of water as a solvent using the polarizable continuum model (PCM) with and without explicit waters with time-dependent density functional theory (TDDFT) using the LRC- ω PBE functional, which has been shown very accurate for the calculation of vertical excitation energies⁸. To estimate the solvent effects in vertical excitations, we must consider non-equilibrium solvation because during the electronic transition the solute undergoes a sudden change in its charge distribution. To describe this non-equilibrium solvent effect, we used the linear response and state specific approach pt(LR+SS), which has been shown to be the most accurate when considering charge transfer transitions⁸. See Table SX for solvation effects.

6.4.3 Marcus Rate for Intersystem Crossing

Here we estimated a Marcus rate for ISC by direct SOC driven by the electronic character of the states and the vibrational density of states by using the Franck-Condon weighted density of states (FCWD), assuming the high temperature limit.⁹ The FCWD accounts for the reorganization energy (λ) and the adiabatic energy difference (ΔE) between the initial and final states at their respective minima. The λ accounts for the energy variation in the initial excited state when switching from the equilibrium geometry to the geometry of the state of interest. For states with

similar shaped PES the transition probability will depend exponentially on the adiabatic energy difference ($\lambda=0$), while states with divergent PES ISC will depend on the $\Delta E + \lambda$. The El-Sayed's rules do not directly apply to the photolysis of Hg complexes because they only address the purely electronic aspects of ISC and also do not account for the multiconfigurational character of the low-lying states of Hg complexes (Table S1,2, MS-CASPT2 wavefunctions).⁹ The reorganization energy was estimated using the equilibrium excited geometries derived from the potential energy surface of HgCl₂ and CH₃HgCl (Table X).

$$k_{ISC}^{IF} = \frac{2\pi}{\hbar} \langle {}^1\Psi | H_{so} | {}^3\Psi \rangle \cdot FCWD$$

$$FCWD = \frac{1}{\sqrt{4\pi\lambda RT}} e^{\left[-\frac{(\Delta E + \lambda)}{4\lambda RT}\right]}$$

6.4.4 Photodissociation of the Hg-Cl bond in CH₃HgCl

From the vertical excitation energies at the ground state geometry, it is unclear if the photodissociation of CH₃HgCl cleaves the C or Cl bond, however, Hg-C bond dissociation is energetically more favorable (17 kcal/mol; Fig 2, Fig S1).

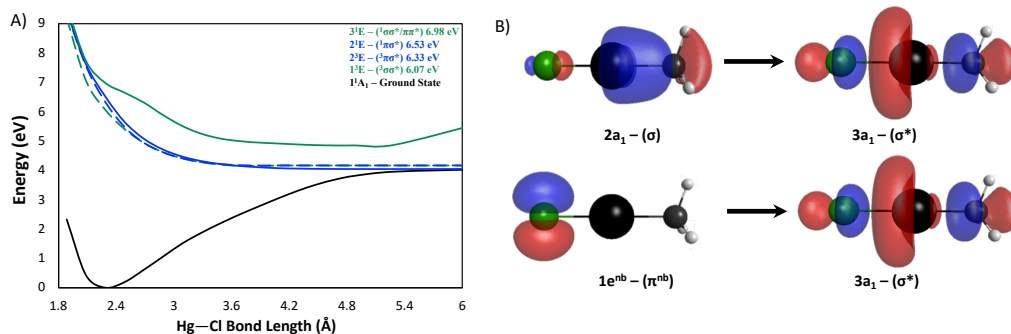


Figure S6.1. Potential energy curves of low-lying excited states of CH₃HgCl. The solid lines represent the singlet states and the dashed lines the triplet states A) PEC as a function of the Hg-Cl bond length in C_{3v} symmetry. Calculations at the MS-CASPT2(8,8)-IPEA(0.25 a.u)/ANO-RCC-VTZP level of theory from the ground state equilibrium geometry calculated at the MP2 level of theory. B) CASSCF orbitals for the triplet state dissociation transition ³2a₁3a₁* (³σσ*) and ^{1,3}1e^{nb}3a₁* (^{1,3}πσ*).

6.6 Supporting Tables

Table S6.1. Vertical electronic transitions of CH₃HgCl computed at the DKH3-SOC-MS-CASPT2-(8,8)/ANO-RCC-VTZP level of theory at the ground state geometry computed at the DKH3-MP2. Vertical excitation in eV (ΔE) and oscillator strengths (f) for the spin-free (SF) and spin-orbit (SO) states (left and right parts, respectively), the main orbital excitation which characterizes the SF states (column 2, only weights larger than 5% are given), and the main SF states contributing to the SO states (column 6, only weights larger than 3% are provided). Incremental full configuration vertical excitation energies at the ground state equilibrium geometry for the lowest triplet states computed at the Def2-TZVP level.

Spin-free States						Spin Orbit States			Exp.
SF State	Weight (%)	Excitation n	ΔE (eV)	f (au)	iFCI ΔE (eV)	SF-Weight (%)	ΔE (eV)	f (au)	ΔE (eV)
1 ³ A ₁	68	$\sigma_2 \rightarrow \sigma$	6.07		6.17	98 1 ³ E	6.07	2.32E-08	
	24	$\sigma_1 \rightarrow \sigma$					6.08	4.81E-04	
1 ³ E	94	$\pi \rightarrow \sigma$	6.33		6.17	94 2 ³ E - 3 4 ¹ E	6.27	1.61E-06	
						86 2 ³ E - 3 1 ¹ E ₁	6.30	5.98E-04	
						93 2 ³ E	6.36	6.12E-04	
1 ¹ E	92	$\pi \rightarrow \sigma$	6.53	1.04E-02		80 1 ¹ E - 5 2 ³ E - 8 4 ³ E	6.50	7.46E-03	6.26 ^a
2 ³ E	79	$\sigma_2 \rightarrow \pi$	6.83			95 3 ³ E - 3 1 ¹ E ₁	6.61	3.13E-02	
	8	$\sigma_1 \rightarrow \pi$					6.73	1.89E-02	
						68 3 ³ E - 28 2 ¹ E	6.73	1.89E-02	
						99 3 ³ E	7.07	9.11E-07	
1 ³ A ₁	95	$\pi \rightarrow \pi$	6.94			68 1 ³ A ₁ - 20 1 ³ A ₂ - 7 1 ¹ E	6.85	1.37E-03	
						67 1 ³ A ₁ - 20 1 ³ A ₂ - 8 1 ¹ E	6.86	1.59E-03	
						57 1 ³ A ₁ - 14 4 ¹ E - 10 4 ³ E - 9 1 ¹ A ₂ - 5 2 ³ E	6.92	4.45E-05	
3 ³ E	95	$\pi \rightarrow \pi$	7.11			40 4 ³ E - 34 4 ¹ E - 10 1 ³ A ₁	6.92	3.38E-05	
						90 4 ³ E - 7 1 ¹ E	7.00	4.28E-04	
						99 4 ³ E	7.31	3.85E-05	
2 ¹ E	40	$\sigma_2 \rightarrow \sigma$	6.98	2.12E-01		80 2 ¹ E - 9 1 ³ A ₂ - 6 3 ³ E	7.01	1.32E-01	
	38	$\pi \rightarrow \pi$							
	11	$\sigma_1 \rightarrow \sigma$							
3 ¹ E	73	$\sigma_2 \rightarrow \pi$	7.02	5.75E-02		70 3 ¹ E - 29 3 ³ E	7.17	3.57E-02	
	15	$\sigma_1 \rightarrow \pi$							
4 ¹ E	90	$\pi \rightarrow \pi$	7.13	5.98E-04		50 4 ¹ E - 47 4 ³ E	7.30	1.76E-04	
2 ¹ A ₁	95	$\pi \rightarrow \pi$	7.20	3.74E-05		73 2 ¹ A ₁ - 16 1 ³ A ₁ - 8 1 ³ A ₂	7.40	9.28E-03	
1 ³ A ₂	95	$\pi \rightarrow \pi$	7.25			77 1 ³ A ₂ - 10 2 ¹ E - 7 2 ¹ A	7.30	-	
						76 1 ³ A ₂ - 24 1 ³ A ₁	7.43	-	
						76 1 ³ A ₂ - 24 1 ³ A ₁	7.43	-	
Bond length Hg-C (Å)		2.047						2.061 ^{b,c}	
Bond length Hg-Cl (Å)		2.283						2.282 ^{b,c}	

Table S6.2. Vertical electronic transitions of HgCl₂ computed at the DKH3-SOC-MS-CASPT2-(12,10)/ANO-RCC-VTZP level of theory at the ground state geometry computed at the DKH3-MP2. Vertical excitation in eV (ΔE) and oscillator strengths (f) for the spin-free (SF) and spin-orbit (SO) states (left and right parts, respectively), the main orbital excitation which characterizes the SF states (column 2, only weights larger than 5% are given), and the main SF states contributing to the SO states (column 7, only weights larger than 3% are provided).

Spin Free States						Spin Orbit States				Exp.
SF State	Weight (%)	Excitation	ΔE (eV)	f (au)	ANO-RCC-VQZP ^a	SO Term Symbol	SF-Weight (%)	ΔE (eV)	f (au)	ΔE (eV)
1 ³ Π_g	88	$\pi_g \rightarrow \sigma_g$	5.11		5.15	2 _g	99 1 ³ Π_g	5.07	-	
						1 _g	97 1 ³ Π_g 3 1 ¹ Π_g	5.11	-	
						0 _g ⁺	99 1 ³ Π_g	5.17	-	
						0 _g ⁻	99 1 ³ Π_g	5.17	-	
1 ¹ Π_g	90	$\pi_g \rightarrow \sigma_g$	5.39		5.23	1 _g	97 1 ¹ Π_g - 3 1 ³ Π_g	5.41	-	
1 ³ Π_u	87	$\pi_u \rightarrow \sigma_g$	5.82		5.85	2 _u	99 1 ³ Π_u	5.78	-	
						1 _u	80 1 ³ Π_u - 20 1 ¹ Π_u	5.82	6.56E-04	
						0 _u ⁻	99 1 ³ Π_u	5.88	-	
						0 _u ⁺	99 1 ³ Π_u	5.88	1.53E-04	
1 ³ Σ_u^+	92	$\sigma_u \rightarrow \sigma_g$	6.11		6.22	1 _u	91 1 ³ Σ_u^+ - 3 1 ¹ Π_u	6.11	7.52E-03	
1 ¹ Π_u	88	$\pi_u \rightarrow \sigma_g$	6.13	1.73E-02	5.92	0 ₋	98 1 ³ Σ_u^+	6.13	-	6.21 ^b
						1 _u	66 1 ¹ Π_u - 20 1 ³ Π_u - 3 1 ³ Σ_u^+	6.17	1.94E-02	
1 ³ Σ_g^+	82	$\sigma_g \rightarrow \sigma_g$	6.92		7.00	1 _g	99 1 ³ Σ_g^+	6.93	-	
	6	$\pi_u \rightarrow \pi_u$				0 _g ⁻	99 1 ³ Σ_g^+	6.93	-	
							0 _g ⁺	99 1 ³ Σ_g^+	6.93	
1 ¹ Σ_u^+	50	$\pi_g \rightarrow \pi_u$	6.99	8.29E-02	6.96	0 _u ⁻	86 1 ¹ Σ_u^+ - 16 1 ³ Σ_u	6.95	4.87E-02	
1 ¹ Σ_u^+	40	$\sigma_u \rightarrow \sigma_g$								
2 ³ Σ_u^+	90	$\pi_g \rightarrow \pi_u$	7.02		7.02	1 _u ⁺	71 2 ³ Σ_u^+ - 3 1 ¹ Σ_u	6.85	-	
						0 _u ⁻	71% 2 ³ Σ_u^+ - 3 1 ¹ Σ_u	6.94	-	
1 ³ Δ_u	90	$\pi_g \rightarrow \pi_u$	7.16		7.18	2 _u	46 1 ¹ Δ_u - 54 1 ³ Δ_u	6.91	-	
						1 _u	99 1 ³ Δ_u	6.99	1.06E-04	
						3 _u	99 1 ³ Δ_u	7.37	-	
						2 _u	54 1 ¹ Δ_u - 49 1 ³ Δ_u	7.49	-	
1 ¹ Δ_u	90	$\pi_g \rightarrow \pi_u$	7.21		7.20					
Bond Length Hg-Cl (Å) 2.238									2.240 ^c 2.252 ^d	

Table S6.3. Vertical electronic transitions of CH₃HgX (X = Cl, Br, I, and SCH₃) computed at the DKH3-SOC-MS-CASPT2-(12,10)/ANO-RCC-VTZP level of theory at 4.0 Å Hg-C separated distances from the ground state geometry. Vertical excitation in eV (ΔE) and oscillator strengths (f) for the spin-free (SF) and spin-orbit (SO) states (left and right parts, respectively), the main orbital excitation which characterizes the SF states (column 3, only weights larger than 1% are given), and the main SF states contributing to the SO states (column 7, only weights larger than 3% are provided).

Molecule	Spin Free States				Spin Orbit States	
	SF State	Weight (%)	Excitation	ΔE (eV)	SF- weight (%)	ΔE (eV)
CH ₃ HgCl	S ₀	90	Closed shell	3.29	100 S ₀	3.30
		2	$\sigma 2 \rightarrow \sigma$			
	T ₁	83	$\sigma 2 \rightarrow \sigma$	3.59	100 T ₋₁	3.61
4		$\sigma 1 \rightarrow \sigma$	100 T ₀		3.61	
	S ₁	51	$\pi \rightarrow \sigma$	6.26	80 S ₁ 18 T ₂	6.26
		22	N/A			
CH ₃ HgBr	S ₀	90	Closed shell	3.16	S ₀ 100	3.18
		4	$\sigma 2 \rightarrow \sigma$			
	T ₁	88	$\sigma 2 \rightarrow \sigma$	3.36	100 T ₁	3.37
3		$\sigma 1 \rightarrow \sigma$	100 T ₁		3.37	
	S ₁	44	$\pi \rightarrow \sigma$	5.72	55 S ₁ 44 T ₂	5.61
		44	NA			
CH ₃ HgI	S ₀	89	Closed shell	3.05	99 S ₀	3.06
		3	$\sigma 2 \rightarrow \sigma$			
			3	$\sigma 1 \rightarrow \sigma$		
T ₁	90	$\sigma 2 \rightarrow \sigma$	3.23	99 T ₁	3.24	
	3	$\sigma 1 \rightarrow \sigma$		99 T ₁	3.24	
	S ₁	43	π -sig	5.27	53 S ₁ 48 T ₂	5.03
		51	NA			
CH ₃ HgSCH ₃	S ₀	80	Closed shell	3.06	100 S ₀	3.07
		14	$\sigma 2 \rightarrow \sigma$			
	T ₁	93	$\sigma 2 \rightarrow \sigma$	3.25	100 T ₁	3.27
2		$\sigma 1 \rightarrow \sigma$	100 T ₁		3.27	
	S ₁	38	$\pi \rightarrow \sigma$	5.10	99 S ₁	5.11
		60	N/A			

Table S6.4. Vertical electronic transitions of HgX_2 ($X = \text{Cl}, \text{Br}, \text{I}, \text{ and } \text{SCH}_3$) computed at the DKH3-SOC-MS-CASPT2-(12,10)/ANO-RCC-VTZP level of theory at 4.0 Å Hg-X separated distances from the ground state geometry. Vertical excitation in eV (ΔE) and oscillator strengths (f) for the spin-free (SF) and spin-orbit (SO) states (left and right parts, respectively), the main orbital excitation which characterizes the SF states (column 3, only weights larger than 1% are given), and the main SF states contributing to the SO states (column 7, only weights larger than 3% are provided).

Molecule	Spin Free States				Spin Orbit States	
	SF State	Weight (%)	Excitation	ΔE (eV)	SF- weight (%)	ΔE (eV)
HgCl ₂	S ₀	34	closed shell	3.52	S ₀ 98% S ₀	3.52
		56	$\sigma_u \rightarrow \sigma_g$			
	S ₁	90	$\pi_g \rightarrow \sigma_g$	3.79	S ₁ 64% S ₁ 34% T ₁ 1% T ₂	3.77
		T ₁	90		$\pi_g \rightarrow \sigma_g$	T ₋₁ 99% T ₁
	T ₀ 51% T ₂ 38% T ₁ 11% S ₁			3.79		
T ₂	91	$\sigma_u \rightarrow \sigma_g$	3.83	T ₊₁ 54% T ₂ 45% T ₁	3.79	
				T ₋₁ 98% T ₁	3.85	
T ₀ 48% T ₂ 24% S ₁ 28% T ₁	3.89					
T ₊₁ 45% T ₂ 54% T ₁	3.89					
HgBr ₂	S ₀	20	closed shell	3.16	S ₀ 84 S ₀ 16 T ₁	3.10
		73	$\sigma_u \rightarrow \sigma_g$			
	S ₁	92	$\pi_g \rightarrow \sigma_g$	3.34	S ₁ 65 S ₁ 29 T ₁	3.23
		T ₁	92		$\pi_g \rightarrow \sigma_g$	T ₋₁ 99 T ₁
	T ₀ 58 T ₂ 37 T ₁ 4 S ₁			3.26		
T ₂	92	$\sigma_u \rightarrow \sigma_g$	3.39	T ₊₁ 64 T ₂ 35 T ₁	3.26	
				T ₋₁ 83 T ₁ 16 S ₁	3.60	
T ₀ 37 T ₂ 30 S ₁ 33 T ₁	3.66					
T ₊₁ 35 T ₂ 64 T ₁	3.67					
HgI ₂	S ₀	21	closed shell	2.97	S ₀ 74 S ₀ 25 T ₁	2.79
		68	$\sigma_u \rightarrow \sigma_g$			
	S ₁	90	$\pi_g \rightarrow \sigma_g$	3.12	S ₁ 51 S ₁ 47 T ₁	2.89
		T ₁	90		$\pi_g \rightarrow \sigma_g$	T ₋₁ 98 T ₁
	T ₀ 64 T ₂ 19 T ₁ 16 S ₁			2.91		
T ₂	90	$\sigma_u \rightarrow \sigma_g$	3.15	T ₊₁ 64 T ₂ 34 T ₁	2.91	
				T ₋₁ 73 T ₁ 25 S ₀	3.68	
T ₀ 34 T ₂ 32 S ₁ 32 T ₁	3.75					
T ₊₁ 34 T ₂ 64 T ₁	3.75					
Hg(SCH ₃) ₂	S ₀	20	closed shell	2.70	S ₀ 99 S ₀	2.71
		71	$\sigma_u \rightarrow \sigma_g$			
	S ₁	92	$\pi_g \rightarrow \sigma_g$	2.94	S ₁ 78 S ₁ 21 T ₁	2.93
		T ₁	92		$\pi_g \rightarrow \sigma_g$	T ₋₁ 87 T ₁ 12 T ₂
	T ₀ 87 T ₁ 12 T ₂			2.97		
T ₂	91	$\sigma_u \rightarrow \sigma_g$	3.01	T ₊₁ 78 T ₁ 21 S ₁	2.99	
				T ₋₁ 99 T ₂	3.03	
T ₀ 87 T ₂ 12 T ₁	3.03					
T ₊₁ 27 T ₂ 12 T ₁	3.03					

Table S6.5. Vertical electronic transitions of CH₃HgBr computed at the DKH3-SOC-MS-CASPT2-(8,8)/ANO-RCC-VTZP level of theory at the ground state geometry computed at the DKH3-MP2. Vertical excitation in eV (ΔE) and oscillator strengths (f) for the spin-free (SF) and spin-orbit (SO) states (left and right parts, respectively), the main orbital excitation which characterizes the SF states (column 2, only weights larger than 5% are given), and the main SF states contributing to the SO states (column 6, only weights larger than 3% are provided). **The bolded SO spin free percent contribution indicates significant singlet and triplet mixing and it is no longer possible to determine the singlet versus triplet states.**

Spin Free States					Spin Orbit States			Exp.	
SF State	Weight (%)	Excitation	ΔE (eV)	f (au)	SF-Weight (%)	ΔE (eV)	f (au)	ΔE (eV)	
1 ³ E	94	$\pi \rightarrow \sigma$	5.70		95 1 ³ E 73 1 ³ E - 18 2 ¹ E - 4 2 ³ E 83 1 ³ E - 13 2 ³ E	5.55 5.60 5.88	3.29E-06 2.60E-03 4.86E-03		
2 ³ E	60 21	$\sigma 2 \rightarrow \sigma$ $\sigma 1 \rightarrow \sigma$	5.71		73 2 ³ E - 25 1 ³ E 82 2 ³ E - 14 1 ¹ E 82 2 ³ E - 14 1 ¹ E	5.68 5.70 5.70	4.38E-06 3.31E-03 3.28E-03		
1 ¹ E	95	$\pi \rightarrow \sigma$	5.88	1.50E-02	58 1 ¹ E - 22 1 ³ E - 12 2 ³ E - 5 3 ³ E	5.98	7.24E-03	6.19 ^a	
1 ³ A ₁	93	$\pi \rightarrow \pi$	6.39		66 1 ³ A ₁ - 25 1 ³ A ₂ - 5% 1 ¹ E 66 1 ³ A ₁ - 25 1 ³ A ₂ - 5% 1 ¹ E 78 1 ³ A ₁ - 5 3 ³ E - 4 2 ¹ A ₁	6.21 6.21 6.41	8.42E-04 9.18E-04 2.12E-06		
3 ³ E	95	$\pi \rightarrow \pi$	6.55		49 3³E 43% 3¹E - 2 1³E* 66 3 ³ E 15% 4 ¹ E - 12 4 ³ E 92 3 ³ E 3% 4 ¹ E - 3 4 ³ E	6.27 6.47 6.65	5.06E-06 8.38E-05 7.40E-04		
2 ¹ E	21 53 15	$\sigma 2 \rightarrow \sigma$ $\pi \rightarrow \pi$ $\sigma 1 \rightarrow \sigma$	6.55	7.87E-02	89 2 ¹ E - 8 4 ³ E	6.56	8.66E-02		
3 ¹ E	94	$\pi \rightarrow \pi$	6.61	6.98E-06	31 3¹E - 26 3³E - 10 1²A₂ - 18 4³E*	6.91	1.60E-04		
Bond length Hg-C (Å)								2.055	2.073 ^{b,c}
Bond Length Hg-Br (Å)								2.407	2.406 ^{b,c}

Table S6.6. Vertical electronic transitions of CH₃HgI computed at the DKH3-SOC-MS-CASPT2-(8,8)/ANO-RCC-VTZP level of theory at the ground state geometry computed at the DKH3-MP2. Vertical excitation in eV (ΔE) and oscillator strengths (f) for the spin-free (SF) and spin-orbit (SO) states (left and right parts, respectively), the main orbital excitation which characterizes the SF states (column 2, only weights larger than 5% are given), and the main SF states contributing to the SO states (column 6, only weights larger than 3% are provided). **The bolded SO spin free percent contribution indicates significant singlet and triplet mixing and it is no longer possible to determine the singlet versus triplet states.**

Spin Free States					Spin Orbit States			Exp.
SF State	Weight (%)	Excitation	ΔE (eV)	f (au)	SF Weight (%)	ΔE (eV)	f (au)	ΔE (eV)
1 ³ E	93	$\pi \rightarrow \sigma$	5.19		97 1 ³ E – 2 3 ³ E 65 1³E – 30 1¹E* 74 1 ³ E – 16 2 ³ E	4.92 4.98 5.50	5.73E-08 2.73E-03 2.80E-02	
2 ³ E	60 21	$\sigma 2 \rightarrow \sigma$ $\sigma 1 \rightarrow \sigma$	5.27		65 2 ³ E – 32 1 ³ E 72 2³E – 21 1¹E* 72 2³E – 21 1¹E*	5.13 5.14 5.14	1.95E-07 1.69E-03 1.69E-03	
1 ¹ E	93	$\pi \rightarrow \sigma$	5.36	8.96E-03	32 1¹E – 25 2³E – 11 1³E – 4 1³A₁*	5.75	2.13E-03	5.39 ^{a,b}
1 ³ A ₁	93	$\pi \rightarrow \pi$	5.93		59 1 ³ A ₁ – 30 1 ³ A ₂ – 10 1 ¹ E 59 1 ³ A ₁ – 30 1 ³ A ₂ – 10 1 ¹ E 76 1 ³ A ₁ – 12 4 ³ E – 10 1 ³ E	5.61 5.61 5.93	1.21E-03 1.21E-03 3.71E-08	
3 ³ E	95	$\pi \rightarrow \pi$	6.07		51 3³E 46 1¹E* 56 3³E – 18 4¹E – 12 4¹E* 99 3 ³ E	5.66 6.00 6.06	1.75E-06 1.74E-03 8.15E-06	
2 ¹ E	14 68 11	$\sigma 2 \rightarrow \sigma$ $\pi \rightarrow \pi$ $\sigma 1 \rightarrow \sigma$	6.12	1.64E-02	48 2¹E – 34 4³E – 16 1³A₂*	6.11	2.72E-05	6.01 ^{a,b}
3 ¹ E	94	$\pi \rightarrow \pi$	6.13	4.82E-06	30 3³E – 33 3¹3E – 32 4³E*	6.45	5.78E-06	
Bond length Hg–C (Å)			2.064					2.087 ^{c,d}
Bond Length Hg–I (Å)			2.580					2.528 ^{c,d}

Table S6.7. Vertical electronic transitions of HgBr₂ computed at the DKH3-SOC-MS-CASPT2-(8,8)/ANO-RCC-VTZP level of theory at the ground state geometry computed at the DKH3-MP2. Vertical excitation in eV (ΔE) and oscillator strengths (f) for the spin-free (SF), the main orbital excitation which characterizes the SF states (column 2, only weights larger than 5% are given). For SO states and SF contributions please see ref⁷

SF State	Weight (%)	Excitation	ΔE (eV)	f (au)	ANO-RCC-VQZP ^a	Expt.
1 ³ Π_g	90	$\pi_g \rightarrow \sigma_g$	4.57		4.56	
1 ¹ Π_g	90	$\pi_g \rightarrow \sigma_g$	4.83		4.75	
1 ³ Π_u	88	$\pi_u \rightarrow \sigma_g$	5.18		5.17	
1 ³ Σ_u^+	93	$\sigma_u \rightarrow \sigma_g$	5.44		5.46	
1 ¹ Π_u	88	$\pi_u \rightarrow \sigma_g$	5.45	2.01E-02	5.34	5.48 ^b
2 ³ Σ_u^+	91	$\pi_g \rightarrow \pi_u$	6.47		6.47	
1 ¹ Σ_u^+	50	$\pi_g \rightarrow \pi_u$	6.41	1.15E-01	6.35	6.58 ^b
	40	$\sigma_u \rightarrow \sigma_g$				
1 ³ Δ_u	91	$\pi_g \rightarrow \pi_u$	6.61		6.61	
1 ¹ Δ_u	90	$\pi_g \rightarrow \pi_u$	6.64		6.63	
1 ³ Σ_g^+	54	$\sigma_g \rightarrow \sigma_g$	6.68		6.70	
	36	$\pi_u \rightarrow \pi_u$				
Bond Length Hg-Br (Å)						2.374 ^c

Table S6.8. Vertical electronic transitions of HgI₂ computed at the DKH3-SOC-MS-CASPT2-(8,8)/ANO-RCC-VTZP level of theory at the ground state geometry computed at the DKH3-MP2. Vertical excitation in eV (ΔE) and oscillator strengths (f) for the spin-free (SF), the main orbital excitation which characterizes the SF states (column 2, only weights larger than 5% are given). For SO states and SF contributions please see ref⁷

SF State	Weight (%)	Excitation	ΔE (eV)	f (au)	ANO-RCC-VQZP ^a	Expt.
1 ³ Π_g	90	$\pi_g \rightarrow \sigma_g$	3.90		4.04	
1 ¹ Π_g	88	$\pi_g \rightarrow \sigma_g$	4.12		4.17	
1 ³ Π_u	92	$\pi_u \rightarrow \sigma_g$	4.34		4.53	
1 ³ Σ_u^+	92	$\sigma_u \rightarrow \sigma_g$	4.60		4.87	
1 ¹ Π_u	87	$\pi_u \rightarrow \sigma_g$	4.58	7.75E-03	4.65	4.69 ^b
2 ³ Σ_u^+	90	$\pi_g \rightarrow \pi_u$	5.85		5.83	
1 ¹ Σ_u^+	42	$\pi_g \rightarrow \pi_u$	5.67	1.70E-01	5.73	5.96 ^b
	48	$\sigma_u \rightarrow \sigma_g$				
1 ³ Δ_u	89	$\pi_g \rightarrow \pi_u$	5.98		5.96	
1 ¹ Δ_u	90	$\pi_g \rightarrow \pi_u$	6.01		5.96	
1 ³ Σ_g^+	25	$\sigma_g \rightarrow \sigma_g$	6.06		6.12	
	64	$\pi_u \rightarrow \pi_u$				
Bond Length Hg-I (Å)		2.369				2.554,2.559 ^c

References

1. Roos, B. O., Taylor, P. R. & Siegbahn, P. E. M. A Complete Active Space SCF Method (CASSCF) Using a Density Matrix Formulated Super-CI Approach. *Chem. Phys.* **48**, 1680 (1980).
2. Finley, J., Malmqvist, P. Å., Roos, B. O. & Serrano-Andrés, L. The multi-state CASPT2 method. *Chem. Phys. Lett.* **288**, 299–306 (1998).
3. Andersson, K., Malmqvist, P. Å. & Roos, B. O. Second-order perturbation theory with a complete active space self-consistent field reference function. *J. Chem. Phys.* **96**, 1218–1226 (1992).
4. Heß, B. A., Marian, C. M., Wahlgren, U. & Gropen, O. A mean-field spin-orbit method applicable to correlated wavefunctions. *Chem. Phys. Lett.* **251**, 365–371 (1996).
5. Reiher, M. & Wolf, A. Exact decoupling of the Dirac Hamiltonian. I. General theory. *J. Chem. Phys.* **121**, 2037–2047 (2004).
6. Peng, D. & Hirao, K. An arbitrary order Douglas-Kroll method with polynomial cost. *J. Chem. Phys.* **130**, (2009).
7. Sitkiewicz, S. P., Rivero, D., Oliva-Enrich, J. M., Saiz-Lopez, A. & Roca-Sanjuán, D. Ab initio quantum-chemical computations of the absorption cross sections of HgX 2 and HgXY (X, y = Cl, Br, and I): Molecules of interest in the Earth's atmosphere. *Phys. Chem. Chem. Phys.* **21**, 455–467 (2019).
8. Mewes, J. M. *et al.* Experimental benchmark data and systematic evaluation of two a posteriori, polarizable-continuum corrections for vertical excitation energies in solution. *J. Phys. Chem. A* **119**, 5446–5464 (2015).
9. Penfold, T. J., Gindensperger, E., Daniel, C. & Marian, C. M. Spin-Vibronic Mechanism for Intersystem Crossing. *Chem. Rev.* **118**, 6975–7025 (2018).

Chapter 7 Conclusion

The investigation of mercury (Hg) extends back to antiquity, and was carried out by alchemists vying to transmute base metals into gold and doctors working to treat disease. Hg continues to be used in modern times in manufacturing applications such as batteries and lightbulbs and in artisanal gold mining activities throughout the world. Despite the long and rich history of “element 80,” many aspects of the underlying environmental chemistry remain poorly understood. The study of the environmental photochemistry of Hg reported in this dissertation has expanded our understanding and applicability of Hg stable isotope measurements. Our work has also opened new avenues of future research. Based on the body of work presented here, the authors hope to inspire the investigation of the excited states of environmentally relevant Hg complexes to gain a better understanding of the global biogeochemical cycle of Hg and of its unusual MIF behavior and underlying mechanisms.

7.1 Summary of Key Findings

7.1.1 The marine biogeochemical cycle of Hg

Throughout the course of the research reported in this dissertation, a number of important advancements have been realized in our understanding of the marine biogeochemical cycle of Hg. These break-throughs were possible by the collaborative effects of isotope geochemists at the University of Michigan, oceanographers at the University of Hawai’i, and biologists and microbiologists at Rutgers University. Our collective efforts resulted in the first measurements of open ocean precipitation, marine particles, and zooplankton.

At Station ALOHA in the North Pacific Subtropical Gyre (Chapter 2), we demonstrated that rainfall represents the major source of Hg to marine pelagic waters. We also found that the main source of Hg below the mixed layer is particulate Hg, that the isotopic composition of zooplankton and particles indicates demethylation of MeHg in the water column, and that surface zooplankton track diurnal photochemical degradation of MeHg.

Intrigued by the diurnal and elevated $\Delta^{199}\text{Hg}$ signatures in surface zooplankton we investigated the incorporation of MeHg into marine zooplankton in the Central and North Pacific Ocean. Zooplankton are the entry point of MeHg in the marine foodweb (Chapter 4). The zooplankton isotopic composition demonstrates that only small inorganic complexes of MeHg are available for uptake and bioaccumulation in marine waters. MeHg coordinated to larger organic complexes are not bioavailable to plankton, and therefore photochemical degradation of Hg complexed to dissolved organic matter does not reduce the pool of MeHg that ends up in pelagic fish. Instead, the pool of MeHg available for bioaccumulation is predominately reduced by intracellular photochemical degradation by phytoplankton. Finally, we have greatly expanded our understanding of the marine Hg cycle and we have identified key mechanisms that control the mobility and toxicity of MeHg prior to bioaccumulation in marine fish.

7.1.2 Photochemical decomposition and reduction of Hg

In addition to building a greater understanding of the marine biogeochemical cycle of Hg, the research presented here has elucidated important aspects of the photochemical transformations of Hg that lead to the $\Delta^{199}\text{Hg}$ values preserved in biological samples. These results have improved our ability to catalog Hg stable isotopes signatures in natural environments, while also increasing our understanding of the controlling factors of photochemical decomposition and reduction of Hg that limit the Hg available to aquatic foodwebs in surface waters.

First, we investigated the photochemistry of MeHg by analyzing the isotopic composition of flying fish living in the surface ocean (Chapter 3). There are well known drawbacks to applying laboratory and field experiments to investigate chemical reactions in marine environments. Laboratory experiments cannot fully simulate the conditions of the open ocean, and this it is difficult to get a complete understanding of the controlling parameters of naturally occurring chemical reactions. While *in situ* field experiments may be successful at estimating degradation rates in realistic environmental conditions, the experiments are not adequate to fully constrain the controlling factors of the reaction. The Hg stable isotope composition of natural samples record a unique photochemistry signature that incorporates all the intricacies of the environment. The strong correlation between $\Delta^{199}\text{Hg}$ and $\Delta^{201}\text{Hg}$ found in flying fish across wide regions of the Atlantic and Pacific Ocean and in zooplankton and pelagic fish in the North Pacific Subtropical Gyre^{1,2} suggest that the role of solar irradiance, dissolved organic matter, and water chemistry may alter the MeHg photodecomposition kinetics but not the reaction mechanism. We suggest that if there were multiple MeHg photodecomposition pathways the open ocean flying fish would not display a strong complementary correlation between $\Delta^{199}\text{Hg}$ to $\delta^{202}\text{Hg}$ (Fig 2), because $\delta^{202}\text{Hg}$ would vary with the different decomposition pathways.

Motivated by the strong correlations between $\Delta^{199}\text{Hg}$ and $\Delta^{201}\text{Hg}$, and between $\Delta^{199}\text{Hg}$ and $\delta^{202}\text{Hg}$ in natural samples we investigated the Hg isotope fractionation during the photochemical reduction of Hg(II) complexed to organic ligands or chlorine (Chapter 4). Our experiments demonstrated that the sign and rate of magnetic isotope effects (MIE) depend on the complexing ligand, dissolved oxygen, and pH. Importantly, we found that MDF and MIE are induced at different steps in the reaction, highlighting the potential role of photophysical processes in MIE. Finally, we demonstrated that in environments with elevated Cl concentrations, where HgCl_2

species dominate, photochemical reduction does not yield MIE. This implies that in surface marine waters the photoreduction of inorganic Hg will not result in significant MIE.

In our efforts to understand the dominant mechanism that degrades the pool of Hg available to marine organisms and results in the elevated $\Delta^{199}\text{Hg}$, we investigated the photochemical decomposition of MeHg in seawater (Chapter 5). The $\Delta^{199}\text{Hg}$ and $\delta^{202}\text{Hg}$ from these experiments suggest there are two distinct pools of MeHg available for photochemical decomposition in marine waters. The experiments of MeHg coordinated to organic ligands resulted in a $\Delta^{199}\text{Hg}/\delta^{202}\text{Hg}$ slope of 4.1, while the group of experiments that included natural seawater from Station ALOHA and deionized water had a $\Delta^{199}\text{Hg}/\delta^{202}\text{Hg}$ slope of 11.3. This much higher slope represents the photochemical decomposition of reactive inorganic complexes of MeHg (MeHg^+ and MeHgOH). Large zooplankton and flying fish have a $\Delta^{199}\text{Hg}/\delta^{202}\text{Hg}$ slope closer to 4.1 suggesting that the isotopic signatures preserved in marine organisms are controlled by photodecomposition of MeHg coordinated to organic ligands. We concluded that these Hg isotopic signatures are a result of intracellular photodecomposition of MeHg by phytoplankton, because in open ocean waters there are not enough thiol organic ligands to coordinate with Hg in seawater.

7.1.3 The Hg magnetic isotope effect

$\Delta^{199}\text{Hg}$ and $\Delta^{201}\text{Hg}$ signatures have been proven to be excellent tools for tracking and investigating the biogeochemical cycle of Hg. However, it was unclear why Hg complexes were susceptible to this type of MIF and what aspects of photochemistry $\Delta^{199}\text{Hg}$ values represented. In Chapter 6, we investigated computationally the photolysis of CH_3HgX and HgX_2 complexes ($X = \text{Cl}, \text{Br}, \text{I}, \text{and } \text{SCH}_3$). Our simulations demonstrated that CH_3HgX will typically result in (+) MIE, while the photolysis of HgX_2 may yield (+) and (-) MIE. This explains why (-) MIE associated with CH_3Hg complexes has never been recorded experimentally or in natural samples, while (-)

MIE has been exclusively recorded in samples associated with HgX_2 type complexes (Blum et al., 2014 see figure 2).³ Our results also demonstrate that Hg complexes with heavy atoms like Br and I may not exhibit MIE due to significant spin-orbit coupling compared to Cl and SCH_3 . Finally, we suggest that the photolysis of $\text{CH}_3\text{HgSCH}_3$ and $\text{Hg}(\text{SCH}_3)_2$ may contribute to the MIE recorded in nature because these complexes absorb light in the sunlight spectrum. However, the MIE by $\text{Hg}(\text{SCH}_3)_2$ may be limited by intersystem crossing induced by spin-orbit interactions at Hg-S bond separated distances. The competition between spin-orbit coupling and hyperfine coupling in separated radical pairs explain why in natural samples the anomalies in ^{199}Hg and ^{201}Hg associated with the photolysis of HgX_2 type complexes are significantly reduced compare to MeHgX .³

7.2 Future Directions

The results of this dissertation raise a number of new and exciting scientific questions that need to be addressed to advance our understanding of the biogeochemical cycle of Hg. We presented substantial evidence for, and highlight the importance of, gaining a greater understanding of dissolved Hg speciation in marine waters, intracellular photodecomposition of MeHg by phytoplankton, and the mechanism controlling the magnetic isotope effect. In our goal of understanding the environmental chemistry of Hg we propose a multidisciplinary approach combining experiment, theory and field observations.

7.2.1 Experimental: Photochemistry and Phytoplankton Isotope Experiments

Throughout this dissertation, we indicated that once dissolved MeHg is inside phytoplankton the elevated intracellular thiol concentrations facilitate multivalent complexation to thiol ligands to $\text{MeHg}(\text{thiol})_{2-3}$ similarly to the $\text{Hg}(\text{II})$ species⁴, which leads to photodegradation resulting in the same isotopic signature preserved in surface large zooplankton and pelagic marine

fish.² However, there are not any experimental studies of higher order MeHgthiol complexes or photodegradation; and phytoplankton intracellular photodegradation of MeHg has only been investigated for one strain of marine phytoplankton (*Isocrysis galbana*).⁵

To understand MeHg transformations at the base of the food web and to test the hypothesis that phytoplankton intracellular MeHg photodegradation is mediated by MeHg(thiol)₂₋₃ complexes, we propose to investigate the Hg MIF signatures during the photochemical degradation of multiple MeHg(thiol)₁₋₃ complexes and to catalog the Hg stable isotope signatures of intracellular photodegradation of a wide range of species of phytoplankton. In particular, it is important to extend the study of intracellular photodegradation of MeHg to marine diatoms, the most abundant species of phytoplankton in marine waters.

It is also critical to enhance our investigations of MeHg speciation in marine waters and in phytoplankton. There has been some research using X-ray absorption fine structure spectroscopy (using synchrotron radiation) to investigate the complexation of inorganic Hg(II) in dissolved organic matter.⁶⁻⁸ We suggest this would be an appropriate technique for investigating the speciation of MeHg within marine phytoplankton to ascertain whether MeHg may form higher multivalent coordination complexes with thiols ligands.

7.2.2 Theoretical: Mass Independent Hg Stable Isotope Fractionation

To accurately interpret $\Delta^{199}\text{Hg}$ and $\Delta^{201}\text{Hg}$ signatures in nature we must investigate the susceptibility of environmentally relevant MeHg complexes to undergo direct photolysis and evaluate the role of relativistic effects on the mechanism for the MIE. We propose detailed studies of the photochemical decomposition of MeHg coordinated to multiple thiol complexes using high level quantum chemical *ab initio* methods with relativistic effects. This will allow us to determine the likelihood of the MIE by conducting quantum dynamic calculations to determine non-adiabatic

couplings (e.g conical intersection and intersystem crossing). Subsequently, we believe investigations of the role of hyperfine coupling with inclusion of relativistic effects is crucial for determining the extend and rate of the MIE in natural samples.

7.2.3 Field observations: Analysis of Hg Concentrations and Isotopes of Marine Phytoplankton and Zooplankton

To date there have not been any Hg stable isotope measurements of marine phytoplankton and marine phytoplankton are a critical part of the biogeochemical cycle of Hg. It has been shown in the North Pacific Ocean that small surface dwelling (25 m; 0-2 mm) zooplankton exhibit a $\Delta^{199}\text{Hg}$ diurnal signature and that Hg stable isotope signatures ($\Delta^{199}\text{Hg}$, $\Delta^{201}\text{Hg}$, and $\delta^{202}\text{Hg}$) are quite different than the larger (1-5 mm) and deeper (125-1250 m) zooplankton.² Apart from the different bulk Hg isotopic composition, the larger and deeper zooplankton do not exhibit any diurnal trends and $\Delta^{199}\text{Hg}$ values are invariant below the twilight zone. These results warrant further study to determine the role of phytoplankton, up to the depths that small zooplankton exhibit diurnal trends, and why surface large zooplankton have a substantially different Hg stable isotopic composition than small zooplankton.

7.2.4 Final Remarks

The research work presented here suggests that Hg stable isotopes could be used to investigate key aspects of photochemical reactions occurring in nature, in a similar manner as C and H isotopes have been used for determining reaction mechanisms relevant to environmental and biomedical science.⁹⁻¹² This will ameliorate a major limitation in the study of biogeochemical cycles, where laboratory experiments cannot mimic complex natural environments and thus limits the interpretation of environmental data. To develop this methodology, it is imperative to improve Hg stable isotope theory in conjunction with specific experiments; this will allow the scientific

community to use Hg stable isotopes in organisms to determine chemical reaction mechanisms, rates, and relevant Hg species in the environment. A better understanding of the MIE will also have significant impact in chemistry by improving our understanding of the radical pair mechanism. The radical pair mechanism is thought to mediate the light-dependent magnetic compass in birds¹³ and operate in photosynthetic reaction centers of phytoplankton.¹⁴ However, no studies of the radical pair mechanism has incorporated relativistic effects or heavy elements. Finally, our research suggests that it is of great importance to improve our understanding of MeHg and thiol ligands in natural environments, given their central role in controlling the mobility and toxicity of Hg. Centuries after Geber formulated one of the first descriptions of a chemical bond by sublimating Hg and sulfur¹⁵, we still have much to learn about these two elements.

References

1. Blum, J. D., Popp, B. N., Drazen, J. C., Anela Choy, C. & Johnson, M. W. Methylmercury production below the mixed layer in the North Pacific Ocean. *Nat. Geosci.* **6**, 879–884 (2013).
2. Motta, L. C. *et al.* Mercury cycling in the North Pacific Subtropical Gyre as revealed by mercury stable isotope ratios. *Global Biogeochem. Cycles* 2018GB006057 (2019). doi:10.1029/2018GB006057
3. Blum, J. D., Sherman, L. S. & Johnson, M. W. Mercury Isotopes in Earth and Environmental Sciences. *Annu. Rev. Earth Planet. Sci.* **42**, 249–269 (2014).
4. Jalilehvand, F., Leung, B. O., Izadifard, M. & Damian, E. Mercury(II) cysteine complexes in alkaline aqueous solution. *Inorg. Chem.* **45**, 66–73 (2006).
5. Kritee, K., Motta, L. C., Blum, J. D., Tsui, M. T. & Reinfelder, J. R. Photo-microbial visible light-induced magnetic mass independent fractionation of mercury in a marine microalga. *Earth Sp. Chem.* (2017). doi:10.1021/acsearthspacechem.7b00056
6. Song, Y. *et al.* Thermodynamics of Hg(II) Bonding to Thiol Groups in Suwannee River Natural Organic Matter Resolved by Competitive Ligand Exchange, Hg L III -Edge EXAFS and ¹H NMR Spectroscopy. *Environ. Sci. Technol.* **52**, 8292–8301 (2018).

7. Skyllberg, U., Qian, J. & Frech, W. Combined XANES and EXAFS Study on the Bonding of Methyl Mercury to Thiol Groups in Soil and Aquatic Organic Matter. *Phys. Scr.* 894 (2005). doi:10.1238/physica.topical.115a00894
8. Skyllberg, U., Bloom, P. R., Qian, J., Lin, C. M. & Bleam, W. F. Complexation of mercury(II) in soil organic matter: EXAFS evidence for linear two-coordination with reduced sulfur groups. *Environ. Sci. Technol.* **40**, 4174–4180 (2006).
9. Schnedermann, C. *et al.* Evidence for a vibrational phase-dependent isotope effect on the photochemistry of vision. *Nat. Chem.* **10**, 1–7 (2018).
10. Lu, S., Li, W. W., Rotem, D., Mikhailova, E. & Bayley, H. A primary hydrogen-deuterium isotope effect observed at the single-molecule level. *Nat. Chem.* **2**, 921–928 (2010).
11. Kahsai, A. W., Rajagopal, S., Sun, J. & Xiao, K. Monitoring protein conformational changes and dynamics using stable-isotope labeling and mass spectrometry. *Nat. Protoc.* **9**, 1301–1319 (2014).
12. Hay, S. & Scrutton, N. S. Good vibrations in enzyme-catalysed reactions. *Nat. Chem.* **4**, 161–168 (2012).
13. Hore, P. J. & Mouritsen, H. The Radical-Pair Mechanism of Magnetoreception. *Annu. Rev. Biophys.* **45**, 299–344 (2016).
14. Zill, J. C. *et al.* Photo-CIDNP in the Reaction Center of the Diatom *Cyclotella meneghiniana* Observed by ¹³C MAS NMR the solid-state photo-CIDNP effect in a new kingdom of the tree of life. *Zeitschrift für Phys. Chemie* **231**, 347–367 (2017).
15. Newman, W. R. *The ‘Summa perfectionis’ of Pseudo-Geber: A Critical Edition, Translation and Study.* William R. Newman. (E.J Brill, 1991). doi:10.2307/2865163